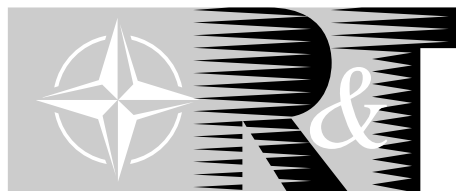


NORTH ATLANTIC TREATY ORGANISATION

RTO-EN-027



RESEARCH AND TECHNOLOGY ORGANISATION

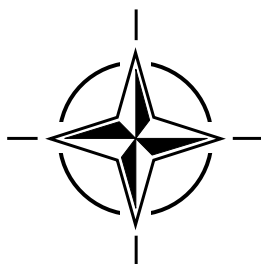
BP 25, 7 RUE ANCELLE, F-92201 NEUILLY-SUR-SEINE CEDEX, FRANCE

RTO LECTURE SERIES 228

Military Application of Space-Time Adaptive Processing

(Les applications militaires du traitement adaptatif espace-temps)

The material in this publication was assembled to support a Lecture Series under the sponsorship of the Sensors and Electronics Technology Panel (SET) and the Consultant and Exchange Programme of RTO presented on 16-17 September 2002 in Istanbul, Turkey, on 19-20 September 2002 in Wachtberg, Germany and on 23-24 September 2002 in Moscow, Russia.



Published April 2003

Distribution and Availability on Back Cover

This page has been deliberately left blank

Page intentionnellement blanche

NORTH ATLANTIC TREATY ORGANISATION



RESEARCH AND TECHNOLOGY ORGANISATION

BP 25, 7 RUE ANCELLE, F-92201 NEUILLY-SUR-SEINE CEDEX, FRANCE

RTO LECTURE SERIES 228

Military Application of Space-Time Adaptive Processing

(Les applications militaires du traitement adaptatif espace-temps)

The material in this publication was assembled to support a Lecture Series under the sponsorship of the Sensors and Electronics Technology Panel (SET) and the Consultant and Exchange Programme of RTO presented on 16-17 September 2002 in Istanbul, Turkey, on 19-20 September 2002 in Wachtberg, Germany and on 23-24 September 2002 in Moscow, Russia.



The Research and Technology Organisation (RTO) of NATO

RTO is the single focus in NATO for Defence Research and Technology activities. Its mission is to conduct and promote cooperative research and information exchange. The objective is to support the development and effective use of national defence research and technology and to meet the military needs of the Alliance, to maintain a technological lead, and to provide advice to NATO and national decision makers. The RTO performs its mission with the support of an extensive network of national experts. It also ensures effective coordination with other NATO bodies involved in R&T activities.

RTO reports both to the Military Committee of NATO and to the Conference of National Armament Directors. It comprises a Research and Technology Board (RTB) as the highest level of national representation and the Research and Technology Agency (RTA), a dedicated staff with its headquarters in Neuilly, near Paris, France. In order to facilitate contacts with the military users and other NATO activities, a small part of the RTA staff is located in NATO Headquarters in Brussels. The Brussels staff also coordinates RTO's cooperation with nations in Middle and Eastern Europe, to which RTO attaches particular importance especially as working together in the field of research is one of the more promising areas of initial cooperation.

The total spectrum of R&T activities is covered by the following 7 bodies:

- AVT Applied Vehicle Technology Panel
- HFM Human Factors and Medicine Panel
- IST Information Systems Technology Panel
- NMSG NATO Modelling and Simulation Group
- SAS Studies, Analysis and Simulation Panel
- SCI Systems Concepts and Integration Panel
- SET Sensors and Electronics Technology Panel

These bodies are made up of national representatives as well as generally recognised 'world class' scientists. They also provide a communication link to military users and other NATO bodies. RTO's scientific and technological work is carried out by Technical Teams, created for specific activities and with a specific duration. Such Technical Teams can organise workshops, symposia, field trials, lecture series and training courses. An important function of these Technical Teams is to ensure the continuity of the expert networks.

RTO builds upon earlier cooperation in defence research and technology as set-up under the Advisory Group for Aerospace Research and Development (AGARD) and the Defence Research Group (DRG). AGARD and the DRG share common roots in that they were both established at the initiative of Dr Theodore von Kármán, a leading aerospace scientist, who early on recognised the importance of scientific support for the Allied Armed Forces. RTO is capitalising on these common roots in order to provide the Alliance and the NATO nations with a strong scientific and technological basis that will guarantee a solid base for the future.

The content of this publication has been reproduced directly from material supplied by RTO or the authors.

Published April 2003

Copyright © RTO/NATO 2003
All Rights Reserved

ISBN 92-837-1064-9



Printed by St. Joseph Print Group Inc.

(A St. Joseph Corporation Company)

1165 Kenaston Street, Ottawa, Ontario, Canada K1G 6S1

Military Application of Space-Time Adaptive Processing

(RTO EN-027 / SET-057)

Executive Summary

Surveillance of the ground by air- and spaceborne sensors has proven to be an essential part of modern warfare. Recent conflicts (Gulf, Bosnia, Afghanistan) have demonstrated the value of information gathered by air- and spaceborne sensors. Among the available sensors, radar has important advantages over optical sensors (IR, Visible), such as day and night/all-weather operation, penetration of foliage, obscurants, smoke and dust. Detection of moving targets on the ground is a primary goal of remote earth observation. However, radar echoes from targets have to compete with strong ground clutter returns. The target detection performance of conventional MTI radar (moving target indication) is strongly degraded by the Doppler spread of the clutter returns induced by the radar platform motion. Therefore, slow targets may not be detectable. For example, for a satellite, a space shuttle or even a fast aircraft most moving targets are ‘slow’. Space-time adaptive processing (STAP) is capable of compensating for the platform motion induced Doppler spread of the clutter echoes so that optimum detection of slow moving targets is possible. Prerequisite for STAP is a coherent radar with a multichannel array antenna. There will be no future air- or spaceborne military radar without STAP capability.

This lecture series gives a comprehensive overview of the broad field of space-time adaptive processing. The series starts with a lecture by Dr. Melvin in which the basics and the theoretical background are expanded. The lecture ‘Doppler properties of airborne clutter’ by Dr. Klemm gives an introduction to the principles of STAP. The impact of the platform motion on the nature of clutter returns is discussed in some detail. Optimum STAP processing is addressed as well. In the second lecture Dr. Farina gives an introduction to the problems of using STAP with synthetic aperture radar which is used for ground and ground target imaging at high resolution. Both papers by Dr. Abramovich deal with theory and application of STAP techniques to Over-The-Horizon (OTH) radar which is used to monitor potential intruders moving towards the borders of the friendly country. This application appears in a new light since the terrorist attacks on the 11 September 2001. The lecture ‘STAP architectures and limiting effects’ by Dr. Klemm deals with suboptimum processor architectures with the capability of clutter rejection in real-time as well as an overview of degrading effects and remedies against them. Dr. Farina’s second paper is focused on STAP processor architectures for real-time processing which is of predominant importance for practical implementation of STAP. In his second lecture Dr. Melvin explains the various radar configurations (airborne, spaceborne, bistatic) and expands on STAP techniques against terrain scattered jamming. In summary, this Lecture Series presents a unique overview of the state of the art in STAP research and offers a variety of material for all those being involved in this magic scientific area, e.g., students, university teachers, researchers, industrial system designers, and military users.

The material in this publication was assembled to support a Lecture Series under the sponsorship of the Sensors and Electronics Technology Panel (SET) and the Consultant and Exchange Programme of RTO presented on 16-17 September 2002 in Istanbul, Turkey, on 19-20 September 2002 in Wachtberg, Germany and on 23-24 September 2002 in Moscow, Russia.

Les applications militaires du traitement adaptatif espace-temps

(RTO EN-027 / SET-057)

Synthèse

La surveillance de la terre par des capteurs aéroportés et spatiaux est devenu un facteur essentiel de la guerre moderne. Des opérations récentes (la guerre du Golfe, la Bosnie, l'Afghanistan), ont démontré l'intérêt des informations fournies par les capteurs aéroportés et spatiaux. Comparé aux autres capteurs (optiques et infrarouges, visibles), le radar offre des performances complémentaires telles qu'un fonctionnement tous temps, jour et nuit, une longue portée et la capacité de voir au travers du feuillage, de la fumée, du brouillard et de la poussière. La détection de cibles mobiles terrestres est l'un des objectifs primaires de la télédétection depuis la terre. Cependant, les retours de cible sont souvent mélangés avec de forts retours de fouillis de sol. Les performances en détection de cibles des radars MTI classiques se trouvent fortement dégradées par l'étalement Doppler des retours de fouillis induits par les mouvements de la plate-forme radar. Les cibles évoluant à basse vitesse peuvent, par conséquent, rester indétectables. Par exemple, depuis un satellite, une navette spatiale ou un avion supersonique, la plupart des cibles mobiles apparaissent comme « lentes ». Le traitement adaptatif espace-temps (STAP) peut compenser l'étalement Doppler des retours de fouillis pour permettre la détection optimale des cibles évoluant à basse vitesse. Le STAP nécessite un radar cohérent associé à une antenne réseau multivoies. Tous les radars aéroportés et spatiaux militaires futurs seront équipés de STAPs.

Ce cycle de conférences présente un tour d'horizon complet du vaste domaine du traitement adaptatif espace-temps. Le programme débute par une communication présentée par le Dr. Melvin, qui expose les principes de base et la théorie fondamentale. La conférence sur « Les caractéristiques Doppler du fouillis aérien » présentée par le Dr. Klemm propose une introduction aux principes du STAP. L'impact des mouvements de la plate-forme sur la nature du fouillis est examiné dans le détail. L'optimisation du traitement STAPSQ est également couvert. La deuxième communication, présentée par le Dr. Farina, fournit une introduction aux problèmes de la mise en œuvre de STAP pour les radars à ouverture synthétique utilisés pour l'imagerie de la terre et d'objectifs au sol à haute résolution. Les deux communications du Dr. Abramovich traitent de la théorie et de l'application de techniques STAP aux radars transhorizon (OTH) utilisés pour suivre la trajectoire d'intrus potentiels se dirigeant vers les frontières d'un pays ami. Cette application revêt une importance particulière depuis les attaques terroristes du 11 septembre 2001. La communication « Architectures STAPS et effets restrictifs » par le Dr. Klemm traite d'architectures sous-optimales de processeur en vue de l'élimination de fouillis, et donne un aperçu de leurs effets dégradants ainsi que des remèdes éventuels. La deuxième communication du Dr. Farina est axée sur des architectures de processeur STAPS pour le traitement en temps réel, qui est d'une importance capitale pour la mise en œuvre effective du STAP. La deuxième communication du Dr. Melvin explique les différentes configurations radar (aéroporté, spatial, bistatique) et développe les techniques STAP contre le brouillage diffusé. En résumé, ce cycle de conférences présente un tour d'horizon unique de l'état actuel de la recherche en matière de STAP et propose divers éléments d'information destinés à tous ceux qui travaillent dans ce domaine technique fort intéressant, par exemple les étudiants, les chercheurs, les concepteurs de systèmes industriels, et les militaires.

Cette publication a été rédigée pour servir de support de cours pour le Cycle de conférences 228, organisé par la Commission de la technologie des capteurs et des dispositifs électroniques (SET) dans le cadre du programme des consultants et des échanges de la RTO du 16-17 septembre 2002, à Istanbul, Turquie, du 19-20 septembre 2002 à Wachtberg, Allemagne et 23-24 septembre 2002 à Moscou, Russie.

Contents

	Page
Executive Summary	iii
Synthèse	iv
List of Authors/Lecturers	vi
	Reference
Space-Time Detection Theory	1
by W.L. Melvin	
Doppler Properties of Airborne Clutter	2
by R. Klemm	
STAP for SAR	3
by A. Farina	
Stochastic-Constraints Method in Nonstationary Hot-Clutter Cancellation	4
Part I: Fundamentals and Supervised Training Applications	
by Y.I. Abramovich	
STAP Architectures and Limiting Effects	5
by R. Klemm	
Algorithms for Real-Time Processing	6
by A. Farina	
Application of STAP in Advanced Sensor Systems	7
by W.L. Melvin	
Stochastic-Constraints Method in Nonstationary Hot-Clutter Cancellation	8
Part II: Unsupervised Training Applications	
by Y.I. Abramovich	

List of Authors/Lecturers

Lecture Series Director: Dr. Richard KLEMM
FGAN-FHR/EL
Neuenahrer Str. 20
53343 Wachtberg
GERMANY

Course Lecturers

Dr. Yuri I. ABRAMOVICH
CCSIP SPRI Building
Technology Park
Adelaide
Mawson Lakes, SA 5095
AUSTRALIA

Dr. Alfonso FARINA
Alenia Marconi Systems
Technical Directorate
Radar and Technology Division
Via Tiburtina Km. 12.400
00131 Rome
ITALY

Dr. William L. MELVIN
Georgia Tech Research Institute
Sensors & Electromagnetic
Applications Laboratory
7220 Richardson Road
Smyrna, GA 30080
UNITED STATES

Space-Time Detection Theory

William L. Melvin

Georgia Tech Research Institute
7220 Richardson Road, Smyrna, GA 30080, USA

bill.melvin@gtri.gatech.edu

Summary

Radar systems must detect targets in the presence of clutter and jamming (colored noise) signals. By exploiting signal diversity, space-time adaptive processing (STAP) improves radar detection performance in colored noise-limited environments. This set of lecture notes describes fundamental aspects of space-time detection theory in Gaussian noise. We first describe basic detection theory; key aspects of the discussion include the formation of a sufficient statistic, threshold setting, matched filtering, and the notion of a whitening filter. We then examine the role space-time signal diversity plays in enhancing target detection performance in colored noise environments. Next, we define commonly used performance metrics, including signal-to-interference-plus-noise ratio (SINR) loss factors. The latter part of the paper describes practical aspects of space-time detection: we consider various detector structures, estimation of unknown parameters, and the impact of clutter heterogeneity on detection performance.

1. Introduction

Target detection serves as the primary goal of radar. Moving target indication (MTI) is a common radar mission involving the detection of airborne or surface moving targets. The signal-to-noise ratio (SNR) – a characterization of the noise-limited performance of the radar against a target with radar cross section σ_T at range r – is approximated as

$$SNR(\phi, \theta) = \left(\frac{P_t G_t(\phi, \theta)}{4\pi r^2} \right) \left(\frac{\sigma_T}{4\pi r^2} \right) \left(\frac{A_e}{N_{in} F_n L_{rf}} \right), \quad (1)$$

where P_t is peak transmit power, $G_t(\phi, \theta)$ is antenna gain, A_e is the effective receive aperture area, N_{in} is the input noise power, F_n is the receiver noise figure and L_{rf} represents radio frequency (RF) system losses [1]. Assuming the noise is uncorrelated (white) and Gaussian, the probability of detection is a one-to-one function of both SNR and probability of false alarm. It is also important to point out that by maximizing SNR, the processor maximizes probability of detection. In light of (1), by increasing power-aperture $P_t A_e$, the radar designer ensures detection of targets with diminishing radar cross section at farther range. System constraints and cost limit the deployable power-aperture product.

In addition to noise-limited constraints, the aerospace radar system design must accommodate the impact of ground clutter and jamming on moving target detection. Clutter and jamming represent colored noise; unlike white noise, clutter and jamming exhibit a degree of correlation. Either individually, or collectively, we refer to clutter and jamming as interference. Interference increases the amount of ambiguity in the target decision process. In other words, as the interference increases, it becomes more difficult to decide whether a target is present in a given observation. Analogous to the white noise detection scenario, the probability of detection depends on both signal-to-interference-plus-noise ratio (SINR) and the specified false alarm rate. Since $SINR \leq SNR$, interference always degrades detection performance in comparison with the noise-limited case.

Signal diversity, in the form of spatial and temporal degrees of freedom (DoF), greatly enhances radar detection in the presence of colored noise. Specifically, the appropriate application of space-time DoFs maximizes signal-to-interference-plus noise ratio (SINR) when the target competes with ground clutter and barrage jamming. Clutter exhibits correlation in both spatial and temporal dimensions, while jamming is predominantly correlated in angle for modest bandwidth. Space-time adaptive processing (STAP) involves

adaptively (or dynamically) adjusting the two-dimensional filter response in an attempt at maximizing the filter's output SINR, and consequently, improving radar detection performance.

The objective of this set of lecture notes is to develop the basic theory of space-time detection. Six sections comprise this paper. In the next section, we begin by considering basic elements of hypothesis testing and detection theory. The important notions of matched filtering and whitening arise from this discussion. Subsequently, in Section 3 we describe the importance of signal diversity in advanced radar sensor design. Radar offers signal diversity in the following dimensions: spatial, slow-time (or Doppler), fast-time (or range), polarization and multi-scan. An appropriate selection of these available degrees of freedom (DoF) is necessary for effective performance enhancement. Herein, our interest lies in the space and slow-time dimensions. (In a companion paper [2], we describe the simultaneous application of space and fast-time DoFs to mitigate terrain scattered jamming.) After discussing signal diversity, we develop several typical STAP performance metrics in Section 4; the metrics enable comparison of competing STAP techniques and non-adaptive processing schemes. Section 5 investigates several practical STAP implementation structures. STAP is a data domain implementation of an optimum filter; practical implementation issues include estimating unknown quantities, alleviating computational burden and minimizing training data requirements. Another issue of practical concern is clutter heterogeneity. Clutter heterogeneity degrades STAP performance by exacerbating the estimation of the interference covariance matrix, an essential STAP component. Thus, we devote the final section of the paper – Section 6 – to issues centering on covariance estimation errors resulting from clutter heterogeneity.

The following is a list of the more common variables used in this paper:

P_D = probability of detection;

P_{FA} = probability of false alarm;

$p_X(x)$ = probability density function of X ;

η, η' = detection threshold;

N = number of slow-time pulses;

M = number of spatial channels;

ϕ, θ = azimuth and elevation angles;

f_d = Doppler frequency;

$s_s(\phi, \theta)$ = spatial steering vector;

$v_s(\phi, \theta)$ = surrogate spatial steering vector;

$s_{s-t}(\phi, \theta, f_d)$ = space-time steering vector;

$v_{s-t}(\phi, \theta, f_d)$ = surrogate space-time steering vector;

$x_{k/s} \in C^{Mx1}$ = spatial snapshot, kth range realization

$x_k \in C^{NMx1}$ = space-time snapshot, kth range realization;

y_k = (scalar) filter output;

w_k = space-time weight vector;

R_k = space-time covariance matrix;

\hat{R}_k, \hat{w}_k = estimated covariance matrix and estimated weight vector.

In general, a boldface, lowercase variable indicates a vector quantity; a boldface, upper case variable indicates a matrix; and, a variable with a caret is an estimate. Additionally, an optimum filter implies clairvoyant knowledge of the statistics of the signal environment. Primary data, or test cells, are those ranges the processor tests for target presence. Secondary data and training data are synonymous, and indicate those range cells used to estimate the unknown characteristics of the primary data. Superscripts "T" or "H" applied to a vector or matrix denote the transpose or hermitian (conjugate transpose) operations. The notation $a \sim \text{CN}(\mu_a, R_a)$ indicates that a is complex normal (Gaussian) with mean μ_a and covariance matrix R_a , and $b \sim N(\mu_b, R_b)$ implies b is normally distributed with mean μ_b and covariance matrix R_b .

2. Basic Detection Theory

The primary objective of a radar is to detect a target at a given range; in fact, radar is an acronym for “radio detection and ranging.” This section of the paper describes the basics of radar detection. Additionally, we unify detection theory and predominant notions of adaptive filtering. Excellent sources of further information on radar detection include [3-6]. The whitening operation, matched filtering, and SINR are the key elements of this unification.

Clutter, jamming and receiver noise are random variables evolving in time. For instance, we can never precisely predict the clutter voltage. Rather, we can describe the statistical distribution of clutter, jamming and thermal receiver noise. Similarly, the target amplitude is a random variable; the famous Swerling models are usually used to describe target amplitude fluctuation [1]. Due to the random nature of the radar signal environment, ambiguity as to whether or not a target is present is always a concern. The goal of detection theory is to provide a rational procedure for confidently determining, in a statistical sense, which of two possible models – target present or target absent – generated a given observation. Hypothesis testing is the cornerstone of detection theory.

Prior to our hypothesis testing discussion, we briefly provide some germane background information. The probability density function (pdf), given as $p_X(x)$, describes the relative frequency behavior of random variable X . The joint pdf between X and Y is $p_{X,Y}(x,y)$. If we consider n trials, and then observe specific occurrences of $X = x$ a total of n_x times, and the simultaneous occurrence of $X = x$ and $Y = y$ a total of n_{xy} times, then $p_X(x) \approx n_x/n$ and $p_{X,Y}(x,y) \approx n_{xy}/n$; similarly, we find $p_Y(y) \approx n_y/n$ for random variable Y . In hypothesis testing, the conditional probability density is most significant. Thus, we ponder the probability associated with observing Y given that we have already observed certain behavior in X . We may then define the conditional probability density as $p_{Y|X}(y|x) = p_{X,Y}(x,y)/p_X(x) \approx (n_{xy}/n)/(n_x/n)$. If X and Y are statistically independent, then $p_{X,Y}(x,y) = p_X(x)p_Y(y)$, since $p_{Y|X}(y|x) = p_Y(y)$ as a result of the fact that knowledge of X has no bearing on our estimating the probability that $Y = y$.

Radar detection is a binary hypothesis testing application. The Neyman-Pearson criteria (NPC) are most commonly used to implement this hypothesis testing procedure since no *a priori* probabilities are necessary in the decision mechanism. In radar, the NPC aids in deciding between the two hypotheses: H_0 and H_1 . H_0 is known as the null hypothesis and corresponds to the case of target absence, while H_1 is the alternative hypothesis and indicates target presence. The NPC nomenclature includes the probability of detection, P_D , and the probability of false alarm, P_{FA} :

$$\begin{aligned} P_D &= \Pr[\text{choose } H_1 | H_1 \text{ is true}] = \int_{T_1} p_{X|H_1}(x|H_1)dx; \\ P_{FA} &= \Pr[\text{choose } H_1 | H_0 \text{ is true}] = \int_{T_1} p_{X|H_0}(x|H_0)dx, \end{aligned} \quad (2)$$

where T_1 defines the “target present” decision region. The goal of the NPC is then to maximize P_D while maintaining $P_{FA} \leq \gamma$, where γ is the maximum false alarm rate the radar system and associated data processor can tolerate.

Figure 1 shows the relationship between P_D , P_{FA} and the threshold setting η . Observe a fundamental truth from this figure: lowering the threshold to increase P_D necessarily increases P_{FA} , and viceversa. The regions of overlap among the two pdf’s signifies the ambiguity in the decision-making process. The NPC detector provides an optimum mechanism for determining target presence or absence in light of this ambiguity.

Applying the NPC in an optimization procedure (see [3-4] for details) leads to a decision mechanism known as the likelihood ratio test (LRT), which is given by

$$\Lambda(x) = \frac{p_{X|H_1}(x | H_1)}{p_{Y|H_0}(x | H_0)} > \eta. \quad (3)$$

The LRT is the detector! It compares the ratio of the two likelihood functions, $p_{X|H_m}(x | H_m)_{m=0,1}$, to the threshold setting; if the value exceeds the threshold, the processor declares target presence, while if the ratio is less than the threshold setting, the processor assumes the null hypothesis.

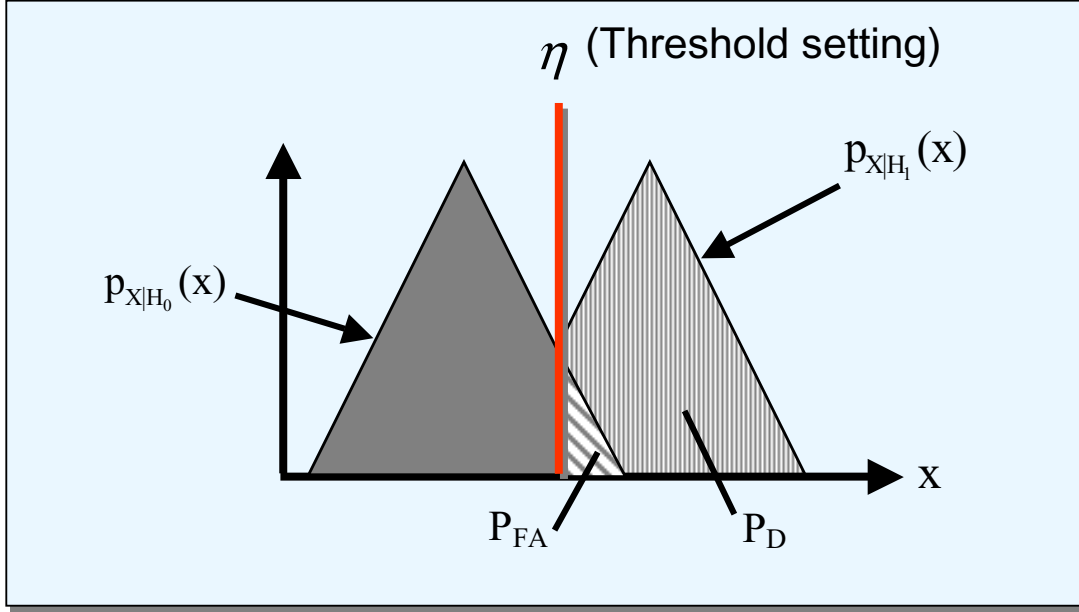


Figure 1. Relationship between P_D , P_{FA} and threshold setting, η .

It is commonplace to apply a monotonic operation to simplify the LRT. For example, the natural logarithm is often applied to reduce expressions involving exponential functions. A sufficient statistic results after manipulating the LRT into a canonical form involving a function of the observed data. We denote the sufficient statistic as

$$\Psi(x) \begin{cases} > \eta' \\ < \end{cases} \quad (4)$$

We obtain the modified threshold in (4) by deriving the pdf of $\Psi(x)$ under the null hypothesis condition and then solving

$$P_F = \int_{\eta'}^{\infty} p_{\Psi(x)|H_0}(\Psi(x) | H_0) dx = \gamma \quad (5)$$

for η' . As one might expect, we ascertain detection performance by calculating the pdf of $\Psi(x)$ under the alternative hypothesis case.

Application of the LRT is best understood through example. For this reason, let's consider a colored Gaussian noise (CGN) scenario. Our hypotheses are given as

$$H_i : \mathbf{x} = \mathbf{s}_i + \mathbf{n} \quad (6)$$

for $i = 0, 1$, where \mathbf{x} is the vector observation, \mathbf{s}_1 is the target signal, $\mathbf{s}_0 = \mathbf{0}$, and \mathbf{n} is the interference vector. Also, suppose \mathbf{x} represents a coherent dwell of N pulses, spaced by the pulse repetition interval, T_p , i.e.,

$$\mathbf{x} = \begin{bmatrix} x(0) & x(T_p) & \cdots & x((N-1)T_p) \end{bmatrix}^T. \quad (7)$$

The joint pdf of (7) is

$$p_{\mathbf{x}|H_i}(\mathbf{x} | H_i) = p_{\mathbf{n}}(\mathbf{x} - \mathbf{s}_i). \quad (8)$$

Assuming that \mathbf{n} is distributed according to a complex Gaussian distribution with zero mean and covariance matrix $\mathbf{R}_n = E[\mathbf{n}\mathbf{n}^H]$, then

$$p_n(\mathbf{n}) = \frac{1}{\pi |\mathbf{R}_n|} \exp(-\mathbf{n}^H \mathbf{R}_n^{-1} \mathbf{n}). \quad (9)$$

Forming the LRT using (8)-(9), then taking the natural log and simplifying yields

$$\text{Re}(\mathbf{s}_i^H \mathbf{R}_n^{-1} \mathbf{x}) - \frac{\mathbf{s}_i^H \mathbf{R}_n^{-1} \mathbf{s}_i}{2} \stackrel{H_1}{>} \frac{1}{2} \ln(\eta) \stackrel{H_0}{<} \frac{1}{2} \ln(\eta). \quad (10)$$

The first term on the left-hand side of (10) is a whitening filter, $\mathbf{R}_n^{-1/2}$, while $\mathbf{R}_n^{-1/2} \mathbf{s}_i$ is a linearly transformed matched filter. The matched filter maximizes SNR (in the noise-limited case); hence, in the presence of colored-noise, the detector first whitens (decorrelates) the colored-noise, and then applies a matched filter as in the noise-limited case. The whitening filter and matched filter will be discussed in further detail in subsequent sections.

It then follows from (10) that a sufficient statistic is

$$\Psi(\mathbf{x}) = \text{Re}(\mathbf{s}_i^H \mathbf{R}_n^{-1} \mathbf{x}) \stackrel{H_1}{>} \eta'; \quad \Psi(\mathbf{x}) \sim N\left(\text{Re}(\mathbf{s}_i^H \mathbf{R}_n^{-1} \mathbf{s}_i), \mathbf{s}_i^H \mathbf{R}_n^{-1} \mathbf{s}_i\right). \quad (11)$$

The threshold and performance of the detector in (11) are then given by

$$P_{FA} = Q\left(\frac{\ln(\eta) + \mathbf{s}_i^H \mathbf{R}_n^{-1} \mathbf{s}_i}{2\sqrt{\mathbf{s}_i^H \mathbf{R}_n^{-1} \mathbf{s}_i}}\right); \quad P_D = Q\left(\frac{\ln(\eta) - \mathbf{s}_i^H \mathbf{R}_n^{-1} \mathbf{s}_i}{2\sqrt{\mathbf{s}_i^H \mathbf{R}_n^{-1} \mathbf{s}_i}}\right), \quad (12)$$

where $Q(x) = \frac{1}{\sqrt{2\pi}} \int_x^\infty e^{-\alpha^2/2} d\alpha$ is the right-tail distribution (complementary cumulative distribution) of a Gaussian variate with zero mean and variance of unity. Numerical tables provide values of $Q(x)$ and $Q^{-1}(x)$ [3]. We then use the expression for P_{FA} and $Q^{-1}(x)$ to calculate the threshold η .

Figure 2 shows an upper and lower bound on $Q(x)$. The important observation from (12) and Figure 2 concerns the role of the factor $\mathbf{s}_i^H \mathbf{R}_n^{-1} \mathbf{s}_i$; this term represents the SINR. As $\mathbf{s}_i^H \mathbf{R}_n^{-1} \mathbf{s}_i$ increases, the argument in (12) decreases for the P_D calculation and so detection performance improves. In effect, the argument in (12) for P_{FA} increases, and so the false alarm rate decreases below the specification unless the threshold is increased. An increase in SINR serves to separate the pdf's for null and hypothesis conditions, making it easier to distinguish target absence from target presence. Figure 3 clarifies this point by comparing the histograms for null and alternative hypothesis with three different values of signal-to-noise ratio. We plot the amplitude of the complex observations; in the null hypothesis case this yields a Rayleigh distribution, while

for the alternative hypothesis we have the well-known Rician distribution [6]. Adequate SNR or SINR is essential to acceptable detection performance.

The appropriate exploitation of signal diversity can be used in the Gaussian case to maximize SINR, hence yielding maximal detection performance for any specified false alarm rate. Perhaps the simplest example of the benefits of signal diversity involves sidelobe noise jamming. For a single channel system, the jamming enters the sidelobes of the antenna and masks target detection over all Doppler. However, since the noise jammer is spatially correlated, spatial sampling of the jammer waveform using multiple spatial channels provides information on the jammer direction of arrival. This information can then be used to construct a whitening filter to mitigate all signals coming from the jamming angle. Effectively, the detector implements a constrained matched filtering operation, where the constraint places a filter null in the jammer direction. The consequent increase in SINR leads to greatly improved detection performance, as our prior discussion indicates.

Ground clutter exhibits a two-dimensional correlation in angle and slow-time. The seminal result on space-time detection theory for radar application is given by Brennan and Reed in [5]. Using the hypothesis testing theory of the prior discussion, we have the mathematical framework to develop Brennan and Reed's result. Herein, we elect to synopsize the key aspects of this development.

Consider the hypotheses

$$H_0: \mathbf{x}_{k/H_0} = \mathbf{x}_{k/I} + \mathbf{x}_{k/N}; \quad H_1: \mathbf{x}_{k/H_1} = \mathbf{s}_T + \mathbf{x}_{k/H_0}, \quad (13)$$

where $\mathbf{x}_{k/H_m} \in \mathbb{C}^{NMx1}$ is the space-time snapshot for N pulses and M spatial channels for the kth range realization and hypothesis H_m . Additionally, $\mathbf{x}_{k/H_0} \sim CN(\mathbf{0}, \mathbf{R}_k)$, where \mathbf{R}_k is the null-hypothesis covariance matrix, $\mathbf{s}_T \in \mathbb{C}^{NMx1}$ is the space-time signal vector, and $\mathbf{x}_{k/I} \in \mathbb{C}^{NMx1}$ and $\mathbf{x}_{k/N} \in \mathbb{C}^{NMx1}$ are space-time interference and noise snapshots. Each space-time snapshot is organized as

$$\mathbf{x}_k = \begin{bmatrix} \mathbf{x}_{k/s}^T(0) & \mathbf{x}_{k/s}^T(T_p) & \cdots & \mathbf{x}_{k/s}^T((N-1)T_p) \end{bmatrix}^T \in \mathbb{C}^{MNx1} \quad (14)$$

where $\mathbf{x}_{k/s}(n) \in \mathbb{C}^{Mx1}$ is the spatial snapshot for the nth pulse. The detector involves forming a function of the filter output, $y_k = \mathbf{w}_k^H \mathbf{x}_k$, where $\mathbf{w}_k \in \mathbb{C}^{NMx1}$ is the space-time weight vector. The pdf for the two hypothesis of (13) are

$$p(y_{k/H_i}) = \frac{1}{\sqrt{2\pi\sigma_y^2}} \exp\left(-\frac{|y_{k/H_i} - \mu_{y/H_i}|^2}{2\sigma_y^2}\right), \quad i = 0, 1; \quad (15)$$

with the mean and interference-plus-noise variance given by

$$\begin{aligned} \mu_y &= E[y_k] = \begin{cases} 0 & \text{for } H_0; \\ \mathbf{w}_k^H \mathbf{s}_T & \text{for } H_1 \end{cases} \\ \sigma_y^2 &= E[(y_k - \mu_y)(y_k - \mu_y)^*] = \mathbf{w}_k^H \mathbf{R}_k \mathbf{w}_k. \end{aligned} \quad (16)$$

Upon forming the LRT and algebraically manipulating, we find a sufficient statistic taking the simple form

$$|y_k| \underset{H_0}{<} \underset{H_1}{>} \eta'. \quad (17)$$

The pfd's of (17) for null and alternative hypotheses are Rayleigh and Rician, respectively [5]. Armed with the distributions, we can then determine the threshold setting and detection performance. The threshold is calculated from

$$P_{FA} = \Pr\left[|y_k| > \eta' | \mathbf{x}_{k/\mathbf{H}_0}\right] = \exp\left(\frac{-(\eta')^2}{2\sigma_y^2}\right). \quad (18)$$

Detection performance is given by

$$P_D = Q_M(\alpha, \beta) = \int_{\beta}^{\infty} v \exp\left(\frac{-(v^2 + \alpha^2)}{2}\right) I_0(\alpha v) dv; \text{ where,} \quad (19)$$

$$v = \frac{r}{\sigma_y}, \quad r = |y_k|, \quad \alpha^2 = \frac{a^2}{\sigma_y^2} = \text{SINR}_{\text{out}}, \quad a = |\mathbf{w}_k^H \mathbf{s}_T|, \quad \text{and} \quad \beta = \frac{\eta'}{\sigma_y}.$$

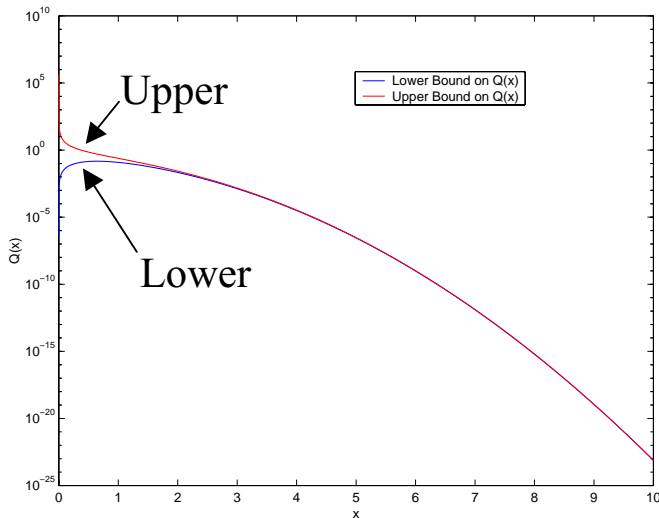


Figure 2. Upper and lower bounds on the complementary cumulative distribution for a Gaussian variate.

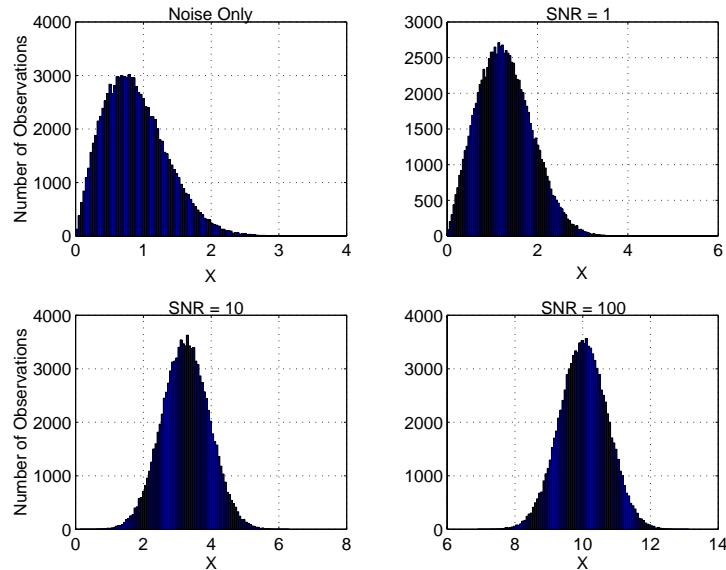


Figure 3. Comparison of noise-only histogram with signal-plus-noise histograms for varying SNR.

$I_0(\cdot)$ is the modified Bessel function of the first kind and order zero. $Q_M(\alpha, \beta)$ is known as Marcum's Q and is a monotonically increasing function of the square-root of SINR and monotonically decreasing function of normalized threshold setting, β ; numerical techniques are required to solve for P_D in (19).

The receiver operating characteristic (ROC) characteristic of the space-time detector in (17) is shown in Figure 4. The different curves shown in the figure correspond to different false alarm rates. Observe that as the false alarm rate increases – implying a decrease in the threshold – the detection probability increases.

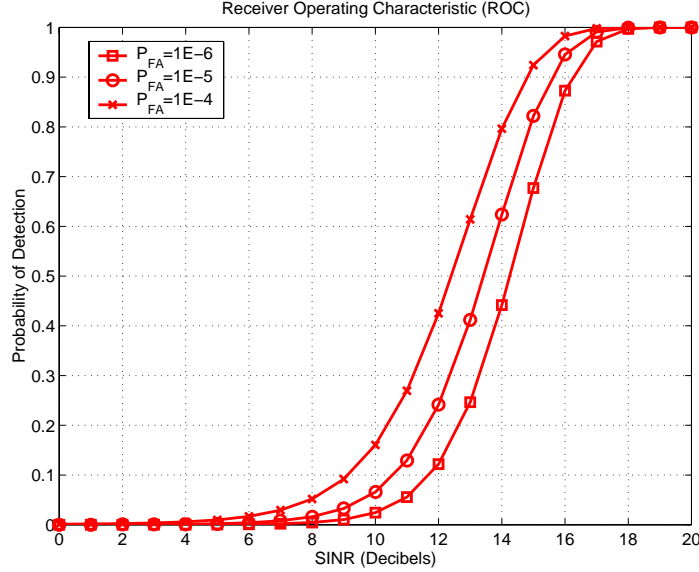


Figure 4. Receive operating characteristic for space-time detector.

3. Signal Diversity

Pulsed radar sensors can potentially measure angle (azimuth, elevation or cone angle), Doppler (slow-time), range (fast-time), polarization, and the multi-scan behavior of target and interference behavior. Different classes of interference exhibit varying correlation over the available sensor measurement spaces. Table 1 describes different interference types and their respective correlation properties.

Table 1. Correlation Characteristics of Some Interference Types

Interference Type	Correlation Characteristics	Comments
Ground Clutter	Azimuth (or cone angle) and Doppler, polarization response may differ from clutter.	Space and slow-time adaptive processing (STAP) can mitigate clutter, polarization may aid the detection of very slow targets.
Narrowband Noise Jamming	Angle (azimuth and elevation).	Spatial null suppresses jamming signal.
Wideband Noise Jamming	Angle and fast-time.	Variation with wavelength must be compensated with fast-time processing, also helps with channel mismatch.
Hot Clutter	Angle and fast-time.	Jammer waveform often correlated in fast-time.
Cold and Hot Clutter	Angle, slow-time and fast-time.	Requires 3-D STAP.

The ability to separate interference and target characteristics in the chosen measurement spaces enables the processor to enhance the target while mitigating the interference. Inherently, the processor takes advantage of the differences in correlation properties to maximize SINR in the multidimensional detection space, thereby maximizing detection performance. Figure 5 provides a notional view of the impact of signal diversity on detection performance. In this figure, X, Y and Z are Fourier transforms of measurement domains x, y and z; hence, Figure 5 is a three-dimensional power spectral density (PSD). The inverse Fourier transform of the PSD yields the correlation function. Notice the separability of the target from the interference in the three-dimensional space. However, projecting the data into any two-dimensional data space, we observe the masking of the target by the interference. When the target shares the same space as the interference, filtering

has little or no impact on SINR. In the three-dimensional space, the detection processor can construct a filter to maximize the gain on the target while nulling the interference.

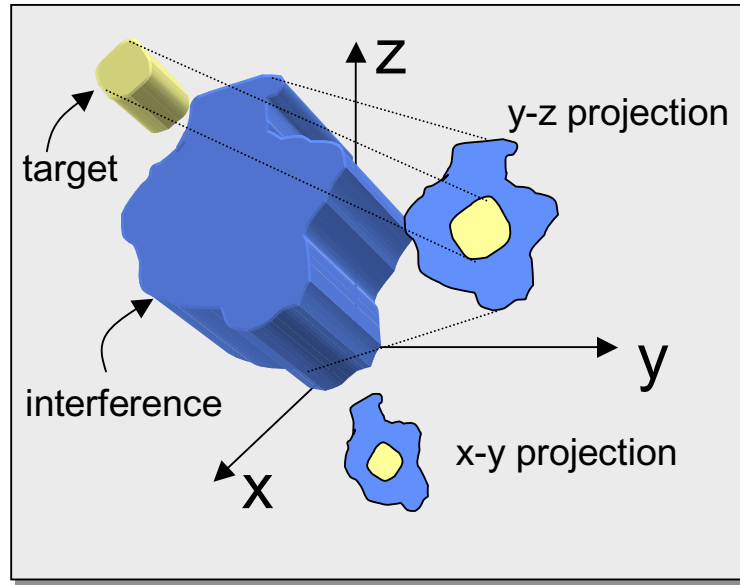


Figure 5. Notional view of the importance of signal diversity on target detection. In three dimensions, the target and interference are separable, and hence more detectable, while in two dimensions the interference masks the target.

The impact of ground clutter on detection performance serves as our primary focus. For this reason, the remainder of the paper considers the space (azimuth or cone angle) and slow-time (Doppler) dimensions. Figure 6 shows the PSD for simulated ground clutter; observe the coupling in angle and Doppler marked by those two-dimensional frequencies with larger clutter power values. The dashed line denotes the transmit direction. The processor searches for targets along this line at all Doppler. Mainlobe clutter – located near zero Doppler and zero angle – impedes the detection of slow-moving targets. Endo-clutter detection refers to detection of low radial velocity (low Doppler) targets existing in the diffraction-limited clutter regions. Additionally, sidelobe clutter – present at those Doppler frequencies away from zero Doppler – masks the detection of faster moving, exo-clutter targets. Figure 7 shows the corresponding space-time filter response. The filter places a null on the clutter ridge. This matched two-dimensional response leads to maximal SINR.

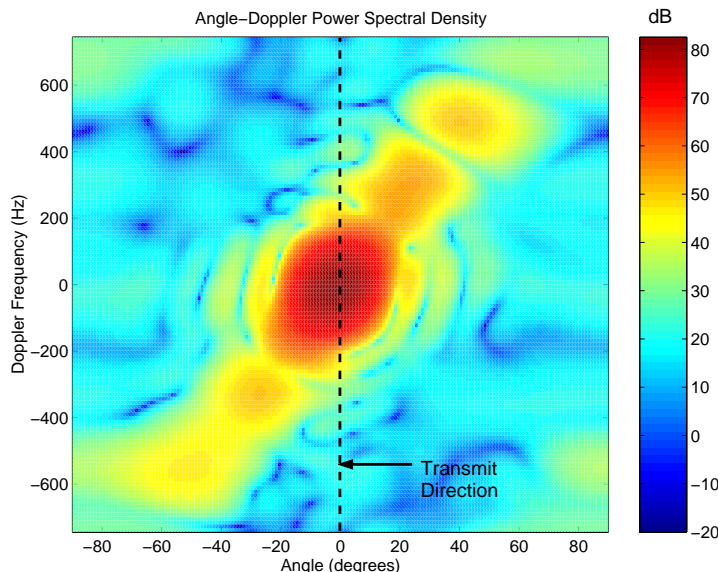


Figure 6. Power spectral density for ground clutter.

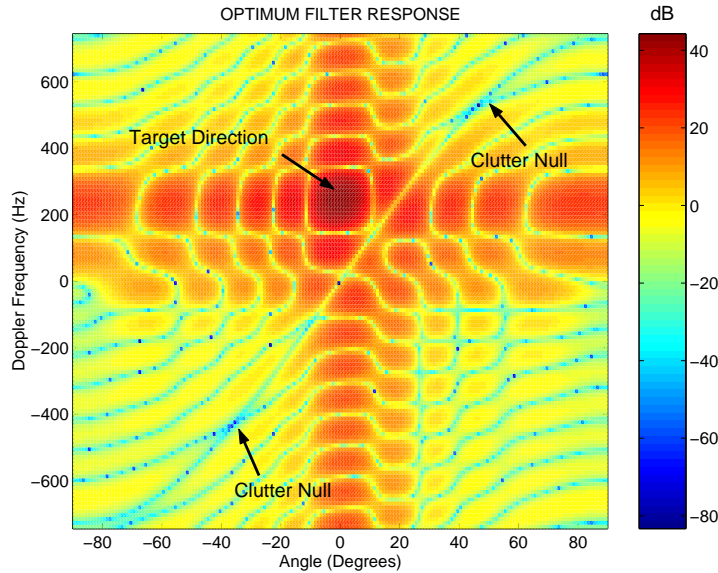


Figure 7. Space-time optimal filter response.

Signal diversity is an essential component in enhancing the detection of slow moving and/or weak targets competing with ground clutter returns. Choosing other measurement spaces, with perhaps the exception of polarization, will not help improve performance. As can be seen from Figures 6-7, it would be very difficult, if not impossible, to detect a target at zero angle and zero Doppler. Yet, since STAP is a member of the class of super-resolution algorithms, the processor can detect targets very close to mainbeam clutter.

4. Performance Metrics

We briefly consider several of the more useful performance metrics used to characterize STAP performance. We begin by describing the difference between adaptive and optimal processors.

STAP is a data domain implementation of an optimal filter. In developing the space-time detector in (13)-(19), we pointed out that by maximizing SINR, the processor maximizes P_D . The results in these equations are valid for any weight vector \mathbf{w}_k . We are interested in the weight vector leading to maximal SINR, which is given as

$$\mathbf{w}_k = \mu \mathbf{R}_k^{-1} \mathbf{s}_{s-t}(\phi, \theta, f_d), \quad (20)$$

where μ is an arbitrary constant and $\mathbf{s}_{s-t}(\phi, \theta, f_d)$ is the target space-time steering vector. The space-time steering vector is

$$\mathbf{s}_{s-t}(\phi, \theta, f_d) = \mathbf{s}_t(f_d) \otimes \mathbf{s}_s(\phi, \theta), \quad (21)$$

with $\mathbf{s}_t(f_d) \in \mathbb{C}^{N \times 1}$ representing the temporal (Doppler) steering vector pointing to Doppler frequency f_d , and $\mathbf{s}_s(\phi, \theta) \in \mathbb{C}^{M \times 1}$ denoting the spatial steering vector for a signal at azimuth ϕ and elevation θ . The space-time steering vector is the normalized response of the radar sensor to a target with a specified angle of arrival and Doppler frequency, i.e., $\mathbf{s}_T = \alpha \mathbf{s}_{s-t}(\phi, \theta, f_d)$ for complex amplitude α .

We now consider a short proof on the optimality of (20). Observe that

$$SINR = \frac{E[y_s y_s^*]}{E[y_{I+N} y_{I+N}^*]} = \frac{P_s}{P_{I+N}} = E[|\alpha|^2] \frac{\mathbf{w}_k^H \mathbf{s}_{s-t} \mathbf{s}_{s-t}^H \mathbf{w}_k}{\mathbf{w}_k^H \mathbf{R}_k \mathbf{w}_k}, \quad (22)$$

where y_s is the signal-only filter output, y_{I+N} is the null hypothesis filter output, and P_s and P_{I+N} represent output signal power and null hypothesis output power. Additionally, we have removed the space-time steering vector's dependence on angle and Doppler for notational convenience. Next, let $\mathbf{w}_k = \mathbf{A}\mathbf{z}$ and $\tilde{\mathbf{s}} = \mathbf{A}^H\mathbf{s}_{s-t}$, where $\mathbf{A} = \mathbf{R}_k^{-1/2}$. Substituting these expressions into (22) yields

$$P_{I+N} = \mathbf{w}_k^H \mathbf{R}_k \mathbf{w}_k = \mathbf{z}^H \mathbf{A}^H \mathbf{R}_k \mathbf{A} \mathbf{z} = \mathbf{z}^H \mathbf{z}; \quad P_s = E[|\alpha|^2] |\mathbf{z}^H \tilde{\mathbf{s}}|^2. \quad (23)$$

Inserting (23) into (22) gives

$$\frac{P_s}{P_{I+N}} = \frac{E[|\alpha|^2] |\mathbf{z}^H \tilde{\mathbf{s}}|^2}{\mathbf{z}^H \mathbf{z}}. \quad (24)$$

Using the Schwarz Inequality, we find

$$|\mathbf{z}^H \tilde{\mathbf{s}}|^2 = \left| \sum_m [\mathbf{z}]_m [\tilde{\mathbf{s}}]_m \right|^2 \leq \mathbf{z}^H \mathbf{z} \tilde{\mathbf{s}}^H \tilde{\mathbf{s}}. \quad (25)$$

Notice that an optimal value for \mathbf{z} is $\mathbf{z}_{opt} = \mu \tilde{\mathbf{s}}$; with this selection, the SINR is maximal. Hence,

$$\mathbf{w}_{k,opt} = \mu \mathbf{A} \mathbf{A}^H \mathbf{s}_{s-t} = \mu \mathbf{R}_k^{-1} \mathbf{s}_{s-t}, \quad (26)$$

which is the result we desire.

Several comments are in order. First of all, $\mathbf{A} = \mathbf{R}_k^{-1/2}$ is a whitening filter since $E[\mathbf{A}\mathbf{x}_k \mathbf{x}_k^H \mathbf{A}^H] = \mathbf{I}_{NM}$ (i.e., the whitening filter decorrelates the colored noise input, hence making it look like white noise). In the white noise case, \mathbf{s}_{s-t} is the matched filter; it has a bandpass response with angle and Doppler and maximizes SNR. We may thus interpret the optimal weight vector as

$$\mathbf{w}_{k,opt} = \underbrace{(\mathbf{R}_k^{-1/2})}_{\text{Whitening Filter}} \underbrace{(\mathbf{R}_k^{-1/2} \mathbf{s}_{s-t})}_{\text{Warped Matched Filter}}. \quad (27)$$

The warped matched filter accommodates the linear transformation applied to the space-time signal vector during the whitening stage. Finally, keep in mind that SINR is a function of both angle and Doppler.

In the STAP case, both the covariance matrix and target space-time steering vector are unknown. For this reason, the processor must estimate both quantities. To handle the unknown steering vector, the processor sweeps across a series of pre-calculated space-time steering vectors, $\mathbf{v}_{s-t}(\phi, \theta, f_d)$, covering several angle bins about the transmit direction and the whole Doppler space. Performance degradation resulting from steering vector mismatch is generally slight. Covariance estimation is more complicated. Commonly, we use the estimate

$$\hat{\mathbf{R}}_k = \frac{1}{K} \sum_{m=1}^K \mathbf{x}_m \mathbf{x}_m^H, \quad (28)$$

where \mathbf{x}_m are training (secondary data) taken from ranges adjacent to the test (primary) cell [7]. The adaptive weight vector is

$$\hat{\mathbf{w}}_k = \beta \hat{\mathbf{R}}_k^{-1} \mathbf{v}_{s-t}(\phi, \theta, f_d), \quad (29)$$

where β is a constant typically set to $\beta=1$ or $\beta=\sqrt{\mathbf{v}_{s-t}^H(\phi, \theta, f_d) \hat{\mathbf{R}}_k^{-1} \mathbf{v}_{s-t}(\phi, \theta, f_d)}$.

If the secondary data are multivariate Gaussian and independent and identically distributed (iid) with respect to the null-hypothesis of the primary data, (28) is a maximum likelihood estimate. Selecting the number K of secondary data to obtain a suitable estimate via the calculation of (28) is addressed in [7]. Specifically, Reed, Mallett and Brennan have shown that

$$E\left[\left(\text{SINR} | \hat{\mathbf{w}}_k\right) / (\text{SINR}_{\text{optimum}})\right] = (K + 2 - NM) / (K + 1). \quad (30)$$

The famous Reed-Mallett-Brennan (RMB) Rule then states that for the adaptive processor to attain an SINR loss of -3 dB in comparison with the optimal processor requires $K = 2NM - 3$. The RMB Rule assumes the secondary data are iid.

Since a one-to-one correspondence exists between SINR and P_D in the Gaussian case, SINR loss factors are very convenient and commonly used metrics of STAP performance [8]. We may write the output SINR as

$$\begin{aligned} \text{SINR}(\phi, \theta, f_d) &= \text{SNR}(\phi, \theta) \times L_{s,1}(\phi, \theta, f_d) \times L_{s,2}(\phi, \theta, f_d); \\ 0 \leq L_{s,1}(\phi, \theta, f_d), L_{s,2}(\phi, \theta, f_d) &\leq 1. \end{aligned} \quad (31)$$

$\text{SNR}(\phi, \theta)$ follows from (1). $L_{s,1}(\phi, \theta, f_d)$ and $L_{s,2}(\phi, \theta, f_d)$ are SINR loss factors: $L_{s,1}(\phi, \theta, f_d)$ characterizes the loss in signal-to-noise ratio due to colored noise, while $L_{s,2}(\phi, \theta, f_d)$ measures the loss in SINR resulting from the error between optimal (known) and adaptive (estimated) weight vectors. $L_{s,1}(\phi, \theta, f_d)$ captures the impact of both the system design and signal processing algorithm selection on performance in interference-limited environments. Definitions of both SINR loss factors are

$$L_{s,1}(\phi, \theta, f_d) = \frac{\text{SINR}(\phi, \theta, f_d)|_{\hat{\mathbf{w}}_k}}{\text{SNR}(\phi, \theta)}; \quad L_{s,2}(\phi, \theta, f_d) = \frac{\text{SINR}(\phi, \theta, f_d)|_{\hat{\mathbf{w}}_k}}{\text{SINR}(\phi, \theta, f_d)|_{\mathbf{w}_k}} = \frac{\text{Adaptive Output SINR}}{\text{Optimal Output SINR}}. \quad (32)$$

Substituting (32) into (31) yields the identity $\text{SINR}(\phi, \theta, f_d) = \text{SINR}(\phi, \theta, f_d)|_{\hat{\mathbf{w}}_k}$.

Figure 8 shows the $L_{s,1}$ term for the optimal space-time processor (STP) and the conventional digital beamformer (DBF) followed by Hanning-weighted Doppler processing (DOP). This example corresponds to the same interference environment shown in Figure 6, except the dwell has been doubled. The poor performance of the conventional approach is a consequence of the short dwell and small aperture used in this example. However, the example does highlight the tremendous performance potential of STAP (in an iid environment, the STAP SINR loss curve appears similar to the optimal STP $L_{s,1}$ curve of Figure 8, with a downward shift of a few decibels). The 0 dB line in Figure 8 corresponds to noise-limited performance. From the SINR loss curves, we derive another very important STAP metric: the minimum detectable velocity (MDV). The MDV follows from a specification of the maximum tolerable SINR loss if the system is to meet detection performance requirements. If, for example, 5 dB is the tolerable loss, the radar system MDV in our example is $\pm(\lambda/2) \times (60 \text{ Hz}) = \pm 9 \text{ m/s}$ for the optimal STP, where $\lambda = 0.3 \text{ m}$ is the RF wavelength.

The optimal and adaptive filter responses are also useful metrics. Given a weight vector, we compute the filter output response by sweeping across all space-time steering vectors of interest, viz.

$$H_{\text{optimal}}(\phi, \theta, f_d) = \left| \mathbf{w}_k^H \mathbf{s}_{s-t}(\phi, \theta, f_d) \right|^2; \quad H_{\text{adaptive}}(\phi, \theta, f_d) = \left| \hat{\mathbf{w}}_k^H \mathbf{s}_{s-t}(\phi, \theta, f_d) \right|^2. \quad (33)$$

An example of the optimal response is given in Figure 7; the filter is tuned to broadside and 250 Hz. Doppler.

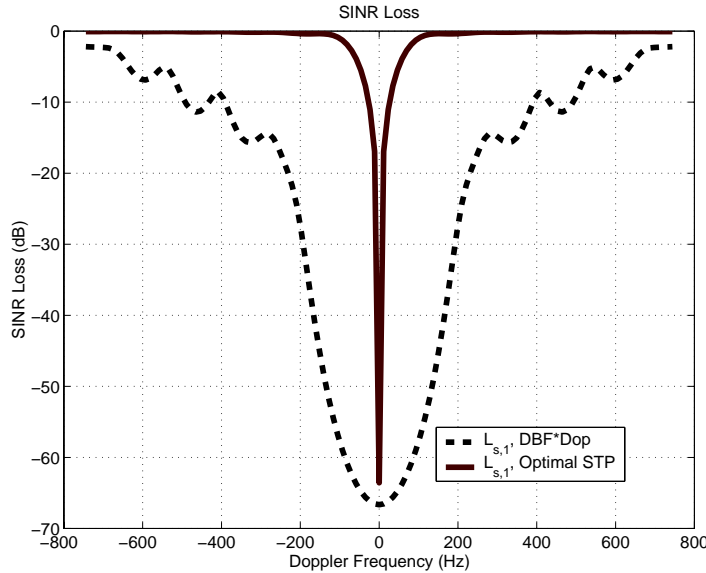


Figure 8. Example SINR loss curves.

5. Space-Time Detector Structures

In this section we begin by briefly considering some normalizations applied in STAP-type detectors. Then, we discuss the concept of interference rank, examine several reduced-rank or reduced-dimension processing schemes, and consider the role of diagonal loading in STAP implementation.

Recall, in (20) and (29) the optimal or adaptive weight vector includes arbitrary scalars μ and β , respectively. While a particular selection of either scalar does not affect SINR, certain selections are convenient in subsequent processing. A commonly used detector and normalization is given by

$$\left| \mathbf{w}_k^H \mathbf{x}_k \right|^2 = \frac{\left| \mathbf{s}_{s-t}^H \mathbf{R}_k^{-1} \mathbf{x}_k \right|^2}{\mathbf{s}_{s-t}^H \mathbf{R}_k^{-1} \mathbf{s}_{s-t}} \stackrel{H_1}{>} \eta_1 \stackrel{H_0}{<} \eta_0 \quad (34)$$

where $\mu = 1/\sqrt{\mathbf{s}_{s-t}^H \mathbf{R}_k^{-1} \mathbf{s}_{s-t}}$ in this case [9]. Let $\tilde{\mathbf{w}}_k = \mathbf{R}_k^{-1} \mathbf{s}_{s-t}(\phi, \theta, f_d)$, such that $\mathbf{w}_k = \mu \tilde{\mathbf{w}}_k$. Then, $1/\mu^2$ equals the output noise power of the filter with weight vector $\tilde{\mathbf{w}}_k$. In the unknown covariance case, we substitute the form in (28) into (34), yielding the modified sample matrix inversion (MSMI) detection statistic. In this case, (34) becomes

$$\left| \hat{\mathbf{w}}_k^H \mathbf{x}_k \right|^2 = \frac{\left| \mathbf{s}_{s-t}^H \hat{\mathbf{R}}_k^{-1} \mathbf{s}_{s-t} \right|^2}{\mathbf{s}_{s-t}^H \hat{\mathbf{R}}_k^{-1} \mathbf{s}_{s-t}} \stackrel{H_1}{>} \eta_1 \left(\mathbf{s}_{s-t}^H \hat{\mathbf{R}}_k^{-1} \mathbf{s}_{s-t} \right); \quad \hat{\mathbf{w}}_k = \hat{\mathbf{R}}_k^{-1} \mathbf{s}_{s-t}, \quad (35)$$

where we further calculate η_1 for the single channel, single pulse case with the noise variance set to unity. The term $1/\beta^2 = \mathbf{s}_{s-t}^H \hat{\mathbf{R}}_k^{-1} \mathbf{s}_{s-t}$ modifies the threshold to account for varying interference power levels (and integration gain). As shown in [9], this normalization leads to a constant false alarm rate (CFAR) property. As the noise power increases, the threshold increases to maintain CFAR, and vice versa.

Kelly formulated the generalized likelihood ratio test (GLRT) of the form

$$\frac{\left| \mathbf{s}_{s-t}^H \hat{\mathbf{R}}_k^{-1} \mathbf{x}_k \right|^2}{\mathbf{s}_{s-t}^H \hat{\mathbf{R}}_k^{-1} \mathbf{s}_{s-t} \left(1 + \frac{1}{K} \mathbf{x}_k^H \hat{\mathbf{R}}_k^{-1} \mathbf{x}_k \right)} \stackrel{H_1}{>} K \eta_2, \quad (36)$$

where K is the number of secondary data samples [10]. This detector also possesses the CFAR property. It differs in form from (34) as a result of different modeling assumptions: in the GLRT, the detector assumes the covariance matrix is unknown. The derivation of (36) generally follows the same LRT development described in the initial sections of this report. Observe the detector can be written

$$\left| \hat{\mathbf{w}}_k^H \mathbf{x}_k \right|^2 \stackrel{H_1}{>} \left(\eta_1 \mathbf{s}_{s-t}^H \hat{\mathbf{R}}_k^{-1} \mathbf{s}_{s-t} \right) \left[\frac{K\eta_2}{\eta_1} \left(1 + \frac{1}{K} \mathbf{x}_k^H \hat{\mathbf{R}}_k^{-1} \mathbf{x}_k \right) \right]. \quad (37)$$

A data dependent threshold modifies the MSMI threshold to account for the finite number of training data. As K becomes large, the test statistic approaches the MSMI result.

Figure 9 provides a block diagram of the overall process. Essentially, a STAP filter suppresses interference. The scalar filter output is multiplied by a data-dependent “threshold multiplier” – either $1/\hat{\alpha}^2$ or $1/\hat{\alpha}^2$ multiplied by the factor in brackets on the far right-hand side of (37) – and then compared to a fixed threshold.

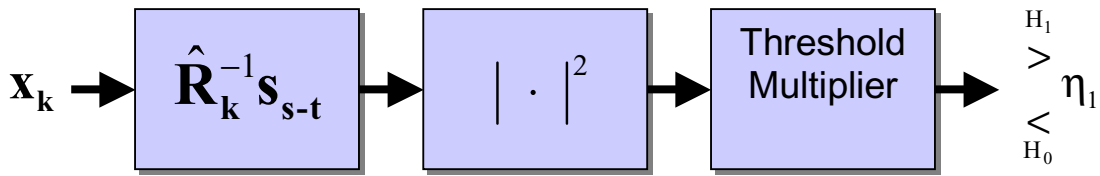


Figure 9. Embedded CFAR in STAP processing.

Other normalizations are possible. For instance, the minimum variance beamformer chooses $\mu_{MV} = 1/\mathbf{s}_{s-t}^H \hat{\mathbf{R}}_k^{-1} \mathbf{s}_{s-t}$ [11]. This normalization accordingly affects the interpretation of the data.

STAP is effectively a catch-all for a class of linear filters involving SINR maximization of the input data [8]. We can broadly characterize the class of STAP methods into two sub-groups: reduced-dimension (RD) STAP and reduced-rank (RR) STAP. RD-STAP involves data-independent transformations and bin selection, whilst RR-STAP is a data-dependent approach. We'll consider these two sub-groups in turn. The ultimate goals of either RD-STAP or RR-STAP include reducing computational burden and reducing required sample support.

Figure 10 is an overview of RD-STAP methods. The processor can transform the space-time data via the data independent transformation

$$\check{\mathbf{x}}_k = \mathbf{T}^H \mathbf{x}_k \in \mathbb{C}^{PQ \times 1}, \quad (38)$$

where \mathbf{T} is the transformation matrix and ideally $PQ \ll NM$. Common transformations include beamforming and Doppler processing steps. By analogy to our prior discussion, the required optimal RD weight vector yielding maximum SINR in the reduced space is

$$\check{\mathbf{w}}_k = (\mathbf{T}^H \mathbf{R}_k \mathbf{T})^{-1} \mathbf{T}^H \mathbf{s}_{s-t}. \quad (39)$$

In practice, the RD-STAP weight vector is given by

$$\hat{\mathbf{w}}_k = \hat{\mathbf{R}}_k^{-1} \check{\mathbf{v}}; \quad \hat{\mathbf{R}}_k = \frac{1}{K'} \sum_{m=1}^{K'} \check{\mathbf{x}}_m \check{\mathbf{x}}_m^H; \quad \check{\mathbf{v}} = \mathbf{T} \mathbf{v}_{s-t}, \quad (40)$$

where $K' \ll K$ indicates a reduction in required secondary data. Also, RD-STAP computational burden is $O(P^3Q^3)$, which typically is far less than for the space-time case with computational load $O(N^3M^3)$.

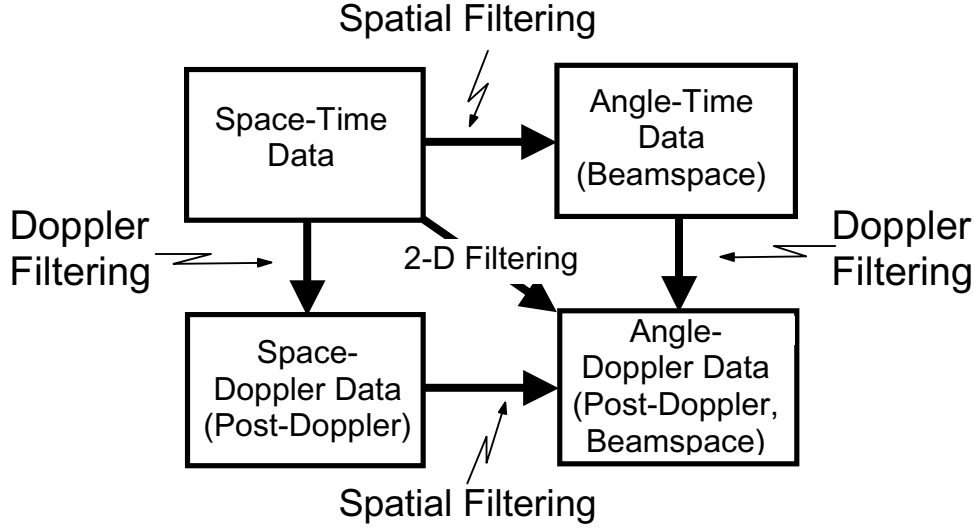


Figure 10. Overview of reduced-dimension STAP methods.

Examples of RD-STAP techniques are available in [8, 12-13]. The Factored Time-Space (FTS) algorithm is a post-Doppler method suitable for long coherent dwells and higher radial velocity targets. The FTS method essentially involves spatial notching of the clutter in a given Doppler filter. Since FTS provides no temporal adaptivity, it is not a true STAP algorithm. To enhance performance with only modest increase in required sample support and computational burden, DiPietro proposed the Extended Factored Algorithm (EFA) [12]. The EFA method involves adaptively combining several adjacent Doppler filters (typically three) and all spatial channels. The EFA method often exhibits performance very close to the theoretical joint-domain (JD) space-time bound. To provide diversity in spatial and temporal DoF, Wang developed the Joint Domain Localized (JDL) technique [13]. JDL is a post-Doppler, beamspace method. Basically, the processor forms multiple beams, then Doppler processes each beam, and finally selects a collection of adjacent angle-Doppler bins over which to adapt the filter response. JDL provides good performance with very low training data requirements and very modest computational burden. Three adjacent beams by three adjacent Doppler bins is a typical localized JDL processing regions [13]. Figure 11 shows the SINR loss for each of the RD-STAP methods for the same example shown in Figure 8; we compare performance against the upper bound given by the JD space-time filter. Each RD-STAP method uses secondary data support of twice the processor's DoF. Note, our discussion did not include an example of a joint pre-Doppler and angle method.

Reduced-rank STAP methods involve data-dependent transformations and selections [14-15]. Consider the following formulation of the optimal weight vector

$$\mathbf{w}_k = \frac{1}{\lambda_o} \left[\mathbf{s}_{s-t}(\phi, \theta, f_d) - \sum_{m=1}^{NM} \frac{\lambda_m - \lambda_o}{\lambda_m} \alpha_m \mathbf{q}_m \right] \quad (41)$$

where λ_m is an eigenvalue of \mathbf{R}_k with eigenvector \mathbf{q}_m , $\lambda_o = \min(\lambda_m)$ and α_m is the projection of the m^{th} eigenvector onto the quiescent response given by \mathbf{s}_{s-t} . In the adaptive case, we substitute $\hat{\mathbf{R}}_k$ for \mathbf{R}_k . Thus, we can view STAP as a pattern synthesis problem: based on a sensing of the environment, the processor places notches in the quiescent pattern to mitigate interference. Notice from (41) that no subtraction occurs for eigenvalues at the noise floor. The principal components (PC) method involves truncating the summation in (41) to accommodate only the largest eigenvalue terms. A benefit of this approach is a reduction in training data support. However, computational burden remains high, since the processor must compute eigenvalues and eigenvectors. An alternative, yet similar, approach to the PC method is given in [15] and is known as the Principal Components Inverse (PCI) method. Specifically, the processor computes

$$\mathbf{x}'_k = (\mathbf{I}_{NM} - \mathbf{Q}_I \boldsymbol{\Omega}_I \mathbf{Q}_I^H) \mathbf{x}_k = \mathbf{x}_k - \sum_{m=1}^p \frac{\lambda_{I/m}}{\lambda_m} \alpha_{x/m} \mathbf{q}_m \quad (42)$$

where \mathbf{Q}_I is the collection of interference eigenvectors (corresponding to each column), $\boldsymbol{\Omega}_I$ is the matrix enabling perfect subtraction of the designated interference term in \mathbf{x}_k , $\alpha_{x/m}$ is the projection of the m^{th} eigenvector onto the data snapshot, and $\lambda_{I/m}$ is a non-zero eigenvalue of the interference-only eigenvector. In practice, we cannot estimate the interference-only eigenvector, and so for strong, low-rank interference we can set $\lambda_{I/m} = \lambda_m$, or $\boldsymbol{\Omega}_I = \mathbf{I}_{NM}(:,1:P)$ for the P dominant components. Since

$$\mathbf{Q}_I \mathbf{Q}_I^H + \mathbf{Q}_N \mathbf{Q}_N^H = \mathbf{I}_{NM}, \quad (43)$$

where \mathbf{Q}_N is the collection of noise eigenvectors (corresponding to each column), we can express (42) as

$$\mathbf{x}'_k = \mathbf{Q}_N \mathbf{Q}_N^H \mathbf{x}_k. \quad (44)$$

Equation (44) indicates that PCI can operate by using the noise subspace information. This stands in contrast to the PC method using the dominant subspace. Using our familiar example found in Figure 8 and Figure 11, Figure 12 compares the SINR loss for the PC and PCI methods against the upper bound defined by the JD STAP solution. The adaptive solution involves a secondary data set of one times the joint domain processor's total DoF, i.e. $K = NM$. The interference subspace has dimension 40, and so we use all 40 principal components for the PC method and all 312 noise subspace components for the PCI approach. Armed with this information, observe that both methods very closely follow the optimal performance. In practice, choosing the correct number of components is challenging and an incorrect selection can lead to performance degradation.

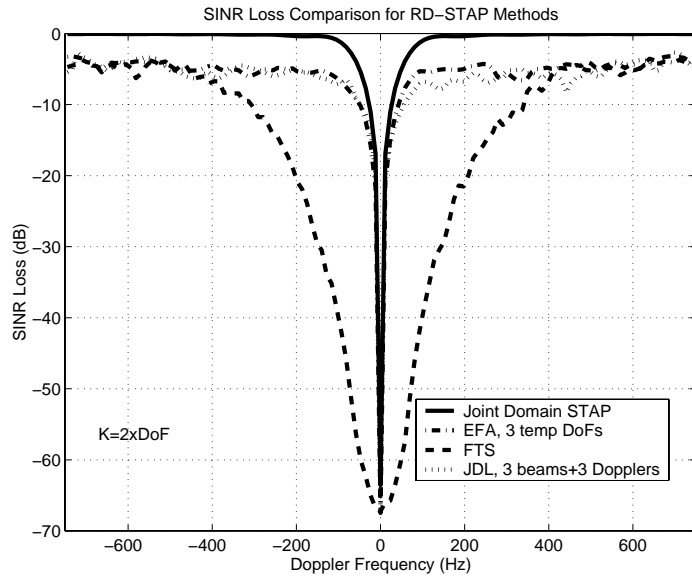


Figure 11. SINR loss for RD-STAP methods.

Oftentimes, the covariance estimate is ill-conditioned or exhibits a perturbed noise subspace. In such cases, diagonal loading can be used to tailor performance [16]. As the name implies, diagonal loading involves adding an identity matrix to the covariance estimate to stabilize the noise floor and condition the covariance matrix estimate for subsequent numerical processing. From (41) we find that if the noise eigenvalues are perturbed, the processor subtracts a noise eigenvector from the quiescent response. Noise eigenvectors exhibit random sidelobe behavior. Hence, the adaptive filter response for low secondary data set sizes shows elevated sidelobes. High sidelobes can be problematic, leading for instance to sidelobe target detection. Diagonal loading cures this problem.

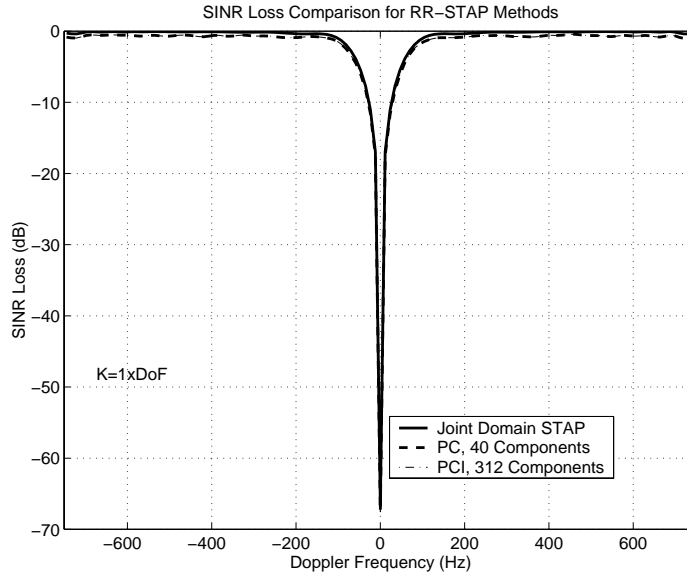


Figure 12. SINR loss for RR-STAP methods.

6. Heterogeneous Clutter Effects

Adaptive processing requires secondary (training) data to estimate unknown quantities. For example, traditional, CFAR circuits [6], which involve scalar adaptive processing, typically select ten range bins on each side of the test and guard cells to estimate the ambient interference power. STAP similarly requires a training interval to estimate the null hypothesis covariance matrix. However, in contrast with the scalar CFAR case, the potentially high dimensionality of STAP requires training data selection over large regions. Suppose a STAP-based radar has $N = 32$ (thirty-two pulse dwell) and $M = 11$ (eleven spatial channels). The minimum training set is then on the order of $2NM = 704$ range bins. If the instantaneous bandwidth is 1 MHz, training data comes from a region extending over 10 km! Over the 10 km interval, the changing cultural features of the clutter environment lead to range-angle variation of ground clutter returns. This range-angle variation in then ground clutter return is known as clutter heterogeneity [17-18].

Common STAP training approaches include the following methods: block selection, windowed block selection and sliding window. In the block selection approach, the processor selects training data sequentially from a given region and then applies it to a distinct primary data region. The windowed block selection is a variant of the block selection technique; the training data is chosen sequentially about the primary data region, with each half of the training data coming from opposite sides of the primary data regions. In the sliding window approach, the processor attempts to localize training data within the vicinity of the primary data. Thus, the processor chooses training data symmetrically about the test data and adjacent guard cells. The sliding window approach is most computationally intense, but numerical techniques are available to alleviate the computational burden of both covariance estimation and covariance matrix inversion.

As a result of clutter heterogeneity, the precise yet unknown covariance matrix of a given range cell does not match other ranges. Hence, heterogeneous clutter environments are no longer iid. The non-iid environment gives rise to increased covariance estimation errors when using (28). Specifically, since $\mathbf{R}_p \neq \mathbf{R}_m$ in non-iid environments, where p and m indicate the training vector indices and $p \neq m$, it stands to reason that

$$E\left[\hat{\mathbf{R}}_k\right] = E\left[\frac{1}{K} \sum_{m=1}^K \mathbf{x}_m \mathbf{x}_m^H\right] = \frac{1}{K} \sum_{m=1}^K E\left[\mathbf{x}_m \mathbf{x}_m^H\right] = \frac{1}{K} \sum_{m=1}^K \mathbf{R}_m \quad (45)$$

In other words, in heterogeneous clutter environments, the covariance matrix estimate tends to an average characteristic of the training data. For this reason, instantaneous performance can be poor.

Clutter heterogeneity manifests as a modification of certain components and the addition of additional terms. The angle and Doppler behavior of ground clutter is well defined and results from sensor geometry and

the platform velocity vector [8]. However, clutter amplitude and spectral width can vary, and target-like signals lead to extra components. Table 2 synopsizes the various classes of clutter heterogeneity and their impact on STAP performance.

The covariance estimation errors due to clutter heterogeneity lead to increased SINR loss, i.e. $L_{s,2}$ further approaches zero. Clutter heterogeneity is a challenge to STAP implementation, since adaptive and optimal performance does not necessarily converge with increasing number of training vectors. This realization is driving new STAP approaches holding the potential for robust performance in light of clutter heterogeneity and other behavior (see the last entry in Table 2) leading to non-iid training data.

Table 2. Taxonomy of Clutter Heterogeneity

Heterogeneity Type	Cause	Impact on Adaptive Radar
Amplitude	Shadowing and obscuration, range-angle dependent change in clutter reflectivity, strong stationary discrete, sea spikes, urban centers, land-sea interfaces, etc.	Null depth depends on eigenvalue ratio – MLE “averaging” leads to underestimated eigenvalue magnitude, and consequently, uncancelled clutter and increased false alarm rate.
Spectral	Intrinsic clutter motion due to soft scatterers (trees, windblown fields, etc.), ocean waves; CNR-dependent spectral mismatch.	Null width set to mean spread – too narrow for some range cells, thereby leading to uncancelled clutter, seriously degraded MDV.
Moving Scatterers	Ground traffic, weather, insects and birds, air vehicles.	Mainlobe nulling, false sidelobe target declarations, distorted beam patterns, exhausts DoF.
Some Other Effects	Chaff, hot clutter, multi-bounce/ multipath, impact of platform geometry (e.g., non-sidelooking or bistatic) on angle-Doppler behavior over range.	Combination of above effects.

7. Summary

In this set of lecture notes, we consider fundamental aspects of space-time adaptive detection theory. Section 2 describes the basics of hypothesis testing and relates this information to space-time detection. We introduce the likelihood ratio test in this section and through example demonstrate its use. Additionally, we describe the important whitening filter and matched filter concepts, relating them to the detection statistic. We then describe the application of signal diversity to advanced sensor design in Section 3. Signal diversity helps cull the weak target signal masked by interference. We provide an example showing the space-time characteristics of ground clutter and the advantage space-time degrees of freedom offer in enhancing detection performance. Section 4 first develops the maximum signal-to-interference-plus-noise ratio (SINR) filter, which maximizes the probability of detection in the Gaussian case. We then describe commonly used STAP performance metrics. We overview space-time detector structures in Section 5. In this section we first begin by examining STAP normalizations leading to a constant false alarm rate (CFAR) property. We then describe the philosophy behind reduced-dimension and reduced-rank STAP methods. Reduced-dimension STAP involves data independent transformations to characterize interference behavior in a smaller subspace. Advantages of reduced-dimension STAP include a requirement for smaller training data sets and minimal computational burden. Reduced-rank techniques involve data dependent transformations to derive a stochastic basis describing the interference properties. The principal component reduced-rank technique can achieve the upper bound on SINR performance when properly applied. We also introduce the principal components inverse method in this section. The paper concludes with a brief discussion of clutter heterogeneity. We define clutter heterogeneity and describe its impact on STAP implementation.

References

[1] M.I. Skolnik, Introduction to Radar Systems, 2nd Ed., McGraw Hill, New York, NY, 1980.

- [2] W.L. Melvin, "Application of STAP in advanced sensor systems," *Proceedings of the Research and Technology Agency, North Atlantic Treaty Organization (RTA-NATO) Lecture Series 228 – Military Applications of Space-Time Adaptive Processing*, September 2002.
- [3] D.H. Johnson and D.E. Dudgeon, Array Signal Processing: Concepts and Techniques, Prentice-Hall, Englewood Cliffs, NJ, 1993.
- [4] J.V. DiFranco and W.L. Rubin, Radar Detection, Artech-House, Dedham, MA, 1980.
- [5] L.E. Brennan and I.S. Reed, "Theory of adaptive radar," *IEEE Trans. AES*, Vol. 9, No. 2, March 1973, pp. 237-252.
- [6] N. Levanon, Radar Principles, John Wiley & Sons, New York, 1988.
- [7] I.S. Reed, J.D. Mallett, and L.E. Brennan, "Rapid convergence rate in adaptive arrays," *IEEE Trans. AES*, Vol. 10, No. 6, November 1974, pp. 853-863.
- [8] R. Klemm, Space-Time Adaptive Processing: Principles and Applications, IEE Radar, Sonar, Navigation and Avionics 9, IEE Press, 1998.
- [9] W.S. Chen and I.S. Reed, "A new CFAR detection test for radar," *Digital Signal Processing*, Vol. 1, Academic Press, 1991, pp. 198-214.
- [10] E.J. Kelly, "An adaptive detection algorithm," *IEEE Trans. AES*, Vol. AES-22, No. 1, March 1986, pp. 115-127.
- [11] S. Haykin, Adaptive Filter Theory, Third Ed., Prentice-Hall, Upper Saddle River, NJ, 1996.
- [12] R.C. DiPietro, "Extended factored space-time processing for airborne radar," *Proc. 26th Asilomar Conf.*, Pacific Grove, CA, Oct. 1992, pp. 425-430.
- [13] H. Wang and L. Cai, "On adaptive spatial-temporal processing for airborne surveillance radar systems," *IEEE Trans. AES*, Vol. 30, No. 3, July 1994, pp. 660-670.
- [14] W.F. Gabriel, "Using spectral estimation techniques in adaptive processing antenna systems," *IEEE Trans. AP*, Vol. 34, No. 3, March 1986, pp. 291-300.
- [15] D.W. Tufts, I. Kirssteins and R. Kumaresan, "Data-adaptive detection of a weak signal," *IEEE Trans. AES*, Vol. AES-19, No. 2, March 1983, pp. 313-316.
- [16] B.D. Carlson, "Covariance matrix estimation errors and diagonal loading in adaptive arrays," *IEEE Trans. AES*, Vol. 24, No. 4, July 1988, pp. 397-401.
- [17] W.L. Melvin, "Space-time adaptive radar performance in heterogeneous clutter," *IEEE Trans. AES*, Vol. 36, No. 2, April 2000, pp. 621-633.
- [18] W.L. Melvin, J.R. Guerci, M.J. Callahan, M.C. Wicks, "Design of adaptive detection algorithms for surveillance radar," in *Proc. IEEE 2000 Int'l Radar Conf.*, Alexandria, VA, 7-12 May 2000, pp. 608-613.

This page has been deliberately left blank

Page intentionnellement blanche

Doppler Properties of Airborne Clutter

Richard Klemm

FGAN-FHR, Neuenahrer Str. 20, D 53343 Wachtberg, Germany

Tel +49 228 9435 377; Fax +49 228 9435 618; email r.klemm@fgan.de

Abstract

Detection of slowly moving targets by air- and spaceborne MTI radar is heavily degraded by the motion induced Doppler spread of clutter returns. Space-time adaptive processing (STAP) can achieve optimum clutter rejection via implicit platform motion compensation. In this report the fundamentals and properties of STAP applied to air- and spaceborne MTI radar are summarised. The effect of platform motion on the characteristics of airborne clutter is discussed. The performance of the optimum space-time processor is shown. Comparison with spatial or temporal only techniques illustrate the importance of space-time processing.

1 Introduction

The main application of space-time adaptive processing (STAP) is the suppression of clutter received by a moving radar. In this case we talk about space-slow time (pulse-to-pulse) processing. The radar platform motion causes clutter returns to be Doppler shifted. The Doppler shift is proportional to the platform velocity and the angle of arrival. The total of all clutter arrivals sums up in a Doppler broadband clutter echo. Targets whose Doppler frequencies fall into the clutter Doppler bandwidth may be difficult to detect. It should be noted that most moving targets are "slow" or low Doppler targets, either because they are slow or exhibit a low Doppler due to their motion direction. For a radar on a satellite (10 km/s) all targets near the ground (jet aircraft 300 m/s) are slow targets.

Other important techniques operate in the space-fast time (range equivalent) domain. They are used to either suppress jammers in broadband array radar or for mitigating terrain scattered jamming.

Space-time processing needs space-time data to operate on. Space-time data are obtained from a radar which has a phased array antenna with multiple outputs (spatial dimension), and transmits coherent pulse trains (temporal dimension).

1.1 The principle of adaptive clutter suppression

1.1.1 Practical application: adaptive clutter filter for surveillance radar

The following experiment conducted in the early 1970's (BÜHRING & KLEMM [6]) is described briefly to illustrate the principle of adaptive clutter filtering. This filter was designed to suppress weather clutter with unknown centre Doppler frequency and bandwidth. This adaptive MTI system was operated with a conventional groundbased surveillance radar with rotating reflector antenna. Figure 1 shows the block diagram of an adaptive FIR filter based on the prediction error filter principle. The filter coefficients were estimated in real-time and the echo data were clutter filtered during the following revolution of the antenna.

In Figure 2 the filtering effect is demonstrated using simulated clutter. The picture shows a photograph of a PPI (pla position indicator) screen. The zero Doppler filter has been switched off so that a lot of ground clutter can be noticed. The spokes are the simulated clutter (for simplicity this clutter was simulated independent of range). The available radar operated in L-band which is quite insensitive to weather. Therefore, to have reproducible clutter conditions a hardwired simulator was developed. The clutter filter was adapted based on clutter data in the window on the right. As can be seen the clutter has been removed and a (true) target is visible.

Figure 3 and 4 show suppression of a real weather cloud before and after filtering. Except for a few false alarms the weather clutter has been removed. The air targets (big spots on the left) did not do us the favour to enter our measurement window, they just bypass it¹.

¹No responsible pilot will enter a thunder storm deliberately.

1.2 The History of STAP

In the following two sections a brief review of the history of research and experimental work on STAP is given.

1.2.1 Theoretical work (Table 1)

Table 1 includes a number of publications which represent milestones in the evolution of STAP. This selection of papers is certainly not exhaustive but to our opinion representative. In some cases merely the earliest papers rather than the most significant papers are quoted. In the meantime special journal issues (# 20,21) and tutorials (# 12,19,20) on STAP are available.

The original idea of reducing the clutter spectrum via motion compensation originates from ANDERSON (# 1). This paper was written before digital technology was available. The DPCA technique SKOLNIK (# 2) was also originally invented for use with implementation in microwave technology. This technique compensates physically or electronically for the platform motion in a non-adaptive fashion. The paper by BRENNAN & REED (# 3) is the basis for all future space-time processing. It deals with interference rejection in broadband arrays. This principle was analysed in some detail by COMPTON (# 7). The first paper on STAP was written by BRENNAN et al. (# 4). Here the optimum (maximum likelihood) processor applied to clutter rejection for moving radar has been described and analysed. Starting from (# 4) KLEMM discovered that the size of the clutter subspace is about $N + M$ under certain conditions which gave rise to manyfold research on subspace processor architectures (# 8, 9, 12, 13, 18, 20). Later on an extension of this result became known as "Brennan's Rule" (# 10). Problems of real-time implementation of STAP processors have been discussed by FARINA et al. (# 11). WARD (# 15) presented angle and Doppler estimation errors for STAP radar. ENDER (# 17) demonstrated the detection and re-positioning of moving targets in SAR images obtained with the multi-channel SAR AER II. DOHERTY et al. and JOUNY et al. (# 16) used STAP techniques to mitigate the effect of terrain scattered jamming. STAP in conjunction with bistatic radar has been discussed by KLEMM (# 23). A recent trend of moving reconnaissance function from airborne to space-borne platforms can be noticed (COVAULT (# 24)). Besides the STAP research activities in the USA and Europe some considerable interest of Chinese scientists in STAP can be noticed (# 6).

1.2.2 Experiments and Systems (Table 2)

In Table 2 experimental and operational STAP systems are listed. The first (non-adaptive) DPCA experiment involving an array antenna has been carried out by Tsandoulas (# 1). The NRL (# 3) and MCARM experiments (# 4) use linear sidelooking arrays. Both programs lead to many detailed investigations on possibilities of airborne clutter rejection. A large number of publications originate from these programs, dealing with various research topics such as clutter homogeneity, sidelobe Doppler clutter, knowledge-based MTI processing, subspace techniques (e.g., $\Sigma - \Delta$), and bistatic operation (# 11). The Mountaintop program (# 5) was started in 1990 to study advanced processing techniques and technologies to support the requirements of future airborne early warning radar platforms. In particular the effect of terrain scattered jamming has been studied. In Europe the AER II program (# 7, Germany), the DO-SAR experiment (# 8, Germany) and the DERA experiment (# 9, UK) have been conducted.

There are three operational systems with space-time ground clutter rejection capability (Joint STARS (# 2), AN/APG-76 (# 6), and the AN/APY-6). The first one has a 3-aperture sidelooking array antenna and has been flown in the Gulf War. The AN/APG-76 is a forward looking nose radar and the AN/APY-6 has both sidelooking and forward looking capability. From the available literature it is not obvious whether these system are based on adaptive algorithms (STAP) or used some non-adaptive DPCA-like techniques.

1.2.3 Historical note

The non-adaptive DPCA technique has been described already in SKOLNIK ed. [39]. Research on space-time adaptive processing started with the paper by BRENNAN et al. [4] in 1976 on space-time MTI (moving target

indication) processing for airborne radar. Very little has been published in the following years. In 1983 the author introduced the concept of eigenanalysis of the space-time clutter covariance matrix which opened the horizon towards subspace techniques for real-time applications [21]. A number of follow-up papers by the author have been concerned with various suboptimum approaches based on order reducing transforms of the signal subspace. These papers have been summarized in a book on STAP (KLEMM [26]). Since 1990 research activities on STAP increased tremendously, particularly in the USA (e.g. WARD [46], WANG & CAI [43]), in China (e.g. WANG & BAO [44]), in the UK (RICHARDSON & HAYWARD [35]), and in Italy FARINA et al. [15]).

#	year	subject	authors
1	1958	First paper on motion compensated MTI	Anderson [1]
2	1970	DPCA	Skolnik [39]
3	1973	Theory of adaptive radar	Brennan & Reed [3]
4	1976	First paper on STAP	Brennan et al. [4]
5	1983	Dimension of clutter subspace	Klemm [21]
6	≈ 1987	First Chinese papers	e.g. Wang & Bao [44]
7	1988	Broadband jammer cancellation	Compton [9, 8]
8	1990	Space-time FIR filter	Klemm & Ender [22]
9	1992	Spatial transform techniques	Klemm [23]
10	1992	Brennan's Rule	Brennan & Staudaher [5]
11	1992	Real-time implementation of STAP	Farina et al. [15]
12	1994	Report on STAP	Ward [46]
13	1994	Beam/Doppler space processing	Wang & Cai [43]
14	1995	STAP for forward looking arrays	Richardson & Hayward [35] Klemm [24]
15	1995	Angle/velocity estimation with STAP radar	Ward [47]
16	1995	Mitigation of terrain scattered jamming	Doherty [11], Jouny et al. [20]
17	1996	STAP for SAR	Ender [13]
18	1996	$\Sigma - \Delta$ STAP	Wang et al. [45]
19	1996	Effect of platform maneuvers	Richardson et al. [36]
20	1998	IEE Colloquium on STAP	Klemm (chair) [25]
21	1998	Textbook on STAP	Klemm [26]
22	1998	Effect of range walk	Kreyenkamp [33]
23	1999	IEE ECEJ special issue on STAP	Klemm (ed) [28]
24	1999	IEEE Trans. AES: Special issue on STAP and Adaptive Arrays	Melvin (ed.)[32]
25	1999	STAP with bistatic radar	Klemm [27]
26	1999	STAP for future observation satellites	Covault [10]

Table 1. Some milestones in STAP research

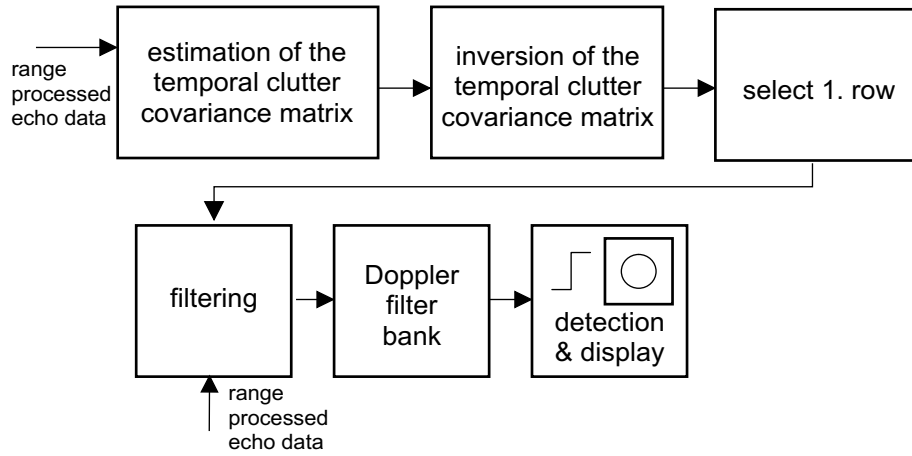


Figure 1: Block diagram of adaptive temporal clutter filter

#	year	system	authors
1	1973	DPCA with array antenna (flight experiment)	Tsandoulas [42]
2	1991	Joint STARS antenna	Shnitzkin [38]
3	1992	NRL experiment	Lee & Staudaher [34]
4	1994	MCARM experiment	Babu [2]
5	1994	Mountaintop	Titi [41]
6	1996	AN/APG-76 sidelooking airborne array radar	Tobin [40]
7	1996	AER II	Ender [12]
8	1996	Dornier's DO-SAR	Hippler & Fritsch [19]
9	1996	DERA STAP experiment	Coe et al. [7]
10	1998	AN/APY-6 airborne array radar	Gross & Holt [16]
11	1999	STAP with bistatic radar	Sanyal et al. [37]

Table 2. Existing STAP systems



Figure 2: Adaptive suppression of simulated weather clutter



Figure 3: Weather clutter before adaption



Figure 4: Weather clutter after adaption

2 Principle of air- and spaceborne MTI radar

In this section some important features of airborne clutter echoes are briefly discussed. The efficiency of space-time clutter suppression depends significantly on these properties. For definition of the geometry see Figure 5. It shows two important cases (sidelooking and forward looking arrays).

2.1 Effect of Platform Velocity

2.1.1 Models of clutter and target

The results presented in this paper have been calculated on the basis of simple models for target and interference. For the sake of brevity we give here only the models as used in the evaluation. For more details the reader is referred to [26, chapter 2].

Clutter

The $NM \times NM$ clutter covariance matrix has the form

$$\mathbf{Q} = \begin{pmatrix} \mathbf{Q}_{11} & \mathbf{Q}_{12} & \dots & \mathbf{Q}_{1M} \\ \mathbf{Q}_{21} & \mathbf{Q}_{22} & \dots & \mathbf{Q}_{2M} \\ \vdots & \vdots & \ddots & \vdots \\ \mathbf{Q}_{M1} & \mathbf{Q}_{M2} & \dots & \mathbf{Q}_{MM} \end{pmatrix} \quad (1)$$

where the indices of the submatrices m, p denote time (pulse repetition intervals) while the indices i, k run inside the submatrices and denote space (sensors). N is the number of sensors and M the number of coherently processed echoes. The elements of \mathbf{Q} are integrals over a full range circle

$$\begin{aligned} q_{ln}^{(c)} &= P_c \int_{\varphi=0}^{2\pi} \rho_{mp} \rho_{i-k} \\ &\quad \times D^2(\varphi) L^2(\varphi) G(\varphi, m) G^*(\varphi, p) \\ &\quad \times \Phi_{m-p}^{(t)}(\varphi, v_p) \Phi_{i-k}^{(s)}(\varphi) d\varphi + P_N \\ &\quad m, p = 1 \dots M \quad i, k = 1 \dots N \end{aligned} \quad (2)$$

where P_c is the clutter power at the single element at a certain instant of time and P_N the receiver noise power. The other symbols denote as follows: φ azimuth, s. Figure 5; A complex clutter amplitude; $D(\varphi)$ sensor directivity pattern; $L(\varphi)$ clutter reflectivity; ρ_{ik} spatial (sensor-to-sensor) correlation which is not considered here; ρ_{mp} temporal (echo-to-echo) correlation; $G(\varphi, m)$ transmit directivity pattern. The temporal and spatial phase terms are as follows

$$\begin{aligned} \Phi_m^{(t)}(\varphi) &= \exp[j \frac{2\pi}{\lambda} 2v_p m T \cos \varphi \cos \theta] \\ \Phi_i^{(s)}(\varphi) &= \exp[j \frac{2\pi}{\lambda} (x_i \cos \varphi + y_i \sin \varphi) \\ &\quad \times \cos \theta - z_i \sin \theta] \end{aligned} \quad (3)$$

The indices l, n of the $NM \times NM$ covariance matrix are related to the sensor indices i, k and echo indices m, p through

$$l = (m-1)N + i \quad m = 1 \dots M; \quad i = 1 \dots N \quad (4)$$

$$n = (p-1)N + k \quad p = 1 \dots M; \quad k = 1 \dots N \quad (5)$$

Noise

Receiver noise is assumed to be uncorrelated in space and time

$$E\{n_m n_p^*\} = \begin{cases} P_n & : m = p \\ 0 & : m \neq p \end{cases} \quad (6)$$

$$E\{n_i n_k^*\} = \begin{cases} P_n & : i = k \\ 0 & : i \neq k \end{cases} \quad (7)$$

where P_n denotes the white noise power.

Target

A target at azimuthal position φ_t moving at a radial velocity v_{rad} produces the following space-time signal at the array output

$$\begin{aligned} s_{mi}(\varphi_t) = & A \exp[j \frac{2\pi}{\lambda} \\ & \times (2v_{rad}mT + (x_i \cos \varphi_t + y_i \sin \varphi_t) \cos \theta \\ & - z_i \sin \theta)] \\ & m = 1 \dots M \quad i = 1 \dots N \end{aligned} \quad (8)$$

2.1.2 The Isodops

Surfaces of constant Doppler are given by cones. Intersections of such cones with the planar ground results in a set of hyperbolae as shown in Figure 6 for horizontal flight and flat earth. The radar platform moves from left to right. Maximum Doppler is encountered at 0° (positive Doppler) and 180° (negative Doppler), zero Doppler at 90° 270° .

2.1.3 Impact of Array Geometry

Only one quadrant of the isodop field is shown in Figure 7 (thin curves).

The axis of a linear array in sidelooking orientation coincides with the flight path. Therefore, curves of constant look direction are again hyperbolae on the ground (fat curves). The beam traces of a linear sidelooking array coincide with the isodops. This means that the clutter Doppler is range independent. This important property has implications on clutter rejection.

The axis of a forward looking linear array is perpendicular to the flight axis. Therefore, the set of beam traces are rotated by 90° , s. Figure 8. Now one can notice that beam traces and isodops cross each other frequently. For a forward looking array the Doppler frequency of clutter echoes depends obviously on range. The range dependency occurs especially at short range, that is, where the range is of the order of magnitude of the platform height above ground.

2.1.4 Azimuth-Doppler Clutter Trajectories

Figure 9 shows the trajectories of clutter spectra in the azimuth² (abszissa) - Doppler (ordinate) plane. The four plots have been calculated for different crab angles ψ . For $\psi = 0^\circ$ (sidelooking array) all the clutter power is located on the diagonal of the plot while for increasing crab angle one obtains ellipses. Finally, $\psi = 90^\circ$ means a forward looking array, with the clutter power located on a circular trajectory.

Clutter echoes depend in general on range. First of all the backscattered clutter power decreases with range according to the radar equation: $P_c \propto \frac{1}{R^3}$.

² $\cos \varphi$

Doppler-range dependence

The range dependence of the clutter Doppler frequency has already been addressed in the context of isodops. It follows from the above considerations that the clutter Doppler is constant with range for a sidelooking array. Therefore, all four curves calculated for different ranges coincide (Figure 9a). From Figure 9d it is obvious that for a certain look direction the Doppler frequency increases with range in case of a forward looking array³.

2.2 Comparison of Spatial, Temporal and Space-Time Processing

The principle of space-time adaptive processing for clutter rejection in moving radars is illustrated in Figure 11. A sidelooking sensor configuration was assumed. The clutter spectrum extends along the diagonal of the $\cos \varphi - \omega_D$ plot. Notice the modulation by the transmit beam.

Conventional *temporal* processing means that the projection of the clutter spectrum onto the ω_D axis is cancelled via an inverse filter. Such filter is depicted in the back of the plot. As can be seen the clutter notch is determined by the projected clutter mainlobe which is a Doppler response of the transmit beam. Slow targets are attenuated.

Spatial processing as being used for jammer nulling requires that the clutter spectrum is projected onto the $\cos \varphi$ axis. Applying an inverse spatial clutter filter, however, forms a broad stop band in the look direction so that the radar becomes blind. Both fast and slow targets fall into the clutter notch.

Space-time processing exploits the fact that the clutter spectrum is basically a narrow ridge. A space-time clutter filter, therefore, has a two-dimensional *narrow* clutter notch so that even slow targets fall into the passband.

³This follows from the depression angle term $\cos \theta$ in (3).

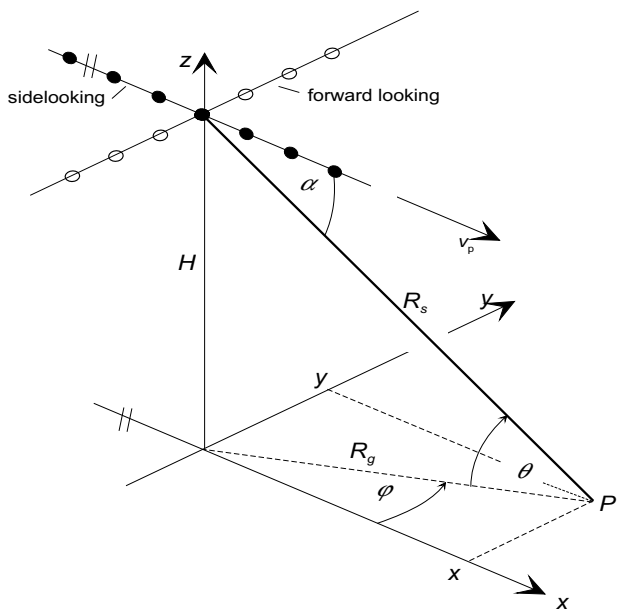


Figure 5: Geometry of airborne antenna arrays

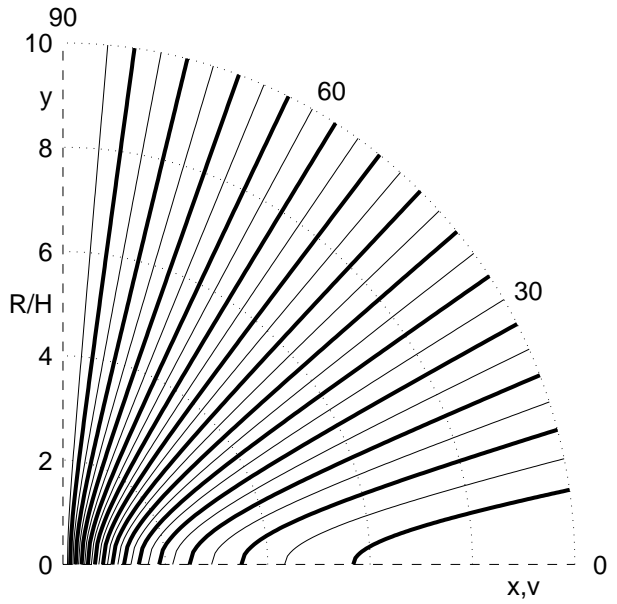


Figure 7: Beam traces (fat) and isodops for sidelooking array

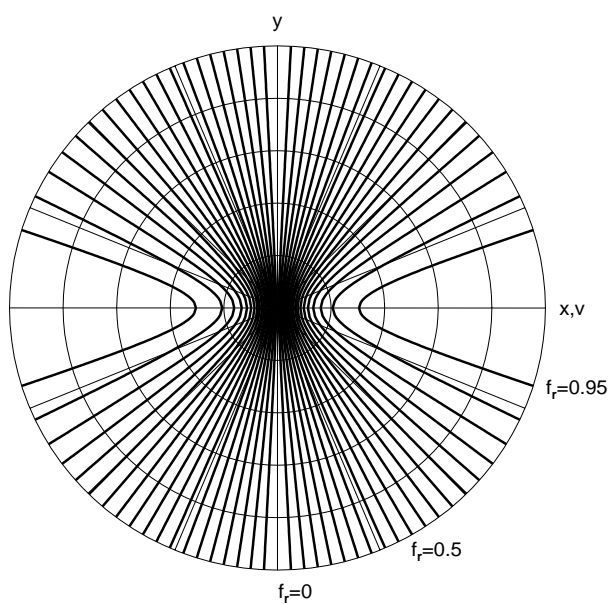


Figure 6: The isodops

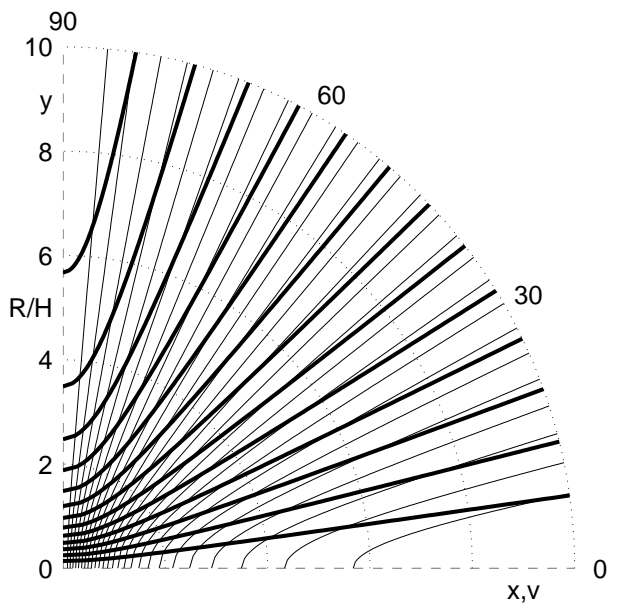


Figure 8: Beam traces (fat) and isodops for forward looking array

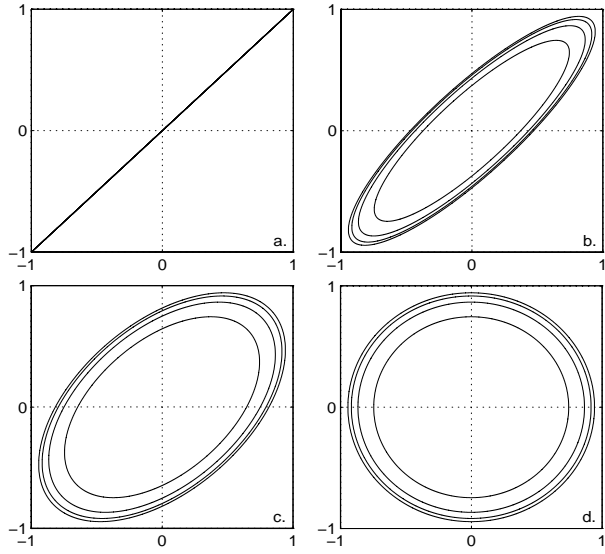


Figure 9: $f_r - \cos \varphi$ clutter trajectories for linear arrays: a. $\psi = 0^\circ$; b. $\psi = 30^\circ$; c. $\psi = 60^\circ$; d. $\psi = 90^\circ$; from inside to outside: $R/H = 1.5; 2; 2.5; 3$

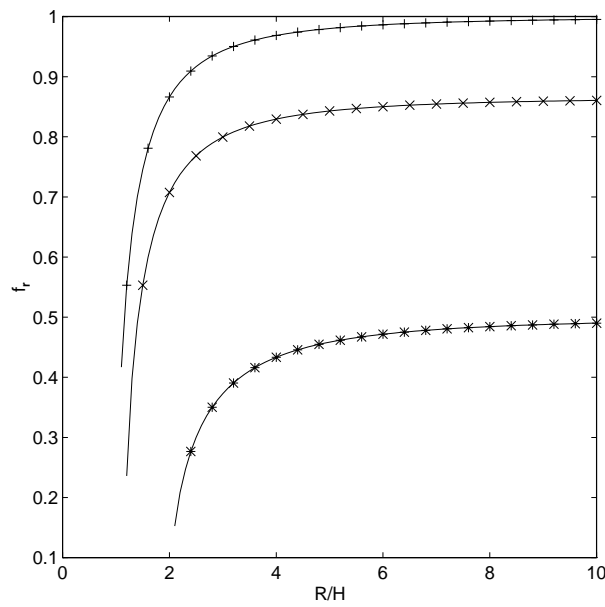


Figure 10: Range dependence of the clutter Doppler frequency for forward looking array: + $\beta = 90^\circ$ (look direction=flight direction); $\times \beta = 60^\circ$; * $\beta = 30^\circ$

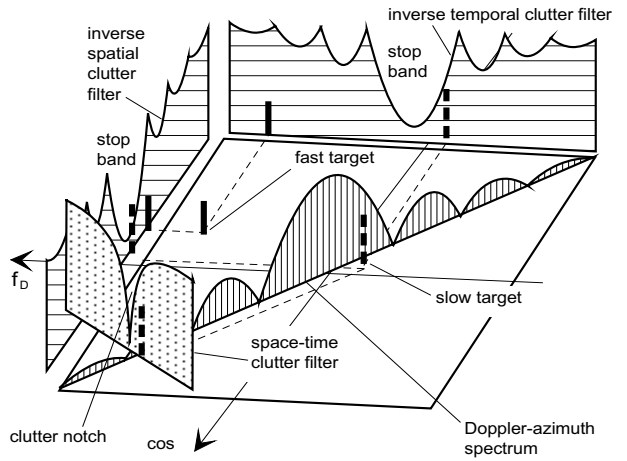


Figure 11: Principle of space-time clutter filtering (sidelooking array antenna)

3 Characteristics of Air- and Spaceborne Clutter

3.1 The Space-time Covariance Matrix

The space-time covariance matrix was defined in eqs. 1, 2. Figs. 12, 13 show the modulus of typical space-time covariance matrices. As can be seen from Fig. 12 the spatial submatrices are unity matrices with the diagonal shifted with the temporal indices M, p . In case of pure spatial processing we would deal with a $N \times N$ unity matrix only. In this case no substantial gain in clutter rejection can be achieved. Through spacetime processing we obtain the other correlation ridges in the matrix which provide the correlation required for clutter cancellation. If we use directive sensors and a directive transmit array some additional correlation comes up as can be seen in Fig. 13. Fig. 14 shows a space-time covariance matrix for noise jamming. As can be seen there is no temporal correlation.

3.2 Clutter Spectra

3.2.1 Eigenspectra

The concept of eigenanalysis of space-time clutter covariance matrices was introduced by the author [21]. The eigenspectrum (rank ordered sequence of eigenvalues) shows how large the clutter subspace is.

The elements of the space-time covariance matrix are calculated as

$$q_{ln} = E\{c_{im}c_{kp}^*\} + P_w \delta_{ikmp} \quad (9)$$

where c_{im} is the space-time clutter signal. The spatial (sensor) indices i, k and the temporal (echo pulse) indices m, p are related with the matrix indices through

$$l = (m - 1)N + i \quad m = 1 \dots M; \quad i = 1 \dots N \quad (10)$$

$$n = (p - 1)N + k \quad p = 1 \dots M; \quad k = 1 \dots N \quad (11)$$

P_w is the receiver noise power and δ_{ikmp} the Kronecker symbol. It was found in [21] that for a sidelooking equidistant array and the PRF chosen so that DPCA conditions are fulfilled (see section 4.1.1) the number of eigenvalues is

$$N_e = N + M - 1.$$

This figure determines the minimum size of the number of degrees of freedom of the space-time clutter filter.⁴

3.2.2 Power Spectra

Based on the space-time clutter+noise covariance matrix azimuth-Doppler spectra can be generated, either by 2D Fourier transform of the covariance matrix, or by use of one of the well-known high resolution power estimators.

Let us consider a covariance matrix of the form

$$\mathbf{R} = E\{\mathbf{x}\mathbf{x}^*\} = \mathbf{S} + \mathbf{N} \quad (12)$$

where \mathbf{N} is the noise component and \mathbf{S} includes all kind of signal or interference. Then the output of a signal matched filter is simply

$$y_{SM}(\Theta) = \mathbf{x}^* \mathbf{s}(\Theta) \quad (13)$$

and the normalised power output is

$$P_{SM}(\Theta) = \frac{\mathbf{s}^*(\Theta) \mathbf{R} \mathbf{s}(\Theta)}{\mathbf{s}^*(\Theta) \mathbf{s}(\Theta)} \quad (14)$$

⁴Actually in [21] it reads $N_e = N + M$. The correct number is $N_e = N + M - 1$.

$s(\Theta)$ is a steering vector which seeks for signal components $s(\Theta_i)$ in \mathbf{R} . $P(\Theta)$ attempts to become maximum wherever the steering vector $s(\Theta)$ coincides with a signal vector $s(\Theta_i)$ in \mathbf{R} . For sinusoidal signals the signal matched filter becomes the 2D Fourier transform.

Fig. 18 shows a 2D Fourier clutter spectrum. One recognises the main beam response and the sidelobe response along the diagonal. In addition there are spurious Doppler and azimuthal sidelobes which are responses of the spatial and temporal FT to the main beam clutter. Notice that only the clutter along the diagonal is physical clutter, the sidelobes along the Doppler and azimuth axes are artifacts. Similar relations can be observed if Hamming weighting is applied in space and time (Fig. 19).

The minimum variance estimator has proven to be the most useful because its response is closest to the clutter contained in the covariance matrix. In analogy with (19) the minimum variance estimator becomes

$$\mathbf{w}_{MV} = \gamma \mathbf{R}^{-1} \mathbf{s} \quad (15)$$

with $\gamma = (\mathbf{s}^* \mathbf{R}^{-1} \mathbf{s})^{-1}$. The output power is

$$P_{MV}(\Theta) = (\mathbf{s}^*(\Theta) \mathbf{R}^{-1} \mathbf{s}(\Theta))^{-1} \quad (16)$$

Figures 20 and 21 show typical MV clutter spectra (F is the normalised Doppler frequency) for sideways and forward looking linear arrays. For the sidelooking array the clutter power is distributed on the diagonal⁵ of the plot while in case of a forward looking configuration the clutter is distributed on a semi-circle. Notice that in this example the individual sensors have sensor patterns which blank the rear semi-plane out. Otherwise the clutter power of the forward looking array would be distributed on a full circle.

⁵The wavy shape of the trajectory is due to the fact that we used φ instead of $\cos \varphi$ for the abscissa.

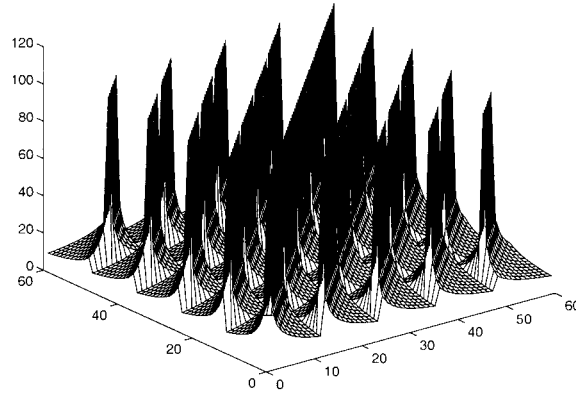


Figure 12: Modulus of the clutter covariance matrix vs horizontal and vertical index (sidelooking linear array, $N=12$, $M=5$, omnidirectional sensors and transmission)

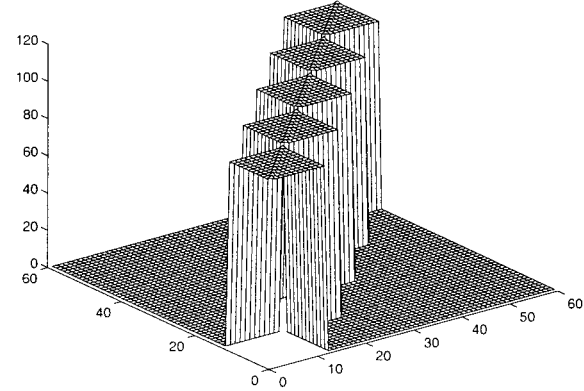


Figure 14: Jammer covariance matrix (sidelooking array, $N=12$, $M=5$, 1 jammer, absolute values)

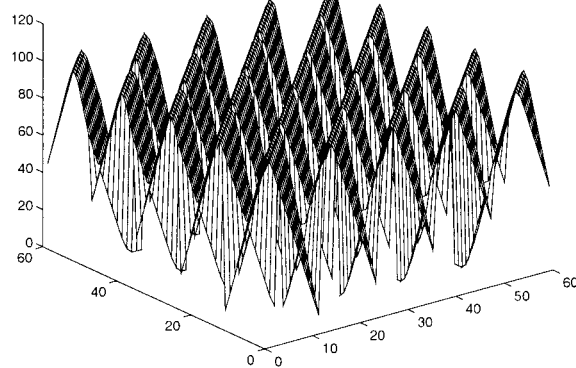


Figure 13: Modulus of the clutter covariance matrix vs horizontal and vertical index (sidelooking linear array, $N=12$, $M=5$, directive sensors and transmission)

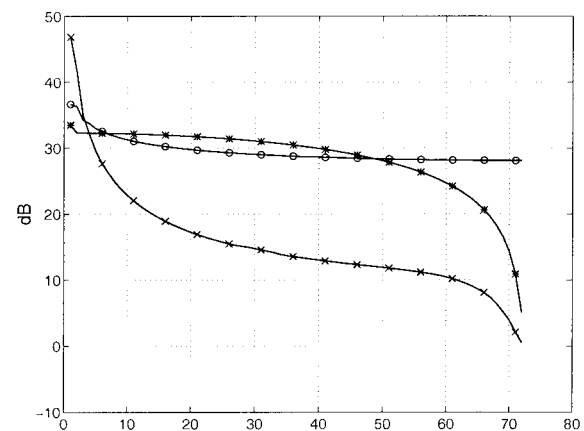


Figure 15: Eigenspectra of a spatial covariance matrix. $N = 72$, $M = 1$; \circ omnidirectional sensors and transmission; $*$ directive sensors; \times directive sensors and transmission

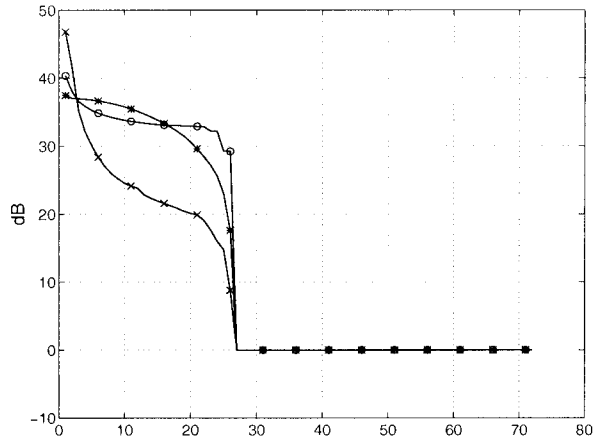


Figure 16: Eigenspectra of a *space-time* covariance matrix (sidelooking array). $N = 24$, $M = 3$; \circ omnidirectional sensors and transmission; $*$ directive sensors and transmission; \times directive sensors and transmission

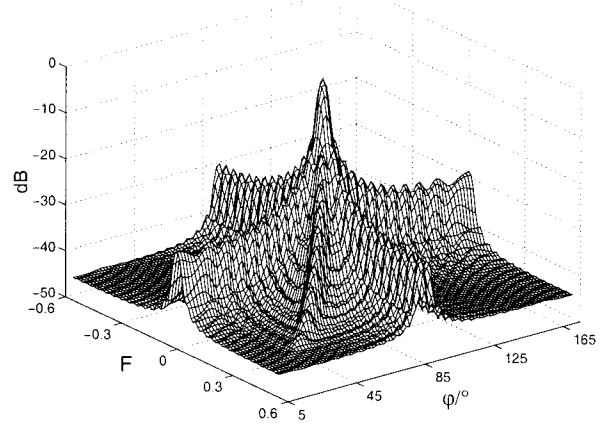


Figure 18: Fourier clutter spectrum (sidelooking array, $\varphi_L = 90^\circ$)

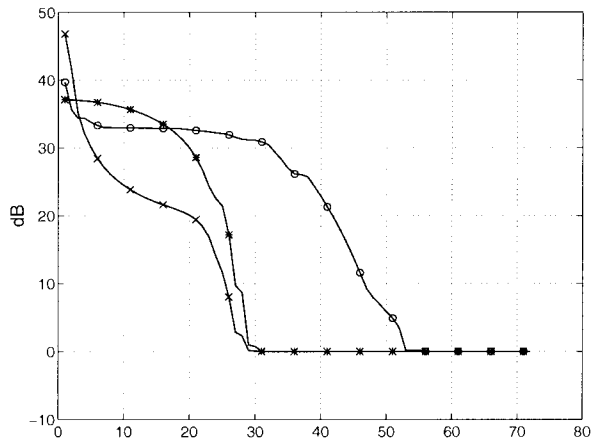


Figure 17: Eigenspectra of a *space-time* covariance matrix (forward looking array). $N = 24$, $M = 3$; \circ omnidirectional sensors and transmission; $*$ directive sensors and transmission; \times directive sensors and transmission

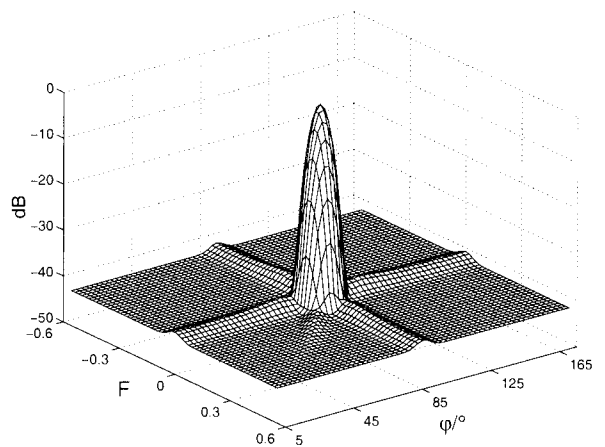


Figure 19: Fourier clutter spectrum with spatial and temporal Hamming weighting (sidelooking array, $\varphi_L = 0^\circ$)

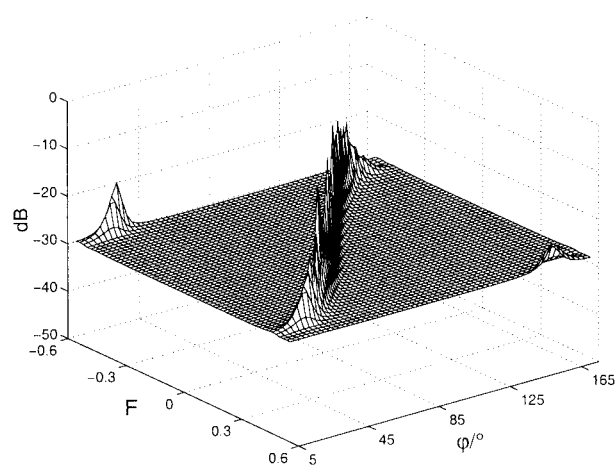


Figure 20: MV clutter spectrum (sidelooking array,
 $\varphi_L = 45^\circ$)

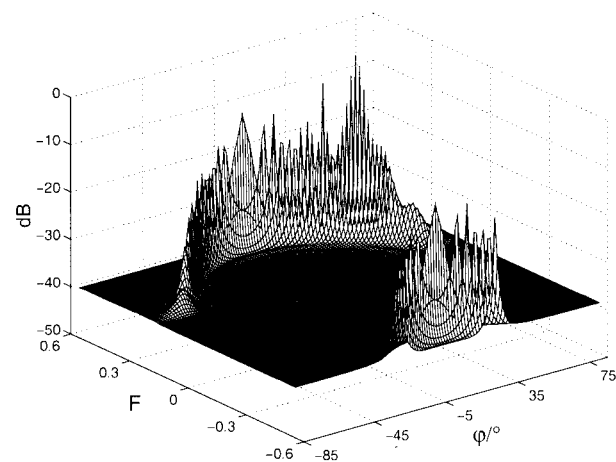


Figure 21: MV spectrum for forward looking linear array

4 The Optimum Space-Time Processor

4.1 Historical: The Displaced Phase Center Antenna (DPCA)

4.1.1 The DPCA technique

DPCA (displaced phase centre antenna) is a technique which compensates physically for the motion of the radar platform to reduce the effect of motion induced Doppler spread of clutter returns. Consider two antennas in sidelooking configuration as shown in Figure 22. At time $m = 1$ they assume the dashed position, at time $m = 2$ the solid one. As can be noticed the first antenna at $m = 1$ assumes the position of the second sensor at time $m = 2$. This is equivalent to having one antenna fixed in space⁶ for the duration of one pulse interval. Clutter suppression is done by subtracting so that the clutter remainder becomes $\epsilon = q_2 - c_{21}$. If $c_{12} = c_{21}$ perfect cancellation is obtained. Notice that this technique was implemented in RF technology long time before the age of digital signal processing.

4.1.2 A note on DPCA and STAP

For more than 3 decades the DPCA principle (motion compensation by spatial coincidence of sensor positions, s. section 4.1.1 and Figure 22) has been considered the physical background of space-time clutter rejection. More recently, numerical investigations have shown that forward looking arrays (which do not have the DPCA property) work as well with space-time adaptive processing.

This reveals that the function of STAP is not based on a DPCA geometry. The space-time filtering is just based on the fact that airborne clutter echoes are signals depending on the two variables space and time, and they are *bandlimited* in the Doppler as well as in the azimuth dimension. If such signals are properly sampled in space (sensor displacement) and time (PRF) any kind of filtering can basically be applied without aliasing losses. The property of slow target detection is based on the special shapes of such clutter spectra (narrow ridge). STAP is not based on DPCA. DPCA is merely a special case of STAP. The DPCA property plays a role in the context of compensating for the effects of system bandwidth.

4.2 The LR-Test for 2-D Vector Quantities

The principle of detecting a signal vector s before a noisy background given by q is briefly summarized. Let us define the following complex vector quantities:

$$\mathbf{q} = \begin{pmatrix} \mathbf{q}_1 \\ \mathbf{q}_2 \\ \vdots \\ \mathbf{q}_N \end{pmatrix}; \quad \mathbf{s} = \begin{pmatrix} \mathbf{s}_1 \\ \mathbf{s}_2 \\ \vdots \\ \mathbf{s}_N \end{pmatrix}; \quad \mathbf{x} = \begin{pmatrix} \mathbf{x}_1 \\ \mathbf{x}_2 \\ \vdots \\ \mathbf{x}_N \end{pmatrix} \quad (17)$$

where $\mathbf{q}_m, \mathbf{s}_m$ and \mathbf{x}_m are the spatial subvectors (signals at the array output) at the m -th pulse repetition interval. In general the noise vector consists of a correlated part \mathbf{c} (e.g. jammer, clutter) and an uncorrelated part \mathbf{n} (e.g. receiver noise):

$$\mathbf{q} = \mathbf{c} + \mathbf{n} \quad (18)$$

The signal vector \mathbf{s} is assumed to be deterministic. \mathbf{x} is the actual data vector which may be noise only ($\mathbf{x} = \mathbf{q}$) or signal-plus-noise ($\mathbf{x} = \mathbf{q} + \mathbf{s}$). The problem of extracting \mathbf{s} optimally out of the background noise \mathbf{q} is solved by applying the well-known linear weighting

$$\mathbf{w}_{\text{opt}} = \gamma \mathbf{Q}^{-1} \mathbf{s} \quad (19)$$

⁶Due to the factor of 2 in the Doppler term $2mv_p T$ the antenna motion during one PRI is only half the antenna spacing. It is important that phase coincidence of clutter echoes occurs.

A block diagram of the optimum processor is shown in Fig. 23. The spatial dimension is given by the N antenna elements while the temporal dimension is given by shift registers where M subsequent echoes are stored. These space-time data are multiplied with the inverse of the space-time adaptive clutter covariance matrix for clutter cancellation. The output signal are then fed into a space-time weighting network whose coefficients form a space-time replica (beamformer and Doppler filter) of the desired signal.

4.2.1 Performance of the Optimum Processor

The efficiency of any linear processor \mathbf{w} can be characterized by the improvement factor⁷ which is defined as the ratio of signal-to-noise power ratios at output and input, respectively

$$IF = \frac{\frac{P_s^{out}}{P_n^{out}}}{\frac{P_s^{in}}{P_n^{in}}} = \frac{\frac{\mathbf{w}^* \mathbf{s} \mathbf{s}^* \mathbf{w}}{\mathbf{w}^* \mathbf{Q} \mathbf{w}}}{\frac{\mathbf{s}^* \mathbf{s}}{\text{tr}(\mathbf{Q})}} = \frac{\mathbf{w}^* \mathbf{s} \mathbf{s}^* \mathbf{w} \cdot \text{tr}(\mathbf{Q})}{\mathbf{w}^* \mathbf{Q} \mathbf{w} \cdot \mathbf{s}^* \mathbf{s}} \quad (20)$$

Figs. 24 and 25 show examples for the improvement factor in the azimuth-Doppler plane for sidelooking and forward looking linear arrays. Along the clutter trajectory we have now a clutter notch.

4.2.2 Comparison with 1-dimensional Methods

The question is, how much is the advantage of space-time processing versus conventional techniques. Such a comparison has been made in Fig. 26. The optimum space-time processor is compared with a beamformer cascaded with an optimum temporal clutter filter, and simple Beamforming plus Doppler filtering. The advantage of space-time processing is obvious.

4.2.3 Range-Doppler Matrix

Plotting clutter power or IF versus Doppler and range results in the range-Doppler Matrix. Figures 27 and 28 show examples for sidelooking and forward looking . For sidelooking radar (Figure 27) the clutter trajectory is a straight vertical line which corresponds to the fact that the clutter Doppler is range independent, compare with Figure 7. For forward looking radar we notice a certain dependency of the clutter Doppler with range, especially at short range, which is consistent with Figure 8.

4.3 Optimum Processor and Eigencanceller

The Eigencanceler is a zero noise approximation of the optimum processor. It is given by

$$\mathbf{P} = \mathbf{I} - \mathbf{E}(\mathbf{E}^* \mathbf{E})^{-1} \mathbf{E}^* \quad (21)$$

where \mathbf{E} is the matrix of eigenvectors belonging to the interference component in \mathbf{Q} . Figure 29 shows a comparison of the optimum processor and the eigencanceller. The curves are almost identical, except for the clutter notch. Here the optimum processor suppresses the interference down to the noise level whereas the eigencanceler forms an exact null. The eigencanceler needs less training data for adaptation than the optimum processor which can be a significant advantage for real-time operation.

⁷The expression *improvement factor* is commonly used for characterizing *temporal* (i.e., pulse-to-pulse) filters for clutter rejection. The same formula may be used for *spatial* applications (array processing) in the context of interference or jammer suppression. Then instead of *improvement factor* the term *gain* is used. Since our main objective is clutter rejection we prefer the term *improvement factor* or its abbreviation IF.

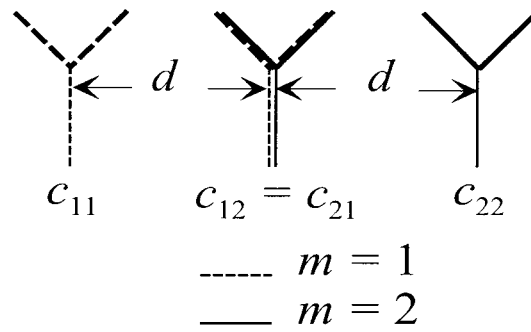


Figure 22: Principle of a 2-pulse DPCA clutter canceller

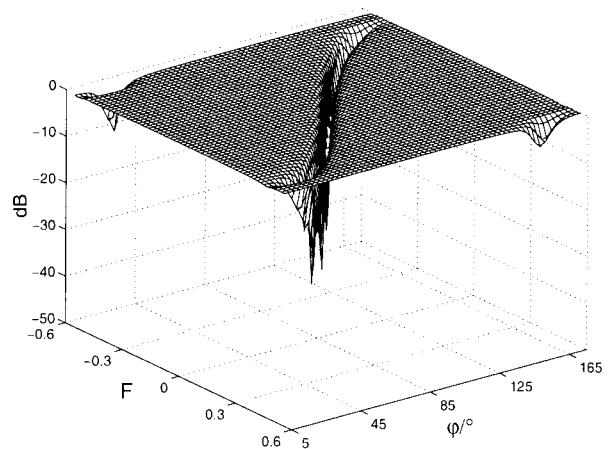


Figure 24: Improvement factor for sidelooking array

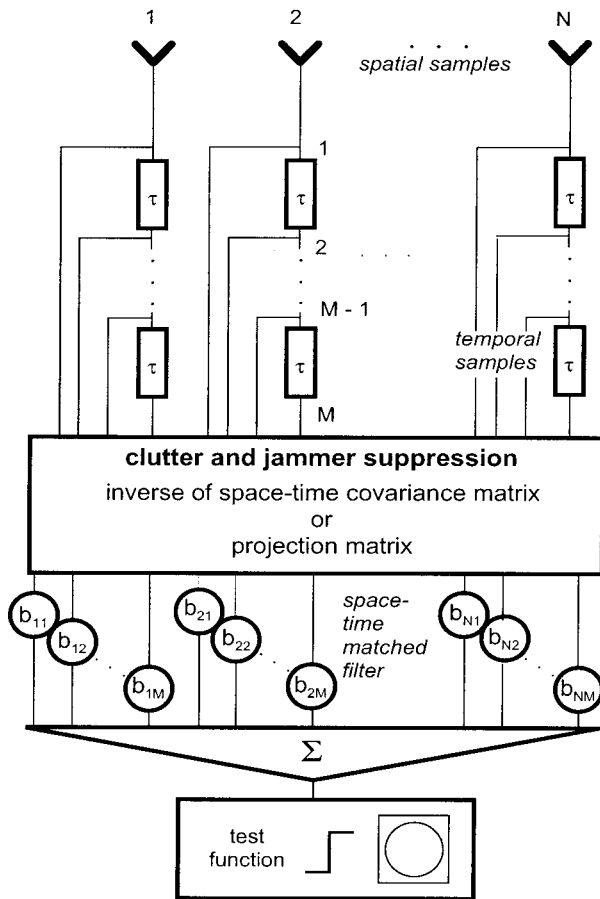


Figure 23: The optimum adaptive space-time processor

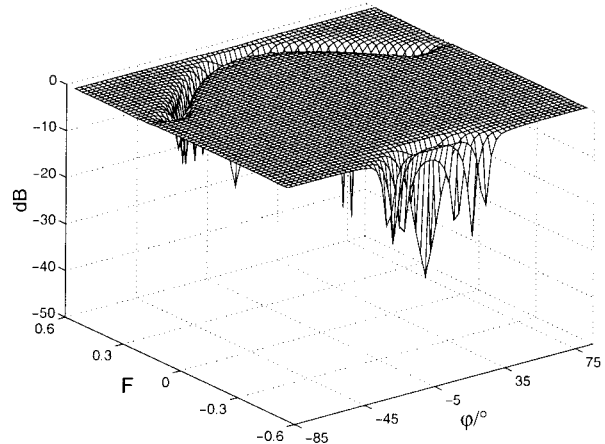


Figure 25: Improvement factor for forward looking array

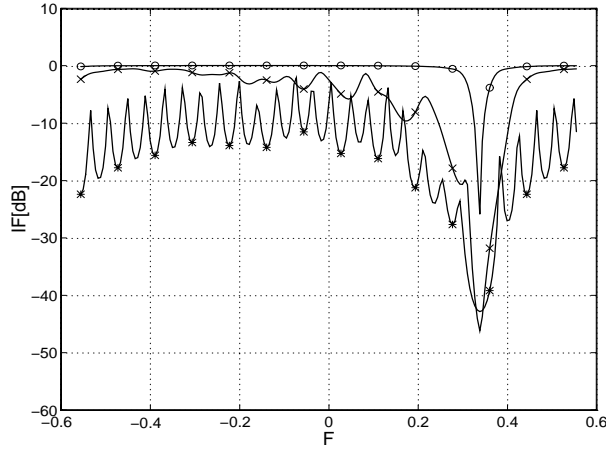


Figure 26: The potential of space-time adaptive processing: \circ optimum processing; $*$ beamformer + Doppler filter; \times beamformer + adaptive temporal filter

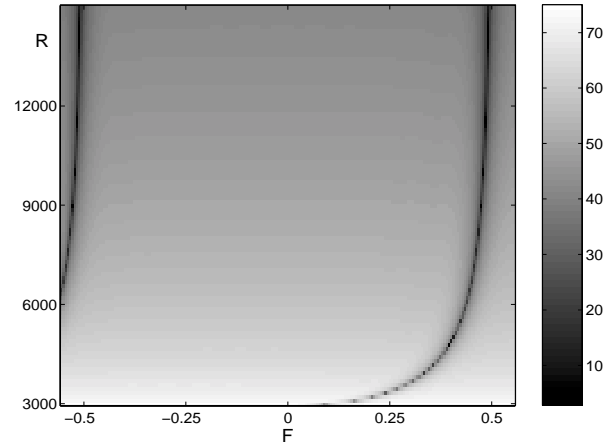


Figure 28: Range-Doppler Matrix (greytones denote IF/dB, $R = \text{range}/\text{m}$, FL , $\varphi_L = 0^\circ$)

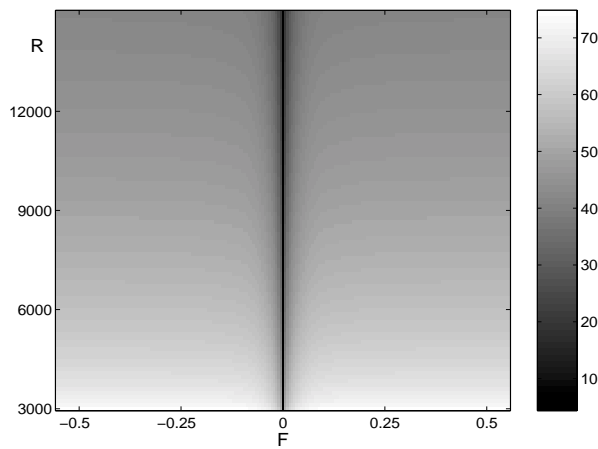


Figure 27: Range-Doppler Matrix (greytones denote IF/dB, $R = \text{range}/\text{m}$, SL , $\varphi_L = 90^\circ$)

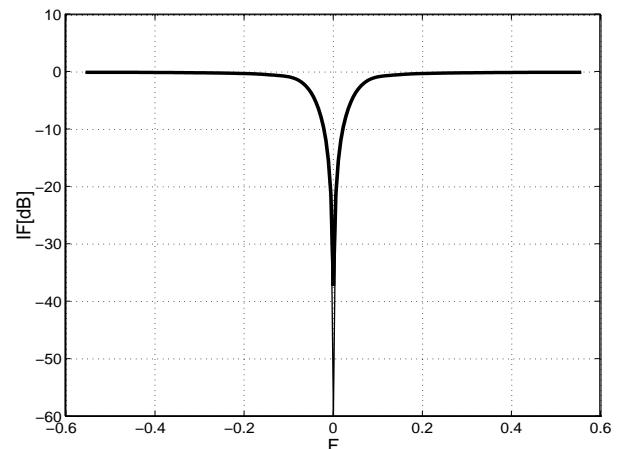


Figure 29: Comparison of optimum and orthogonal projection processing

References

- [1] Anderson, D. B., "A Microwave Technique to Reduce Platform Motion and Scanning Noise in Airborne Moving Target Radar", *IRE WESCON Conv. Record*, Vol. 2, pt. 1, 1958, pp. 202-211
- [2] Babu, S. B. N., Torres, J. A., Lamensdorf, D., "Space-Time Adaptive Processing for Airborne Phased Array Radar, *Proc. of the Conf. on Adaptive Antennas*, 7-8 November 1994, Melville, New York 11747, pp. 71-75
- [3] Brennan, L. E., Reed, I. S., "Theory of Adaptive Radar", *IEEE Trans. AES*, Vol. 9, No 2, March 1973, pp. 237-252
- [4] Brennan, L. E., Mallett, J. D., Reed, I. S., "Adaptive Arrays in Airborne MTI", *IEEE Trans. AP*, Vol. 24, No. 5, 1976, pp. 607-615
- [5] Brennan, L. E., Staudaher, F. M., "Subclutter Visibility Demonstration", *Technical Report RL-TR-92-21, Adaptive Sensors Incorporated*, March 1992
- [6] Bühring, W., Klemm, R., "Ein adaptives Filter zur Unterdrückung von Radarstörungen mit unbekanntem Spektrum" (An adaptive filter for suppression of clutter with unknown spectrum), *FREQUENZ*, Vol. 30, No. 9, September 1976, (in German), pp. 238-243
- [7] Coe, D. J., White, R. G., "Experimental moving target detection results from a three-beam airborne SAR", *AEU*, Vol. 50, No. 2, March 1996
- [8] Compton, R. T. jr., "The Bandwidth Performance of a Two-Element Adaptive Array with Tapped Delay-Line Processing", *IEEE Transaction on Antenna and Propagation*, Vol. AP-36, No. 1, January 1988, pp. 5-14
- [9] Compton, R. T. jr., "The Relationship Between Tapped Delay-Line and FFT Processing in Adaptive Arrays", *IEEE Transaction on Antenna and Propagation*, Vol. AP-36, No. 1, January 1988, pp. 15-26
- [10] Covault, C., "Space-based radars drive advanced sensor technologies", *Aviation Week & Space Technology*, April 5, 1999, pp. 49-50
- [11] Doherty, J. F., "Suppression of Terrain Scattered Jamming in Pulse Compression Radar", *IEEE Transactions on Signal Processing*, Vol. 2, No. 1, January 1995, pp. 4-6
- [12] Ender, J., "The airborne experimental multi-channel SAR system", *Proc. EUSAR'96*, 26-28 March 1996, Koenigswinter, Germany, pp. 49-52 (VDE Publishers)
- [13] Ender, J., "Detection and Estimation of Moving Target Signals by Multi-Channel SAR", *Proc. EUSAR'96*, 26-28 March 1996, Koenigswinter, Germany, pp. 411-417, (VDE Publishers). Also: *AEU*, Vol. 50, March 1996, pp. 150-156
- [14] Ender, J., "Experimental results achieved with the airborne multi-channel SAR systems AER II.The airborne experimental multi-channel SAR system", *Proc. EUSAR'98*, 25-27 May 1998, Friedrichshafen, Germany
- [15] Farina, A., Timmoneri, L., "Space-time processing for AEW radar", *Proc. RADAR 92*, Brighton, UK, 1992, pp. 312-315
- [16] Gross, L.A., Holt, H.D., "AN/APY-6 realtime surveillance and targeting radar development", *Proc. NATO/IRIS Conference*, 19-23 October 1998, paper G-3
- [17] Haimovich, A. L., Bar-Ness, Y., "An Eigenanalysis Interference Canceler", *IEEE Trans. Signal Processing*, Vol. 39, No. 1, January 1991, pp. 76-84

- [18] Ayoub, T. F., Haimovich, A. M., Pugh, M. L ., "Reduced-rank STAP for high PRF radar", *IEEE Trans. AES*, Vol. 35, No. 3, July 1999, pp. 953-962
- [19] Hippler, J., Fritsch, B., "Calibration of the Dornier SAR with trihedral corner reflectors", *Proc. EU-SAR'96*, 26-28 March 1996, Koenigswinter, Germany, pp. 499-503, (VDE Publishers)
- [20] Jouny, I. I., Culpepper, E., "Modeling and mitigation of terrain scattered interference", *IEEE Antennas and Propagation Symposium*, 18-23 June, 1995, Newport Beach, USA, pp. 455-458
- [21] Klemm, R., "Adaptive Clutter Suppression for Airborne Phased Array Radar", *Proc. IEE*, Vol. 130, No. 1, February 1983, pp. 125-132
- [22] Klemm, R., Ender, J., "New Aspects of Airborne MTI", *Proc. IEEE Radar 90*, Arlington, USA, 1990, pp. 335-340
- [23] Klemm, R., "Antenna design for airborne MTI", *Proc. Radar 92*, October 1992, Brighton, UK, pp. 296-299
- [24] Klemm, R., "Adaptive Airborne MTI: Comparison of Sideways and Forward Looking Radar", *IEEE International Radar Conference*, Alexandria, VA, May 1995, pp. 614-618
- [25] Klemm, R., ed., *Digest of the IEE Colloquium on STAP*, 6 April 1998, IEE, London, UK
- [26] Klemm, R., Space-Time Adaptive Processing - Principles and Applications *IEE Publishers*, London, UK, 1998)
- [27] Klemm, R., "Comparison between monostatic and bistatic antenna configurations for STAP", *IEEE Trans. AES*, April 2000
- [28] Klemm, R., (ed.), Special issue on "Space-Time Adaptive Processing", *IEE ECEJ*, February 1999
- [29] Klemm, R., "Space-time adaptive FIR filtering with staggered PRI", *ASAP 2001*, MIT Lincoln Lab., Lexington, MA, USA, 13-15 March 2001, pp.
- [30] Klemm, R., "Doppler properties of airborne clutter", *RTO SET Lecture Series 228* (this volume)
- [31] Koch, W., Klemm, R ., "Grouns target tracking with STAP radar", *IEE Proc. Radar, Sonar and Navigation*, 2001
- [32] Melvin, W. L., (ed.), Special issue on "Space-Time Adaptive Processing and Adaptive Arrays", *IEEE Trans. AES*, April 2000
- [33] Kreyenkamp, O., "Clutter covariance modelling for STAP in forward looking radar", *DGON International Radar Symposium 98*, September 15-17, 1998, München, Germany
- [34] Lee, F. W., Staudaher, F., "NRL Adaptive Array Flight Test Data Base", *Proc. of the IEEE Adaptive Antenna Systems Symposium*, Melville, New York, November 1992
- [35] Richardson, P. G., Hayward, S. D., "Adaptive Space-Time Processing for Forward Looking Radar", *Proc. IEEE International Radar Conference*, Alexandria, VA, USA, 1995, pp. 629-634
- [36] Richardson, P. G., "Effects of maneuvre on space-time adaptive processing performance", *Proc. IEE Radar'97*, 14-16 October 1997, Edinburgh, Scotland, pp. 285-289
- [37] Sanyal, P. K., Brown, R. D., Little, M. O., Schneible, R. A., Wicks, M. C., "Space-time adaptive processing bistatic airborne radar", *IEEE National Radar Conference*, 20-22 April 1999, Boston, USA, pp. 114-118

- [38] Shnitkin, H., "A Unique JOINT STARS Phased Array Antenna", *Microwave Journal*, January 1991, pp. 131-141
- [39] Skolnik, M., *Radar Handbook*, 1st Ed., McGraw-Hill, New York, 1970
- [40] Tobin, M., "Real-Time Simultaneous SAR/GMTI in a Tactical Airborne Environment", *Proc. EUSAR'96*, 26-28 March, 1996, Koenigswinter, Germany, pp. 63-66, (VDE Publishers)
- [41] Titi, G. W., "An Overview of the ARPA/NAVY Mountaintop Program", *IEEE Adaptive Antenna Symposium*, Melville, New York November 7-8, 1994
- [42] Tsandoulas, G. N., "Unidimensionally Scanned Phased Arrays", *IEEE Trans. on Antennas and Propagation*, Vol. AP28, No. 1, Novemver 1973, pp. 1383-1390
- [43] Wang, H., Cai, L., "On Adaptive Spatial-Temporal Processing for Airborne Surveillance Radar Systems", *IEEE Trans. AES*, Vol. 30, No. 3, July 1994, pp. 660-670
- [44] Wang Z., Bao Z., "A Novel Algorithm for Optimum and Adaptive Airborne Phased Arrays", *Proc. SITA'87*, 19-21 November 1987, Tokyo, Japan, pp. EE2-4-1
- [45] Wang, H., Zhang, Y., Zhang, Q., "An Improved and Affordable Space-Time Adaptive Processing Approach", *Proc. International Conference on Radar (ICR'96)*, Beijing, China, 8-10 October 1996, pp. 72-77
- [46] Ward, J., "Space-Time Adaptive Processing for Airborne Radar", *Technical Report No. 1015*, Lincoln Laboratory, MIT, December 1994
- [47] Ward, J., "Cramer-Rao Bounds for Target Angle and Doppler Estimation with Space-Time Adaptive Processing Radar", *Proc. 29th ASILOMAR Conference on Signals, Systems and Computers*, 30 October-2 November 1995, pp. 1198-1203

STAP for SAR

A. Farina

Technical Directorate, Radar & Technology Division

Alenia Marconi Systems

Via Tiburtina Km. 12.400, 00131 Rome, Italy

tel: +39-06-4150-2279; fax: +39-06-4150-2665, e.mail: afarina@amsjv.it

Key words: moving target detection and imaging, Synthetic Aperture Radar, Space Time adaptive processing.

1. SUMMARY

This paper describes the application of STAP (Space Time Adaptive Processing) to Synthetic Aperture Radar (SAR) systems. SAR is a microwave sensor that allows us to have a high resolution mapping of electromagnetic (e.m.) backscatter from an observed scene. A two-dimensional image is provided in the radar polar coordinates, i.e.: slant range and azimuth. High resolution in slant range is obtained by transmitting a coded waveform, with a large value of the time - bandwidth product, and coherently processing the echoes in a filter matched to the waveform. High resolution along the transversal direction is achieved by forming a synthetic aperture. This requires: (i) to put the radar on board of a moving platform, e.g.: an aircraft or a satellite; (ii) to record the e.m. signals from each scatterer which is illuminated by the moving antenna beam in successive instants of time, and (iii) to coherently combine the signals – via a suitable azimuthal matched filter – thus focusing the sliding antenna pattern in a narrower synthetic beam [AUS84]. The advantage of combining SAR and STAP is evident: the detected moving target is shown on top on the SAR image of the sensed scene. The paper is organised as follows. The description of the technical problem to tackle is in section 2; also a look to the state of the art is included. It is well known that the SAR image of a moving target presents a number of aberrations: these are briefly reviewed in section 3. Signal processing schemes are described in Section 4 which is the core of the paper. We move from a suitable modification of the conventional MTI and Pulse Doppler (PD), to Along Track Interferometry (ATI) SAR, to Displaced Phase Center Antenna (DPCA) – the predecessor of STAP. Finally the last described processing scheme is the one that combines the data in the three domains: space, time and frequency. Some of the schemes are tested with simulated data. The paper concludes with a perspective to future work, and a collection of references for further readings.

2. DESCRIPTION OF THE PROBLEM AND STATE OF THE ART

In many applications (e.g.: surveillance) of SAR, it is desirable to detect and possibly produce focused images of moving objects. A moving low RCS object is not easily detectable against strong echoes scattered from an extended fixed scene. When detected, its resulting image is smeared and ill positioned with respect to the stationary background. These shortcomings are a direct consequence of the SAR image formation process. The cross-range high resolution in a SAR is obtained by taking advantage of the relative motion, supposed known, between the sensor and the scene. If, however, there is an object moving in an unpredictable manner, the image formation process does not function properly. Basically, the main degradations due to the target motion are the following. (i) The range migration through adjacent resolution cells (due to the radial velocity of target respect to radar) causes a reduction of the signal-to-clutter power ratio, which can seriously impair the detection capabilities. Furthermore, range migration causes a decrease in the integration time and a consequent loss of resolution. (ii) Even in the absence of range migration, or after its correction, the phase shift induced by the motion causes: an ill-positioning (along track) of the target image with respect to ground, mainly owing to

the range component of the relative radar-target velocity; a smearing of the image is also due to the uncompensated cross-range velocity and/or range acceleration.

A first possibility that has been studied of discriminating the moving target signals from the fixed scene returns is on the basis of their different Doppler frequency spectra; see, for instance, [DDB94] and the quoted references. In fact, the target spectrum has a Doppler centroid approximately linearly proportional to the along-range velocity of target and a spectrum width depending on the azimuthal velocity and the radial acceleration components of target. Assuming that the radar pulse repetition frequency (PRF) is high enough to make available a region in the Doppler frequency domain not occupied by the stationary scene, the method works as follows (see Section 4.1 for details). First transform a sequence of radar target returns to the frequency domain. Second, locate spectral bands, outside the narrow band frequency around origin corresponding to stationary scene, and determine the centre frequencies of such bands. Third, translate each outlying spectral band to the origin, convert the resulting signal back to the time domain and correlate with the reference function of the conventional SAR. The correlator output will show the peaks in the correct locations of the targets. A refinement of this basic technique aims at the image formation of each target: it is obtained by matching also the width, not only the mean value, of spectral band outside the stationary scene Doppler spectrum. The method suffers however of three shortcomings. (i) it requires the use of a high PRF which causes a corresponding reduction of the SAR swath width and an increase of the data throughput. (ii) It does not correctly focus the image of a target having a quite arbitrary path. The spectrum of the target echoes alone is not sufficient; we need to know the instantaneous phase law to form the synthetic aperture with respect to the moving target. (iii) It does not succeed with a target whose motion has a small range velocity component, so that its spectrum is superimposed on the clutter (i.e.: on the stationary scene) spectrum. A distinct advantage of this system is related to the possibility to use it with conventional, non multi-channel phased-array radar antennas.

More powerful methods have been conceived to overcome these drawbacks; they are based on the use of more than one antenna, on board the moving platform, to cancel the clutter and detect the slowly moving targets. The radar system uses an array of antennas, mounted on the platform along the flight direction, and corresponding receiving channels. This makes available a certain number of space samples (echoes received from different antenna elements) and time samples (echoes collected at different time instants). These echoes are coherently combined, with proper weights, in a space-time processor to cancel the echo backscattered from the ground and enhance the target echo. Space-time effectively reduces the lower bound on the minimum detectable target velocity that would be established by using only frequency filtering. It measures the relative phase between two or more coherent signals, received from different antennas, rather than the Doppler frequency shift within a single receiving channel. Instead of using a mono-dimensional filtering, clutter cancellation is the result of a powerful two-dimensional (in the temporal frequency, i.e.: Doppler, and in the spatial frequency, i.e.: azimuth angle) filtering. Furthermore this method does not require necessarily to work with high PRF values. This is the STAP approach: see [WAR94], [KLE98] and [KLE99] for details. The way to the full fledged STAP wasn't immediate: it passed to the ATI applied to SAR (described in Section 4.2) and to the DPCA (see Section 4.3); both techniques being essentially based on the use of the echoes captured by two antennas.

A refinement of ATI-SAR was the VSAR (Velocity SAR) method [FPO97]. In a way similar to the progression from a two-pulse canceller to a bank of Doppler filters to reject clutter and detect moving targets in a conventional search radar, the technique can be generalised to a linear array of identical antennas. For each channel a complex SAR image is calculated. A Fourier transform along the physical aperture (i.e.: the channel number) is applied to each pixel, and this corresponds to a multiple beam former. For each Fourier cell the related image shows the scene for a certain range of radial velocities (velocity SAR image [FPO97]). This method hasn't however originally designed to suppress clutter, since no attempt is made to subtract signals. The requirement to cancel the echoes from stationary scatterers leads directly to adaptive space-time filtering.

Once detected the presence of a moving target, we have to estimate its phase modulation law to be able to form a high resolution image of it. A method for providing the estimate is by means of time-frequency analysis

of the received signal. This, combined with STAP, brings to the joint space-time-frequency processing presented in detail in Section 4.4. The time-frequency representation is obtained by evaluating the Wigner-Ville Distribution (WVD) of the signal. This distribution is a signal representation consisting in the mapping of the signal onto a plane whose coordinates are time and frequency. The WVD, in particular, produces a mapping such that the signal energy is concentrated along the curve of the instantaneous frequency. This frequency is obtained as the centre of gravity of the WVD; the instantaneous phase is derived by integration of the instantaneous frequency. The clutter echoes are cancelled by the adaptive space-time processor, where the space-time covariance matrix of clutter is estimated on-line and used to evaluate the optimal weights of the two-dimensional filter. The time-frequency analysis provides an estimation of the instantaneous frequency of the possibly present moving target, and – by integration – the original instantaneous phase. The phase is used to compensate for the shift due to the relative target-radar motion.

3. ABERRATIONS DUE TO TARGET MOTION

There are some interesting effects that occur with moving targets. A moving target with a radial component of velocity v_r results in a Doppler shift on each echo of

$$f_D = \frac{2v_r f_0}{c} \quad (1)$$

where f_0 is the radar carrier frequency and c is the velocity of propagation. Thus the Doppler history of the sequence of echoes is shifted in frequency (Figure 1), and is matched filtered (with a small mismatch) with an azimuth shift which is the product of the Doppler shift and the slope of the Doppler history

$$f_D \cdot \frac{r\lambda}{2v/d} = \frac{v_r r}{v} \quad (2)$$

where v is the platform speed, r is the platform-target range and d is the along track dimension of the antenna (the real aperture). It is well known that an image from an aircraft-borne SAR of a moving train having a component of velocity in the range direction appears shifted, so it appears to be travelling not along the railway track, but displaced to the side! As another example, a ship in a satellite SAR image with a radial velocity of 10 m/s at a range of 1,200 km would experience an azimuth shift of 1.7 km. On the other hand, the ship wake (which is stationary) appears in the correct position. Thus the ship appears not at the tip of the wake, but displaced in azimuth. This effect is visible in a number of space-borne SAR images. From the knowledge of the geometry, and of the azimuth shift, it is possible to estimate the target velocity.

4. PROCESSING SCHEMES

In the following several processing schemes for detection and imaging of moving target are described.

4.1 MTI+PD

The material of this Section is derived by [DDB94] that describes the work done by Colleagues of the Author. The processing technique, referred to as moving target detection and imaging (MTDI), has been derived by the well known moving target detection (MTD) processing widely used in conventional ground-based radars. A range-Doppler SAR processing is adopted; the raw data are firstly processed along the range direction and then along the azimuth. An azimuth processor is developed to detect the presence of a moving point like target in

each range cell and to measure its velocity components. The method is valid under the following hypotheses, namely:

- the target velocity is bounded within a minimum detectable and a maximum unambiguous values, and
- the SAR system and the moving target cause a negligible range migration.

The mathematical model of the echo received by the radar antenna during the synthetic aperture time interval is reported in this section. Fig. 2 sketches the geometry of a SAR system and a moving object of interest. The antenna, on board of an aircraft, moves along the azimuth direction x . The antenna beam pattern is directed orthogonal to the flight path; θ (the off-nadir angle) is the angle formed by the normal to the ground and the line from the radar to the central point of the scene; v_x and v_y are the velocity components of the target along the reference coordinates. Along the azimuth, the radar transmits pulse trains with repetition frequency, PRF, each pulse having a linear frequency modulation (chirp). To account for some unpredictable changes in the environment wherein the transmitter operates, an unknown initial phase ϕ_0 , modeled as a random variate uniformly distributed in $(0, 2\pi)$ is assumed in the transmitted signal. At the n th azimuth position of the antenna, the transmitted pulse is expressed as

$$T_n(t) = A \cos(2\pi f_0 t + \alpha t^2 + \phi_0), -\tau/2 \leq t \leq \tau/2 \quad (3)$$

where:

- A and τ are the pulse amplitude and the pulse width, respectively,
- f_0 is the carrier frequency,
- $\alpha=2\pi B/\tau$ is the chirp rate, and
- B is the chirp bandwidth.

Consider now a point-like scatterer on a completely absorbing background; the echo received by the antenna at the n th azimuth position, after down frequency conversion, can be modeled as

$$S_n(t) = Al\sigma_0 g_0(\theta, \varphi) \exp(j(\alpha(t-t_d)^2) \exp(j4\pi R_n/\lambda + \phi_0) + \eta(t-t_d) \quad (4)$$

where:

- σ_0 is the complex reflection coefficient of the scattering point,
- $g_0(\theta, \varphi)$ is the antenna gain evaluated at the angular coordinates θ and φ of the target,
- $R(t)$ is the radar-target range and $R_n=R(t_n)=R(n/\text{PRF})$,
- l is the attenuation factor accounting for propagation losses,
- $t_d=2R_n/c$ is the time delay due to the two-way path,
- λ is the wavelength, and
- $\eta(t)$ is the system noise.

The relative radar-target motion induces a Doppler modulation on the signal received along the azimuth direction: it is a linear frequency modulation (azimuth chirp), characterized by two parameters, a frequency shift (Doppler centroid) and a frequency rate (Doppler rate). For narrow azimuth beam width, the expressions for the Doppler centroid and the Doppler rate are

$$F_{dc} = \frac{2v_y \sin \theta}{\lambda} \quad (5)$$

$$F_{dr} = \frac{2(V - v_x)^2}{\lambda R_0} \quad (6)$$

where V is the platform speed and R_0 is the range between the platform and the scene center. The above approximation leads to a useful expression for the bandwidth of the azimuth chirp, i.e.

$$B_d = \frac{2(V - v_x)}{L} = F_{dr} T_i \quad (7)$$

with L being the along-track antenna length and T_i the integration time, i.e. the time during which the target is illuminated by the antenna main lobe. The signal $S_n(t)$, sampled at the proper frequency F_c , is stored as a column in the holographic matrix Ξ . The dimensions, N_{sr} and N_{sa} , of the matrix Ξ represent the number of range and the azimuth samples, respectively. The entry S_{mn} of Ξ can be re-parameterized to elicit the dependence on the Doppler centroid F_{dc} and the Doppler rate F_{dr} , namely

$$S_{mn} = Al\sigma_0 g_0(\vartheta, \varphi) \exp(j\alpha(t_m - t_d)^2) \cdot \exp(j2\pi(F_{dr}t_n^2 + F_{dc}t_n)) \exp(j\phi_0) + \eta(t_m - t_d) \quad (8)$$

where $t_m = m/F_c$ is the range time (fast time) and t_n is the azimuth time (slow time). A conventional SAR processor, designed to provide the image of a stationary scene, works separately along the range and the azimuth directions. Specifically, at the first stage each column of the holographic matrix is convolved with the impulse response function (IRF) h_r of the range filter yielding the range-compressed data. At the second stage, each row of the resulting matrix is convolved with the IRF h_a of the azimuth filter, thus providing the final image. Useful expressions for h_r and h_a , derived from (8), are

$$h_r(t_m) = \exp(j\alpha t_m^2), \quad m = 1, 2, \dots, N_t \quad (9)$$

$$h_a(t_n) = \exp(j2\pi F_{dr0} t_n^2), \quad n = 1, 2, \dots, N_a \quad (10)$$

where F_{dr0} is the Doppler rate (6) for $v_x=0$. The conventional processing fails when the convolutions are implemented by means of (9) and (10) on the signals coming from moving objects for which $F_{dr} \neq F_{dr0}$ and $F_{dc} \neq 0$.

In MTD technique the Doppler frequency shift is used as a means of detecting moving targets embedded in a strong ground backscatter (clutter). A delay-time canceller behaves as a filter to reject the low Doppler components associated with the clutter and to preserve the high Doppler components of the moving targets. The canceller is cascaded with a bank of narrow-band filters (channels), uniformly spread in the PRF interval. When matched filtering is performed, only that Doppler channel containing the target echo will supply a significantly nonzero output. These concepts are amenable to extension to SAR application: in fact, for sensing and imaging purposes, the stationary scene resembles clutter and the point-like moving object represents the target. It appears convenient to refer to this approach as MTI, since it is the natural extension of MTD to SAR. However, some novel problems, arise when we deal with SAR. First, the representation of the signal returned by a scatterer results in an intrinsically two-dimensional problem. In the airborne case, however, the dwell-time is usually short and the range cell migration is avoided. Whenever the SAR system parameters do not induce range migration by themselves, a moving target could be still displaced over more range lines if its radial velocity is high enough to encompass more range lines during the integration time, i.e. if

$$N_{rcm} = \frac{v_y \sin \theta T_i}{\delta_r} > 1 \quad (11)$$

where N_{rcm} is the number of range migration cells and δ_r is the range resolution of the SAR system. Assuming an airborne SAR operating at millimetric wavelengths (for example $T_i=0.2s$, $\theta=45^\circ$, $\delta_r=4$ m), and substituting the numerical values in (11), a maximum target speed of 30 m/s along the range direction is allowed to avoid range migration ($N_{rcm} < 1$). Under these assumptions the pattern is not truly bi-dimensional and the processing can be performed by a separate filtering of the rows and the columns of the holographic matrix. Another

problem which arises when dealing with moving targets is the aliasing effect due to the broadening and shifting of the signal spectrum. Assume, in fact, that $PRF = B_d$: in this case a radial velocity component of the target causes a Doppler shift according to (5) and a significant aliasing cannot be avoided. Furthermore, if the target velocity v_x is opposite to that of the platform, an increase of the nominal bandwidth occurs according to (7). As a consequence of these concurrent phenomena, the azimuth compression cannot be perfectly achieved and the target is not correctly imaged. If instead the sampling frequency PRF complies with the Nyquist theorem (that is, for example, if $PRF \gg B_d$), then the discrete and the analogue representations can be considered equivalent. More precisely, the PRF must be constrained by the inequality

$$PRF \geq 2[F_{dcmax} + (T_i/2)F_{drmax}] \quad (12)$$

where F_{dcmax} and F_{drmax} are available from (6) and (5) on substituting the quantities v_x and v_y with their maximum values. The basic considerations leading to the MTI algorithm as a means of detecting moving targets are discussed below. When the system PRF complies with Eq. (12), the ground echo and the echoes of the moving targets are spectrally separated: the former is concentrated in $[-B_d/2, B_d/2]$ and the latter are allocated in $(-PRF/2, -B_d/2) \cup (B_d/2, PRF/2)$.

The scheme of the MTI processor is shown in Fig. 3. The raw data are stored in the holographic matrix and fed into the range processor. Then, the spectrum of the azimuth line is computed via a fast Fourier transform (FFT) and split throughout the N_{dc} channels, each one encompassing a bandwidth as large as B_d . The rejection of the ground echo is performed leaving out the channel centered on the zero Doppler frequency, after phase compensation of the platform speed V . The processing that follows performs azimuth compression on each stream of data. The procedure consists in evaluating the product between the data coming from a single channel and a suitable reference function, making an inverse Fourier transform and comparing the maximum value attained by the signal with a threshold. Finally, if a moving point is detected, a fine estimate of the chirp parameters – as discussed in [DDB94] – is provided to improve the performance of the imaging forming algorithm. The range of detectable velocities is limited between a minimum detectable and a maximum unambiguous values. The minimum and maximum velocities correspond to a Doppler displacement equal to the first and the last available Doppler channel center frequencies, respectively. Conservative values (with respect to the off-nadir angle) are

$$v_{min} = \frac{\lambda B_d}{2} = \frac{\lambda V}{L} \quad (13)$$

$$v_{max} = \frac{\lambda}{4}(PRF - B_d) \quad (14)$$

For airborne SAR's operating at millimetric wavelengths, values of 1 m/s for v_{min} and 20 m/s for v_{max} are found using a PRF of 10 kHz.

In [DDB94] the problem of probing the presence of a chirp signal embedded in a disturbance environment (backscattering by fixed scene and thermal noise) is modeled as a binary decision test; also the detection performance are found. Details are in the quoted reference.

A high quality image of moving targets calls for suitable procedures for estimating the chirp parameters. Here we introduce two algorithms for Doppler centroid and Doppler rate estimation. The algorithms are suited for airborne SARs and point-like targets. The chirp parameters are related to the moving point velocities through (5) and (6), the knowledge of the former allows one to recover the latter.

Doppler centroid estimate. The target radial velocity causes a Doppler frequency shift given by (5). The algorithm discussed here involves a correlation between the power spectrum of the azimuth signal and that of a reference signal, namely a chirp signal with no Doppler shift and nominal Doppler rate. The correlation peak is centered on the searched Doppler shift. More formally, the algorithm consists of the following steps

- Discrete Fourier transformation (DFT) of the azimuth signal,

$$X(m) = \sum_{n=0}^{N_{ba}-1} x(n)e^{-j2\pi nm/N_{ba}} \quad (15)$$

where N_{ba} is the azimuth FFT block length, and computation of the power spectrum,

$$S_x(m) = |X(m)|^2 \quad (16)$$

- Extraction of a subset of samples $S(m)$ from $S_x(m)$ according to the following rule: once the channel where detection occurs is selected, pick up all samples encompassing a bandwidth as large as $2B_d$ centered around the channel reference frequency. So we are ensured that only a small amount of the signal energy is left.
- Evaluation of the cross-correlation $R_s(m)$ between $S(m)$ and reference spectrum $S_r(m)$

$$R_s(m) = S(m) \otimes S_r(-m) \quad (17)$$

where denotes \otimes convolution.

- When the point-like target moves along v_x , a mismatch occurs between the signal and the reference spectra. As a consequence, the cross-correlation function no longer produces a sharp peak. However, a good accuracy can still be provided using an energy balancing algorithm. Thus, define

$$\begin{aligned} \varepsilon_1 &= \sum_{\Omega_1} \bar{R}_s(m) \\ \varepsilon_2 &= \sum_{\Omega_2} \bar{R}_s(m) \end{aligned} \quad (18)$$

where Ω_1 indicates the set of samples belonging to the lower frequencies ($m=1, \dots, n_1$, say) and Ω_2 indicates the corresponding set belonging to the upper frequencies ($m=n_1+1, \dots, n_p$, say) (n_p is the total number of points of $R_s(m)$). We select n_1 so that the difference $|\varepsilon_1 - \varepsilon_2|$ is minimum. The knowledge of n_1 can be used for the evaluation of the Doppler centroid.

Airborne SAR autofocus. The Doppler rate is the other parameter required to perform a sharp focusing of the target echo. A widely used algorithm for Doppler rate estimation is based on the multi-look technique; unfortunately, this technique does not work well if applied to airborne SAR's. Consider, in fact, the Doppler rate resolution achievable by this algorithm [DDB94]

$$\delta F_{dr} = \frac{F_{dr0}^2}{F_{dr0} + \Delta f \frac{B_d}{N_L}} \quad (19)$$

where: N_L is the number of looks, Δf is the center-looks distance. Table 1 reports the values assumed by the above-specified parameters, together with the Doppler resolution, for typical space-borne and airborne SAR systems. It is easy to observe that the resolution is good for Seasat SAR but poor for the airborne SAR. In [DDB94] a new algorithm is introduced which performs an accurate estimation of the Doppler rate for both

space-borne and airborne SAR's provided that the Doppler centroid has been previously corrected. Consider the modulus of the mutual energy ϵ between the received signal $x(t)$ and the signal $x_r(t)$

$$|\epsilon(\beta)| = \frac{1}{T_1} \left| \int_{-T_1/2}^{T_1/2} x(t, F_{dr}) x_r^*(t, \beta) dt \right| \quad (20)$$

where β is the Doppler rate to be estimated. The received chirp $x(t, \beta)$, after Doppler centroid correction, can be simply expressed as

$$X(t, F_{dr}) \cong \exp \{j F_{dr} t^2\} \quad (21)$$

If we choose

$$x_r(t, \beta) = \exp \{j \beta t^2\} \quad (22)$$

and collect all inessential terms in a complex constant K , we obtain

$$|\epsilon(\beta)| = \left| K \int_{-T_1/2}^{T_1/2} e^{j(F_{dr} - \beta)t^2} dt \right| \quad (23)$$

which can be approximated as

$$|\epsilon(\beta)| = \left| K \sum_{k=N_a/2}^{N_a/2-1} \exp \{j[(F_{dr} - \beta)t_k^2]\} \right| \quad (24)$$

Expression (24) can be regarded as the integration of N_a pulses having the same modulus, but time varying phase. The integration process leads to the maximization of the cross-energy modulus if and only if $(F_{dr} - \beta)$ is equal to zero or, in other words, if the estimated Doppler rate is equal to the true one. Thus, the estimation rule amounts to evaluating the maximum of expression (24), with respect to β , namely

$$\hat{\beta} = \max_{\beta \in \Omega_\beta} |\epsilon(\beta)| \quad (25)$$

where Ω_β is a suited domain for β .

After the estimation of F_{dc} and F_{dr} , the azimuth signal can be correctly compressed by means of a classical SAR azimuth processing to obtain the position and the reflectivity of targets. Moreover, v_x and v_y can be evaluated by applying Eqs. (5) and (6). The algorithms above have been simulated to check their ability to generate correctly focused images of moving and stationary point-like targets over a fixed background; the successful results are reported in [DDB94].

Table 1

	Seasat SAR	Airborne SAR
f_{dr0}	520 Hz/s	3112 Hz/s
Δf	967 Hz	300 Hz
B_d	1389 Hz	400 Hz
N_L	4	4
δf_{dr}	0.8 Hz/s	292 Hz/s

4.2 ALONG TRACK INTERFEROMETRY (ATI) – SAR

In a similar manner to DPCA (see Section 4.3), along-track interferometry (ATI) uses two displaced antennas connected to two receiving channels. For each channel a SAR image can be generated. The time delay between the azimuth signals can be compensated during the azimuth compression using two different reference signals, incorporating the azimuth chirps generated in the two channels by a common point scatterer. If the first image is multiplied by the complex conjugate of the second, the remaining phase is zero for stationary objects and non-zero otherwise. If the two receivers are spatially separated by the distance d , the interferometric phase is approximated by $\phi = -(2\pi/\lambda)d(v_r/v_a)$, where v_r is the radial velocity of the target.

An example of parameters for ATI SAR is: $d = 1m$, $v_a = 100m/s$, $\lambda = 3cm$, $v_r = 1m/s$, $\phi = 120^\circ$. ATI-SAR was originally developed to measure the speed ocean surfaces; in [END99] the capability of SAR to detect slowly moving targets is shown on live data. In [GIE02] an in-depth analysis of the capabilities of ATI-SAR to detect moving targets is presented. In this section some analytical and simulation results concerning detection of moving target is presented. ATI-SAR has the following limitation: to have a high phase sensitivity, the two antennas have to be widely separated, but this leads to a comb of blind velocities $v_{\text{blind}} = kv_a\lambda/d$, where k is an integer: this limits the useful target velocity interval; moreover, the above mentioned distortions in the SAR image of moving target (Section 3) remain.

The probability density function (pdf) of the interferogram phase ϕ for just stationary clutter and thermal noise has been found to be [LHM94].

$$p(\phi) = \frac{1}{2\pi} \frac{1 - |\gamma|^2}{|\gamma|^2 \cos^2 \phi} \left\{ 1 + \frac{|\gamma| \cos \phi \cdot \cos^{-1} [\gamma \cos \phi]}{\left[1 - |\gamma|^2 \cos^2 \phi \right]^{0.5}} \right\}$$

where

$$\gamma = \frac{E\{i_1 i_2^*\}}{(E\{|i_1|^2\} E\{|i_2|^2\})^{0.5}} \quad (26)$$

$$\gamma = \frac{\gamma_c}{1 + 1/CNR}$$

Clutter and noise are independent random processes with zero mean and Gaussian pdf. Radar echoes i_1, i_2 received by the two antennas at the same time have a correlation coefficient γ which depends on the endogenous correlation coefficient of clutter γ_c and the clutter-to-noise power ratio $CNR = P_c/P_n$: thus the presence of noise reduces the clutter coherence. In practice, the interferometric phase is estimated by averaging n looks as follows

$$\phi = \arg \left(\frac{1}{n} \sum_{k=1}^n i_1(k) i_2^*(k) \right) \quad (27)$$

The corresponding pdf becomes

$$p(\varphi) = \frac{\Gamma(n+1/2)(1-|\gamma|^2)^n \beta}{2\sqrt{\pi} \cdot \Gamma(n)(1-\beta^2)n+1/2} + \frac{(1-|\gamma|^2)^n}{2\pi} {}_2F_1(n, 1; 1/2; \beta^2)$$

$$\pi < \varphi \leq \pi \quad (28)$$

$$\beta = |\gamma| \cos \varphi$$

where ${}_2F_1(\bullet)$ denotes the Gaussian hypergeometric function. For $n=1$ (28) reduces to (26). Recently a mathematical expression of the pdf has been presented in [GIE02] also for the case of target presence. In the following we illustrate some simulation results concerning the pdf of interferogram in presence of target, clutter and noise.

The mathematical expression (28) plays an important role in finding the detection threshold for a prescribed value of false alarm probability (P_{fa}). By numerical integration the following numerical values for the threshold Th have been found.

$\gamma = 0.9 \rightarrow Th = 1.0505$; $\gamma = 0.98 \rightarrow Th = 0.3802$; $\gamma = 0.99 \rightarrow Th = 0.2301$; the prescribed false alarm probability, the clutter – to- noise power value and the number of averaged looks are: $P_{fa} = 10^{-4}$, $CNR = 20 dB$, $n = 4$. The variation of the detection threshold with the number of averaged looks for $CNR = 20 dB$, $\gamma = 0.98$ and $P_{fa} = 10^{-4}$ is as follows:

$$n = 1 \rightarrow Th = 2.8414; n = 2 \rightarrow Th = 0.9505; n = 4 \rightarrow Th = 0.3802;$$

$$n = 6 \rightarrow Th = 0.3002; n = 10 \rightarrow Th = 0.2201.$$

The target has been modeled as Swerling 1. Figure 4 depicts the histogram of phase interferogram for the following parameters: two antennas, $n = 4$, clutter Doppler phase = 0, $CNR = 20 dB$, $\gamma = 0.98$, target Doppler phase: $\varphi_{target} = 1.3 rad$. It is noted that when the signal-to-clutter power ratio (SCR) is very small in dB, the histogram coincides with the one predicted by equation (28); with the increase of the SCR the peak of the interferogram migrates on the target Doppler phase. Figure 5 illustrates the contour curves with constant detection probability versus target Doppler phase and SCR. The relevant parameters are: two antennas, $CNR = 20 dB$, number of averaged looks $n = 4$, correlation coefficient: $\gamma = 0.98$, $P_{fa} = 10^{-4}$ (detection threshold = 0.3802 rad). The following comments are in order: the contour curves are aliased in the interval $\varphi = [-\pi, \pi]$; detection is practically zero for low values of the target Doppler phase because of the numerical value of the detection threshold; the detection increases with the increase of the SCR value.

Next areas of research are in the field of removal of aliasing by using different values of carrier frequency [PSF01a]. In [PSF00], [PSF01] the possibility to do ATI-SAR with one bit coded SAR signal is demonstrated for moving target detection: this is another lively area of research; it has a bonus in terms of simplicity of processing implementation.

4.3 DPCA

The concept of DPCA: Displaced Phase Center Antenna was conceived by F. R. Dickey, F. M. Staudaher, and M. Labitt; in 1991 they received the IEEE-AESS Pioneer award for this invention [DSL91]. One major application of DPCA is in the JSTARS (Joint Strategic Target Attack Radar Systems) [SHN94]. Figure 6 shows the working principle of the system; it depicts the radar antenna moving along track when two pulses are transmitted and corresponding echoes received. The antenna is divided in two sub-arrays; the whole

antenna transmits two successive pulses, the corresponding echo of the 1st pulse is received by the fore sub-array, the echo of the 2nd pulse is received by the aft sub-array. Due to the aircraft movement, the transmitting and receiving antennas form two bistatic configurations for the two pulses. However, if the antenna dimension, the platform speed and the radar PRF are properly selected, the phase center of the bistatic antenna configuration for the 1st transmitted-received pulse coincides with the phase center of the 2nd transmitted-received pulse. Thus, the clutter is seen at two different time instants from a same radar location: the platform motion has been compensated, consequently the Doppler spectrum of clutter is not spread due to platform motion. The clutter is cancelled by subtracting the echoes of the 1st pulse received by the fore sub-array from the echo of the 2nd pulse received by the aft sub-array; DPCA corresponds to a kind of spatial MTI. Stationary targets should cancel, but echoes from moving targets will give a non-zero result from the subtraction, so they should remain. Coe and White [CWH96] have carried out a theoretical and practical evaluation of this technique. They have found that cancellation of the order of 25 dB is possible. The major DPCA sources of limitations are: loss of receiving aperture, PRF-velocity constraint, performance limited by sub-array mismatch of radiation patterns, two degrees of freedom (DOFs) only, the system is not adaptive. STAP is the natural generalisation of DPCA, in fact it has the following features:

- generalisation of adaptive array of antennas for jammer nulling,
- generalisation of DPCA for clutter cancellation,
- freedom in shaping the null,
- less constraints on the spacing of the antenna elements,
- compensation of platform motion along (as DPCA) and orthogonal to the array thus avoiding clutter spectral spreading.

4.4 SPACE-TIME-FREQUENCY

In this section a method for detecting and imaging objects moving on the ground and observed by a SAR is described. The method is based on the combination of two processing steps: 1) space-time processing which exploits the motion of an antenna array for canceling the echo from background, and 2) time-frequency processing which exploits the difference in time allocation of the instantaneous spectrum corresponding to echoes from the ground or from moving objects, for an adaptive time-varying filtering and for the estimation of target echo instantaneous frequency, necessary for producing a focused image of it. The design and performance of the space-time filter is described in [BFA90], [BFA91], [BFA92], [BFA94]. Some of the theoretical aspects of STAP of interest for this paper are discussed also in a number of publications; [LOM96c] discusses the optimum processing scheme for a special case and an approximation of it realised with a two-dimensional FIR (Finite Impulse Response) filter. Other relevant references are: [FAT92], [LFA96] and [LOM98]. Here we concentrate on the time-frequency step (Section 4.4.1) and on the joint space-time-frequency (Section 4.4.2).

4.4.1 Joint time-frequency analysis by Wigner-Ville distribution

The aim of this section is to show how time-frequency representation by WVD of the echoes received by a SAR provides a useful tool for detection of moving objects and estimation of instantaneous phase shift induced by relative radar-object motion [BFA92]. The phase history is then used to compensate the received signal and to form a synthetic aperture with respect to the moving object, necessary to produce a high resolution image. A method for extracting the instantaneous phase is based on the time-frequency (TF) distribution of received signal. The WVD has been chosen here because it presents some important features concerning detection and estimation issues. There are simple methods for analyzing signals in the TF domain, such as the short-time Fourier transform (STFT), but they do not exhibit the same resolution capabilities in the TF domain as does the WVD. In particular, since the STFT is based on a Fourier transform (FT) applied to a time windowed version of the signal, with the window central instant varying with time, the frequency resolution is inversely proportional to the window duration. The narrower the window, the better is the time resolution, but the worse is the frequency resolution and vice versa. Conversely, the WVD does not suffer from this shortcoming. The

WVD provides a higher concentration of signal energy in the TF plane, around the curve of signal instantaneous frequency (IF). This allows a better estimation of IF in presence of noise and this information is exploited for the synthesis of the long aperture with respect to moving object. On the other hand, the WVD poses other problems since it is not a linear transformation. This causes the appearance of undesired cross-products when more than one signal is present. Mapping of the received signal in TF plane provides a tool for synthesis of the optimal receiver filter without a-priori knowledge of the useful signal, provided that the signal-to-noise ratio be sufficiently large. The TF representation provides a unique tool for exploiting one of the most relevant differences between useful signals and disturbances in the imaging of small moving objects, namely the instantaneous frequency and the bandwidth. In fact, it can be shown that, while the bandwidth occupied by a target echo during the observation interval necessary to form the synthetic aperture mainly depends on radar-object motion, the instantaneous bandwidth is proportional to object size. Therefore the echo corresponding to a small target can occupy a large band during the overall observation time, but its instantaneous bandwidth is considerably narrower (i.e. the echo back-scattered by a point-like target has zero instantaneous bandwidth but it may exhibit a large overall bandwidth). Conversely, the echo from the background and the receiver noise have a large instantaneous bandwidth. Therefore, even if the useful signal and the disturbance may have a large total band, the possibility of tracking the instantaneous bandwidth, made available by the TF representation allows a discrimination of the useful signal from the disturbance not possible by conventional processing. Another important and unique advantage related to use of the WVD is that it allows the recovery of the echo phase history even in the case of undersampling, as shown in [BAR91]. This is particularly important in SAR applications since it allows us to work with PRF lower than the limits imposed by the signal bandwidth occupied during the observation interval. Owing to the target motion, this bandwidth may be considerably larger than the bandwidth occupied by the background echo. According to conventional processing, we should then use a correspondingly higher PRF. Conversely, if the useful signal has a large total bandwidth, but a narrow instantaneous bandwidth, the TF representation prevents superposition of spectrum replicas created by undersampling because, even if the replicas occupy the same bandwidth, they occur at different times. This property allows us to recover the desired information even from undersampled signals. Since the PRF value imposes a limit on the size of the monitored area, due to time - and then range - ambiguities, the possibility of using a low PRF prevents the reduction of the region to be imaged, as well as the increase of the data rate.

The WVD of a signal is defined as:

$$W(t, f) = \int_{-\infty}^{+\infty} s(t + \frac{\tau}{2}) s^*(t - \frac{\tau}{2}) \exp(-j2\pi f\tau) d\tau \quad (29)$$

where $s(t)$ represents the analytic signal. The estimation of the instantaneous frequency of signal is done as follows. Express the signal in terms of its envelope and phase

$$s(t) = a(t) \exp \{j\phi(t)\} \quad (30)$$

It can be shown that the local or mean conditional frequency of the WVD distribution, defined as

$$\langle f \rangle_t = \left\{ \int_{-\infty}^{+\infty} f W(t, f) df \right\} \left\{ \int_{-\infty}^{+\infty} W(t, f) df \right\}^{-1} \quad (31)$$

is equal to the signal IF

$$\langle f \rangle_t = \frac{1}{2\pi} \frac{d\phi(t)}{dt} \quad (32)$$

The estimate of the mean conditional frequency of the WVD then provides the information about the signal IF. This is exactly the information we need for re-phasing the received signal in order to produce a focused image.

Explain now the rationale for using the WVD to detect a moving target and estimate its parameters with SAR data. The received signal is the sum of echo from the moving object, whose phase modulation is unknown, plus clutter (the echo from fixed background), plus noise. The echoes from the fixed scene represent, in our case, a disturbance. The aim is to detect the presence of moving objects and to estimate their motion parameters. The detection and parameter estimation performance depend on the signal-to-clutter power ratio (SCR). If this ratio is small, we have to process first the received signal, in order to improve it as much as possible. This operation can be carried out by matched filtering. However, the matched filter can be defined only if the shape of the useful signal is known, and this is not the case. It turns out that the two operations, detection and parameter estimation, cannot be separated: estimation of the useful signal parameters can be carried out only after having detected the presence of a useful signal; a reliable detection, on the other hand, requires the knowledge of the signal parameters, in order to carry out a proper matched filtering, before the detection itself. It is then necessary to carry on these two kinds of operations contemporaneously. The time-frequency analysis of the received signal, in particular the WVD, provides a powerful tool for achieving the aforementioned requirements and extracting the desired information, namely the energy and the phase history. These two information are what we need for our purposes: the detection of the presence of a moving target is made by comparing the energy with a suitable threshold; the instantaneous phase is used to phase-compensate the received signal, for a correct coherent integration, necessary to imaging purposes. As regards the effect of disturbances in the received signal, it is useful to recall that matched filtering can always be performed by cascading: a clutter cancellation followed by a coherent integration. The first operation does not require knowledge of the useful signal shape, whereas the second operation does. In particular, a correct coherent integration requires knowledge of the signal phase history. The time-frequency analysis aims to facilitate extraction of the signal phase history. Therefore, the sequence of operations to be performed on the received signals is the following: a clutter cancellation is performed first and the output of the cancellation filter is analyzed in the TF domain. If the clutter has been reduced to a power level sufficiently smaller than the useful signal, the parameters estimated by the WVD are correct, within an error depending on the achieved SCR. These parameters provide the information necessary to set up a correct coherent integration. This rather intuitive reasoning for using the WVD in detection and estimation problems is formalized into the framework of the matched filter theory in [BFA92]; here we give a summary of main results concerning the application to SAR problem.

The signal received by a SAR is given by the sum of the echoes from the ground, the echoes from a possible moving object and receiver thermal noise. The echo from the ground can be modelled as a correlated random process, whose power spectral density is proportional to the antenna power radiation pattern. The echo from a moving object is characterised by an unknown modulation, induced by the relative motion between the radar and the object. In SAR imaging, we are interested in the phase modulation induced by the relative radar-target motion. If the transmitted signal is

$$p(t) = a(t) \exp(j2\pi f_0 t) \quad (33)$$

where $a(t)$ is the analytic signal and f_0 is the carrier frequency, the echo received by a point-like scatterer at a distance $r(t)$ from the radar is proportional to

$$p\left(t - \frac{2r(t)}{c}\right) = a\left(t - \frac{2r(t)}{c}\right) \exp(j2\pi f_0 t) \exp\left(j\frac{4\pi}{\lambda} r(t)\right) \quad (34)$$

During the observation interval, the amplitude of each backscattering coefficient can be assumed constant since the aspect angle does not vary by an amount such as to justify a change in the reflectivity characteristics (this assumption underlies all SAR signal processing). The only modulation of interest then is phase modulation. In the formation of the synthetic aperture, we are interested in the last term of the expression

above. The conventional techniques for autofocusing extended scenes compensate only linear and quadratic phase shifts. This means that only slow fluctuations (with respect to the integration time) are compensated. Conversely, the TF approach allows estimation and compensation of any kind of phase history. The distance $r(t)$ can be modelled as the sum of slow and rapid fluctuations, with respect to the observation interval. Slow variations can be expressed as a low-order polynomial, whereas fast variations follows a sinusoidal behavior, whose period is shorter than the time observation interval. The change in the distance causes a phase modulation, which must be compensated to obtain a correct image. The variation of distance can cause migration of the received echo over different range cells, depending on the ratio between the amount of variation and the range resolution. The range migration problem can be faced according to the double-resolution strategy outlined in the next Section 4.4.2. According to the strategy, all the phase estimations are carried out on data whose range resolution is such as to consider the migration negligible. According to the formulation of matched filtering in terms of the WVD, the processing scheme for detecting and estimating the parameters of the echoes from moving objects is sketched in Fig. 7. The received signal is first range-compressed. Then it is processed by a moving target indicator (MTI) filter to reduce the clutter contribution; in Section 4.4.2 we explain how to use STAP. The analysis of the signal in the TF domain allows estimation of the signal instantaneous frequency. Some smoothing can be applied on the WVD to improve the estimation accuracy. The instantaneous frequency is then integrated to obtain the phase modulation to be used for phase compensation of the received signal. At this point an FFT is sufficient to provide the high cross-range resolution image. A threshold is then applied to the envelope signal to check for detection. An example of an image relative to a moving point-like target superimposed on a fixed extended scene is reported in [BFA92]; the simulation results convey a positive feeling on the performance of the processing scheme of Figure 7.

4.4.2 Joint space-time-frequency analysis

The space-time and the time-frequency processing can be combined to form a processor that allows both the cancellation of the clutter echoes and the compensation of the target motion, necessary for the formation of a high cross-range resolution image. The overall space-time frequency processing is shown in Figure 8. The echo from the ground is canceled by means of the space-time processing. Having canceled the background echo, we proceed to the estimation of the target instantaneous frequency which is done by resorting to the WVD. Before proceeding to the estimation, however, some care must be devoted to the range migration problem. In fact, the relative radar/target motion causes not only a phase shift, but also a range migration which cannot be neglected if it overcomes the range resolution. The radar echoes are sampled and arranged in a matrix, whose columns are relative to successive transmitted pulses and the entries of each column contain the echoes coming from different distances. Given a certain point, if its distance from the radar does not vary by an amount bigger than the size of a range resolution cell, the echoes from that point are all stored on one column. If all the points composing the observed scene satisfy this condition, no range migration occurs and the samples can be first processed in range, column by column, and then in cross-range, row by row. If, however, the echoes from some point occupy more than one row, the cross-range processing cannot be performed directly on the collected data, row by row. Some algorithm for compensating the range migration must be applied in order to realign the data, before the cross-range processing. Range migration compensation techniques have already been examined in the literature in the imaging of stationary scenes. The problem is harder in the imaging of moving targets, however, since the radar/target distance is not known. Two main problems arise when dealing with moving targets, in presence of range migration: 1) the migration causes a spreading of the target energy through many range cells, therefore the signal-to-noise ratio, for each range cell, decreases and this causes a loss of detectability, and 2) due to the lack of knowledge of the target range migration law, it is not known a priori which samples of the matrix of the collected data are to be taken for carrying out the estimation of the phase history.

Here we follow a two-step approach for compensating the migration problem: 1) a coarse range resolution, and 2) a fine range resolution analysis (see Figure 9). The rationale of the approach is based on the fact that the migration problem can be neglected if the amount of migration does not exceed the range resolution. Therefore, we can initially work in a low resolution mode, where the range resolution has been degraded by an

amount such as to make the migration negligible. A first detection is performed on these data: if a detection occurs, the processing chain for the estimation of the target echo phase history is enabled. The estimation is carried out in the time-frequency domain, according to the criterion described previously. Having once estimated the phase $\phi(t)$, we can evaluate the law of variation of the distance by exploiting the relationship between phase shift and distance

$$d(t) = \frac{\lambda}{4\pi} \phi(t) \quad (35)$$

By using $d(t)$, we can compensate for the range migration by properly rearranging the data in the matrix containing the received samples. These data can now be phase shifted to compensate for the phase shift induced by the target motion. The data undergo then a full range and cross-range compression for obtaining the high resolution image. The price paid by adopting the two-step resolution approach is the SNR loss inevitably related to the degradation of the range resolution in the coarse resolution mode. It is important to point out that, even if the cause of both phase shift and migration problems is the same, namely the variation of the radar/target distance, the phase shift is much more sensitive to range variation than the range migration. In fact, for example, in an X-band radar ($\lambda=3$ cm), having a range resolution of 1 m, an error on the distance of 7.5 mm causes a phase shift of π radians, while the corresponding range migration is absolutely irrelevant. This means that, having once estimated the phase history by the described procedure, the resulting value for the distance variation $d(t)$ is estimated with a good accuracy.

The performance of the space-time-frequency processing scheme has been evaluated by a simulation program which generates the echoes from an extended surface and from a point-like target and then applies the proposed algorithm [BFA94]. The target has been supposed moving on the terrain (shadowing effects have been neglected) at a constant velocity, in a direction oblique with respect to the radar motion. The velocity parameters have been chosen to make evident the presence of range migration and of cross-range smearing of the target image. The ground reflectivity has been assumed equal to the target reflectivity (this is a quite pessimistic assumption, because in many cases of practical interest, the target reflectivity is higher). The thermal noise, 40 dB below the target return, has also been assumed for the received signal. The ground echo is first canceled, by using a STAP with two-element antenna and two time samples. The two antennas are spaced by $d=vT$. A SAR image is then formed by conventional techniques. The result is shown in Fig. 14 of [BFA94]. The smearing of the moving point-like target is evident. Given the motion parameters, the target has migrated over six range cells. This is the cause for the broadening of the target image even in range, as well as in cross range. Anyway, the target echo causes a detection and initializes the motion estimation channel. The high resolution data are smoothed in range to decrease the range resolution. Then the processor looks for the range cell with the maximum energy content and computes the WVD of that cell only. The frequency history, and then the phase history, are evaluated, according to the procedure outlined previously. The phase history is then used for compensating the range migration and the phase shift on the high resolution range data. The final image is shown in Fig. 15 of [BFA94]. The sharpening of the target image is quite evident.

The method above corrects only the (translation) motion of a point-like target. If focused image of three-dimensional object is required, for recognition purposes, the motion parameters must be estimated to compensate correctly the relative signals ([WCJ90] and [FIE01]). Since the motion of any rigid body can be decomposed as the sum of the translation of a point plus the rotation of the other points around that point, in some cases, depending on the target dimension and kind of motion, the compensation of the only translation motion is not sufficient and we still have to compensate for the rotational motion. This second compensation can be efficiently performed in the frequency domain, by applying, for example, the method proposed in [WCJ90]. Algorithms have been conceived to produce fine resolution images of moving targets having any translation or rotation motions. They require the presence of multiple prominent points in the target image. The echo from a first point is initially analysed. Its phase is computed and subtracted pulse-to-pulse from the phase of the incoming signal. This operation removes the effect of the target translation motion and make this first point effectively the new center of the scene. At this point, if the rotational motion is negligible, conventional

SAR processing yields the focussed image. If, conversely, the rotation cannot be neglected, two other prominent points are required to estimate the rotation parameters. These parameters are used to compensate for the rotational motion in the frequency domain and help in applying the SAR processing correctly. The algorithm requires that the prominent points be separable and that their phases be estimated without interfering with each other. In some cases, however, this assumption might not be met: at high resolution, separability is more likely to occur, but the range migration could complicate the phase estimation problem; at low resolution, the range migration could be negligible, but it is more likely that some prominent points might occupy the same range resolution cell. Further analyses are necessary in the imaging of extended targets when more dominant scatterers occupy the same resolution cell. In this case, in fact, the bi-linearity of the WVD creates undesired cross-product terms which can seriously impair the estimation of the instantaneous frequency. A reduction of these undesired terms could be achieved by resorting to other time-frequency representations, such as the Choi-Williams distribution [COH89]. Another approach to contrast the appearance of undesired cross-product terms is described in [BZA92]. It is shown that it is still possible to estimate the signal parameters, even for multi-component chirp signals embedded in noise, by combining the WVD with the Hough transform.

5. CONCLUSIONS

In this paper processing techniques have been described to combine the SAR and STAP functions; the goal is to obtain a well focused target image in the right place on the image of the stationary scene. It has been shown that the three-dimensional processing in space-time and frequency gives good detection and imaging performance.

6. ACKNOWLEDGEMENTS

Moving target detection and imaging with SAR has been the subject of R&D work for a number of years in Selenia/Alenia (now AMS). The Author acknowledges with thanks the cooperation of a number of Colleagues; notably Professor S. Barbarossa (today with the University of Rome “La Sapienza”) and Dr. E. D’Addio. More recently Dr. A. Gabrielli has cooperated in the development of ATI-SAR work.

7. REFERENCES

- [AUS84] D. Ausherman, A Kozma, J. Walker, H. Jones, E. Poggio, “Developments in radar imaging”. IEEE Trans on Aerospace and Electronic Systems, July 1984, pp. 363-400.
- [BAR91] S., Barbarossa, “Parameter estimation of undersampled signals by Wigner-Ville analysis”. IEEE International Conference on Acoustics, Speech and Signal Proc., ICASSP ’91, Toronto, May, 1991, pp. 3253-3256.
- [BFA90] S. Barbarossa, A. Farina, “A novel procedure for detection and focusing moving objects with SAR based on the Wigner-Ville distribution”. Proc. of IEEE Int. Radar Conf., Arlington, VA, May 7-10, 1990, pp. 44-50.
- [BFA91] S. Barbarossa, A. Farina, “Detection and imaging of moving objects with SAR by a joint space-time-frequency processing”. Proc. of the Chinese International Conference on Radar, Beijing, China, October 22-24, 1991, pp. 307-311.
- [BFA92] S. Barbarossa, A. Farina, “Detection and imaging of moving objects with Synthetic Aperture Radar. Part 2: Joint time-frequency analysis by Wigner-Ville distribution”. IEE Proc., Pt. F., Vol. 139, no. 1, February 1992, pp. 89-97.

[BFA94] S. Barbarossa, A. Farina, "Space-time-frequency processing of synthetic aperture radar signals". IEEE Trans. on Aerospace and Electronic Systems, Vol. AES-30, no. 2, April 1994, pp. 341-358.

[BZA92] S. Barbarossa, A. Zanalda, "A combined Wigner-Ville and Hough transform for cross terms suppression and optimal detection and parameter estimation". Proceedings of the IEEE International Conference on Acoustics, Speech and Signal Processing, ICASSP '92, Mar. 1992, San Francisco.

[COH89] L. Cohen, "Time-frequency distributions – a review", Proc. IEEE, vol. 77, no. 7, 1989, pp. 941-981.

[CWH96] D. J. Coe, R. G. White, "Experimental moving target detection results from a three-beam airborne SAR" Eusar 96, Konigswinter, Germany, 1996, pp. 419-422.

[DDB94] E. D'Addio, M. Di Bisceglie, S. Bottalico, "Detection of moving objects with airborne SAR", Signal Processing, vol. 36, 1994, pp. 149-162.

[DSL91] "IEEE AEES 1991 Awards to F. R. Dickey, F. M. Staudaher, M. Labitt", IEEE AES Magazine, May 1991, vol. 32, p. 32.

[END99] J. H. G. Ender, "Space time processing for multichannel synthetic aperture radar", ECEJ Special Issue on STAP, Vol. 11, No.1, pp. 29-40, February 1999.

[DFM89] E. D'Addio, A. Farina, C. Morabito, "Applications of multidimensional processing to radar systems". Invited paper. Proc. of International Conference on Radar, Versailles, France, pp. 62-78, 24-28 April, 1989.

[FAT92] A. Farina, L. Timmoneri, "Space-time processing for AEW radar". Proc. of IEE Int. Conference on Radar 92, Brighton (UK), 12-13 October 1992, pp. 312-315.

[FIE01] J. R. Fienup, "Detection of moving targets in SAR imagery by focusing". IEEE Trans. on Aerospace and Electronic Systems, Vol. AES-37, No. 3, pp. 794-809, July 2001.

[FPO97] B. Friedlander, B. Porat, "VSAR- a high resolution radar system for detection of moving targets". IEE Proc. on Radar, Sonar and navigation, Vol. 144, No. 4, pp. 205-218, August 1997.

[GIE02] C. Gierull, "Moving target detection with along-track SAR interferometry", DREO TR 2002-000, 09 January 2002.

[KLE98] R. Klemm, "Space-time adaptive processing-principles and applications", IEE Publishers, 1998.

[KLE99] Klemm R., "Introduction to space-time adaptive processing," *Electronics & Communication Engineering Journal*, Vol. 11, No. 1, pp. 5-13, February 1999.

[LHM94] J.S. Lee, K. W. Hoppel, S. A. Mango, A. R. Miller, "Intensity and phase statistics of multilook polarimetric and interferometric SAR imagery", IEEE Trans on Geoscience and Remote Sensing, vol. No. 5, pp. 1017-1028, 1994.

[LFA96] P. Lombardo, A. Farina, "Dual antenna baseline optimisation for SAR detection of moving targets". ICSP- International Conference on Signal Processing, Beijing (P. R. of China), 14-18 October 1996, pp. 431-434.

[LOM96a] P. Lombardo, "Echoes covariance modelling for SAR along-track interferometry", IEEE Int. Symposium IGARSS '96, Lincoln, Nebraska (USA), May 1996, pp. 347-349.

[LOM96b] P. Lombardo, "DPCA processing for SAR moving target detection in the presence of internal clutter motion and velocity mismatch", Microwave Sensing and Synthetic Aperture Radar, EUROPTO series, Vol. 2958, September 1996, Taormina (Italy), pp. 50-61.

[LOM96c] P. Lombardo, "Optimum multichannel SAR detection of slowly moving targets in the presence of internal clutter motion", CIE-ICR '96, International Radar Conference Beijing, China, 8-11 Oct. 1996, pp. 321-325.

[LOM98] P. Lombardo, "Data selection strategies for radar space time adaptive processing", 1998 IEEE Radar Conference, Radar'98, Dallas, Texas (USA), May 12-13, 1998.

[LOM98a] P. Lombardo, "A Joint Domain Localized processor for SAR target detection", European Conference on Synthetic Aperture Radar, EUSAR'98, Friedrichshafen, Germany, 25-27 May 1998.

[PSF00] V. Pascazio, G. Schirinzi, A. Farina, "Along track interferometry by one bit coded SAR signals", The EOS/SPIE Symposium on Remote Sensing, 25-29 September 2000, Barcellona, Spain.

[PSF01] V. Pascazio, G. Schirinzi, A. Farina, "Moving target detection by along track interferometry", Proc. of IGARSS 2001, Sidney (Australia), July 2001.

[PSF01a] V. Pascazio, G. Schirinzi, "Estimation of terrain elevation by multifrequency interferometric wide band SAR data", IEEE Signal Processing Letters, vol. 8, 2001, pp. 7-9.

[SHN94] H. Shnitkin, "Joint STARS phased-array radar antenna", IEEE AES Magazine, October 1994, pp.34-41.

[PDF99] R. Perry, R. Di Pietro, R. Fante "SAR imaging of moving targets", IEEE Trans. on Aerospace and Electronic Systems, Vol. AES-35, No. 1, pp. 188-200, January 1999.

[WAR94] J. Ward, "Space-time adaptive processing for airborne radar", MIT Lincoln Laboratory, Technical report TR-1015, December 13, 1994.

[WCJ90] S. Werness, W. Carrara, L. Joyce, And D. Franczak, "Moving target imaging algorithm for SAR data", IEEE Trans. on Aerospace and Electronic Systems, Vol AES-26, no. 1, pp. 57-67, 1990.

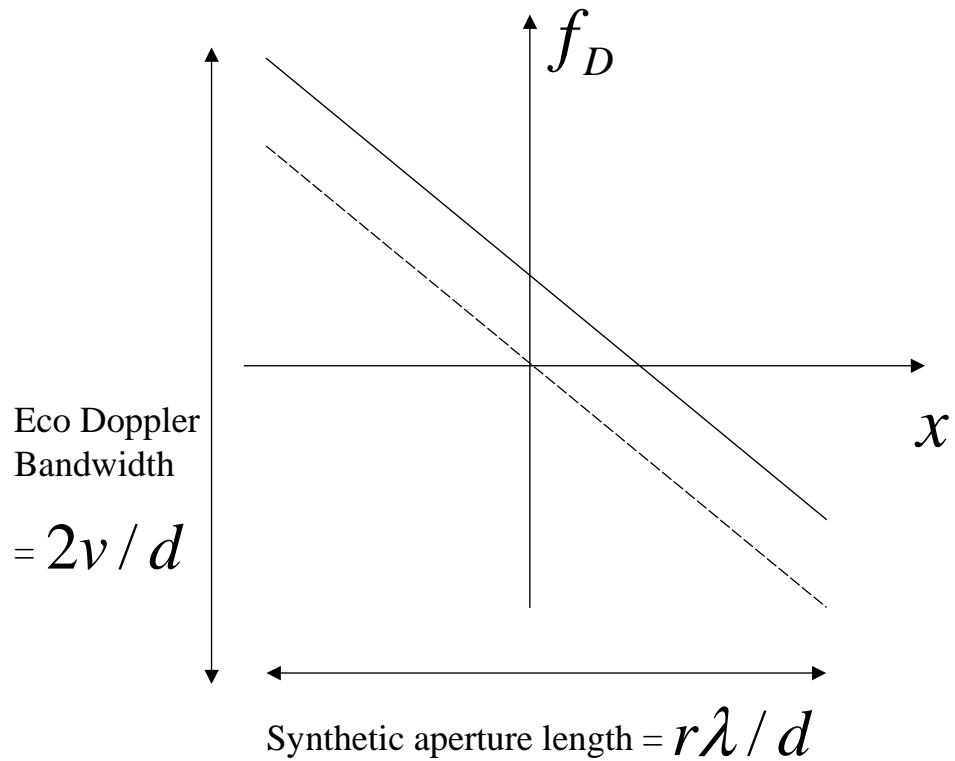


Figure 1: A target with a radial velocity is matched filter by the SAR processing thus producing a corresponding azimuth shift.

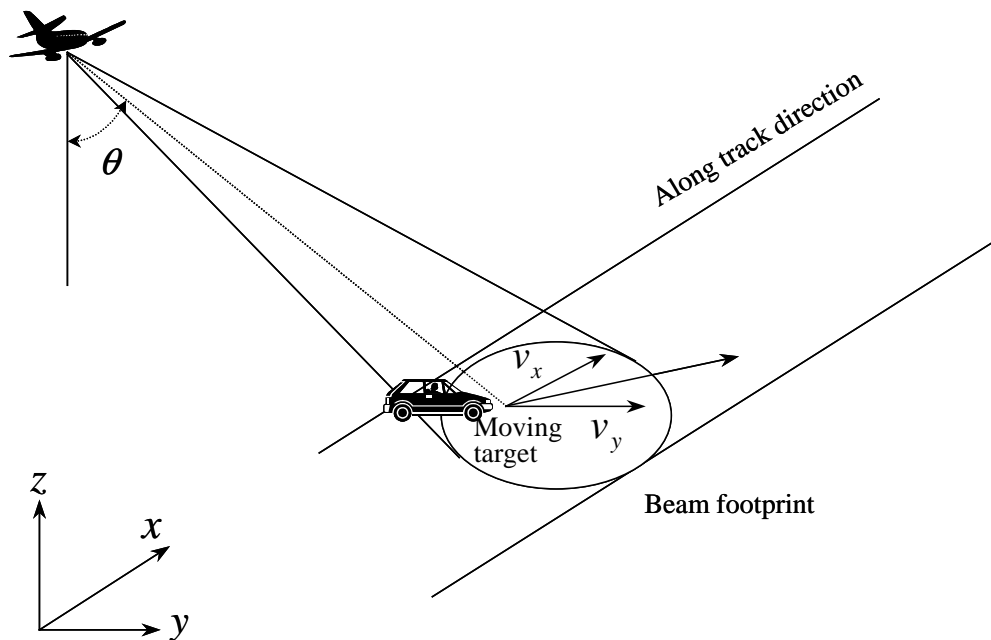


Figure 2: Geometry of SAR and moving target.

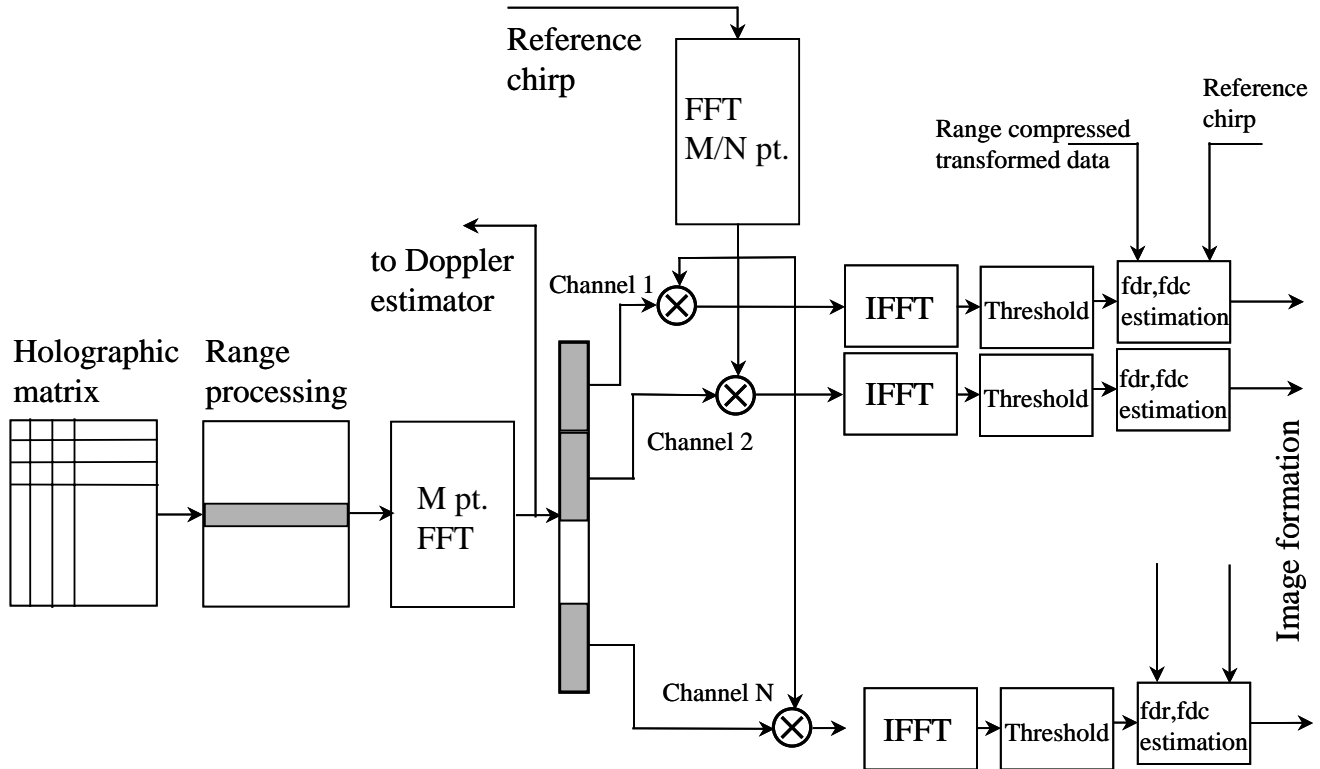


Figure 3: Processing scheme of MTI (after [DDB94]).

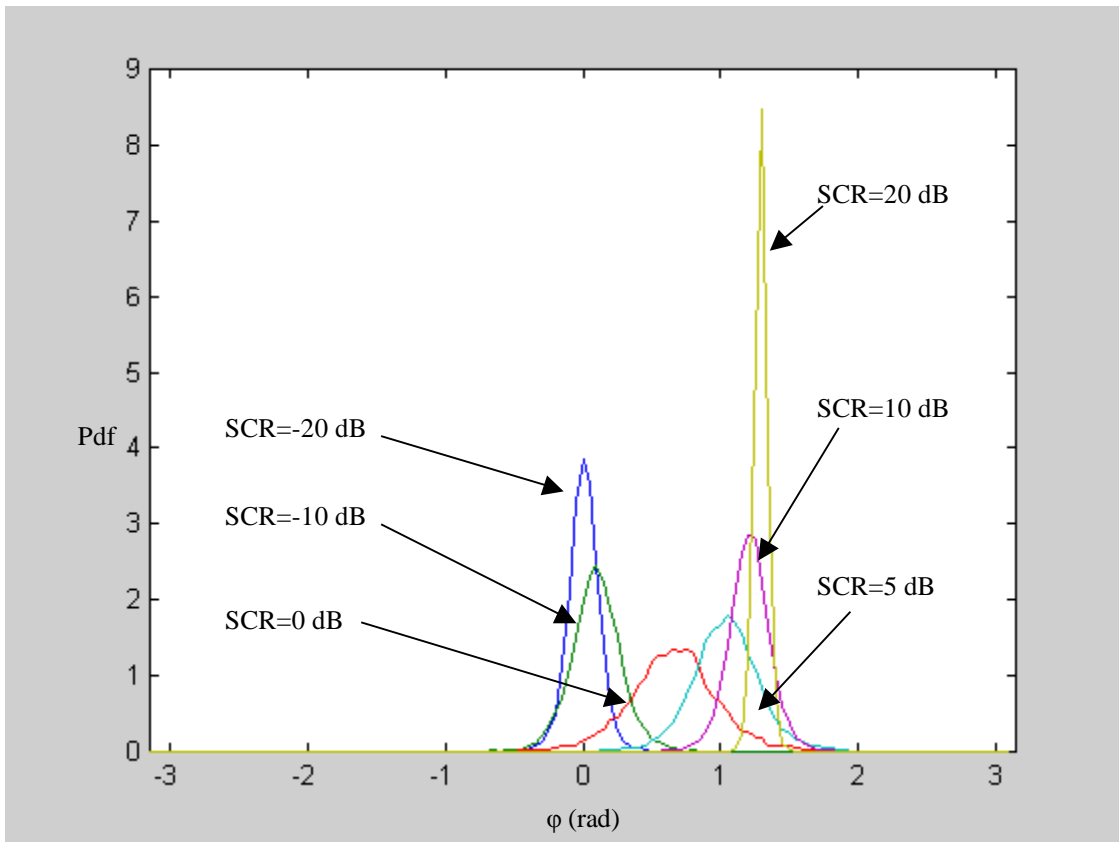


Figure 4: Histogram of phase interferogram.

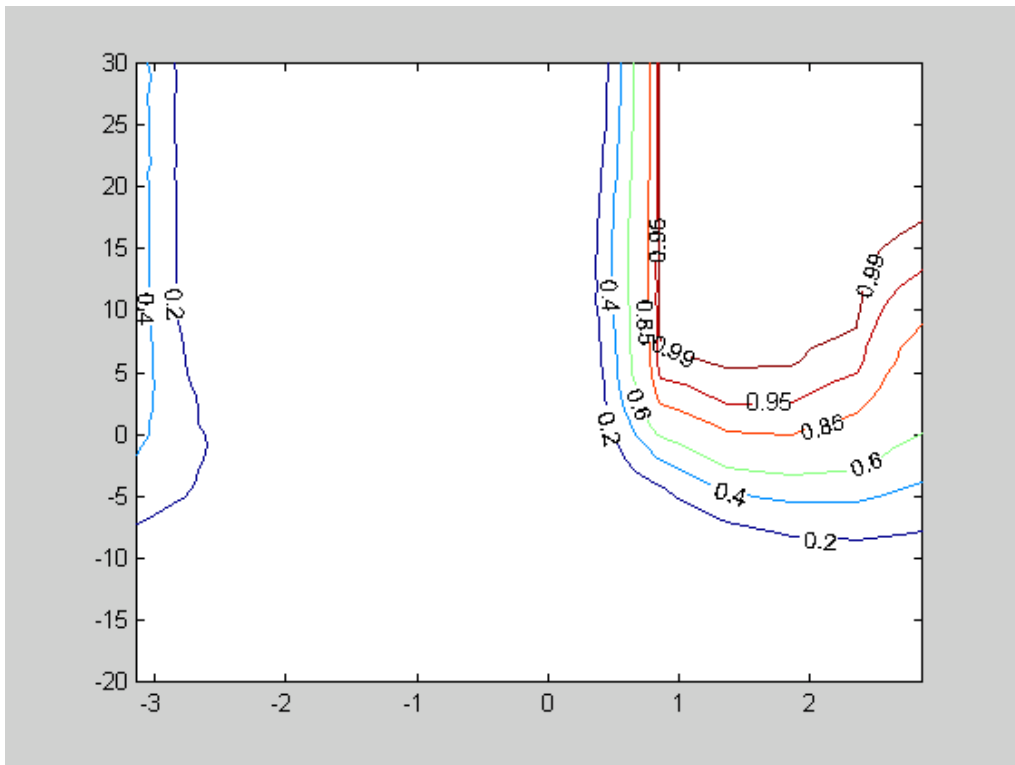
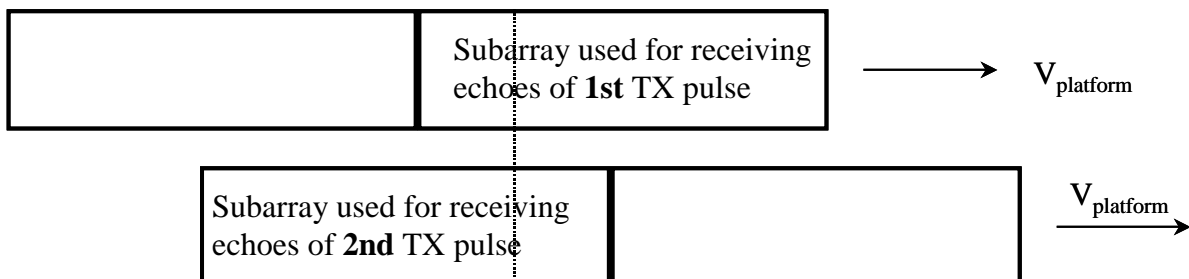


Figure 5: Contour curves with constant Pd versus target Doppler phase and signal to clutter power ratio.

TWO ELEMENT DPCA

Array position when the **1st** pulse is transmitted



Array position when the **2nd** pulse is transmitted

position of TX/RX phase centers for the two pulses

Figure 6: Working principle of DPCA.

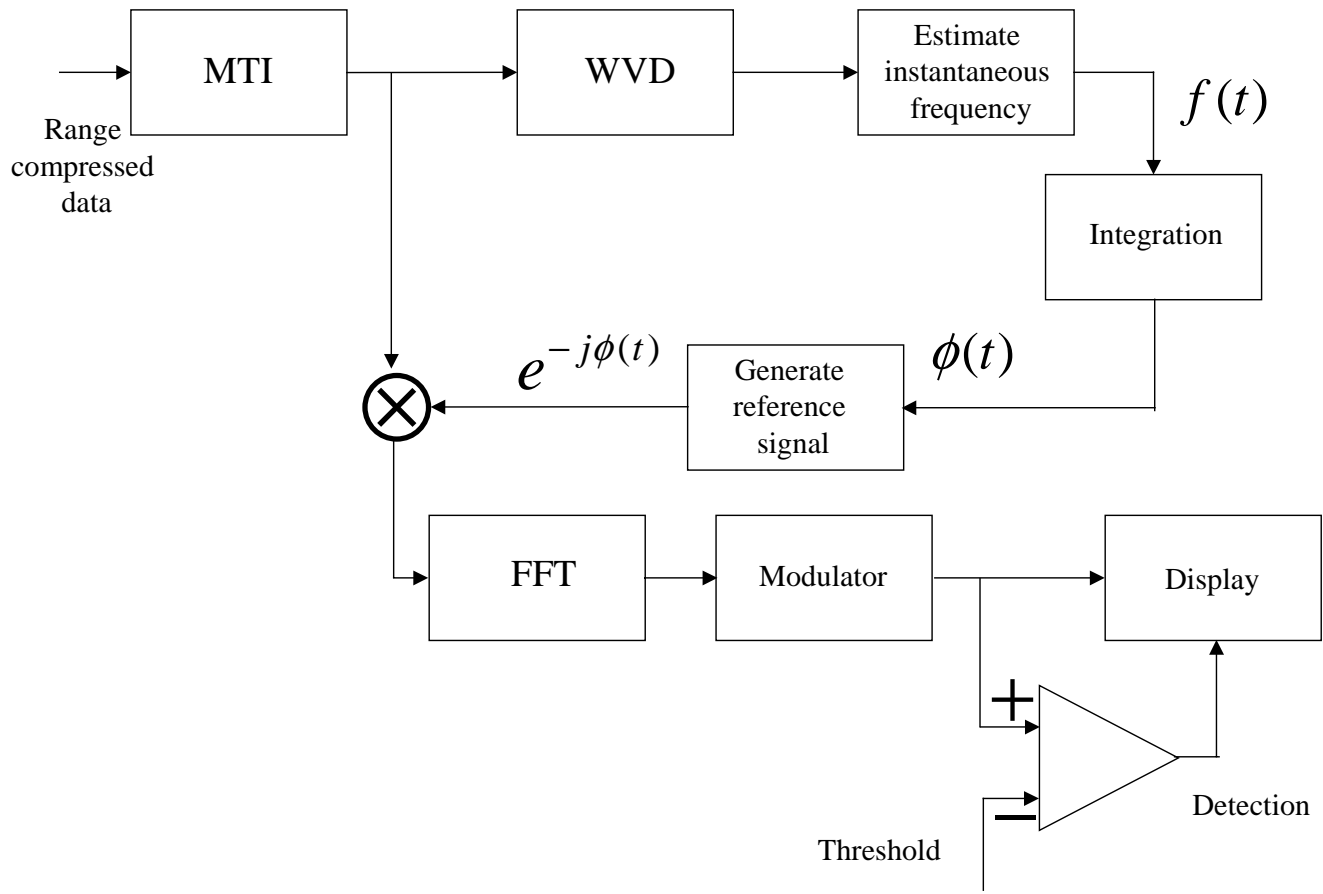


Figure 7: Processing scheme which uses the Wigner-Ville distribution.

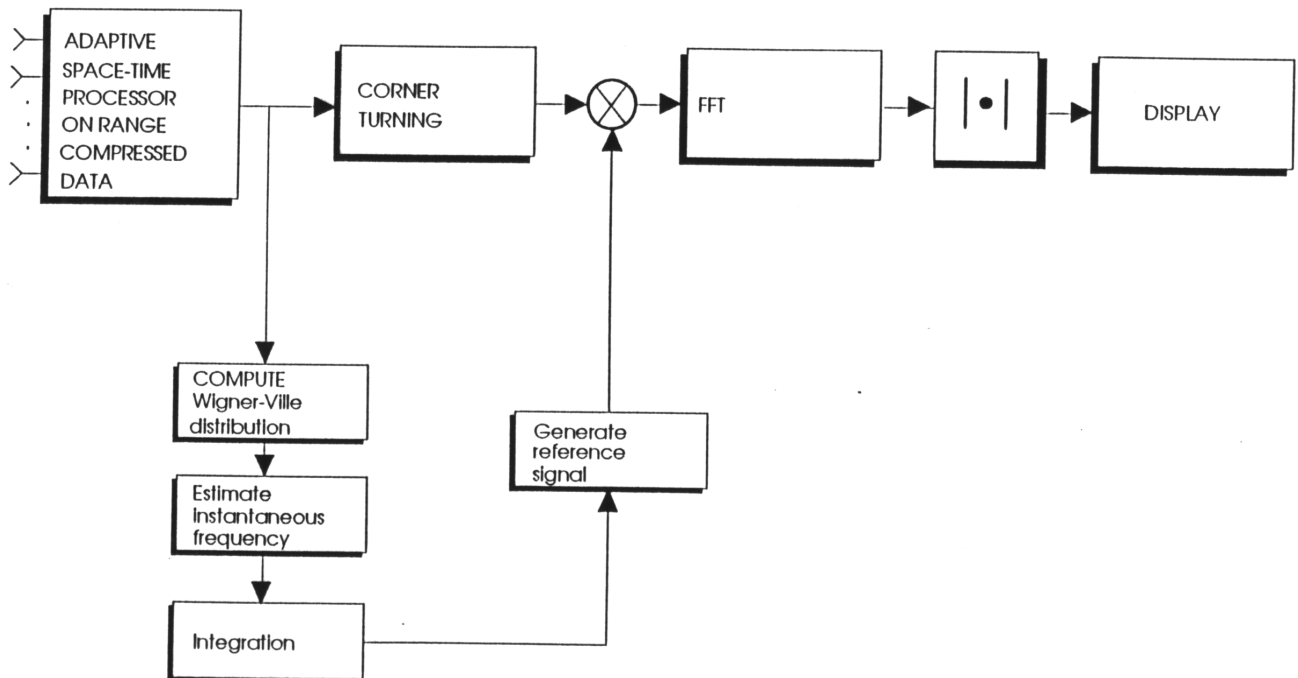


Figure 8. Processing scheme of joint space-time-frequency.

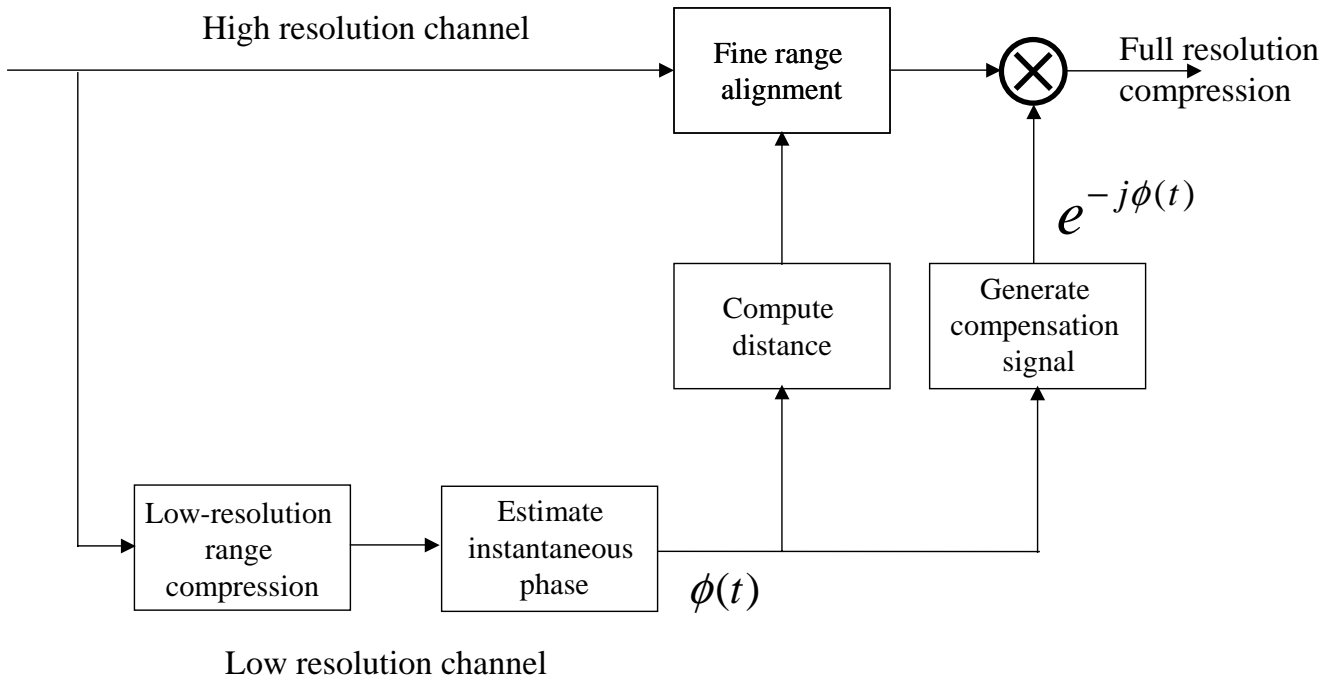


Figure 9: Two-step approach to account for range migration problem.

This page has been deliberately left blank

Page intentionnellement blanche

Stochastic-Constraints Method in Nonstationary Hot-Clutter Cancellation — Part I: Fundamentals and Supervised Training Applications

Prof. Yuri I. Abramovich^{1, 2}

¹ Surveillance Systems Division, Defence Science and Technology Organisation (DSTO)
PO Box 1500, Edinburgh S.A. 5111, Australia

² Cooperative Research Centre for Sensor Signal and Information Processing (CSSIP)
SPRI Building, Technology Park Adelaide, Mawson Lakes S.A. 5095, Australia

yuri@cssip.edu.au

Abstract

We consider the use of spatio-temporal adaptive array processing in over-the-horizon radar applications in order to remove nonstationary multipath interference, known as “hot clutter”. Since the spatio-temporal properties of hot clutter cannot be assumed constant over the coherent processing interval, conventional adaptive techniques fail to provide effective hot-clutter mitigation without simultaneously degrading the properties of the backscattered radar signals, known as “cold clutter”. The approach presented incorporates multiple “stochastic” (data-dependent) constraints to achieve effective hot-clutter suppression, whilst maintaining distortionless output cold-clutter post-processing stationarity.

1. Introduction

This lecture is concerned with adaptive processing of data from high frequency (HF) over-the-horizon radar (OTHR). In general, such radar systems operate by collecting data over a coherent processing interval of time (CPI) which consists of N transmitted pulses or sweeps (in the case of continuous wave (CW) radars), emitted at a pulse repetition frequency of f_r pulses per second. The receiving system consists of M elements, sub-arrays for example, with each element linked to an individual digital receiver. Receiver outputs are sampled at the Nyquist rate of f_t samples per second, resulting in T samples per pulse repetition interval (PRI). The total set of data collected in this manner during a single CPI therefore consists of $M \times N \times T$ samples. Increments in the Nyquist rate (range bins) within a particular PRI are called *fast-time* samples, while those across PRIs are termed *slow-time* samples.

For typical sky-wave OTHR, we have $M = 16$ to 32 , $N = 128$ to 256 and $T \simeq 50$ to 60 [1]; while for surface-wave radars, the CPI may approach 60 or 120 sec [2], so that even with $f_t = 10$ Hz, we have $N = 1000$.

For HF OTHR, an interference signal produced by a single source is typically seen as a multiplicity of interference signals at the receiving antenna array, each mode propagating from source to receiver along a different path.

Various ionospheric layers and inhomogeneities involved in the reflection of interference signals are responsible for the so-called *hot-clutter* phenomenon. If the propagation paths involve reflections from highly perturbed and nonstationary ionospheric regions (such as the equatorial “hot plasma” area or the polar regions), then for hot clutter, nonstationarity of the spatio-temporal covariance matrix over a typical CPI is inevitable. Indeed, spatial nonstationarity of ionospherically propagated interference signals has been observed in HF OTHR, even over the relatively short CPIs typical for aircraft detection [3]. Consideration of this phenomenon is found to be essential for ship detection via skywave propagation, and even more so for HF surface-wave radars where nonstationarity over much longer CPIs leads to a dramatic degradation in the performance of most existing adaptive interference cancellation techniques [3].

It is important to note the critical distinction between hot clutter and ordinary *cold clutter*: the latter is a reflection of the radiated radar signal, while the former refers to the (diffuse) multipath scattered jammer signals.

Of course, the so-called “general fully adaptive” spatio-temporal processing (STAP) described in [4] for example, can theoretically solve the problem of joint hot and cold-clutter suppression [5]. However, in practice this is rarely possible because the dimension of such a fully adaptive system would be MNQ , where Q is the number of fast-time samples involved (number of taps). Indeed, for any HF application with $N \gtrsim 128$, a fully adaptive scheme is totally impractical simply due to the lack of, say, $2MNQ$ training samples.

Thus from a practical viewpoint, we should consider a scheme whereby each “finger beam” is associated with an MQ -variate fast-time STAP to reject the (diffuse) jammer multipath (hot clutter). For HF OTHR applications, the output signals of each beam should be processed by the standard slow-time inter-PRI coherent processing (Doppler spectrum analysis), provided that the cold-clutter slow-time properties at the scalar finger-beam output are not perturbed by the previous fast-time STAP.

Obviously for sufficiently high nonstationarity of the hot-clutter signal, this is a problem since the uncontrolled pattern fluctuations over the CPI introduced by conventional fast-time STAP modulate and consequently decorrelate the cold-clutter signal. For purely spatial adaptive processing, this latter phenomenon has been established both theoretically and experimentally in HF OTHR [6, 3, 7, 8].

Note that if the cold-clutter signal was created by a limited number of point scatterers, it would be possible to “freeze” the receiving antenna pattern in the direction of each point scatterer using standard linear deterministic constraints [9], which are normally used in order to “protect” the antenna pattern in the expected signal direction. Clearly the spatial distribution of cold clutter is generally quite broad, so that it is collected by most of the antenna beam-pattern rather than in just a few directions. Therefore the above method is inappropriate, since we are not able to “freeze” the entire pattern or even a significant part of it without a dramatic degradation in hot clutter rejectability.

Another quite straight-forward approach in avoiding antenna fluctuations is to return to the time-invariant (over CPI) fast-time STAP. The technique of averaging the nonstationary covariance matrix over the CPI has been introduced and tested for HF OTHR applications [6, 3], where it was demonstrated that this approach is appropriate only for extremely short CPIs. The paper [3] defines the typical “stationarity interval” for ionospherically propagated jammers within the dynamic range of contemporary digital receivers to be 100 to 150 μsec , which includes only a few PRIs. Jammer averaging over this interval usually leads to the acceptable degradation of 1 to 3 dB in jamming rejectability compared with “quasi-instantaneous” covariance matrix estimation which uses fast-time training samples in the immediate neighborhood of the analyzed samples within the same PRI, where the delay between the training samples and the operational ranges can be ignored.

Therefore for HF OTHR ($N = 128$), this approach is also completely inappropriate, though the property of “local stationarity” over the short interval of a few consecutive repetition periods will be heavily exploited in what follows.

To summarize, no existing technique is able to provide over sufficiently long CPIs a highly effective hot-clutter-only mitigation without compromising the cold-clutter processing. The main objective of this lecture is to introduce an approach whereby the nonstationary hot-clutter rejection is performed by fast-time STAP updated from PRI to PRI, while the slow-time correlation properties of the cold-clutter scalar output are not affected by the STAP temporal fluctuations.

A spatial-only adaptive processing (SAP) technique involving stochastic constraints was recently introduced to solve this problem [6, 3, 7, 8]. This technique was experimentally verified for HF OTHR, with results reported in [3, 8]. Here we refer to the generalization of this the stochastic-constraints approach to spatio-temporal adaptive rejection of hot clutter which is essentially nonstationary over the CPI [15].

2. SC STAP Algorithm: Model Description

Let the M -variate complex column vector \mathbf{z}_{kt} be the antenna array snapshot corresponding to the k^{th} repetition period and the t^{th} range bin, *ie.* $\mathbf{z}_{kt} \in \mathcal{C}^{M \times 1}$ where k represents “slow time” while t represents “fast time”. In general, we may define the snapshot \mathbf{z}_{kt} to be the mixture

$$\mathbf{z}_{kt} = \mathbf{s}_{kt} + \mathbf{y}_{kt} + \mathbf{x}_{kt} + \boldsymbol{\eta}_{kt} \quad \text{for } k = 1, 2, \dots, N; \quad t = 1, 2, \dots, T \quad (1)$$

where s_{kt} is the desired signal backscattered by a point target; \mathbf{y}_{kt} is the radar signal backscattered by terrain or the sea surface (“cold clutter”); \mathbf{x}_{kt} is the total jamming signal, comprising direct path, specular and diffuse multipath scattering (“hot clutter”); and $\boldsymbol{\eta}_{kt}$ is additive white noise of power $\sigma_{\boldsymbol{\eta}}^2$ with the correlation property

$$\mathcal{E}\{\boldsymbol{\eta}_{kt} \boldsymbol{\eta}_{k't'}^H\} = \sigma_{\boldsymbol{\eta}}^2 \delta(k-k') \delta(t-t') I_M. \quad (2)$$

Typically, the target signal s_{kt} originating from some direction θ_0 takes the form

$$\mathbf{s}_{kt} = a \psi_t \exp\left(i[\omega_d k/f_r + \phi_t]\right) \mathbf{s}(\theta_0) \quad (3)$$

where a is a complex Gaussian-distributed (scalar) amplitude; ψ_t is the signal waveform; ω_d is the target-signal Doppler frequency (in radians); ϕ_t is a range-dependent phase, and $\mathbf{s}(\theta_0)$ is the array manifold (“steering”) vector.

The cold-clutter snapshot \mathbf{y}_{kt} is simulated here as a stationary random M -variate Gaussian process with the correlation property

$$\mathcal{E}\{\mathbf{y}_{kt} \mathbf{y}_{k't'}^H\} = \delta(t-t') R_{k-k'}^{\mathbf{y}} \quad (4)$$

(*ie.* the range sidelobes are ignored) where $R_{k-k'}^{\mathbf{y}}$ is the cold-clutter spatial covariance matrix at the slow-time lag $(k-k')$, and $R_0^{\mathbf{y}}$ is the standard M -variate Hermitian cold-clutter spatial covariance matrix.

The hot-clutter signal \mathbf{x}_{kt} is assumed to be a convolutive mixture of P external interference signals $g_{kt}^{(p)}$, $p = 1, \dots, P$, where each $g_{kt}^{(p)}$ is a complex waveform radiated by the p^{th} jammer at time $(k/f_r + t)$:

$$\mathbf{x}_{kt} = \sum_{\ell=1}^L H_{k\ell} \mathbf{g}_{k,t-\ell+1} \quad (5)$$

where L is the assumed maximum number of propagating paths for any of the P interfering sources, and $H_{k\ell}$ is defined below. The P -variate vector $\mathbf{g}_{kt} = [g_{kt}^{(1)}, \dots, g_{kt}^{(P)}]^T$ consists of complex waveforms radiated by all P sources at time $(k/f_r + t)$.

As usual, we assume that

$$\mathcal{E}\left\{g_{kt}^{(p)} g_{k't'}^{(p')*}\right\} = \delta(p-p') \delta(k-k') \delta(t-t') \sigma_{\mathbf{x}_p}^2 \quad (6)$$

where $\sigma_{\mathbf{x}_p}^2$ is the p^{th} jamming signal power, *ie.* the jammers are assumed to be mutually independent and temporally white (broadband).

For diffuse multipath, L is usually defined as the number of range bins covering some range interval Δ_R involved in the scattering [9, 4]

$$L = \frac{B\Delta_R}{c} = f_t \Delta_R \quad (7)$$

where B is the signal bandwidth, and c is the speed of light. For continuously distributed scatterers, it is more accurate to determine the interval between lines of constant path delay by the range grid, defined by the maximum hot-clutter suppression for continuously distributed clutter. The latter itself is usually defined by the input hot-clutter-to-noise ratio. The larger this ratio is, the smaller the separation should be. This phenomenon has been known for many years [10, 11]; an example of the accurate evaluation of the number L is given in [4] for one particular hot-clutter-to-noise ratio.

The MP -variate matrix $H_{k\ell}$ introduced above in (5) represents the instantaneous total impulse response, relating the radiated jammer signals $g_{kt}^{(p)}$ to the received hot-clutter snapshots \mathbf{x}_{kt} . Naturally $H_{k\ell}$ incorporates the time-varying channel characteristics experienced by each propagation path. For diffuse multipath, the time variation of the synthetic wavefront from the scatterers along each line of constant path delay is defined by a differential Doppler shift along that line. More precisely, the $(i,j)^{\text{th}}$ element of the matrix $H_{k\ell}$ is a complex

coefficient which is practically constant over the k^{th} PRI, and is a measure of the contribution of the j^{th} interference source with relative delay ℓ to the final hot-clutter output at the i^{th} receiver during the k^{th} PRI.

Although the number of interfering sources P is assumed to be strictly less than the number of antenna elements M , the total number of independent sources seen by the antenna array may approach PL . Thus, even for modest P and L , their product may exceed the number of antenna elements M . If

$$PL \geq M \quad (8)$$

then a purely spatial approach will be generally ineffective. On the other hand, it is necessary to emphasize that the product PL itself does not entirely define the best performance of the adaptive technique. For example, if all scatterers are situated in an extremely thin layer (of the ionosphere) with constant path delay (“auroral” scattering), then the rank of the covariance matrix would always be unity for a single jamming source. Therefore in this case, pure SAP would give us the maximum efficiency for distributed scattering cancellation, regardless of the number of such point scatterers. This phenomenon was described in [11].

Equally, pure SAP should deliver effective hot-clutter cancellation for a single jammer if

$$L \ll M. \quad (9)$$

The existence of numerous point scatterers along the path of equal delay over a wide angle means that the main beam direction will be unaffected by SAP, even if this main beam intersects this path [11, 4]. On the other hand, if there is a single scatterer along the path of equal delay which intersects the main beam, then pure SAP would not deliver effective suppression of hot clutter collected by the main beam. To be more accurate, under the condition $L \ll M$, such hot clutter could be rejected, but the main beam would also be affected.

These quite simple considerations are necessary for a clear understanding of the correspondence between SAP and STAP in the hot-clutter mitigation problem.

Hereafter we will be dealing with the general case $PL \geq M$.

If the model of (5) is adopted for some fixed L , then we note that the number of taps Q that are necessary for hot-clutter suppression is defined directly by the model. Let us introduce the MQ -variate “stacked” vector $\tilde{\mathbf{x}}_{kt}$, consisting of Q successive fast-time samples \mathbf{x}_{kt} stacked on top of each other. According to (5), we may write

$$\begin{bmatrix} \mathbf{x}_{kt} \\ \mathbf{x}_{k,t-1} \\ \vdots \\ \mathbf{x}_{k,t-Q+1} \end{bmatrix} = \begin{bmatrix} H_{k0} & \dots & H_{k,L-1} & 0 & \dots & 0 \\ 0 & H_{k0} & \dots & H_{k,L-1} & \ddots & \vdots \\ \vdots & \ddots & \ddots & & \ddots & 0 \\ 0 & \dots & 0 & H_{k0} & \dots & H_{k,L-1} \end{bmatrix} \begin{bmatrix} \mathbf{g}_{kt} \\ \mathbf{g}_{k,t-1} \\ \vdots \\ \mathbf{g}_{k,t-L+1-Q+1} \end{bmatrix} \quad (10)$$

or more compactly

$$\tilde{\mathbf{x}}_{kt} = \tilde{H}_{k\ell} \mathbf{g}_{kt}. \quad (11)$$

The number of rows in the stacked block matrix $\tilde{H}_{k\ell}$ is equal to MQ , while the number of columns is $P(L + Q - 1)$. Thus the stacked noise-free hot-clutter spatio-temporal covariance matrix

$$\tilde{R}_k^{\mathbf{x}} = \mathcal{E}\{\tilde{\mathbf{x}}_{kt} \tilde{\mathbf{x}}_{kt}^H\} \quad (12)$$

is always rank-deficient if

$$MQ > P(L + Q - 1) \quad (13)$$

ie.

$$Q > \frac{P(L-1)}{M-P}. \quad (14)$$

This condition and the basic presentation of (10) are well known in the field of multiple-input-multiple-output (MIMO) systems [12].

For $L = 1$, STAP cannot outperform SAP, as expected. While for $Q = 1$, we find that the covariance matrix is rank-deficient if $M > PL$, *ie.* SAP alone can effectively suppress hot clutter.

It is interesting to note that the number of taps $Q = L$ usually recommended [9, 4] is justified only for $P = M/2$. The number of taps necessary to cope with the maximum number of independent jammers $P_{max} = M - 1$ is

$$Q_{max} \geq P_{max} (L - 1) \quad (15)$$

which again agrees with the results of MIMO studies [12].

Note that when the condition of (13) is satisfied, the rank of the covariance matrix \tilde{R}_k^x is

$$\text{rank} [\tilde{R}_k^x] \lesssim P(L + Q - 1). \quad (16)$$

Thus the condition (13) actually generalizes the well-known condition for spatial suppression of P independent jammers

$$M > P \quad (17)$$

which obviously follows from (13) when $Q = L = 1$.

It is necessary to emphasize that the condition of (13) or (17) guarantees hot-clutter rejectability irrespective of the signal-to-noise ratio (SNR) obtained as a result of such rejection. For independent jammers and pure SAP, the main beam would be affected when the direction of arrival of one of the jammers is close to the target signal direction. For STAP a similar unfortunate scenario may occur, when the target-signal stacked vector \tilde{s}_{kt} (defined similarly to \tilde{x}_{kt} and \tilde{g}_{kt}) can be fairly accurately presented as a linear combination of the columns of $\tilde{H}_{k\ell}$.

Obviously, in practical applications, Q should exceed Q_{min} as defined by (14) because of the additional constraints that are usually imposed.

Suppose now that the number of taps Q is properly chosen, and so our problem is to find an MQ -variate STAP filter \tilde{w}_{kt} with which to process the MQ -variate stacked vector \tilde{z}_{kt} :

$$\tilde{z}_{kt} = \begin{bmatrix} z_{kt} \\ \vdots \\ z_{k,t-Q+1} \end{bmatrix} \quad (18)$$

to form the scalar output $z_{kt} = \tilde{w}_{kt}^H \tilde{z}_{kt}$. We may similarly compute the scalar output sequences which correspond to the target signal s_{kt} , the backscattered cold clutter y_{kt} , and the hot clutter x_{kt} :

$$\begin{aligned} s_{kt} &= \tilde{w}_{kt}^H \tilde{s}_{kt} \\ y_{kt} &= \tilde{w}_{kt}^H \tilde{y}_{kt} \\ x_{kt} &= \tilde{w}_{kt}^H \tilde{x}_{kt}. \end{aligned} \quad (19)$$

The first set of constraints for the STAP vector \tilde{w}_{kt} is designed to ensure the undistorted reception of the target signal. There are several approaches using deterministic linear constraints which can protect the desired signal against distortions caused by temporal adaptivity [9]. For example, we may introduce the set of Q linear constraints such that

$$\tilde{w}_{kt}^H A_Q(\theta_0) = e_Q^T \quad (20)$$

where the $MQ \times Q$ matrix $A_Q(\theta_0) = s(\theta_0) \otimes I_Q$ (\otimes represents the Kronecker product) and the Q -variate column vector $e_Q = [1, 0, \dots, 0]^T$.

Such constraints ensure the distortionless reception of the target signal from the expected DOA θ_0 . If one requires the output signal s_{kt} to be more robust in the presence of pointing errors, constraints on the steering vector derivatives might also be imposed, *eg.*

$$A_{2Q}(\theta_0) = \begin{bmatrix} s(\theta_0) & s'(\theta_0) & 0 & 0 & \dots & 0 & 0 \\ 0 & 0 & s(\theta_0) & s'(\theta_0) & & 0 & 0 \\ \vdots & & & & \ddots & & \vdots \\ 0 & 0 & \dots & 0 & 0 & s(\theta_0) & s'(\theta_0) \end{bmatrix} \quad (21)$$

where

$$\mathbf{s}'(\theta_0) = \left. \frac{\partial \mathbf{s}(\theta)}{\partial \theta} \right|_{\theta=\theta_0} \quad (22)$$

and

$$\tilde{\mathbf{w}}_{kt}^H A_{2Q}(\theta_0) = \mathbf{e}_q^T. \quad (23)$$

In general, we may define an $MQ \times q$ matrix \tilde{A}_q together with the q -variate vector \mathbf{e}_q to implement q linear constraints:

$$\tilde{\mathbf{w}}_{kt}^H \tilde{A}_q(\theta_0) = \mathbf{e}_q^T. \quad (24)$$

The cold clutter is assumed to be a stationary process (in a broad sense), and thus it may be approximated by the multivariate auto-regressive (AR) model of order κ :

$$\mathbf{y}_{kt} + \sum_{j=1}^{\kappa} B_j \mathbf{y}_{k-j,t} = \boldsymbol{\xi}_{kt}. \quad (25)$$

In the above equation, B_j are the M -variate matrices which are the solutions of the multivariate Yule-Walker equations [13]:

$$\begin{bmatrix} R_0^{\mathbf{y}} & R_1^{\mathbf{y}} & \dots & R_{\kappa}^{\mathbf{y}} \\ R_{-1}^{\mathbf{y}} & R_0^{\mathbf{y}} & & \\ \vdots & \ddots & \vdots & \\ R_{-\kappa}^{\mathbf{y}} & \dots & R_0^{\mathbf{y}} & \end{bmatrix} \begin{bmatrix} I_M \\ B_1 \\ \vdots \\ B_{\kappa} \end{bmatrix} = \begin{bmatrix} R_k^{\boldsymbol{\xi}} \\ 0 \\ \vdots \\ 0 \end{bmatrix} \quad (26)$$

where

$$\mathcal{E}\{\boldsymbol{\xi}_{kt} \boldsymbol{\xi}_{k+j,t}^H\} = \begin{cases} R_k^{\boldsymbol{\xi}} & \text{for } j = 0 \\ 0 & \text{for } j \neq 0. \end{cases} \quad (27)$$

Note that the scalar moving average (MA) model is usually considered an alternative to the AR model, however it is now known that even the multivariate MA model can be presented as a multivariate AR model of finite order under surprisingly mild conditions [14] (in the scalar case this order is infinite).

In [15], we derived for this general model the exact analytic solution for a time-varying fast-time STAP filter that maintains the stationarity of the cold-clutter scalar output signal, regardless of the filter's temporal fluctuations. Yet, practically feasible solutions, demonstrated below, may be derived for the simpler scalar multivariate model:

$$\mathbf{y}_{kt} + \sum_{j=1}^{\kappa} b_j \mathbf{y}_{k-j,t} = \boldsymbol{\xi}_{kt} \quad (28)$$

where $B_j = b_j I_m$.

3. SC STAP Algorithm: Practical Routine for Pulse-Waveform (PW) HF OTHR

An operational (practical) approach for purely spatial adaptive processing was introduced in [6, 3, 7, 8]; we shall now generalize this to the STAP case.

In most PW HF OTHR systems, scattering from the Earth's surface (cold clutter) and from targets occupies only a limited range within each repetition period. For sky-wave radar, the finite duration of the oblique backscattered signal (OBS) is dictated by the radar-ionosphere-target geometry. For surface-wave radar, natural attenuation leads to suppression of the backscattered signal far from the end of the repetition period. Naturally these scattered (cold-clutter) signals are submerged in the hot clutter and are not directly available for treatment by stochastic constraints.

Meanwhile, the hot-clutter signal usually occupies the entire repetition period (the entire CPI, actually) and in most cases some region within the PRI can be easily identified as containing hot clutter only. Hence this

operational routine relies on *a priori* information on the distribution of the cold-clutter-free ranges within the PRI.

We have already discussed the “local stationarity” property of the hot clutter over the limited number of consecutive PRIs. Assume for example, the second-order ($\kappa = 2$) cold-clutter AR model of the simple scalar multivariate model (28). We form the fast-time STAP filters $\tilde{\mathbf{w}}_{kt}^{av}$ in the order $k = 1, \dots, N - \kappa$; the first of which ($k = 1$) is stochastically unconstrained, and thereafter are stochastically constrained. We construct this initial STAP filter $\tilde{\mathbf{w}}_{1t}^{av}$ using the hot-clutter-only training samples from some common range region within the first three consecutive PRIs:

$$\tilde{\mathbf{w}}_{1t}^{av} = \left(\tilde{R}_1^{av} \right)^{-1} \tilde{A}_q(\theta_0) \left[\tilde{A}_q^H(\theta_0) \left(\tilde{R}_1^{av} \right)^{-1} \tilde{A}_q(\theta_0) \right]^{-1} \mathbf{e}_q \quad (29)$$

where $\tilde{A}_q(\theta_0)$ and \mathbf{e}_q are the deterministic constraints from (24) and

$$\tilde{R}_1^{av} = \frac{1}{3} \left(\tilde{R}_1^{\mathbf{x}\boldsymbol{\eta}} + \tilde{R}_2^{\mathbf{x}\boldsymbol{\eta}} + \tilde{R}_3^{\mathbf{x}\boldsymbol{\eta}} \right). \quad (30)$$

Due to the “local stationarity” of the hot clutter, we believe that the hot-clutter samples are properly rejected by the STAP filter $\tilde{\mathbf{w}}_{1t}^{av}$ over all ranges of these three initial PRIs, so that the scalar output for operational ranges consists mainly of cold clutter, noise and possible targets, *ie.*

$$\tilde{\mathbf{w}}_{1t}^{avH} \tilde{\mathbf{z}}_{kt} \simeq \tilde{\mathbf{w}}_{1t}^{avH} \tilde{\mathbf{y}}_{kt} + \tilde{\mathbf{w}}_{1t}^{avH} \tilde{\mathbf{s}}_{kt} + \tilde{\mathbf{w}}_{1t}^{avH} \tilde{\boldsymbol{\eta}}_{kt} \quad \text{for } k = 1, 2, 3. \quad (31)$$

Note that $\tilde{\mathbf{w}}_{1t}^{av}$ is a function only of k , not of fast time t . For the next adaptive filter $\tilde{\mathbf{w}}_{2t}^{av}$ (now range-dependent and stochastically constrained), we apply the “sliding-window” average to the next three repetition periods:

$$\tilde{R}_2^{av} = \frac{1}{3} \left(\tilde{R}_2^{\mathbf{x}\boldsymbol{\eta}} + \tilde{R}_3^{\mathbf{x}\boldsymbol{\eta}} + \tilde{R}_4^{\mathbf{x}\boldsymbol{\eta}} \right) \quad (32)$$

to again ensure a proper hot-clutter suppression over these three PRIs. Clearly the moving-average across ($\kappa+1$) adjacent repetition periods also ensures that κ covariances $\tilde{R}_k^{\mathbf{x}\boldsymbol{\eta}}$ are common to each successive average \tilde{R}_k^{av} . The system of κ stochastic constraints corresponding to (31) and (32) may then be written as:

$$\tilde{\mathbf{w}}_{2t}^{avH} \tilde{\mathbf{z}}_{kt} = \tilde{\mathbf{w}}_{1t}^{avH} \tilde{\mathbf{z}}_{kt} \quad \text{for } k = 2, 3. \quad (33)$$

The right-hand sides of these constraints consist of the cold-clutter samples mainly due to (31); whereas (32) ensures that the filter $\tilde{\mathbf{w}}_{2t}^{av}$ properly processes the cold-clutter samples only, since the hot-clutter component is to be rejected.

For an arbitrary slow time k , the operational solution

$$\tilde{\mathbf{w}}_{kt}^{av} = \left(\tilde{R}_k^{av} \right)^{-1} \tilde{A}_{kt} \left[\tilde{A}_{kt}^H \left(\tilde{R}_k^{av} \right)^{-1} \tilde{A}_{kt} \right]^{-1} \mathbf{e}_{q+\kappa} \quad \text{for } k = 2, \dots, N - 2 \quad (34)$$

is defined by the “sliding-window” covariance matrix

$$\tilde{R}_k^{av} = \frac{1}{3} \left(\tilde{R}_k^{\mathbf{x}\boldsymbol{\eta}} + \tilde{R}_{k+1}^{\mathbf{x}\boldsymbol{\eta}} + \tilde{R}_{k+2}^{\mathbf{x}\boldsymbol{\eta}} \right) \quad (35)$$

and the system of stochastic constraints

$$\tilde{A}_{kt} \mathbf{z} = \left[\tilde{A}_q \mid \left(\tilde{I}_{MQ} - \frac{\tilde{\mathbf{s}}(\theta_0) \tilde{\mathbf{w}}_{k-1,t}^{avH}}{\tilde{\mathbf{w}}_{k-1,t}^{avH} \tilde{\mathbf{s}}(\theta_0)} \right) \tilde{Z}_{kt} \right] \quad (36)$$

where $\tilde{Z}_{kt} = [\tilde{\mathbf{z}}_{kt} | \tilde{\mathbf{z}}_{k+1,t}]$. The latter simply means that

$$\begin{aligned} \tilde{\mathbf{w}}_{kt}^{avH} \tilde{\mathbf{z}}_{kt} &= \tilde{\mathbf{w}}_{k-1,t}^{avH} \tilde{\mathbf{z}}_{kt} \\ \tilde{\mathbf{w}}_{kt}^{avH} \tilde{\mathbf{z}}_{k+1,t} &= \tilde{\mathbf{w}}_{k-1,t}^{avH} \tilde{\mathbf{z}}_{k+1,t}. \end{aligned} \quad (37)$$

The generalization of these three equations for arbitrary κ is obvious.

Note that the hot-clutter “quasi-stationarity” over the $(\kappa+1)$ consecutive repetition periods simply means that the signal eigen-subspace dimension of the resulting averaged covariance matrix should still be less than the total number of degrees of freedom in the STAP filter (MQ). Even when the nonstationarity is significant, proper hot-clutter rejection can be achieved with this averaging provided

$$(\kappa+1) [P(L+Q-1)] < MQ. \quad (38)$$

Recall from (13) that $P(L+Q-1)$ is the rank (signal eigen-subspace dimension) of the “intra-sweep” spatio-temporal hot-clutter-only covariance matrix. Obviously the number of taps Q which guarantees this condition is

$$Q > \frac{(\kappa+1) P(L-1)}{M - (\kappa+1) P} \quad (39)$$

with the additional necessary condition

$$M > (\kappa+1) P. \quad (40)$$

To summarize, using the stated hot- and cold-clutter models and operational routines, the above conditions specify the proper choice of purely spatial (M) and total (MQ) degrees of freedom which guarantee high hot-clutter rejectability under almost arbitrary nonstationarity of the hot clutter.

Naturally, the above approach may also be applied to CW OTHR provided there is access to some hot-clutter-only range cells within each PRI.

4. Operational Approach: Finite Sample Size Considerations

The final step towards a truly operational routine is the replacement of the true hot-clutter covariance matrix $\tilde{R}_k^{x\eta}$ by its sample estimate $\hat{\tilde{R}}_k^{x\eta}$. We do this by averaging over all range cells that are free of cold-clutter contamination, for each PRI. For HF OTHR, the size of the hot-clutter training sample used to form $\hat{\tilde{R}}_k^{x\eta}$ is a serious issue. This motivates our investigation into means of reducing the length of the training sequence necessary for hot-clutter cancellation.

One significant contribution has already been made by (14), where the minimum number of taps Q_{min} is given in terms of M , L and P .

According to the famous result of Mallet, Reed and Brennan [16], in order to obtain an average 3 dB loss in SNR compared with the optimum, the number of independent samples T_0 used for estimation of some MQ -variate covariance matrix is

$$T_0 \gtrsim 2MQ. \quad (41)$$

Apart from being too large a number in most cases, this estimate does not leave room for the trade-off between the number of spatial and temporal degrees of freedom.

Less well-known are the results of [17, 18, 19], recently duplicated in [20], which show that by proper diagonal loading:

$$\hat{\tilde{R}}_k^{x\eta} = \beta I_{MQ} + \sum_{t=1}^{T_0} (\tilde{x}_{kt} + \tilde{\eta}_{kt}) (\tilde{x}_{kt} + \tilde{\eta}_{kt})^H \quad \text{for } \beta \gtrsim \sigma_{\eta}^2 \quad (42)$$

the number of snapshots T_0 sufficient for 3 dB losses may be reduced to

$$T_0 \gtrsim 2 \operatorname{rank} \tilde{R}_k^x. \quad (43)$$

Recall that the rank of \tilde{R}_k^x is equal to the signal eigen-subspace dimension of $\tilde{R}_k^{x\eta}$. Where $\tilde{R}_k^{x\eta}$ is not averaged over adjacent PRIs, this dimension is defined by (13) and (16), *i.e.*

$$\operatorname{rank} \tilde{R}_k^{x\eta} \leq P(L+Q-1). \quad (44)$$

This firstly means that the ‘‘blind zone’’ can be dramatically reduced (compared with using $T_0 \gtrsim 2MQ$). Secondly, this is analytical evidence for the conclusion made in [21]. Indeed, according to (43) and (44), in order to decrease the ‘blind zone’, the number of spatial degrees of freedom M should be maximized, followed by the corresponding reduction in temporal degrees of freedom Q .

According to (35) and (42), the operational estimate

$$\hat{\tilde{R}}_k^{av} = \frac{1}{3} \left(\hat{\tilde{R}}_k^{\mathbf{x}\boldsymbol{\eta}} + \hat{\tilde{R}}_{k+1}^{\mathbf{x}\boldsymbol{\eta}} + \hat{\tilde{R}}_{k+2}^{\mathbf{x}\boldsymbol{\eta}} \right) \quad (45)$$

involves $3T_0$ training samples in total. Thus averaging over the (slightly) nonstationary hot-clutter training samples belonging to three consecutive PRIs reduces the random errors for this estimate. Of course, the maximum reduction is obtained when the actual nonstationarity could be ignored:

$$\tilde{R}_k^{\mathbf{x}\boldsymbol{\eta}} \simeq \tilde{R}_{k+1}^{\mathbf{x}\boldsymbol{\eta}} \simeq \tilde{R}_{k+2}^{\mathbf{x}\boldsymbol{\eta}}. \quad (46)$$

Under such extreme circumstances, the total number of necessary training samples ($T_0 = 36$) could even be distributed over these three PRIs.

When there is significant nonstationarity, however, there will be some optimal trade-off in the number of PRIs involved, given that the sample volume T_0 is fixed for each PRI. Indeed by increasing the number of PRIs involved in averaging (K) we increase the signal subspace dimension of the true covariance matrix

$$\tilde{R}_k^{av} = \frac{1}{K+1} \sum_{j=0}^K \tilde{R}_{k+j}^{\mathbf{x}\boldsymbol{\eta}}. \quad (47)$$

On the other hand, we somewhat decrease the random error by use of the estimate

$$\hat{\tilde{R}}_k^{av} = \frac{1}{K+1} \sum_{j=1}^K \hat{\tilde{R}}_{k+j}^{\mathbf{x}\boldsymbol{\eta}}. \quad (48)$$

Clearly the optimum number K is not identical to the minimum number.

Therefore with simulations that involve the true covariance matrices, we expect covariance matrix averaging to introduce some extra losses in hot-clutter rejectability compared with the ideal case of using $\tilde{R}_k^{\mathbf{x}\boldsymbol{\eta}}$. On the other hand, the fully operational routine using a finite training sample volume per PRI gains in the reduction of stochastic errors due to the averaging process.

The curves labeled q_{OSC} and \tilde{w}_{OSC} in Figs. 1, 2 and 3 demonstrate the efficiency of the fully operational routine, involving a loaded sample covariance matrix, (42) and (45) and simulated data [15]. Comparing the output Doppler spectra obtained for range cells with and without targets, we see that the operational SC STAP routine achieves both highly efficient target detection and subclutter visibility protection. The curve in Fig. 1 indicates the signal-to-hot-clutter ratio for the operational filter across all 256 PRIs. While the 36 training samples are not strictly independent (due to multimode propagation), additional stochastic losses are negligible.

These results show that the operational SC STAP approach can deliver remarkably good performance. Since each range bin is processed by an individual fast-time STAP filter, the cost of such performance is a higher computational load. However for HF OTHR applications at least, where the number of range cells is not large and the Nyquist rate f_t is measured in dozens of kHz, this load is reasonable.

5. SC STAP Algorithm: Efficiency Analysis by Real-Data Processing

The most important remaining question to consider is the adequacy of the scalar low-order AR model which is applied to real cold clutter. This question has been partly discussed in [3]. Here we refer to some new real HF OTHR clutter data to illustrate the ability of the proposed SC STAP algorithm to retain the initial subclutter visibility.

The first set of experimental data was collected by the Jindalee facility, located in Alice Springs, Australia [22]. Typical sky-wave sea-scattered signals have been collected by the 32-channel receiver in its ship-detection mode, without noticeable jamming. The interference signals were recorded separately, when the system operated in receive-only mode. This experimental setup allowed us to compare in [15] the initial and “stabilized” cold-clutter spectra with one, two and four constraints.

While a single stochastic constraint is inadequate, with subclutter visibility degrading up to about 15 dB, two and four constraints gave output spectra that are practically identical to the CBF spectra. This provides a justification of our use of the simple AR cold-clutter model for sky-wave OTHR applications.

For surface-wave radars, the sea-clutter is even closer to its theoretical model, introduced in [23]. We present one example from the data set collected by the 12-channel pulse-waveform SW OTHR facility, operating with a PRF of 10 Hz and CPI of 100 seconds. Figs. 4 and 5 together illustrate (a) the standard CBF spectrum corresponding to the filter \tilde{w}_{CBF} , and the output spectra obtained for (b) globally averaged STAP (constant for all PRIs) \tilde{w}_{STAP} , (c) SC STAP with two constraints \tilde{w}_{SC} , and (d) unconstrained STAP \tilde{w}_{STAP} . The first three spectra are indistinguishable, whereas the unconstrained STAP filter fluctuations degrade subclutter visibility significantly. Note that the CBF subclutter visibility (rather poor in this case) is retained without any noticeable broadening of the narrow-band Doppler components (Bragg lines).

These results demonstrate that, despite the complexity of global models that properly describe real HF sea-clutter, we may apply simplistic models locally without major degradation.

6. Summary and Conclusions

We have identified the similarity between HF OTH radars, with respect to the problem of multimode-interference (hot-clutter) rejection utilizing STAP. The problem of nonstationary hot-clutter cancellation via fast-time STAP has been formulated, mainly relying upon recently investigated properties of HF signals propagating through perturbed ionospheric regions.

It has been demonstrated that the standard fast-time STAP algorithms are inappropriate for the removal of nonstationary hot clutter when the backscattered signal (cold clutter) properties must be preserved in some way. Fast-time (intra-PRI) STAP filters that vary from PRI to PRI in an unconstrained fashion cause a severe degradation in the cold-clutter Doppler spectral properties (namely, subclutter visibility). On the other hand, the application of time-independent STAP algorithms, for which the hot-clutter spatio-temporal covariance matrix is averaged over a relatively long CPI, severely degrades the hot-clutter rejectability.

The only previously known approach that can theoretically perform simultaneous hot- and cold-clutter rejection is the “uniform STAP”. This has a problem size defined by MNQ , where M is the number of antenna receivers, N is the number of PRIs within each CPI, and Q is the number of fast-time taps. For all HF OTHR applications, where typical values are $M = 16$ to 32 and $N = 128$ to 256 , this approach is practically useless, simply because of the lack of sufficient training samples needed to adapt the system.

With the goal of overcoming these limitations of the standard approach, this study has investigated the theoretical existence of slow-time-varying fast-time spatio-temporal filters that can provide high hot-clutter rejectability and stationarity of the hot-clutter scalar output signal. We have demonstrated that for a particular multivariate scalar low-order AR model of the cold clutter, data-dependent (“stochastic”) constraints can retain the stationarity of the cold-clutter scalar output.

Operational routines that implement the main principles of the proposed theoretic SC STAP were then introduced (in the context of HF OTHR applications). Here the *a priori* known distinctions between the hot- and cold-clutter distributions in range are exploited. More specifically, the ranges that are always free of cold clutter (in pulse-waveform radar systems) are utilized for accurate hot-clutter covariance matrix estimation. The efficiency of the SC STAP approach has been demonstrated by simulations, conducted for typical HF OTHR scenarios.

These simulations have demonstrated the high efficiency of the SC STAP algorithm, both in hot-clutter rejection and in cold-clutter post-processing.

Finally, real sky-wave and surface-wave OTHR sea-scattered data has been processed in order to show that a simple AR model of the cold clutter can be used locally over a small number of adjacent PRIs in forming stochastic constraints, despite the fact that real cold clutter is globally far from being properly described by this model.

Thus, for typical HF OTHR applications the proposed SC STAP method is verified. The performance achieved comes at a considerable computation cost: each range cell should be processed by an individual STAP filter that should be updated each PRI, ideally. Obviously, each finger-beam requires an individual set of SC STAP filters. Nevertheless, for HF OTHR with a modest number of range cells and a comparatively low bandwidth, this computational load is reasonable.

References

- [1] A.A. Kolosov, *Over-the-horizon radar*, Artech House, Boston, 1987, English translation by W.F. Barton.
- [2] T.M. Blake, “Ship detection and tracking using high frequency surface wave radar,” in *Proc. 7th Int. Conf. on HF Radio Systems and Techniques*, 1997, pp. 291–295.
- [3] Y.I. Abramovich, F.F. Yevstratov, and V.N. Mikhaylyukov, “Experimental investigation of efficiency of adaptive spatial unpremeditated noise compensation in HF radars for remote sea surface diagnostics,” *Soviet Journal of Communication Technology and Electronics*, vol. 38 (10), pp. 112–118, 1993, English translation of *Radioteknika i Elektronika*.
- [4] R. Fante and J.A. Torres, “Cancellation of diffuse jammer multipath by an airborne adaptive radar,” *IEEE Trans. Aero. Elect. Sys.*, vol. 31 (2), pp. 805–820, 1995.
- [5] D. Marshall and R. Gavel, “Simultaneous mitigation of multipath jamming and ground clutter,” in *Proc. Adaptive Sensor Array Processing Workshop*, MIT Lincoln Laboratory, 1996, vol. 1, pp. 193–239.
- [6] Y.I. Abramovich, V.N. Mikhaylyukov, and I.P. Malyavin, “Stabilisation of the autoregressive characteristics of spatial clutters in the case of nonstationary spatial filtering,” *Soviet Journal of Communication Technology and Electronics*, vol. 37 (2), pp. 10–19, 1992, English translation of *Radioteknika i Elektronika*.
- [7] Y.I. Abramovich, A.Y. Gorokhov, V.N. Mikhaylyukov, and I.P. Malyavin, “Exterior noise adaptive rejection for OTH radar implementations,” in *Proc. ICASSP-94*, Adelaide, 1994, vol. 6, pp. 105–107.
- [8] Y.I. Abramovich and A.Y. Gorokhov, “Adaptive OTHR signal extraction under nonstationary ionospheric propagation conditions,” in *Proc. RADAR-94*, Paris, 1994, pp. 420–425.
- [9] L.J. Griffiths, “Linear constraints in hot clutter cancellation,” in *Proc. ICASSP-96*, Atlanta, 1996, vol. 2, pp. 1181–1184.
- [10] Y.I. Abramovich and S.A. Zaytsev, “One interpretation of the optimum algorithm for the detection of a signal masked by distributed interfering reflections,” *Radio Eng. Electron. Phys.*, vol. 24 (5), pp. 25–32, 1979.
- [11] Y.I. Abramovich and V.G. Kachur, “Characteristics of adaptive spatial clutter rejection,” *Radio Eng. Electron. Phys.*, vol. 28 (9), pp. 57–64, 1983.
- [12] A.Y. Gorokhov and P. Loubaton, “Subspace based techniques for blind separation of convolutive mixtures with temporally correlated sources,” *IEEE Trans. on Circuits and Systems – I*, vol. 44 (9), pp. 813–820, 1997.
- [13] S. Haykin, *Adaptive Filter Theory*, Prentice Hall, New Jersey, 1996, 3rd edition.

- [14] K. Abed-Meraïm *et al.*, “Prediction error methods for time domain blind identification of multichannel FIR filters,” in *Proc. ICASSP-95*, Detroit, 1995, pp. 1968–1971.
- [15] Y.I. Abramovich, N.K. Spencer, S.J. Anderson, and A.Y. Gorokhov, “Stochastic-constraints method in nonstationary hot-clutter cancellation — Part I: Fundamentals and supervised training applications,” *IEEE Trans. Aero. Electr. Sys.*, vol. 34 (4), pp. 1271–1292, 1998.
- [16] J.D. Mallet, I.S. Reed, and L.E. Brennan, “Rapid convergence rate in adaptive arrays,” *IEEE Trans. Aero. Electr. Sys.*, vol. 10 (6), pp. 853–863, 1974.
- [17] Y.I. Abramovich, “A controlled method for adaptive optimization of filters using the criterion of maximum SNR,” *Radio Eng. Electron. Phys.*, vol. 26 (3), pp. 87–95, 1981.
- [18] Y.I. Abramovich and A.I. Nevrev, “An analysis of effectiveness of adaptive maximization of the signal-to-noise ratio which utilizes the inversion of the estimated correlation matrix,” *Radio Eng. Electron. Phys.*, vol. 26 (12), pp. 67–74, 1981.
- [19] O.P. Cheremisin, “Efficiency of adaptive algorithms with regularised sample covariance matrix,” *Radio Eng. Electron. Phys.*, vol. 27 (10), pp. 69–77, 1982.
- [20] C.H. Gierull, “Performance analysis of fast projections of the Hung–Turner type for adaptive beamforming,” *Signal Processing (Eurosip special issue on Subspace Methods for Detection and Estimation, Part I)*, vol. 50, pp. 17–28, 1996.
- [21] S.M. Kogon, D.B. Williams, and E.J. Holder, “Beamspace techniques for hot clutter cancellation,” in *Proc. ICASSP-96*, Atlanta, 1996, vol. 2, pp. 1177–1180.
- [22] S.J. Anderson, S.E. Godfrey, and S.M. Wright, “On model identification for distortion correction of OTH radar,” in *Proc. ICASSP-94*, Adelaide, 1994, vol. 6, pp. 129–132.
- [23] D.E. Barrick and J.B. Snider, “The statistics of HF sea-echo Doppler spectra,” *IEEE Trans. Ant. Prop.*, vol. 25 (1), pp. 19–28, 1977.

	Mode 1	Mode 2	Mode 3	Mode 4
jammer direction-of-arrival ($\theta^{1\ell}$) (degrees)	0.5	20.5	39.3	44.9
hot-clutter-to-noise ratio (HCNR) (dB)	30	25	20	35
temporal correlation coefficient ($\rho^{1\ell}$)	1.00	0.90	0.88	0.91
spatial correlation coefficient ($\zeta^{1\ell}$)	1.00	0.91	0.90	0.90

Table 1: Hot clutter simulation parameters.

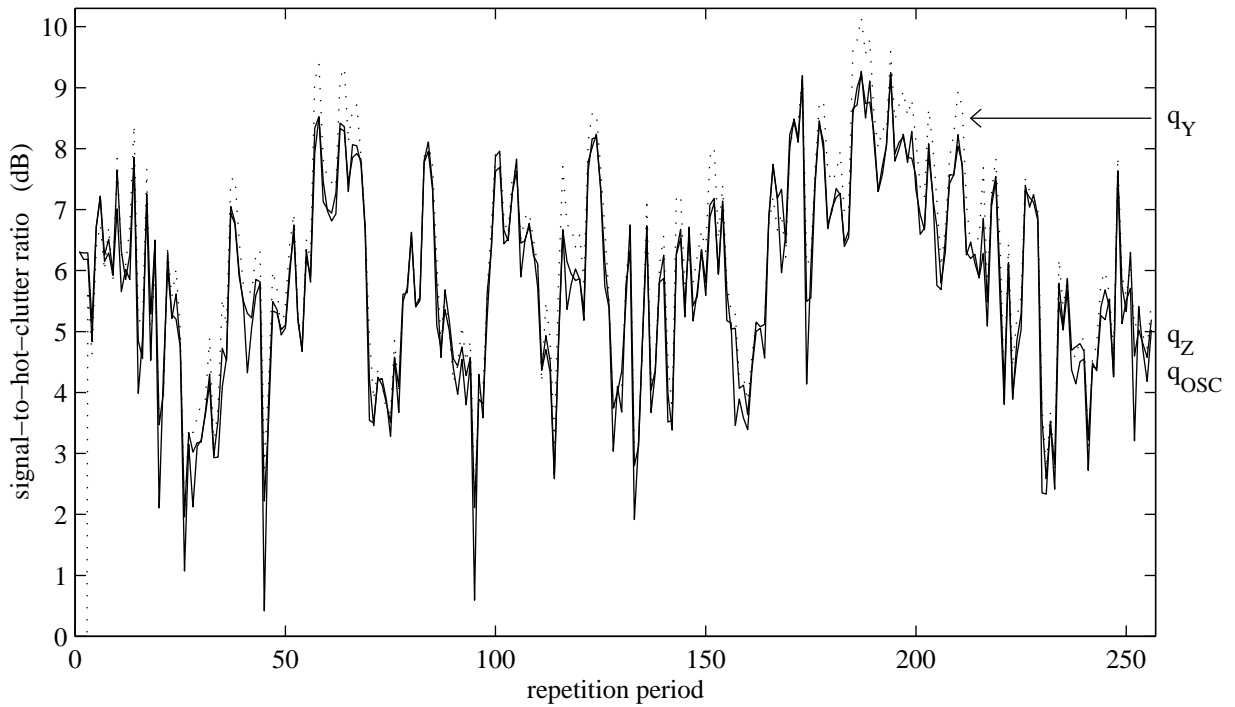


Figure 1: Several stages in the SHRC analysis of the SC STAP operational routine.

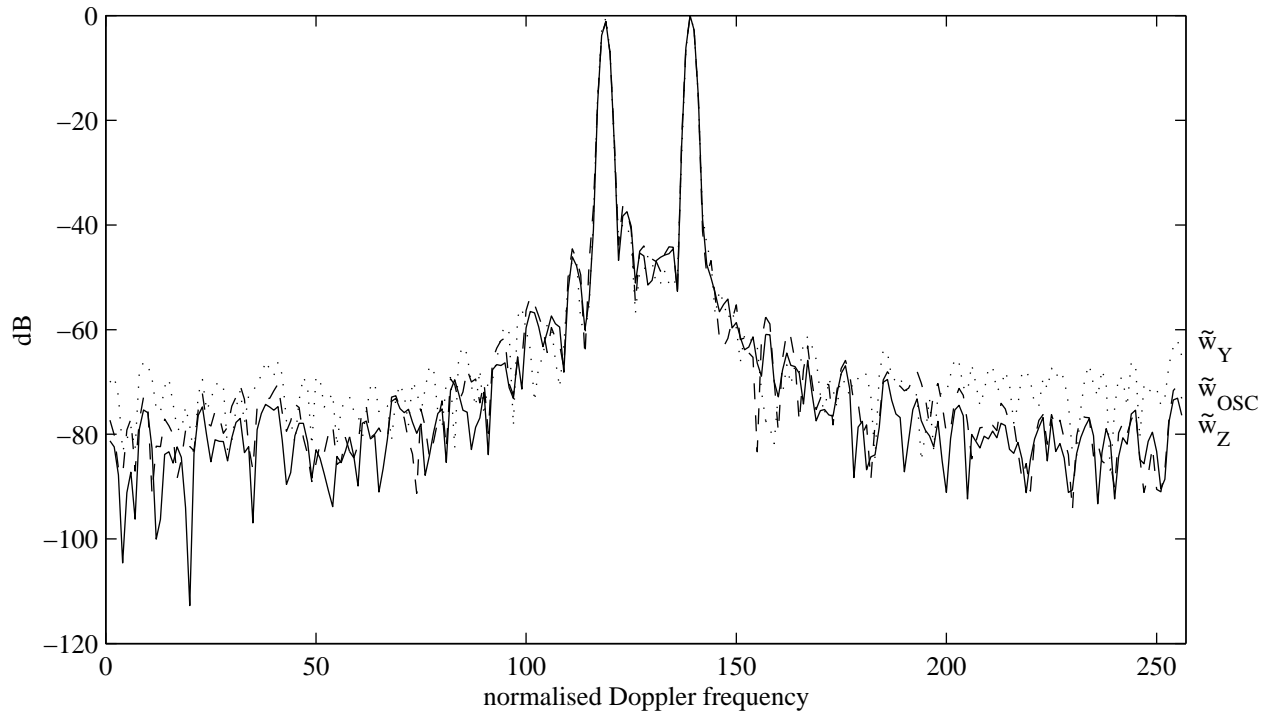


Figure 2: Several stages in the analysis of the weighted FFT Doppler spectra for a range cell containing only cold clutter.

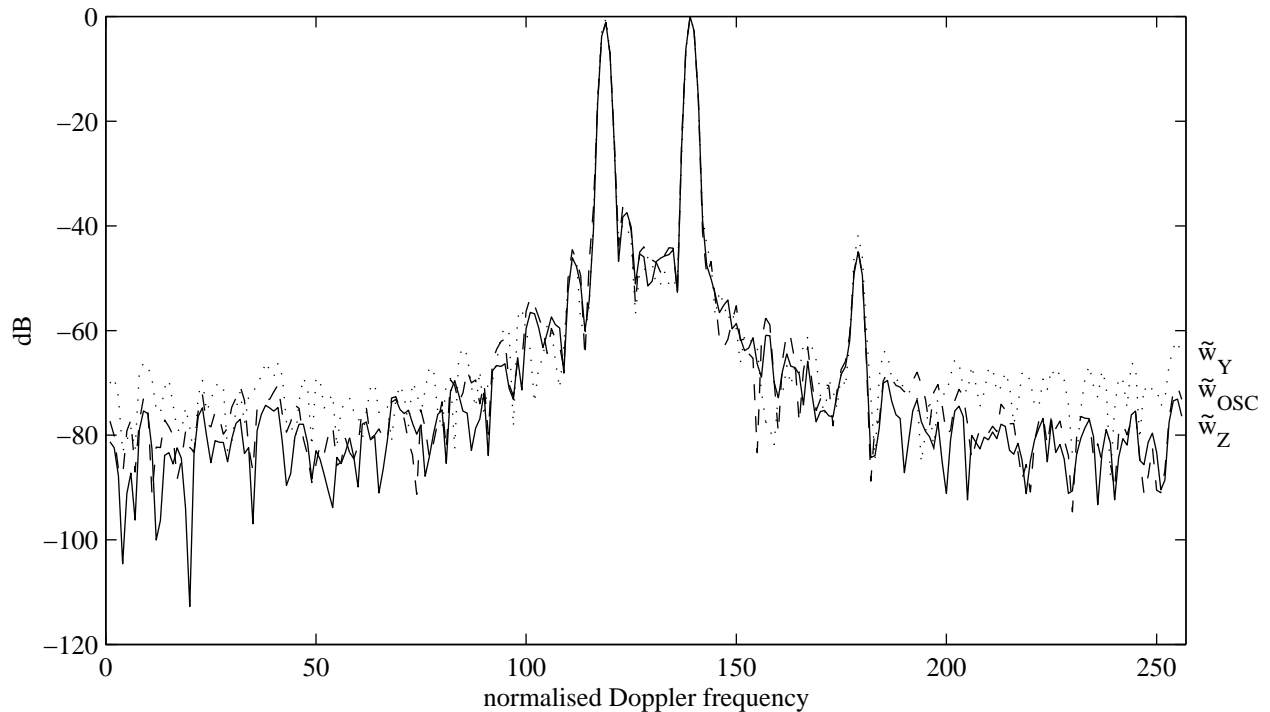


Figure 3: Identical simulation parameters as for Fig. 2, but with a target present.

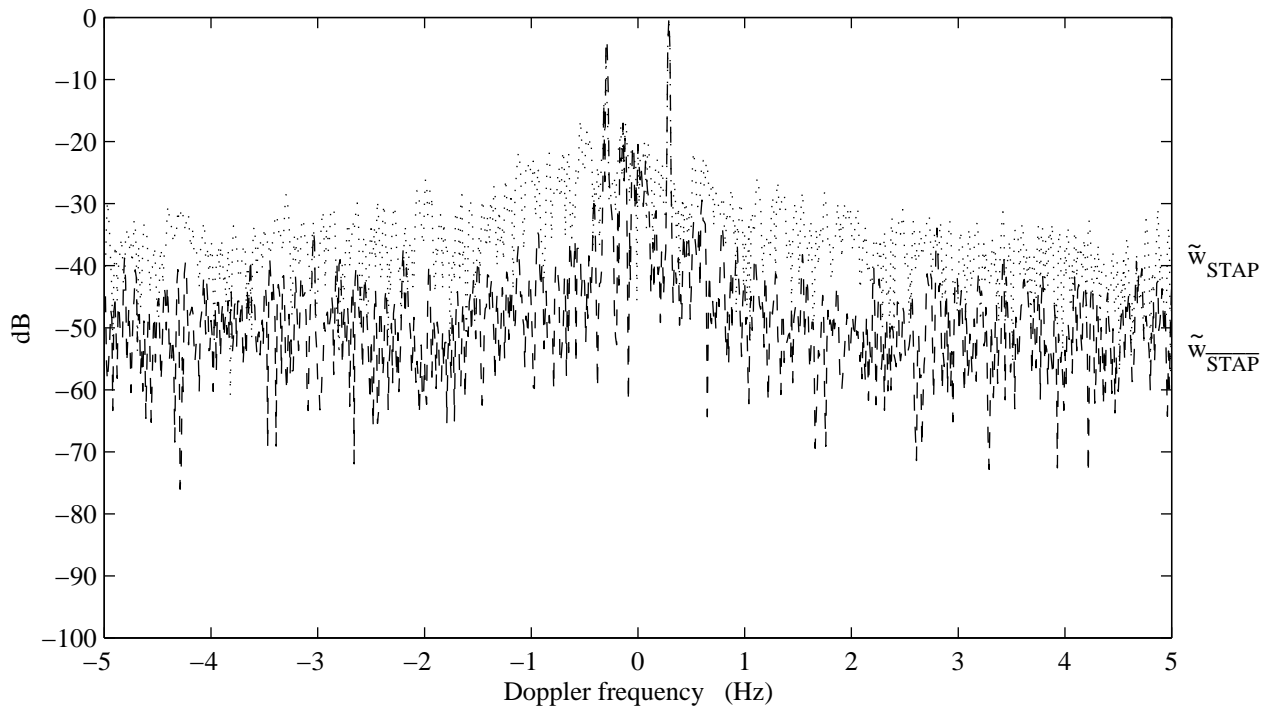


Figure 4: Real SW Doppler spectra processed by two different filters.

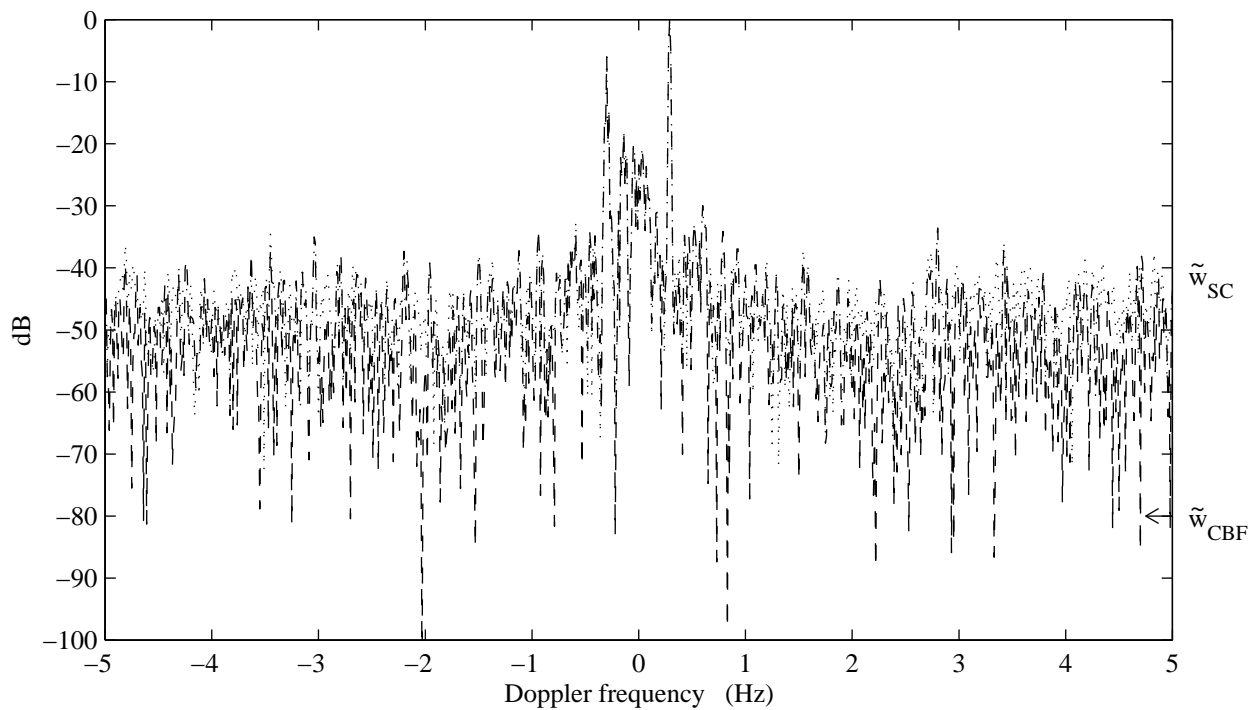


Figure 5: Identical real-data as in Fig. 4, processed by two further filters.

LIST OF MAJOR NOTATION

$I_n \in \mathcal{R}^{n \times n}$ = identity matrix

$\delta(m, n)$ = generalized Kronecker delta function

$\mathbf{e}_n \in \mathcal{R}^{n \times 1} = [1, 0, \dots, 0]^T$

N = number of transmitted pulses or sweeps = number of repetition periods

$k = 1, \dots, N$ = slow-time index variable

f_r = pulse repetition frequency (pulses per second)

M = number of antenna array sensors

f_t = Nyquist rate at which receiver outputs are sampled (samples per second)

T = samples per pulse repetition interval (PRI)

$t = 1, \dots, T$ = fast-time index variable

Q = number of fast-time taps

$\mathbf{z}_{kt} \in \mathcal{C}^{M \times 1}$ = antenna array snapshot for the k^{th} repetition period and the t^{th} range bin

$\mathbf{s}_{kt} \in \mathcal{C}^{M \times 1}$ = target signal

$\mathbf{y}_{kt} \in \mathcal{C}^{M \times 1}$ = cold clutter

$\mathbf{x}_{kt} \in \mathcal{C}^{M \times 1}$ = hot clutter

$\boldsymbol{\eta}_{kt} \in \mathcal{C}^{M \times 1}$ = additive white noise

$\sigma_{\boldsymbol{\eta}}^2 \in \mathcal{R}$ = power of additive white noise

θ_0 = target-signal DOA (degrees)

$\mathbf{s}(\theta_0) \in \mathcal{C}^{M \times 1}$ = antenna array manifold (“steering”) vector for the look direction θ_0

$R_k^{\mathbf{y}} \in \mathcal{H}^{M \times M}$ = cold-clutter spatial covariance matrix at the slow-time lag k

$R_0^{\mathbf{y}} \in \mathcal{H}^{M \times M}$ = standard cold-clutter spatial covariance matrix

P = number of external interference (jamming) signals (index variable $p = 1, \dots, P$)

$g_{kt}^{(p)} \in \mathcal{C}$ = complex waveform representing the p^{th} external interferer (jammer)

L = number of propagating paths for the jammers (index variable $\ell = 1, \dots, L$)

$H_{k\ell} \in \mathcal{C}^{M \times P}$ = instantaneous total impulse response

$\mathbf{g}_{kt} \in \mathcal{C}^{P \times 1}$ = complex waveform vector representing all jammer signals

$\sigma_{\mathbf{x}_p}^2 \in \mathcal{R}$ = the p^{th} jamming signal power

$\tilde{\mathbf{z}}_{kt} \in \mathcal{C}^{MQ \times 1}$ = Q -stacked antenna array snapshot

$\tilde{\mathbf{s}}_{kt} \in \mathcal{C}^{MQ \times 1}$ = Q -stacked target signal snapshot

$\tilde{\mathbf{y}}_{kt} \in \mathcal{C}^{MQ \times 1}$ = Q -stacked cold clutter snapshot

$\tilde{\mathbf{x}}_{kt} \in \mathcal{C}^{MQ \times 1}$ = Q -stacked hot clutter snapshot

$\tilde{\mathbf{w}}_{kt} \in \mathcal{C}^{MQ \times 1}$ = Q -stacked STAP filter

$\tilde{H}_{k\ell} \in \mathcal{C}^{MQ \times P(L+Q-1)}$ = Q -stacked instantaneous total impulse response matrix

$\tilde{\mathbf{g}}_{kt} \in \mathcal{C}^{P(L+Q-1) \times 1}$ = Q -stacked jammer waveform vector

$\tilde{R}_k^{\mathbf{x}} \in \mathcal{H}^{MQ \times MQ} = Q\text{-blocked noise-free hot-clutter spatio-temporal covariance matrix}$
 $z_{kt} \in \mathcal{C} = \text{output from the } Q\text{-stacked STAP filter applied to the } Q\text{-stacked array snapshot}$
 $s_{kt} \in \mathcal{C} = \text{output from the } Q\text{-stacked STAP filter applied to the } Q\text{-stacked target signal}$
 $y_{kt} \in \mathcal{C} = \text{output from the } Q\text{-stacked STAP filter applied to the } Q\text{-stacked cold clutter}$
 $x_{kt} \in \mathcal{C} = \text{output from the } Q\text{-stacked STAP filter applied to the } Q\text{-stacked hot clutter}$
 $q = \text{number of linear constraints imposed on the } Q\text{-stacked STAP filter}$
 $\tilde{A}_q \in \mathcal{C}^{MQ \times q} = Q\text{-stacked general deterministic linear constraint matrix}$
 $\kappa = \text{order of the cold-clutter AR model}$
 $B_j \in \mathcal{C}^{M \times M} = \text{cold-clutter AR model parameters} = \text{Yule-Walker solutions } (j = 1, \dots, \kappa)$
 $\xi_{kt} \in \mathcal{C}^{M \times 1} = \text{innovative noise in AR model}$
 $R_k^{\boldsymbol{\xi}} \in \mathcal{H}^{M \times M} = \text{innovative noise spatial covariance matrix}$
 $\tilde{B}_j \in \mathcal{C}^{MQ \times MQ} = Q\text{-blocked cold-clutter AR model parameters}$
 $\tilde{\xi}_{kt} \in \mathcal{C}^{MQ \times 1} = Q\text{-stacked innovative noise in AR model}$
 $\tilde{R}_k^{\boldsymbol{\xi}} \in \mathcal{H}^{MQ \times MQ} = Q\text{-blocked innovative noise spatial covariance matrix}$
 $\tilde{w}_0 \in \mathcal{C}^{MQ \times 1} = \text{any given constant } Q\text{-stacked STAP filter}$
 $y_{kt}^{(0)} \in \mathcal{C} = \text{cold-clutter scalar output for the above filter}$
 $\tilde{R}_k^{\mathbf{x}\boldsymbol{\eta}} \in \mathcal{H}^{MQ \times MQ} = Q\text{-blocked hot-clutter-plus-noise covariance matrix}$
 $\tilde{s}(\theta_0) \in \mathcal{C}^{MQ \times 1} = Q\text{-stacked steering vector for the look direction } \theta_0$
 $\tilde{Y}_{kt} \in \mathcal{C}^{MQ \times \kappa} = Q\text{-stacked stochastic-constraints matrix}$
 $\tilde{A}_{kt} \in \mathcal{C}^{MQ \times (\kappa+q)} = \text{ideal augmented linear stochastic constraints matrix (cold clutter only)}$
 $b_j \in \mathcal{C} = \text{cold-clutter (simplified scalar) AR model parameters}$
 $r_j \in \mathcal{C} = \text{correlation coefficients of the (simplified scalar) cold-clutter process}$
 $\sigma_{\boldsymbol{\xi}}^2 \in \mathcal{R} = \text{power of the innovative noise in the (simplified scalar) AR model}$
 $\tilde{w}_{kt}^{av} \in \mathcal{C}^{MQ \times 1} = \text{stochastically unconstrained STAP filter (hot-clutter-plus-noise only)}$
 $\tilde{R}_k^{av} \in \mathcal{C}^{MQ \times MQ} = \text{moving-window average of hot-clutter-plus-noise-only samples}$
 $\tilde{A}_{kt}^z \in \mathcal{C}^{MQ \times (\kappa+q)} = \text{operational augmented linear stochastic constraints matrix}$
 $J = \text{order of the generalized Watterson model for ionospherically propagated hot clutter}$
 $\rho^{p\ell} = \text{temporal correlation coefficient}$
 $\zeta^{p\ell} = \text{spatial correlation coefficient}$
 $K = \text{number of PRIs involved in averaging}$

This page has been deliberately left blank

Page intentionnellement blanche

STAP Architectures and Limiting Effects

Richard Klemm

FGAN-FHR, Neuenahrer Str. 20, D 53343 Wachtberg, Germany

Tel +49 228 9435 377; Fax +49 228 9435 618; email r.klemm@fgan.de

Abstract

Detection of slowly moving targets by air- and spaceborne MTI radar is heavily degraded by the motion induced Doppler spread of clutter returns. Space-time adaptive processing (STAP) can achieve optimum clutter rejection via implicit platform motion compensation. In this paper suboptimum receiver architectures are described. The impact of various radar parameters on the performance of STAP processors is demonstrated. Some aspects of jammer suppression will be touched on. The report concludes with an outlook on current and future research topics.

1 Suboptimum Processor Architectures

1.1 Pre-Doppler Techniques

1.1.1 Remarks on Clutter Subspace Techniques

In practice the space-time covariance matrix is not known but has to be estimated from received clutter data. Estimating and inverting the covariance matrix is commonly called the "sample matrix inverse" method (SMI). Due to its complexity SMI is of no value for most applications. It may also suffer from weak convergence in estimating the covariance matrix. There are several ways of reducing the computational workload and accelerating the convergence of adaption. Some of these techniques are listed here briefly. More details of several receiver architectures are given in the paper by WARD in this volume.

1.1.2 Rank reducing techniques

Rank reduction can be obtained by replacing \mathbf{Q}^{-1} in the optimum processor (see (19) in [30]) by a projection matrix orthogonal to the interference subspace (equ. 21 in [30]). Eigenvalue decomposition or Gram-Schmidt factorization are well-known tools. These subspace techniques show more rapid convergence than the SMI method. However, the computational load for filtering the actual data is not reduced since the order of the matrix is maintained (Ayoub [18]).

1.1.3 Order reducing techniques (pre-Doppler)

Order reducing technique reduce the signal and interference vector space before applying the SMI technique. Some of these techniques have been described by the author [26, Chapters 5-6, 9].

1.1.4 Space-Time Transforms

The original $N \times M$ vector space (N number of sensors, M number of echo pulses) is reduced by a linear transform. This transform may consist of the clutter eigenvectors obtained from a pre-calculated "typical" covariance matrix. Alternatively a bunch of beams can be formed so as to cover the whole azimuth range, each of them cascaded with a Doppler filter matched to the clutter Doppler in look direction. In both cases auxiliary channels are formed which are well matched to the interference. Both techniques have the disadvantage that the computational load increases with N and M . Moreover, they show little tolerance against channel errors and bandwidth effects.

Figure 1 shows the principle of the auxiliary channel processor (ACP). One recognises the footprints of various search channels in the look direction (where the clutter maximum shows up) which differ in their target Doppler. Along the clutter spectrum one finds the footprints of auxiliary channels which point in different

directions and at different Doppler frequencies. A block diagram of the processor is shown in Figure 2. In Figure 3 it is demonstrated what happens if the number of channels is reduced below the wellknown rule $N_E = N + M - 1$. Just a small reduction from 48 down to 40 channels results in a strong degradation of the detectability of low Doppler targets. In conclusion, space-time transform architectures are still quite costly and may not be the optimum solution.

1.1.5 Spatial Transforms: Simplification in the Spatial Dimension

Spatial transforms can be obtained by forming subarrays to reduce the number of antenna channels (spatial dimension) and applying the SMI (or projection technique) at subarray level. Alternatively, a symmetric sidelobe canceller concept may be used. For certain antenna arrays configurations (especially linear, rectangular planar or, in general, horizontal cylindrical arrays) both techniques lead to near optimum clutter rejection performance at dramatically reduced computational expense.

For illustration consider Figure 4. It shows the evolution from a linear array via overlapping subarrays to a symmetric sidelobe canceller type of architecture. Notice, that in subfigure c. the sum above the dashed line includes all sensors which are common to *all* subarrays in b. In Figure 5 an implementation of planar patch arrays (rectangular, circular) is indicated. The black patches are part of the main beam while the white and the hatched patches form the auxiliary channels. Figure 6 shows the IF for the overlapping subarry processor according to Figure 4b. As can be seen, for two channels some degradation close to the clutter notch can be noticed. For higher numbers of channels the IF is nearly independent of the number of channels. This is a desirable property.

1.1.6 The Space-Time FIR Filter: Simplification in the Time Dimension

If the PRF is constant during the coherent processing interval space-time FIR filters can obtain near optimum clutter rejection at minimum cost. In conjunction with spatial transforms very efficient¹ space-time processors can be designed. The advantage of the FIR filter concept is that filtering can be accomplished in a pipeline mode as the echo pulses come in. The required number of calculations for filtering can be realised easily with nowadays digital technology. Because the temporal filter length can be very small the filter may be able to cope with non-stationarities caused by platform manueuvres (s. RICHARDSON [36]) or staggered PRF by adaptation during the CPI.

Figure 7 shows the principle of a space-time FIR filter processor, details of the processor are given in Figure 8. In Figure 10 the clutter rejection performance of a FIR filter processor with the optimum space-time processor is compared. The FIR filter processor almost reaches the performance of the optimum processor, except for a small integration loss in the passband which is due to the shortening of the data sequence. The FIR filter must not slide over the edges of the data record, therefore the number of available data reduces to $M - L + 1$ where M is the number of echoes and L the number of temporal filter coefficients.

Figure 9 shows a processor architecture according to Figure 5c (symmetric auxiliary channel processor). The performance of this processor combines the properties of an overlapping subarray processor discussed before with those of the FIR filter.

A FIR filter processor is based on the assumption that the clutter echoes are stationary. This requires in particular that the PRF is constant. If the PRF is not constant because of staggering the FIR filter becomes time dependent. That means, the filter coefficients have to be adapted with each (irregular) pulse repetition interval (KLEMM [29]). The space-time submatrix chosen for calculating the FIR filter coeffients have to be selected for each PRI anew. Figure 11 illustrates how the sliding covariance submatrices relate to the total $N \times M$ (or $K \times M$) covariance matrix. The fat lines indicate which submatrix is associated with a certain step of the filter operation.

¹minimum number of space-time filter coefficients: 4

Figure 12 shows a numerical example. Notice that the abssissa extends between $-2B_c \dots 2B_c$ (four times the clutter bandwidth). Figure 12a shows the Doppler response of a space-time FIR filter with constant constant coefficients used an echo sequence with constant PRI. Ambiguous clutter notches can be noticed. In Figure 12b we used a pseudorandom stagger code. The plot shows the IF achieved by the optimum processor when the PRI is staggered. The ambiguities are removed at the expense of a slight decrease in IF and a little ripple close to the clutter notch. Applying a FIR filter to clutter data with staggered PRI leads to heavy losses in IF (Figure 12c). Matching the FIR filter coefficients to the stagger code by readapting at each PRI gives a reasonable clutter suppression (Figure 12d). The loss compared with the optimum processor (Figure 12b) is about 3 dB. The width of the clutter notch is slightly broadened.

1.1.7 Temporal FIR Filtering after Data Projection

Figure 14 shows the output signals of a moving array due to a stationary source (clutter patch) which causes a spatial frequency across the array. This frequency corresponds to the direction of the source. As can be seen the frequency modulation is fixed in space while the array is moving. The array spacing and the PRF can be chosen in such a way that all signals projected onto a common time axis form an equidistant time series (see the lowest subfigure). For clutter the frequency is bandlimited according to the spatial limits in azimuth $0^\circ \dots 180^\circ$. For a moving target higher frequency components occur as can be seen in Figure 15. It is obvious that clutter rejection can be carried out by a simple high pass filter.

1.2 Post-Doppler Techniques

1.2.1 Frequency domain (post-Doppler) approaches

There are several ways of performing interference cancellation in the frequency domain [46], [26, Chapter 9].

1.2.2 Spatial and Doppler Transforms

The Auxiliary Sensors/Echo Processor (ASEP) applies the symmetric auxliary sensor principle according to Figure 4c in both the spatial and temporal domains, see Figure 13. Now we have $K - 1$ auxiliary sensors (top of figure) and $L - 1$ auxiliary echoes (the white parts in the memory). It can be shown that this processor is very close to the optimum.

1.2.3 Frequency-Dependent Spatial Processing

If the CPI is long (several hundreds of echoes) like for instance in SAR applications the correlation among frequency channels becomes asymptotically zero so that the space-frequency covariance matrix becomes block diagonal. This property can be exploited to reduce the computational cost by omitting spectral cross-terms. Then one ends up with spatial SMI for all individual frequencies. In conjunction with a spatial transform technique this kind of processor can be very efficient. A block diagram is given in Figure 16. Notice that this processor works only for long data sequences as may occur in SAR or HPRF radar whereas the ASEP (see previous section) works independently of the number of echoes. For more details s. WARD [46] and KLEMM [26, Chapter 9].

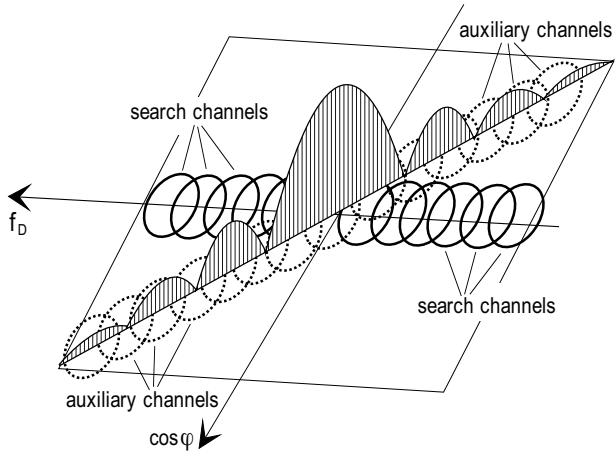


Figure 1: Principle of the auxiliary channel processor (ACP)

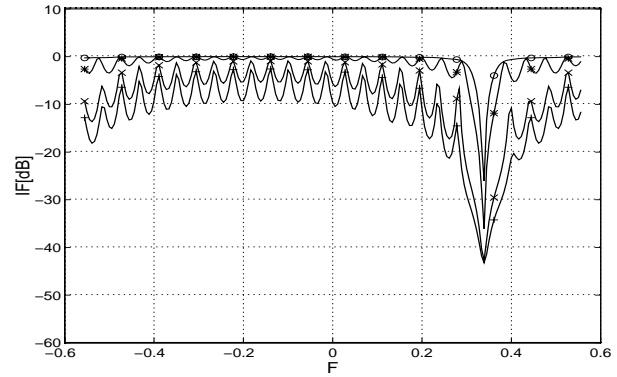


Figure 3: Reduction of the number of channels (FL, ACP): $\circ C = 48$; $*$ $C = 40$; $+ C = 32$; $\times C = 24$

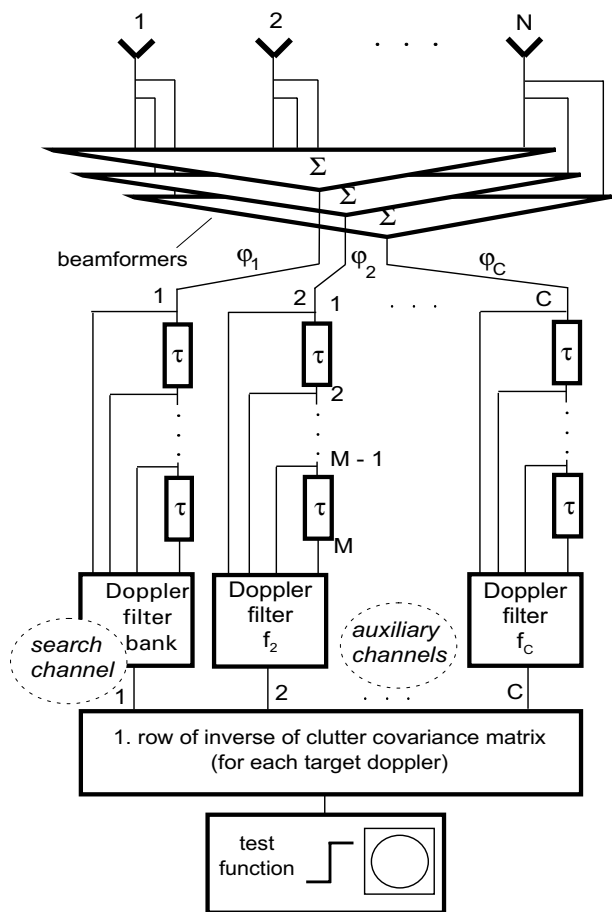


Figure 2: Block diagram of the auxiliary channel processor (ACP)

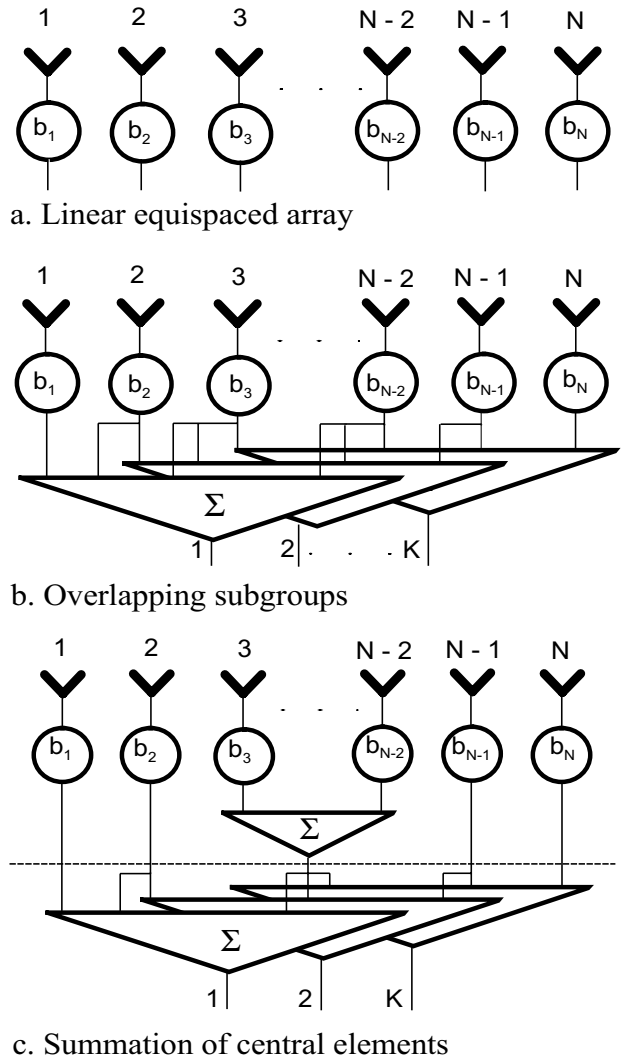


Figure 4: From subarrays to auxiliary elements

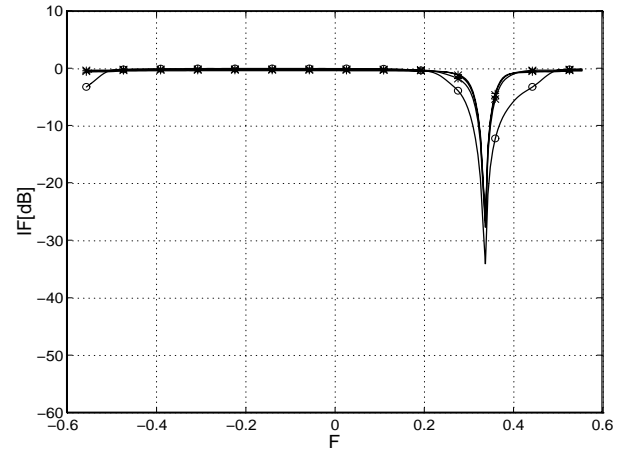
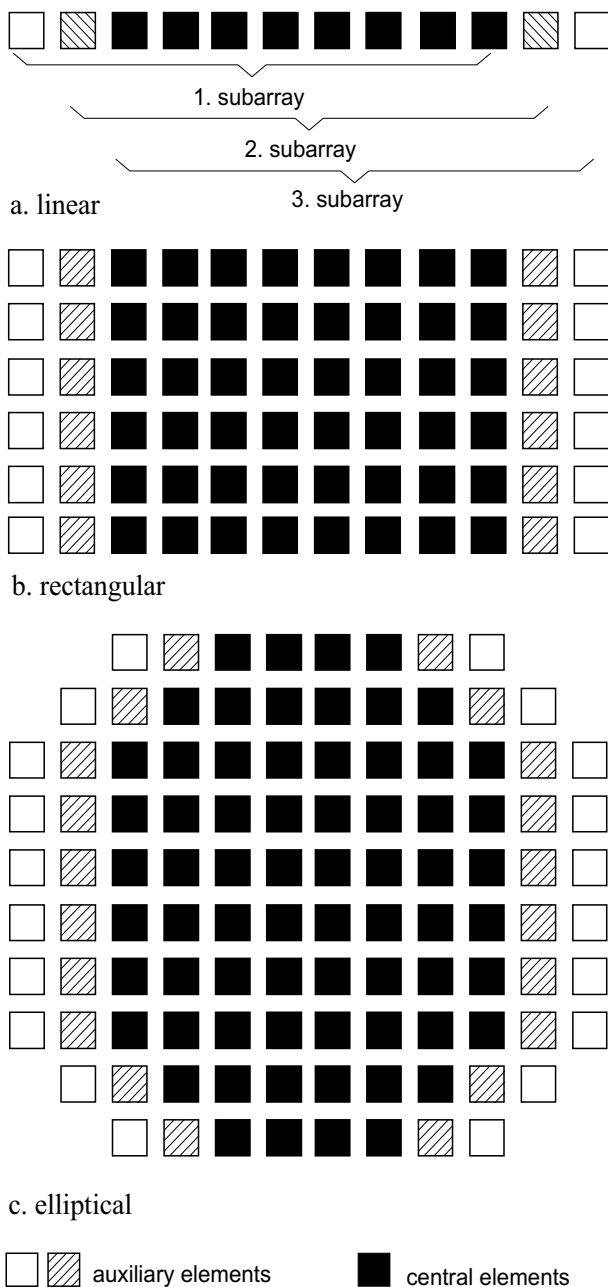


Figure 6: Influence of the number of channels (OUS, FL): $\circ K = 2; * K = 4; \times K = 6; + K = 8$

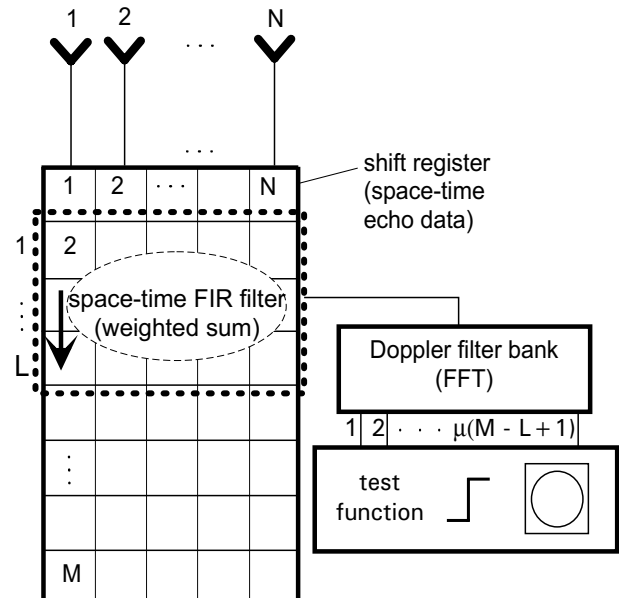


Figure 5: Clutter optimized planar array antennas

Figure 7: Space-time FIR filter processor

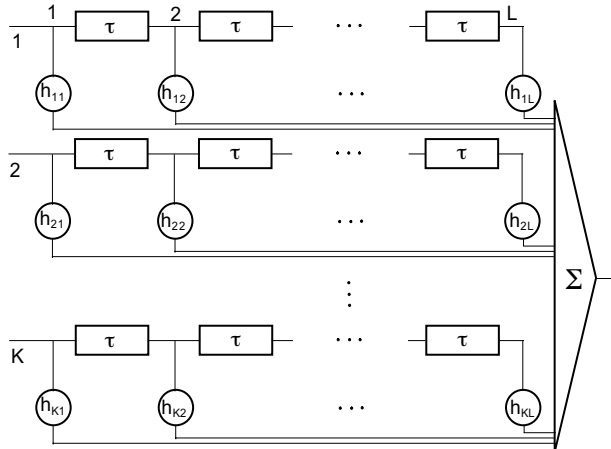


Figure 8: Detailed block diagram of the space-time FIR filter

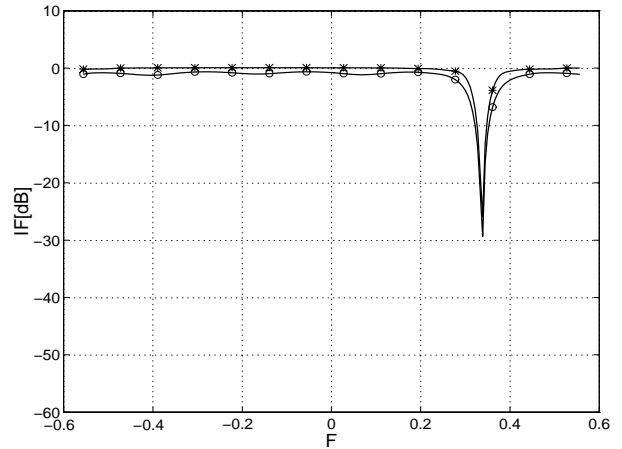


Figure 10: The FIR filter processor (full array, FL): \circ FIR filter processor ($L = 5$); $*$ fully adaptive optimum processor

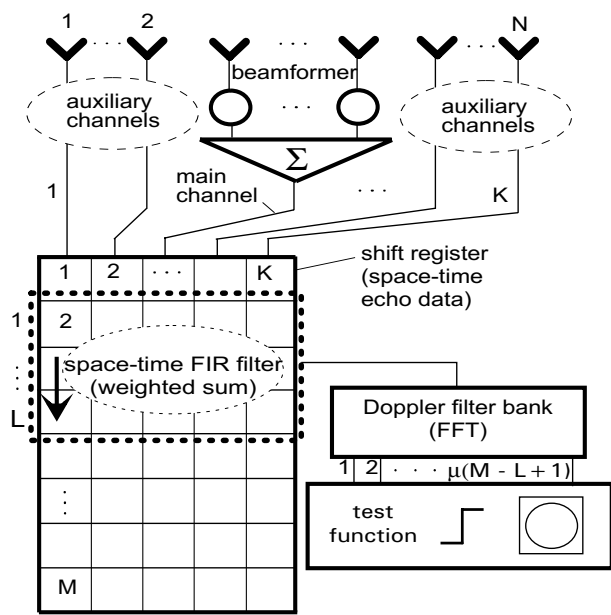


Figure 9: Space-time FIR filter processor with auxiliary element architecture

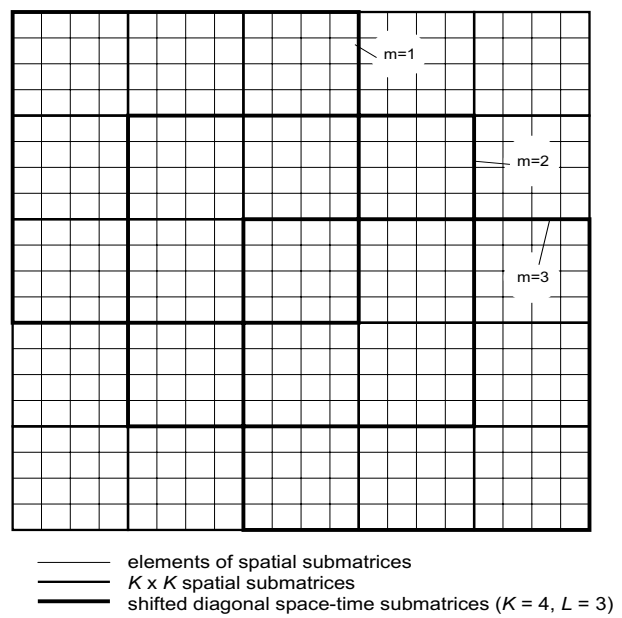


Figure 11: Matrix scheme for space-time FIR filtering,
 $K=4$, $M=5$

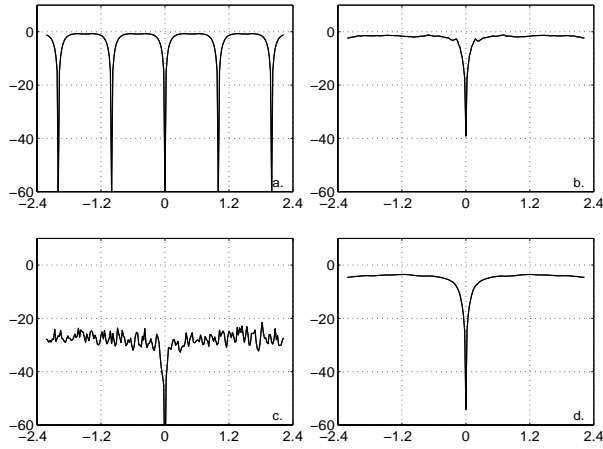


Figure 12: FIR filter with staggered PRI (pseudorandom stagger code, $\epsilon = 0.3$, PRF=3000 Hz, overlapping subarrays). a. no staggering; b. optimum processor with staggered PRI; c. fixed FIR filter with staggered PRI; d. FIR filter with variable coefficients and staggered PRI

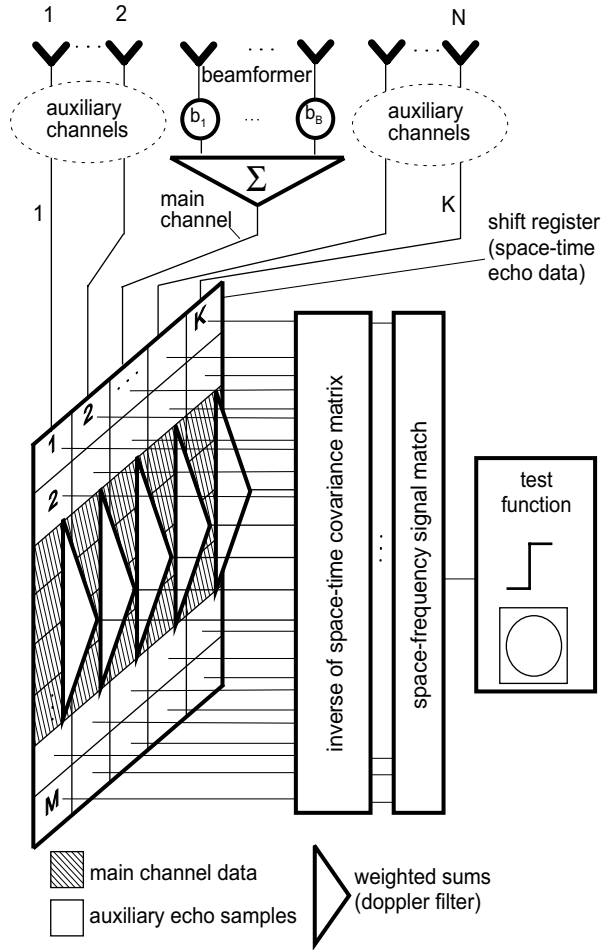


Figure 13: 2-D symmetric auxiliary sensor/echo processor (ASEP)

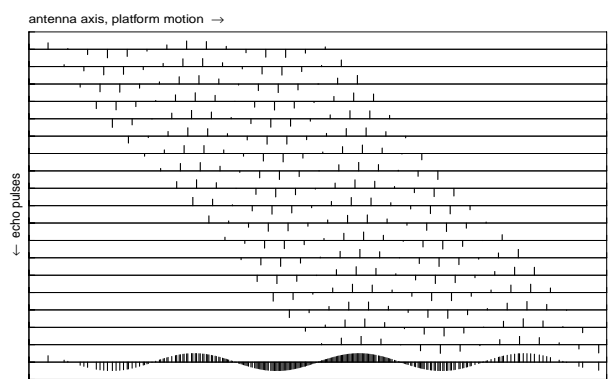


Figure 14: Projection of space-time echo samples onto a common time axis: clutter

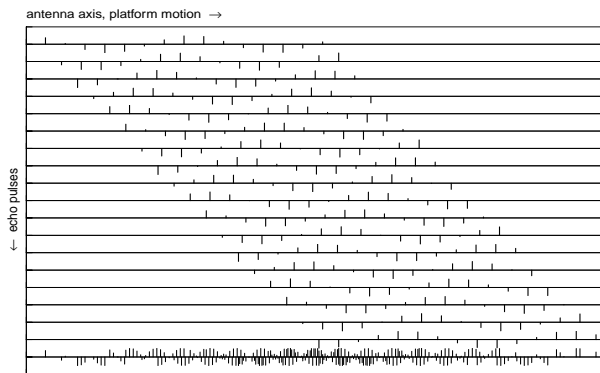


Figure 15: Projection of space-time echo samples onto a common time axis: Doppler target

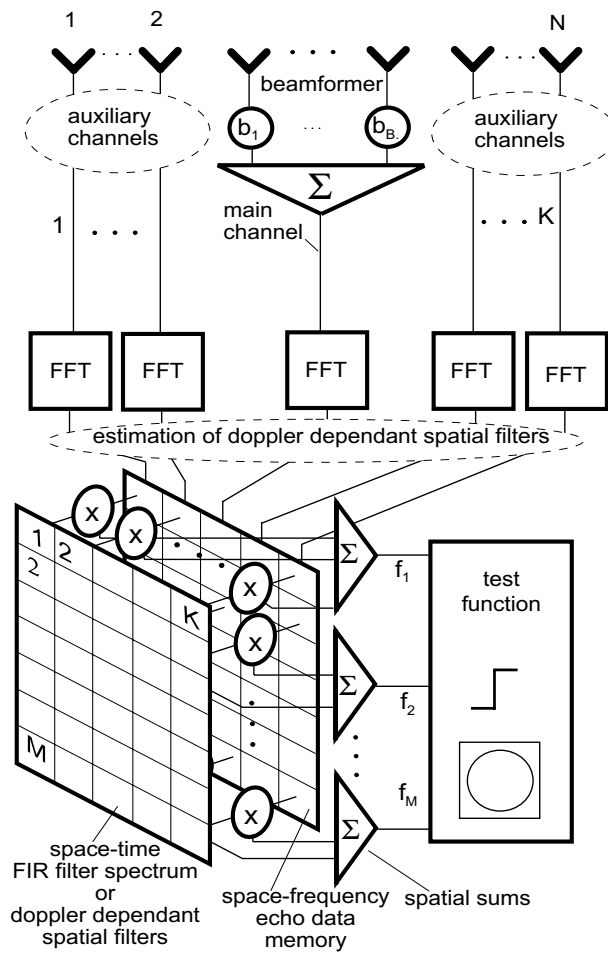


Figure 16: Frequency dependent spatial filter (FDSP)

2 Degrading Effects

2.1 Environmental Effects

2.1.1 Clutter Fluctuation

Internal clutter fluctuations (due to wind or sea state) cause a *temporal* (pulse-to-pulse) decorrelation of clutter echoes. This results in broadening of the clutter spectrum. The effect of clutter fluctuations on the clutter spectrum is shown in Figure 17 for a sidelooking array. Similar results can be expected for a forward looking array.

2.2 Radar Parameters

2.2.1 Effect of System Bandwidth

The system bandwidth causes a *spatial* decorrelation due to travel delays of incoming waves across the array. Therefore, this kind of decorrelation depends on the angle of arrival. It is maximum at endfire and zero at broadside. Moreover, it has been shown that this decorrelation effect does not occur for a sidelooking array. In case a sidelooking array the travel delays are compensated for by the DPCA property (KLEMM & ENDER [22]).

Figure 18 shows the effect of system bandwidth (rectangular frequency response) on the forward looking clutter spectrum. It can be noticed that the spectrum is broadened. The broadening effect is minimum at broadside ($\varphi = 0^\circ$) and becomes maximum towards endfire ($\varphi \pm 90^\circ$).

2.2.2 Effect of Range Walk

Range walk is another effect which can lead to temporal decorrelation of space-time clutter echoes. The influence of range walk on space-time clutter covariance matrices and the associated power spectra has been analysed by KREYENKAMP [33]. The principle of range walk due to radar platform motion is illustrated by Figure 19. It shows two rings of width $R_o - R_i$ which are shifted by

$$d = v_p mT \quad m = 1 \dots M \quad (1)$$

which is the distance the radar passes during the time mT . Both rings denote range bins as seen by the radar at different instances of time.

With the usual assumption that the clutter background consists of a large number of spatially uncorrelated scatterers we can conclude that the correlation between the two instances of time is given by the area where both range rings overlap

$$\rho_{mp}(\varphi) = \frac{\delta_{m-p}(\varphi)}{\Delta_R} \quad m, p = 1 \dots M \quad (2)$$

with $\Delta_R = R_o - R_i$ denoting the width of the range bin. Notice that, opposite to decorrelation by internal clutter motion, the decorrelation due to range walk is azimuth dependant. Obviously the correlation is maximum in the broadsight direction of a sidelooking array (SL) and minimum in forward looking direction (FL).

The distance $\delta(\varphi)$ can be calculated as follows

$$\delta(\varphi) = \sqrt{(x_P(\varphi) - x_Q(\varphi))^2 + (y_P(\varphi) - y_Q(\varphi))^2} \quad (3)$$

where x_P, y_P and x_Q, y_Q are the coordinates of the points P and Q in Figure 19 which can be obtained from simple geometrical relations.

It should be noted that in practice the temporal decorrelation effect due to range walk will be even stronger than described above. The received signal passes normally a bandwidth limiting matched filter so that the output signal is the autocorrelation function of the transmit signal. In case of range walk the individual shape of the matched filter response causes additional decorrelation which depends on the shape of the transmitted

waveform. In the subsequent discussion we omit this aspect and assume that the matched filter response is constant across the range bin.

Figure 20 shows a clutter power spectrum for a forward looking linear array. The effect of range walk can be noticed as ridge in the look direction, i. e., the direction of the transmit beam (here: $\varphi = 45^\circ$). This ridge means, however, a broadening of the spectrum in look direction and, hence a broadening of the associated clutter notch, which in turn means some degradation in low Doppler target detection.

2.2.3 Doppler Spread in Range Gate

For narrowband, i.e., low range resolution radar the range bins may be so large that a Doppler spread inside the range gate becomes significant. This effect will occur only if the clutter Doppler is range dependent, that means, for antenna configurations other than sidelooking. It is shown in Figure 21 (forward looking linear array) that for very low range resolution the Doppler spread effect dominates (a.), that there is an optimum at medium resolution (b.) and for higher resolution the range walk effect dominates (c. and d.).

2.3 Radar Ambiguities

By choosing a certain PRF Doppler and range ambiguities are determined. The effect of both Doppler and range ambiguities is discussed in the sequel.

2.3.1 Doppler Ambiguities

Constant PRF leads to Doppler ambiguities which has two consequences. This means that a Doppler filter bank has an ambiguous frequency response (see upper subfigure in Figure 24) so that the target Doppler can only be estimated modulo PRF. Secondly, the clutter spectrum becomes ambiguous (s. Figure 22) so that ambiguous clutter notches occur (blind velocities). Doppler ambiguities can be avoided by pulse-to-pulse staggering. In Figure 23 we see for example pseudorandom stagger patterns. As can be seen the Doppler responses in Figure 22 become unambiguous, however at the expense of higher Doppler sidelobes. Space-time adaptive processing takes the stagger pattern into account. Figure 25 shows the same clutter spectrum as Figure 24, however with pseudorandom staggering. Except for a small ripple the ambiguities have been removed.

2.3.2 Range Ambiguities

If the pulse repetition frequency ($PRF = \frac{1}{T}$) is chosen so that the radar is range ambiguous the received clutter echo becomes a superposition of clutter components from different ranges. In case of sidelooking radar this does not cause severe problems because all the ambiguous clutter arrivals have the same Doppler frequency. In case of a forward looking radar, however, different arrivals exhibit different Doppler frequencies. This is illustrated in a range-Doppler map² as shown in Figure 26.

The bended curve denotes the trajectory of the primary clutter. Notice the range dependency of the clutter Doppler. The straight line on the right reflects the ambiguous clutter returns. They originate from larger ranges (or: smaller depression angles) and have, therefore, larger Doppler frequencies. It has been shown by the author that the ambiguous clutter portion can be cancelled by "vertical nulling" using a planar array which is adaptive in both dimensions (horizontal and vertical) [24].

Figure 26 shows the ambiguous response of a forward looking linear array. The second clutter notch on the right is due to range ambiguity. Figure 28 shows the same situation, however using a planar 2d adaptive array. As can be noticed the ambiguities have been cancelled.

²This map shows the improvement factor in signal-to-clutter ratio as obtained by optimum processing, s. Chapter 4

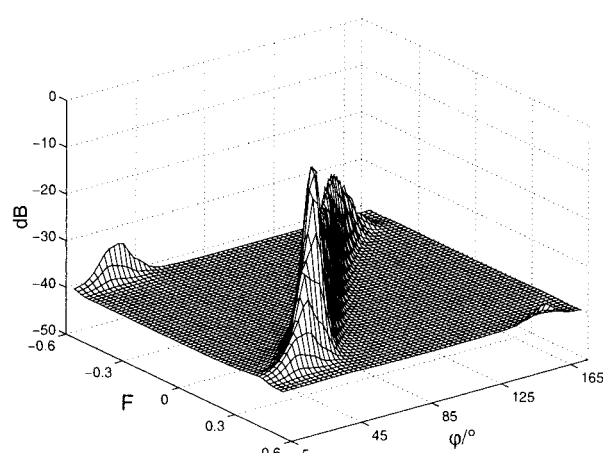


Figure 17: MV spectrum for sidelooking array ($B_c = 0.2$)

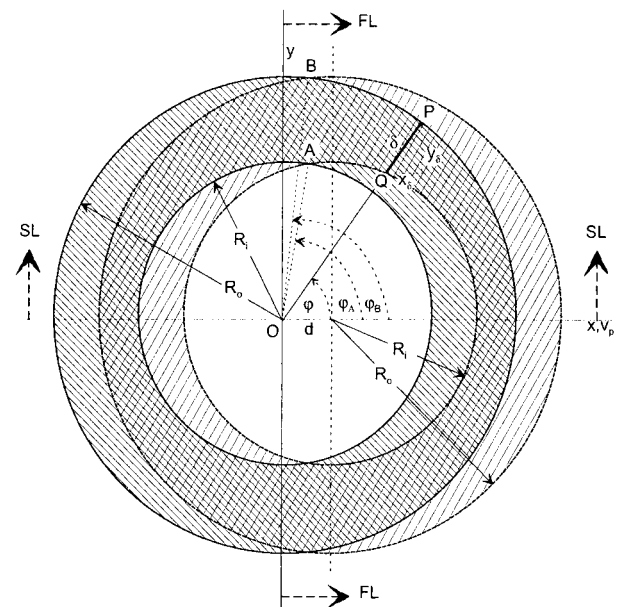


Figure 19: Geometry of range walk (©1999 AEU)

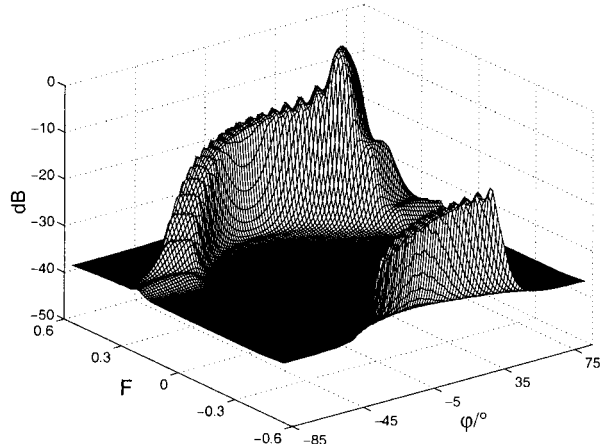


Figure 18: MV spectrum (FL array, rectangular frequency response, $B_s = 0.2$)

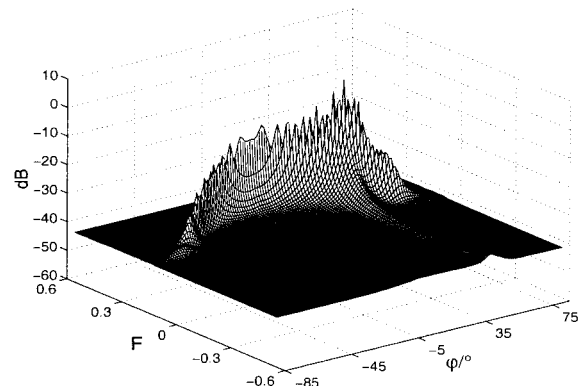


Figure 20: Clutter power spectrum (FL array) with range walk ($\Delta_R = 10m$)

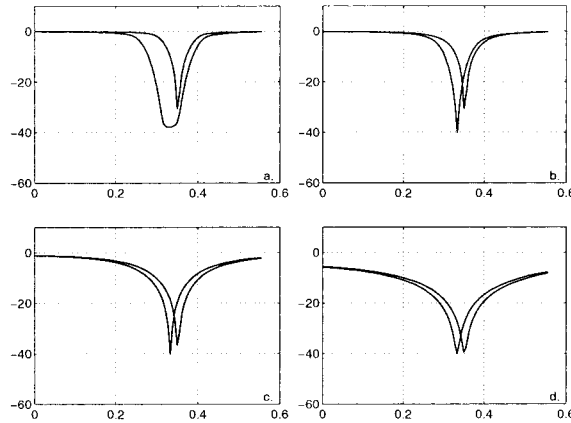


Figure 21: Doppler spread and range walk (IF vs F , FL, $H = 1$ km; left clutter notch: $R_s = 3$ km, right clutter notch: $R_s = 10$ km): a. $\Delta_R = 1500$ m; b. $\Delta_R = 150$ m; c. $\Delta_R = 15$ m; d. $\Delta_R = 1.5$ m

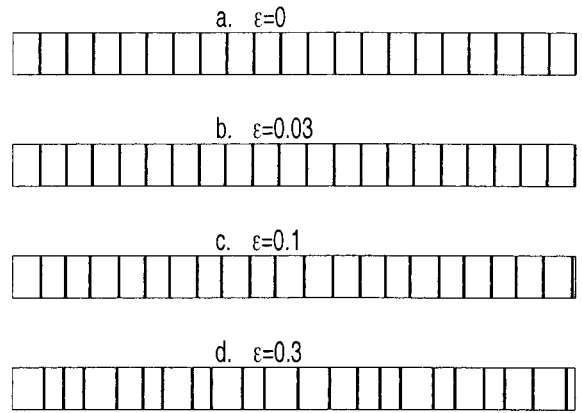


Figure 23: Pseudo-random stagger patterns

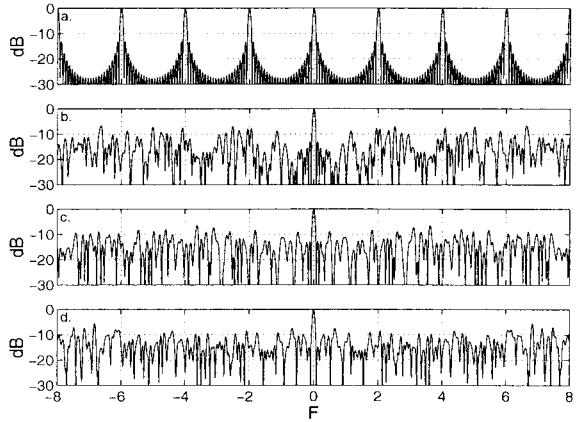


Figure 24: Doppler channel response for pseudo-random staggering: a. $\epsilon = 0$; b. $\epsilon = 0.03$; c. $\epsilon = 0.1$; d. $\epsilon = 0.3$

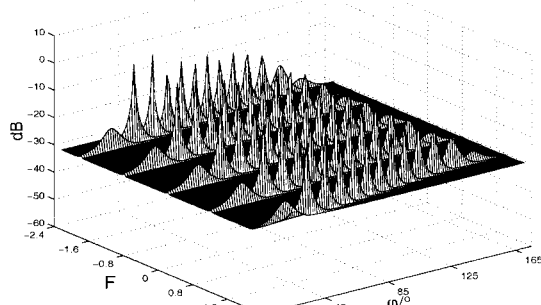


Figure 22: Azimuth-Doppler clutter spectrum without staggering

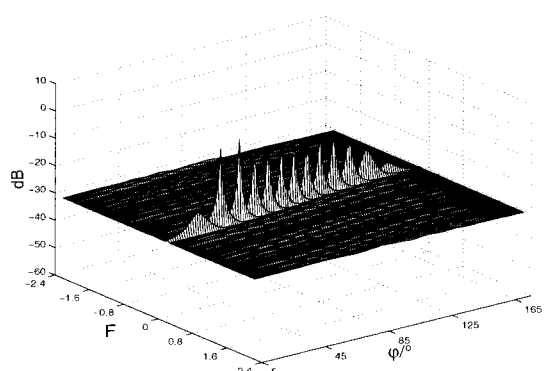


Figure 25: Azimuth-Doppler clutter spectrum with pseudo-random staggering

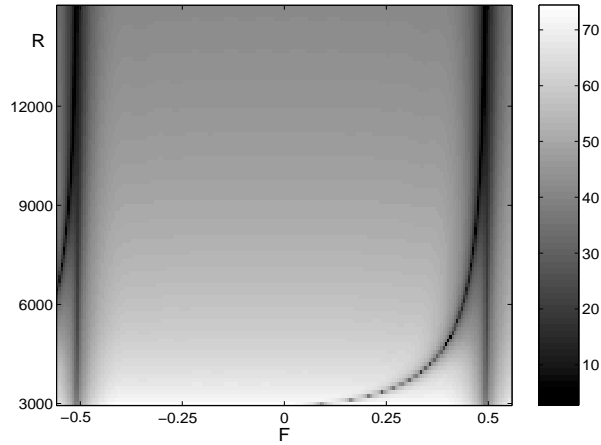


Figure 26: Range-Doppler Matrix (IF[dB] vs R/m and F ; $FL, \varphi_L = 0^\circ$, PRF=Nyquist of clutter band)

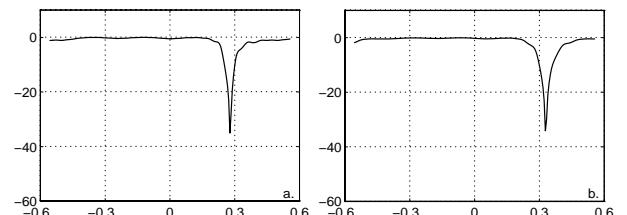


Figure 28: Influence of multiple-time around clutter (IF vs F ; fully adaptive FIR filter processor, planar array with 6 rows of 24 elements each, FL , focused on the first range increment): a. $R_0/H = 1.66$; b. $R_0/H = 3$; c. $R_0/H = 4.33$; d. $R_0/H = 5.66$

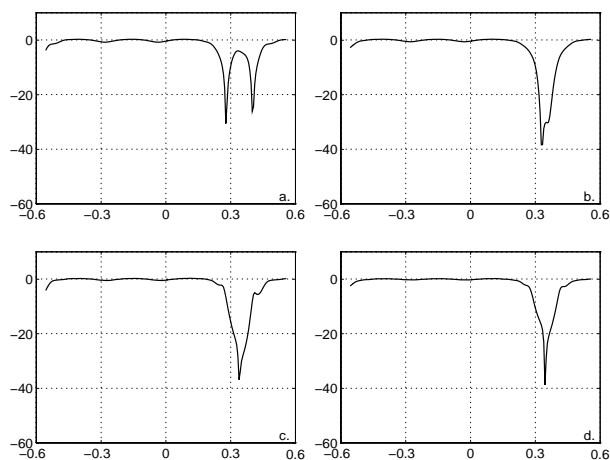


Figure 27: Influence of multiple-time around clutter (IF vs F ; fully adaptive FIR filter processor, linear array, FL): a. $R_0/H = 1.66$; b. $R_0/H = 3$; c. $R_0/H = 4.33$; d. $R_0/H = 5.66$

3 Effect of Jamming

In this chapter the effect of additional jamming is discussed.

3.1 Characterisation of Jamming and Clutter

3.1.1 Eigenspectra

We assume broadband white noise jammers which cover the whole radar bandwidth. Let us first have a look at jammer eigenspectra. Let us assume an array with 24 elements and consider 24 echoes. Figure 29 shows eigenspectra of the space-time jammer covariance matrix for 1, 3, and 5 jammers. As can be seen each jammer produces 24 eigenvalues which is the number of echoes (the temporal dimension). This reflects that the jammers are white in the time dimension. In Figure 30 we see eigenspectra for superposition of clutter and the jammer scenario of Figure 29. Now we notice that each jammer adds $M = 24$ eigenvalues to the clutter eigenvalues.

3.1.2 Power Spectra

Figure 31 shows the well-known clutter spectrum for a sidelooking array and one additional jammer. It can be noticed that the jammer is white along the Doppler axis and discrete in azimuth. In Figure 32 we consider a the clutter spectrum of a forward looking array according with 3 additional jammers.

3.2 Jammer and Clutter Suppression

We consider two cases, simultaneous jammer and clutter suppression and cascading spatial jammer cancellation with space-time clutter only rejection.

3.2.1 Simultaneous Processing

Figure 33 shows the improvement factor for the scenario given by Figure 31. We notice clearly the notches of jammer and clutter. An IF plot for the clutter-jammer scenario given in Figure 32 can be seen in Figure 34.

3.2.2 Cascading Jammer and Clutter Rejection

The principle is illustrated in Figure 35. Since the jammer is discrete in azimuth but white in Doppler it would be sufficient to apply standard *spatial* cancellation techniques to reject the jammer. Adaptation has to be done in a passive interval of the radar operation so that the anti-jamming filter is not corrupted by clutter. Then, in a subsequent space-time mode clutter is suppressed. The idea is that two cascaded filters might be less costly than one filter for simultaneous clutter and jammer suppression. Of course, adaptation of the clutter filter has to be done after the adapted anti-jamming filter. In Figure 35 the anti-jamming filter and the anti-clutter filter are shown schematically.

In Figure 36 a block diagram of a cascaded processor is shown. It should be noted that the fully adaptive anti-jamming filter can be replaced by a symmetric auxiliary sidelobe canceller scheme according to Figure 37 in order to further reduce the number of operations. Figure 38 shows the IF at the output of the adaptive anti-jamming filter for 3 active jammers. Figure 39 shows the clutter+jammer suppression performance of the cascaded processor for different numbers of jammers. Notice that the number of channels at the clutter rejection level is $K = 3$. The clutter notch can be seen clearly. The jammer notches are not visible because the jammer spectra are located in parallel to the Doppler axis (see for illustration Figure 40).

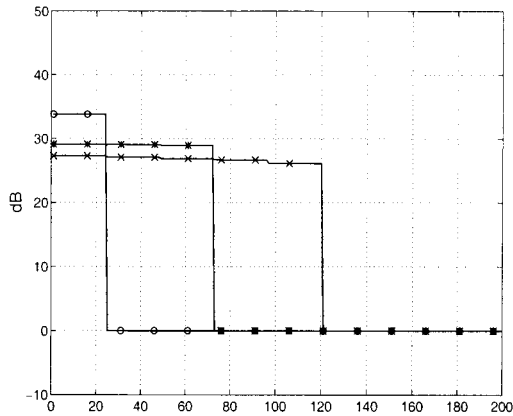


Figure 29: Space-time jammer eigenspectra (SL array): $\circ J = 1$; $*$ $J = 3$; $\times J = 5$

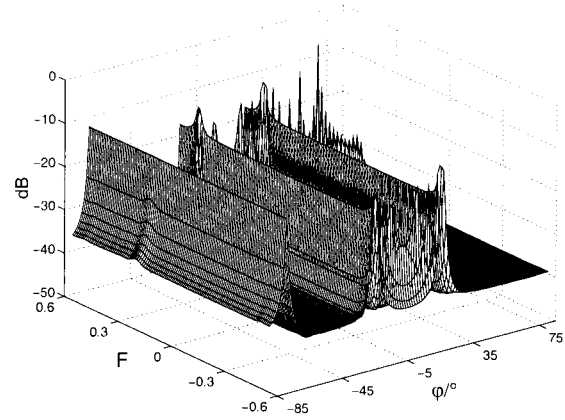


Figure 32: MV jammer+clutter spectrum (FL array, $J = 3$)

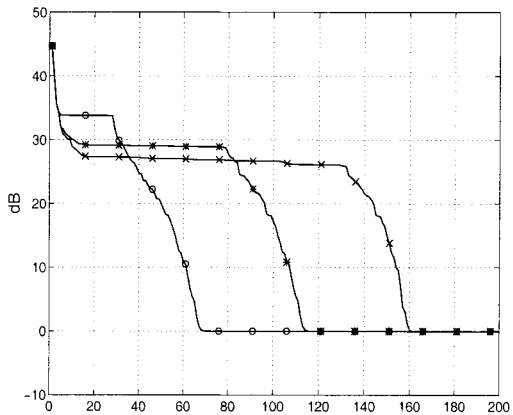


Figure 30: Space-time jammer+clutter eigenspectra (SL array) $\circ J = 1$; $*$ $J = 3$; $\times J = 5$

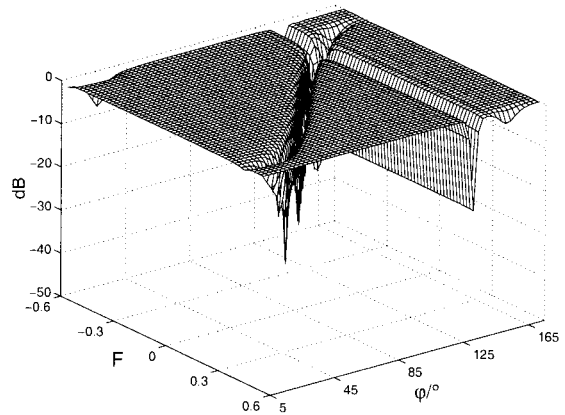


Figure 33: Improvement factor for a jammer+clutter scenario (SL array, $J = 1$)

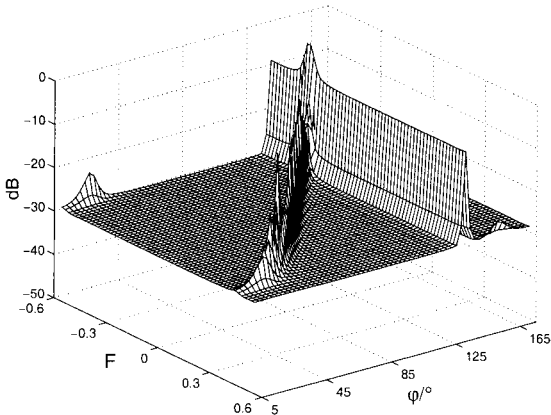


Figure 31: MV jammer+clutter spectrum (SL array, $J = 1$)

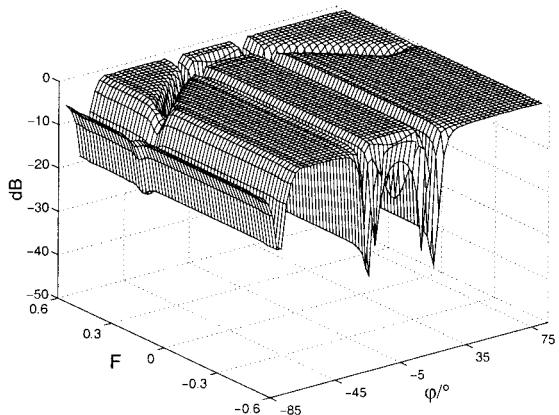


Figure 34: Improvement factor for a jammer+clutter scenario (FL array, $J = 3$)

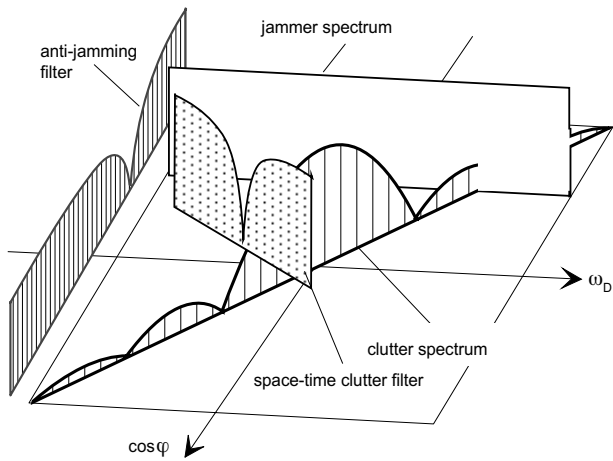


Figure 35: Cascading jammer and clutter filters

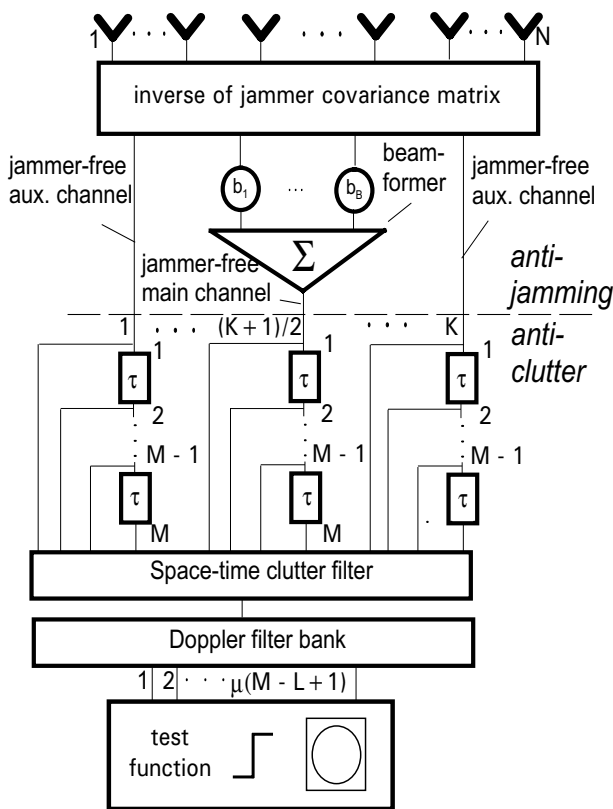


Figure 36: Cascading fully adaptive anti-jamming and auxiliary sensor clutter filters

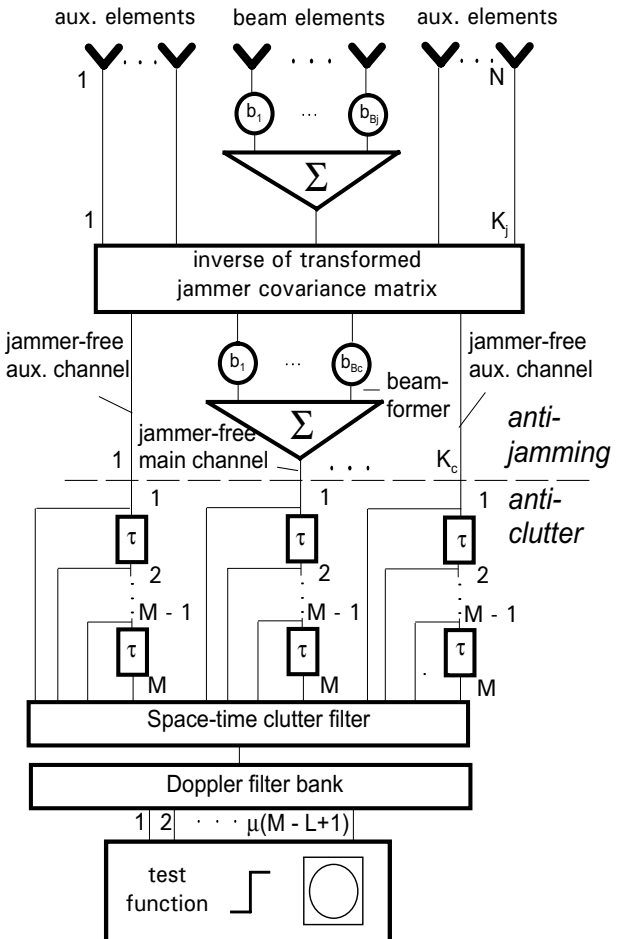


Figure 37: Cascading fully adaptive anti-jamming and auxiliary sensor clutter filters

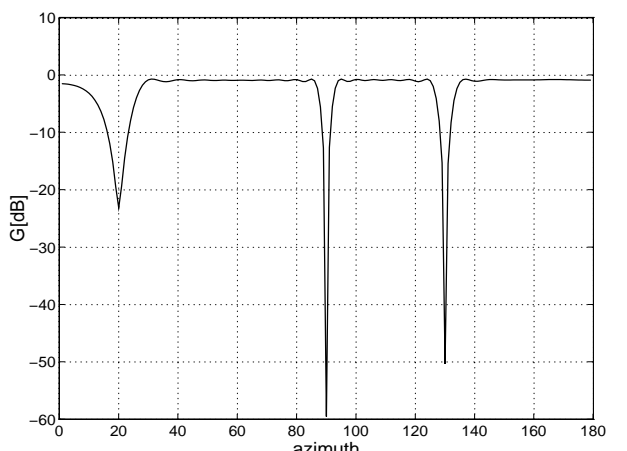


Figure 38: Performance of the anti-jamming processor

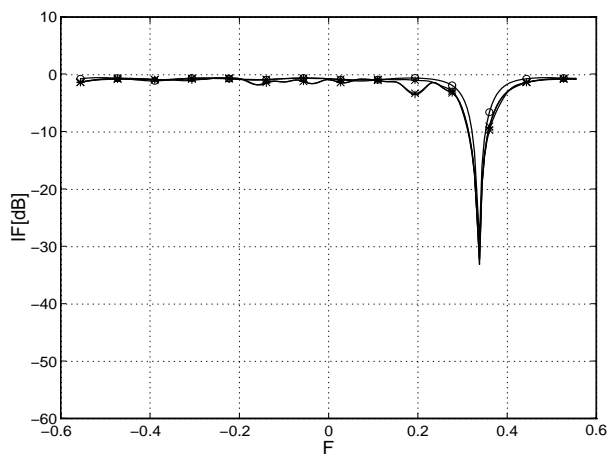


Figure 39: Optimum jammer suppression and auxiliary channel clutter filter cascaded ($N=25$, $K=3$, SL):
 $\circ J = 0$; $*$ $J = 1$; $\times J = 2$; $+ J = 3$

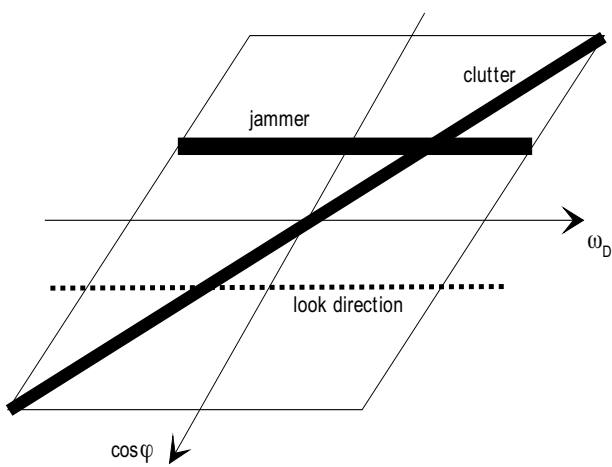


Figure 40: $\varphi-\omega_D$ trajectories of clutter and jammer (sidelooking array)

4 Current and Future Research Topics

4.0.3 STAP for Bistatic Radar

Bistatic radar operation has the advantage that the receiver cannot be located easily by hostile ESM techniques. The philosophy of bistatic radar for military operations is to design a cheap and/or remote transmitter and a displaced receiver with unknown position. Bistatic radar is much more complex in many respects than monostatic radar. In the following a few properties of bistatic STAP radar are briefly presented which differ from monostatic STAP radar.

4.0.4 Review of Monostatic Radar

Let us recall that for a sidelooking array the clutter Doppler is range independent. This follows from the fact that the array and the flight path coincide so that beam traces on the ground and isodops coincide (see Figure 41, receiver and transmitter being in the same location). The clutter trajectories in the azimuth-Doppler plane Figure 42 are straight lines along the diagonal of the azimuth-Doppler plot. Notice that for different ranges the same curves are obtained. The eigenspectrum (Figure 43) of a typical SL clutter covariance matrix follows the rule $N_E = N + M - 1$ (in this example $N=M=24$).

Figure 44 shows the same isodop plot as Figure 41, however for a forward looking array which means that the beamtraces are rotated by 90° . As can be seen there are a lot of intersections between isodops and beam traces which is an indication for the range dependence of the clutter Doppler. The clutter trajectories show circles whose radius is a measure for the range.

4.0.5 Impact of Bistatic Configuration

We focus on sidelooking arrays. Let us consider a certain bistatic configuration shown in Figure 46. Transmitter and receiver are separated and fly in different directions. Looking at the transmit beam traces a lot of intersections between beam traces and isodops can be noticed which tells us that the clutter Doppler is range dependent. This is also confirmed by the clutter trajectories in the azimuth-Doppler plane (Figure 47) which exhibit different shape for different range. Figure 48 shows a clutter power spectrum for the configuration shown in Figure 46. Comparing Figure 47 with Figure 42 or Figure 48 with Figure 42 shows that in bistatic configurations in general the clutter Doppler is range dependent. This has implications on the processing. Clutter rejection may require range dependent adaptation and filtering, and may suffer from shortage in training data. The eigenspectrum shows more than $N_E = N + M - 1$ clutter eigenvalues if no directive sensors are used. For directive sensors the eigenspectrum is very similar to the monostatic case (Figure 43).

In conclusion, sidelooking arrays have beneficial properties in monostatic operation (no clutter Doppler dependency with range) whereas in bistatic configurations this is not fulfilled. As stated before, bistatic configurations are more complex than monostatic ones. We find that this is also true for bistatic STAP operation. It appears, however, from the eigen- or power spectra that processor architectures will be similar to those used in monostatic operation.

4.0.6 Range and Doppler ambiguities

We found out that in bistatic radar configurations the clutter Doppler is range dependant even for a radar with *sidelooking* array antenna. We can, therefore, expect that the multiple ambiguous returns which come from different ranges at different elevation angles will exhibit different Doppler frequencies.

Let us illustrate this by using Figure 50. Figure 50 shows IF curves versus target velocity for a sidelooking array in the bistatic configuration 2 (two aircraft on parallel flight paths). In Figure 50a the ideal case is shown. No range ambiguities have been assumed, and Doppler ambiguities do not occur inside the clutter band ($v_p = 90 \dots 90 \text{ m/s}$) since the PRF has been chosen the Nyquist frequency of the clutter bandwidth (12000 Hz). In Figure 50b the PRF was chosen 4 times the Nyquist rate so that many range ambiguous clutter returns can

be expected. We notice a considerable broadening of the clutter notch³. Using a planar array with additional vertical adaptivity similar to section 2.3.2 compensates to a certain extent for the effect of ambiguous clutter returns so that the resulting clutter notch is narrowed (Figure 50c). Additional PRI staggering according to section 2.3.1 gives no difference since the clutter band is oversampled anyway with the chosen PRF.

4.1 Cramér-Rao Bounds

The next logical step after signal processing and target detection is target parameter estimation (range, Doppler, direction). These parameters are required for subsequent tracking algorithms. The Cramér-Rao bound (CRB) gives the lowest possible standard deviation of the estimated parameters. The CRB is associated with the optimum processor, however, for certain suboptimum techniques (those based on linear transforms, s. Chapter 5) the CRB can be calculated as well.

4.1.1 Optimum Processing

Figures 51 and 52 show the CRB for the optimum processor (Chapter 4) for azimuth and velocity estimation, respectively. The four curves have been calculated for different SNR. A flat clutter-free zone can be recognized. At the Doppler frequency where the processor is matched to the clutter the curves show a peak. This means that the standard deviation of the estimated parameter increases in the region of the clutter notch.

4.1.2 Impact of Radar Parameters

The CRB curves in Figure 53 have been calculated for different numbers of array elements (or: array apertures). It is obvious that the estimation error become larger as the array aperture becomes smaller. In Figure 54 the influence of spatial decorrelation due to the system bandwidth on the CRB is shown. This decorrelation leads to a broadening of the clutter power spectrum (see the example in Figure 18) and, hence to a broadening of the clutter notch of the associated adaptive clutter filter. This in turn means reduced detectability of low Doppler targets and a larger area with increased estimation error.

4.1.3 Suboptimum Transform Techniques

In Figure 55 some CRB curves have been plotted for the ASEP which is a very economic processor architecture (see section 5.2.1). This processor can be described by a linear transform (see [26, Chapter 9]). If the clutter process was multi-variate gaussian the transformed process is gaussian again so that an optimum processor can be designed at the transformed level and, hence, the CRB can be calculated for any type of transform processor. We notice from Figure 55 that the estimation error is slightly raised and the clutter peak is broadened. In conclusion, such transform techniques may achieve almost optimum clutter rejection and target detection performance. The estimation error, however, is more sensitive to such linear transforms.

4.1.4 Tracking with STAP radar

During a tracking phase the radar-target geometry changes with time. Target parameters such as azimuth, elevation, range and Doppler vary continuously.

This effect shall be illustrated by a simple scenario. Consider a slow target on the ground moving in parallel to the flight path of a fast airborne radar. Then one may get a SNIR response from the radar as shown in Figure 56.

Initially, the radar is behind the target. As the target is moving there is a difference in radial velocity determined by both the target and radar velocities. When the radar passes the target we obtain zero radial velocity for both the target and clutter. In this situation the target disappears in the clutter notch. After the radar has passed the target the target comes out of the clutter notch so that the SNIR increases again. After a while

³which in part is a consequence of the short duration of the coherent processing interval owing to the chosen PRF.

the target stops so that it behaves like clutter. As long as the target stops the SNIR is very low. As soon as the target accelerates again the SNIR increases rapidly. Notice that the SNIR is modulated by the sensor pattern while the radar is overtaking the target.

The problem of ground target tracking with a STAP radar has been discussed by KOCH and KLEMM [31]. It is shown in [31] how an intelligent tracking algorithm can exploit the specific properties of the signal output of a STAP radar.

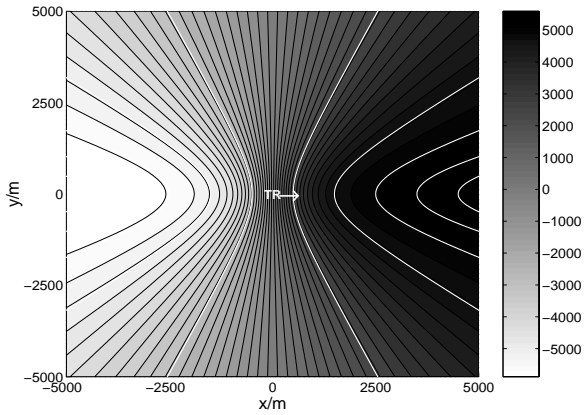


Figure 41: Isodops (black) and beam traces (white) for sidelooking linear array, monostatic (©1998 IEEE)

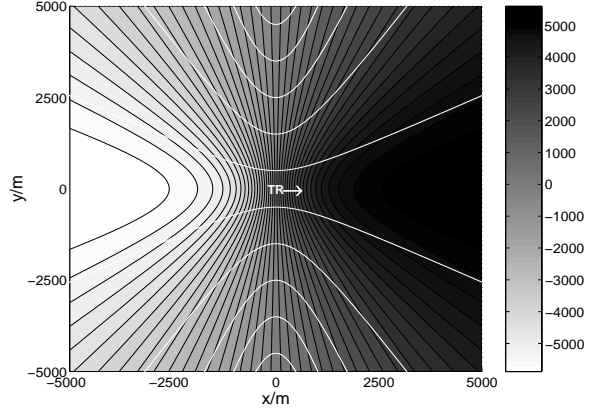


Figure 44: Isodops (black) and beam traces (white) for forward looking linear array, monostatic (©1998 IEEE)

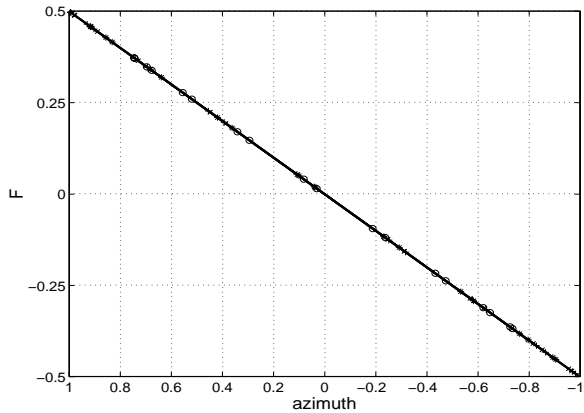


Figure 42: Azimuth-Doppler clutter trajectories (SL):
R = \circ 1 km; $*$ 2 km; \times 4 km; $+$ 10 km (©1998 IEEE)

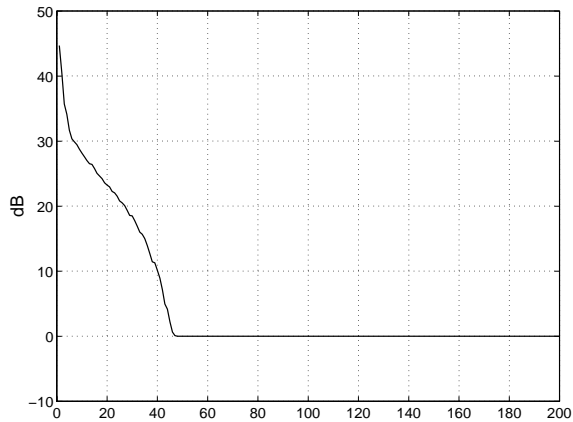


Figure 43: Clutter eigenspectrum (SL), (©1998 IEEE)

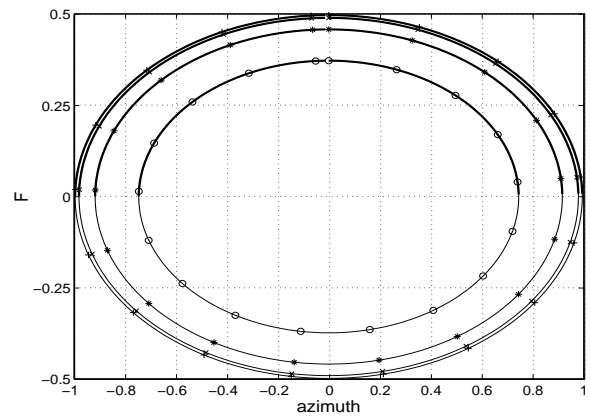


Figure 45: Azimuth-Doppler clutter trajectories (FL):
R = \circ 1 km; $*$ 2 km; \times 4 km; $+$ 10 km (©1998 IEEE)

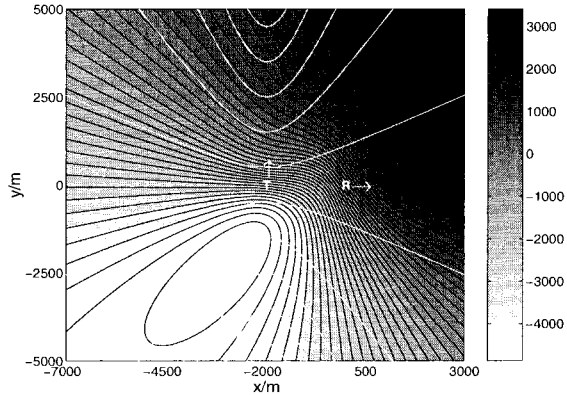


Figure 46: Isodops (black) and beam traces (white), SL, bistatic , (©1998 IEEE)

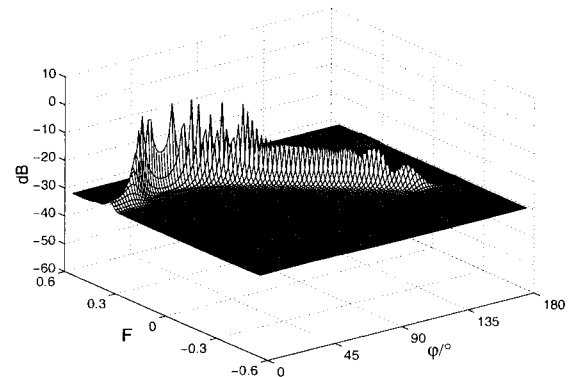


Figure 48: Clutter power spectrum (SL), bistatic (©1998 IEEE)

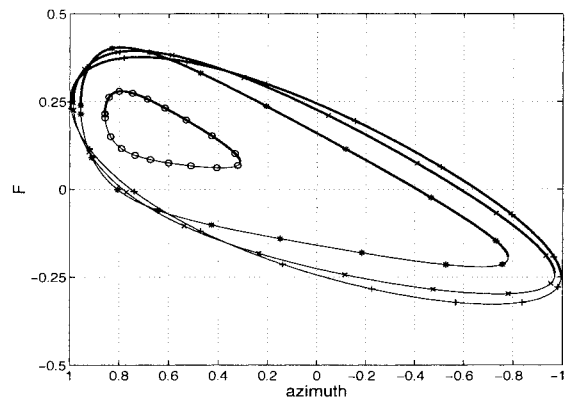


Figure 47: Azimuth-Doppler clutter trajectories (SL): $R = \circ 1 \text{ km}; * 2 \text{ km}; \times 4 \text{ km}; + 10 \text{ km}$ ($\delta_T = 90^\circ$), (©1998 IEEE)

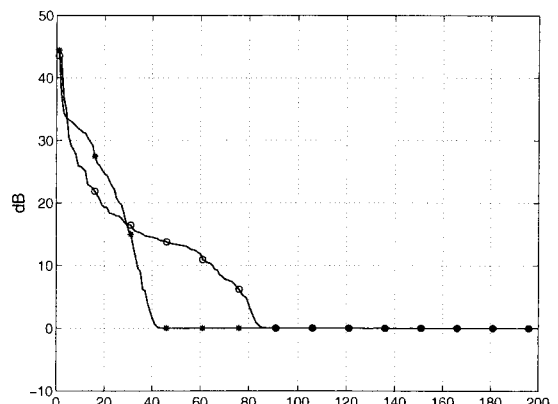


Figure 49: Clutter eigenspectrum (configuration as in Figure 46, SL), \circ omnidirectional sensor patterns; $*$ directive sensor patterns, (©1998 IEEE)

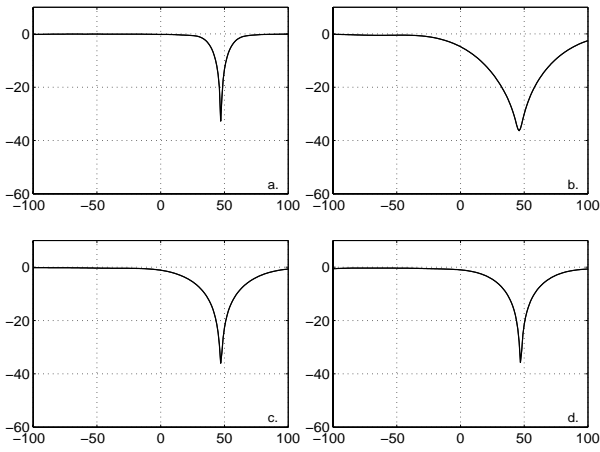


Figure 50: IF vs target velocity (m/s, sidelooking array, configuration 2, $R=10000$ m, $N=M=12$. a. PRF=Nyquist of clutter bandwidth, no range ambiguities; b. PRF=4× Nyquist, with range ambiguities; c. adaptive planar array; d. planar array + randomly staggered PRI

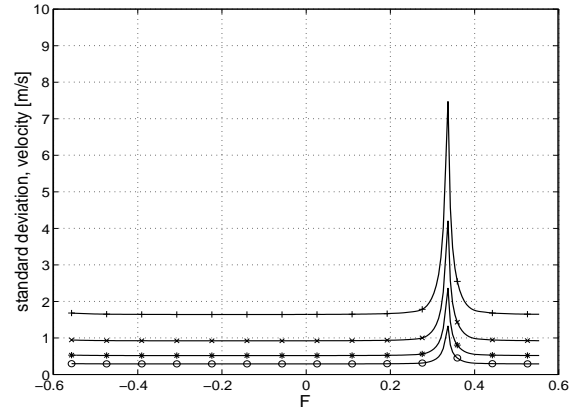


Figure 52: Effect of signal-to-noise-ratio on velocity estimation: $\text{SNR} = \circ 10$ dB; $\ast 0$ dB; $\times -10$ dB; $+$ -20 dB

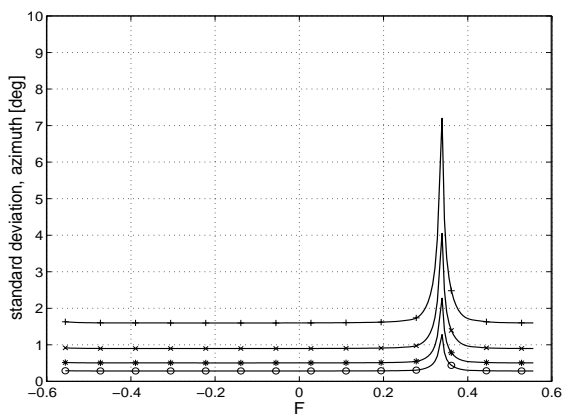


Figure 51: Effect of signal-to-noise-ratio on azimuth estimation: $\text{SNR} = \circ 10$ dB; $\ast 0$ dB; $\times -10$ dB; $+$ -20 dB

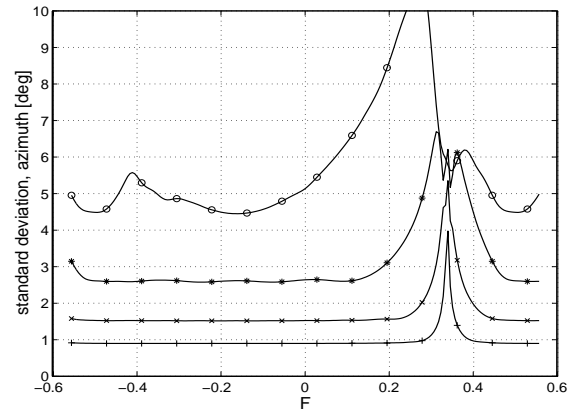


Figure 53: Impact of the array aperture size (azimuth estimation): $N = \circ 3$; $\ast 6$; $\times 12$; $+$ 24

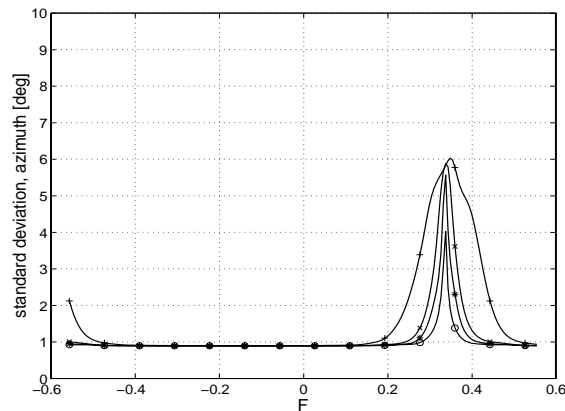


Figure 54: Effect of system bandwidth (FL): SNR =
○ $B_s = 0\%$; * $B_s = 1\%$; × $B_s = 5\%$; + $B_s = 30\%$

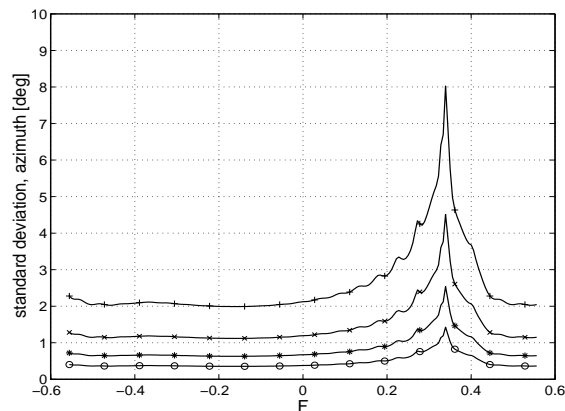


Figure 55: CRB for azimuth estimate (ASEP, $K = 5$, $L = 5$): SNR = ○ 10 dB; * 0 dB; × -10 dB; + -20 dB

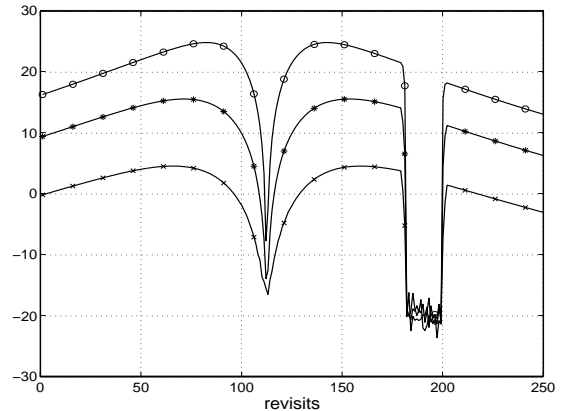


Figure 56: Optimum SNIR vs number of revisit
for different system dimensions: ○ $N=M=24$; *
 $N=M=12$; × $N=M=6$

References

- [1] Anderson, D. B., "A Microwave Technique to Reduce Platform Motion and Scanning Noise in Airborne Moving Target Radar", *IRE WESCON Conv. Record*, Vol. 2, pt. 1, 1958, pp. 202-211
- [2] Babu, S. B. N., Torres, J. A., Lamensdorf, D., "Space-Time Adaptive Processing for Airborne Phased Array Radar, *Proc. of the Conf. on Adaptive Antennas*, 7-8 November 1994, Melville, New York 11747, pp. 71-75
- [3] Brennan, L. E., Reed, I. S., "Theory of Adaptive Radar", *IEEE Trans. AES*, Vol. 9, No 2, March 1973, pp. 237-252
- [4] Brennan, L. E., Mallett, J. D., Reed, I. S., "Adaptive Arrays in Airborne MTI", *IEEE Trans. AP*, Vol. 24, No. 5, 1976, pp. 607-615
- [5] Brennan, L. E., Staudaher, F. M., "Subclutter Visibility Demonstration", *Technical Report RL-TR-92-21, Adaptive Sensors Incorporated*, March 1992
- [6] Bühring, W., Klemm, R., "Ein adaptives Filter zur Unterdrückung von Radarstörungen mit unbekanntem Spektrum" (An adaptive filter for suppression of clutter with unknown spectrum), *FREQUENZ*, Vol. 30, No. 9, September 1976, (in German), pp. 238-243
- [7] Coe, D. J., White, R. G., "Experimental moving target detection results from a three-beam airborne SAR", *AEU*, Vol. 50, No. 2, March 1996
- [8] Compton, R. T. jr., "The Bandwidth Performance of a Two-Element Adaptive Array with Tapped Delay-Line Processing", *IEEE Transaction on Antenna and Propagation*, Vol. AP-36, No. 1, January 1988, pp. 5-14
- [9] Compton, R. T. jr., "The Relationship Between Tapped Delay-Line and FFT Processing in Adaptive Arrays", *IEEE Transaction on Antenna and Propagation*, Vol. AP-36, No. 1, January 1988, pp. 15-26
- [10] Covault, C., "Space-based radars drive advanced sensor technologies", *Aviation Week & Space Technology*, April 5, 1999, pp. 49-50
- [11] Doherty, J. F., "Suppression of Terrain Scattered Jamming in Pulse Compression Radar", *IEEE Transactions on Signal Processing*, Vol. 2, No. 1, January 1995, pp. 4-6
- [12] Ender, J., "The airborne experimental multi-channel SAR system", *Proc. EUSAR'96*, 26-28 March 1996, Koenigswinter, Germany, pp. 49-52 (VDE Publishers)
- [13] Ender, J., "Detection and Estimation of Moving Target Signals by Multi-Channel SAR", *Proc. EUSAR'96*, 26-28 March 1996, Koenigswinter, Germany, pp. 411-417, (VDE Publishers). Also: *AEU*, Vol. 50, March 1996, pp. 150-156
- [14] Ender, J., "Experimental results achieved with the airborne multi-channel SAR systems AER II.The airborne experimental multi-channel SAR system", *Proc. EUSAR'98*, 25-27 May 1998, Friedrichshafen, Germany
- [15] Farina, A., Timmoneri, L., "Space-time processing for AEW radar", *Proc. RADAR 92*, Brighton, UK, 1992, pp. 312-315
- [16] Gross, L.A., Holt, H.D., "AN/APY-6 realtime surveillance and targeting radar development", *Proc. NATO/IRIS Conference*, 19-23 October 1998, paper G-3
- [17] Haimovich, A. L., Bar-Ness, Y., "An Eigenanalysis Interference Canceler", *IEEE Trans. Signal Processing*, Vol. 39, No. 1, January 1991, pp. 76-84

- [18] Ayoub, T. F., Haimovich, A. M., Pugh, M. L., "Reduced-rank STAP for high PRF radar", *IEEE Trans. AES*, Vol. 35, No. 3, July 1999, pp. 953-962
- [19] Hippler, J., Fritsch, B., "Calibration of the Dornier SAR with trihedral corner reflectors", *Proc. EU-SAR'96*, 26-28 March 1996, Koenigswinter, Germany, pp. 499-503, (VDE Publishers)
- [20] Jouny, I. I., Culpepper, E., "Modeling and mitigation of terrain scattered interference", *IEEE Antennas and Propagation Symposium*, 18-23 June, 1995, Newport Beach, USA, pp. 455-458
- [21] Klemm, R., "Adaptive Clutter Suppression for Airborne Phased Array Radar", *Proc. IEE*, Vol. 130, No. 1, February 1983, pp. 125-132
- [22] Klemm, R., Ender, J., "New Aspects of Airborne MTI", *Proc. IEEE Radar 90*, Arlington, USA, 1990, pp. 335-340
- [23] Klemm, R., "Antenna design for airborne MTI", *Proc. Radar 92*, October 1992, Brighton, UK, pp. 296-299
- [24] Klemm, R., "Adaptive Airborne MTI: Comparison of Sideways and Forward Looking Radar", *IEEE International Radar Conference*, Alexandria, VA, May 1995, pp. 614-618
- [25] Klemm, R., ed., *Digest of the IEE Colloquium on STAP*, 6 April 1998, IEE, London, UK
- [26] Klemm, R., Space-Time Adaptive Processing - Principles and Applications *IEE Publishers*, London, UK, 1998)
- [27] Klemm, R., "Comparison between monostatic and bistatic antenna configurations for STAP", *IEEE Trans. AES*, April 2000
- [28] Klemm, R., (ed.), Special issue on "Space-Time Adaptive Processing", *IEE ECEJ*, February 1999
- [29] Klemm, R., "Space-time adaptive FIR filtering with staggered PRI", *ASAP 2001*, MIT Lincoln Lab., Lexington, MA, USA, 13-15 March 2001, pp.
- [30] Klemm, R., "Doppler properties of airborne clutter", *RTO SET Lecture Series 228* (this volume)
- [31] Koch, W., Klemm, R., "Ground target tracking with STAP radar", *IEE Proc. Radar, Sonar and Navigation*, 2001
- [32] Melvin, W. L., (ed.), Special issue on "Space-Time Adaptive Processing and Adaptive Arrays", *IEEE Trans. AES*, April 2000
- [33] Kreyenkamp, O., "Clutter covariance modelling for STAP in forward looking radar", *DGON International Radar Symposium 98*, September 15-17, 1998, München, Germany
- [34] Lee, F. W., Staudaher, F., "NRL Adaptive Array Flight Test Data Base", *Proc. of the IEEE Adaptive Antenna Systems Symposium*, Melville, New York, November 1992
- [35] Richardson, P. G., Hayward, S. D., "Adaptive Space-Time Processing for Forward Looking Radar", *Proc. IEEE International Radar Conference*, Alexandria, VA, USA, 1995, pp. 629-634
- [36] Richardson, P. G., "Effects of manoeuvre on space-time adaptive processing performance", *Proc. IEE Radar'97*, 14-16 October 1997, Edinburgh, Scotland, pp. 285-289
- [37] Sanyal, P. K., Brown, R. D., Little, M. O., Schneible, R. A., Wicks, M. C., "Space-time adaptive processing bistatic airborne radar", *IEEE National Radar Conference*, 20-22 April 1999, Boston, USA, pp. 114-118

- [38] Shnitkin, H., "A Unique JOINT STARS Phased Array Antenna", *Microwave Journal*, January 1991, pp. 131-141
- [39] Skolnik, M., *Radar Handbook*, 1st Ed., McGraw-Hill, New York, 1970
- [40] Tobin, M., "Real-Time Simultaneous SAR/GMTI in a Tactical Airborne Environment", *Proc. EUSAR'96*, 26-28 March, 1996, Koenigswinter, Germany, pp. 63-66, (VDE Publishers)
- [41] Titi, G. W., "An Overview of the ARPA/NAVY Mountaintop Program", *IEEE Adaptive Antenna Symposium*, Melville, New York November 7-8, 1994
- [42] Tsandoulas, G. N., "Unidimensionally Scanned Phased Arrays", *IEEE Trans. on Antennas and Propagation*, Vol. AP28, No. 1, November 1973, pp. 1383-1390
- [43] Wang, H., Cai, L., "On Adaptive Spatial-Temporal Processing for Airborne Surveillance Radar Systems", *IEEE Trans. AES*, Vol. 30, No. 3, July 1994, pp. 660-670
- [44] Wang Z., Bao Z., "A Novel Algorithm for Optimum and Adaptive Airborne Phased Arrays", *Proc. SITA'87*, 19-21 November 1987, Tokyo, Japan, pp. EE2-4-1
- [45] Wang, H., Zhang, Y., Zhang, Q., "An Improved and Affordable Space-Time Adaptive Processing Approach", *Proc. International Conference on Radar (ICR'96)*, Beijing, China, 8-10 October 1996, pp. 72-77
- [46] Ward, J., "Space-Time Adaptive Processing for Airborne Radar", *Technical Report No. 1015*, Lincoln Laboratory, MIT, December 1994
- [47] Ward, J., "Cramer-Rao Bounds for Target Angle and Doppler Estimation with Space-Time Adaptive Processing Radar", *Proc. 29th ASILOMAR Conference on Signals, Systems and Computers*, 30 October-2 November 1995, pp. 1198-1203

This page has been deliberately left blank

Page intentionnellement blanche

Algorithms for Real-Time Processing

A. Farina

Technical Directorate, Radar & Technology Division

Alenia Marconi Systems

Via Tiburtina km. 12.400, 00131 Rome, Italy

Tel: +39-6-41502279, Fax: +39-6-41502665, e-mail: afarina@amsjv.it

Key words: parallel processing, QR decomposition, Inverse QR decomposition, lattice flow graphs, CORDIC.

1. SUMMARY AND INTRODUCTION

This paper describes methodologies for on-line processing of received radar data by a set of N antennas and M pulse repetition intervals (PRIs) for the calculation of space-time adaptive (STAP) filter output. The numerically robust and computationally efficient QR-decomposition (QRD) is used to derive the so called MVDR (Minimum Variance Distortionless Response) and lattice algorithms; the novel inverse QRD (IQRD) is also applied to the MVDR problem. These algorithms are represented as systolic computational flow graphs. The MVDR is able to produce more than one adapted beams focused along different angular directions and Doppler frequencies in the radar surveillance volume. The lattice algorithm offers a computational saving; infact, its computational burden is $O(N^2M)$ in lieu of $O(N^2M^2)$. An analysis of the numerical robustness of the STAP computational schemes is presented when the CORDIC (CO-ordinate Rotation DIgital Computer) algorithm is used to compute the QRD and the IQRD. Benchmarks on general purpose parallel computers and on a VLSI (Very Large Scale Integrated) CORDIC board are presented.

The paper is organized as follows. Section 2 introduces the STAP problem and the basic systolic algorithms to reach real time adaptation. The lattice and its generalization (vectorial lattice) for wideband problems are discussed in section 3. The IQRD based MVDR algorithm is presented in Section 4. Experiments of mapping the basic triangular systolic array onto general purpose parallel computers are discussed in Section 5. The use of VLSI CORDIC board is the theme of Section 6. The MVDR systolic algorithm is applied to off-line process recorded live data; the detection of vehicular traffic is shown (Section 7). Finally, Section 8 gives a perspective for future research.

2. BASELINE SYSTOLIC ALGORITHM

The detection of low flying aircrafts and/or surface moving targets, and the stand-off surveillance of areas of interest require a radar on an elevated platform like an aircraft. The AEW (Airborne Early Warning) radars pose a number of interesting technical problems especially in the signal processing area. The issue is not new: detect target echoes in an environment crowded of natural (clutter), intentional (jammer), and other unintentional RF (especially in the low region of microwaves, e.g. VHF/UHF bands) interference. The challenge is related to the large dynamic range of the received signals, the non-homogeneous and non-stationary nature of the interference, and the need to fulfil the surveillance and detection functions in real time. One technique proposed today to solve the problem is based on STAP [2], [7], [8], [14] to [16]. Essentially, the radar is required to have an array (for instance, a linear array along the aircraft axis) of N antennas each receiving M echoes from a transmitted train of M coherent pulses. Under the hypothesis of disturbance having a Gaussian probability density function and a Swerling target model, the optimum processor is provided by the linear combination of the NM echoes with weights $w = M^{-1}s^*$, envelope detection and comparison with threshold. M is the space-time covariance matrix, i.e. $M = E\{z^*z^T\}$ where z (dimension NMx1) is the collection of the NM disturbance echoes in a range cell, s - the space-time steering vector - is the collection of the NM

samples expected by the target, and $(*)$ stands for complex conjugate. A direct implementation, (via Sample Matrix Inversion, SMI) of the weight equation $\mathbf{w} = \mathbf{M}^{-1}\mathbf{s}^*$ is not recommended. One reason is related to the poor numerical stability in the inversion of the interference covariance matrix especially when large dynamic range signal is expected during the operation; another one is the very high computational cost. There is a need of extremely high arithmetic precision during digital calculation. Note that double precision costs four times as much as single precision. The situation would be different if, instead of operating on the covariance matrix \mathbf{M} , we would operate directly on the data snapshots $\mathbf{z}(k)$, $k=1,2,\dots,n$, where n is the number of snapshots (i.e. : range cells) used to estimate the weights \mathbf{w} . It can be shown that the required number of bits to calculate the weights, within a certain accuracy, by inversion of \mathbf{M} is two times the number of bits to calculate the weights operating directly on the data snapshots $\mathbf{z}(k)$. This is so because the calculation of power values is avoided thus the required dynamic is halved. The algorithms that operate directly on the data are referred to as “data domain algorithms” in contrast to the “power domain algorithms” requiring the estimation of \mathbf{M} .

The QRD is a numerical technique to solve least-square problems, like the one in STAP, that avoids direct computation and inversion of interference covariance matrix [1], [3]. Indicate with \mathbf{Z} the $n \times (NM)$ -dimensional matrix which collects the n data snapshots:

$$\mathbf{Z}(n) = [\mathbf{z}(1) \mathbf{z}(2) \dots \mathbf{z}(n)]^T \quad (1)$$

The weight equation can be written as follows:

$$\mathbf{Z}^H(n) \mathbf{Z}(n) \mathbf{w} = \mathbf{s}^* \quad (2)$$

where $(\bullet)^H$ stands for complex conjugate transpose. Taking the data matrix \mathbf{Z} and operating on it with unitary (i.e. covariance preserving) matrix \mathbf{Q} (with dimension $n \times n$) we are able to transform the matrix \mathbf{Z} in an upper triangular matrix \mathbf{R} (with dimension $NM \times NM$):

$$\mathbf{Q} \mathbf{Z} = \begin{bmatrix} \mathbf{R} \\ \mathbf{0} \end{bmatrix} \quad (3)$$

thus equation (2) can be rewritten as:

$$\mathbf{R}^H \mathbf{R} \mathbf{w} = \mathbf{s}^* \quad (4)$$

which is now easily solved by forward and back-substitution steps as follows. Indicating by a new vector \mathbf{t} the product $\mathbf{R} \mathbf{w}$, equation (4) becomes:

$$\mathbf{R}^H \mathbf{t} = \mathbf{s}^* \quad (5)$$

this can be solved in \mathbf{t} . Subsequently, the additional equation:

$$\mathbf{R} \mathbf{w} = \mathbf{t} \quad (6)$$

is solved in \mathbf{w} . A noticeable improvement of the basic technique allows to calculate the STAP output without extracting the weights, i.e: without performing the two substitutions above (see, for instance [1] at page 147). In summary, either the weight vector \mathbf{w} or the output signal of the STAP are obtained without forming and inverting any covariance matrix. By using a large number of bits the data domain algorithm provides the same results of the power domain algorithm which estimates the covariance matrix $\mathbf{Z}^H(n) \mathbf{Z}(n)$ and derives the weight vector by the conventional Cholesky factorisation of that matrix in equation (2). The noticeable result is related to the far superior performance of the data domain algorithm when using a limited number of bits; in

fact, data domain needs half number of the bits required by the power domain method to reach good interference cancellation and target coherent integration.

The triangularization of the data matrix, see eqn. (3), can be done with the following known methods: Givens rotations, Householder reflections (a generalization of Givens rotations) and Gram Schmidt [1]. Another method to obtain a sparse (actually a diagonal in lieu of triangular) data matrix is the singular value decomposition; the Jacobi and Hestenes are recursive parallel algorithms to efficiently obtain the SVD. The Lanczos is another numerically efficient candidate to solve our real-time STAP problem [4]. The preferred approach in this paper is the one based on Givens rotations. All these methods enjoy the possibility to be mapped onto a parallel processor like a systolic array. This means that the algorithm is readily transformed in a computer architecture; this is not the case for the equation (2) where a single processor computer has the task to perform the indicated operations. Today it is possible to implement the systolic array with custom VLSI technology thus providing compact processors requiring limited prime power. An additional advantage is related to the large data throughput of the parallel processor representing a suitable mean to reach the real-time operation.

The baseline architecture considered for the STAP problem is the trapezoidal one depicted in Figure 1 [3]. This constitutes the generalization of a method, which was originally developed for MVDR beam forming, by QRD. The NM-dimensional triangular array ABC receives the snapshots of data from a set of range cells and outputs from the right-hand side the matrix \mathbf{R} produced as the data descend through the array. The matrix is passed to the right-hand column of cells DE which serves to steer the main beam in the desired angular direction and Doppler frequency. Multiple beams can be formed simply by adding right-hand columns as depicted in Fig. 1; they are constraint post-processors. The bulk of the computation, i.e. the QRD, is common to all of the separate beam forming tasks, and only needs to be performed once.

The MVDR processor in Fig. 1 is designed to operate in the following manner [3]. The triangular processor, in normal adaptive mode (selected by setting a - not shown - input binary flag $f=1$), is fed with sufficient data snapshots to form a good statistical estimate of the environment. The triangular array is then frozen (by setting the input binary flag $f=0$) while a look-direction constraint is input as though it were a data vector $\mathbf{z}(n)$ emerging from the multi channel tapped delay line. This serves to calculate the vector $\mathbf{a} = (\mathbf{R}^H)^{-1} \mathbf{s}^*$ which is captured and stored in the right hand column (also operating in mode $f=0$); this vector needs to determine the STAP output $\mathbf{e}(n) = \mathbf{z}^T(n) \mathbf{R}^{-1} (\mathbf{R}^H)^{-1} \mathbf{s}^*$. Once the vertical columns have been initialized, the adaptive mode of operation ($f=1$) is selected for both the main triangular array and the right hand columns and more data snapshots are presented to the processor. The processor then updates its estimate of the environment (via the stored quantities \mathbf{R} and \mathbf{a}) and simultaneously outputs the STAP signals from the bottom of the column DE.

The number of processing elements in the triangular systolic arrays is $0.5 M^2 N^2$. The MVDR algorithm has a noticeable computational advantage with respect to the SMI which requires $O(N^3 M^3)$ arithmetic operations per sample time. Two types of processing elements are needed within the triangular array: one calculates the sine and cosine of an angle between two input data values, the other rotates the remaining data of the same angle. The calculation of the rotation and the application of the rotation is repeated for each row of the triangular array. A third cell type is used in the look-direction constraint columns. Every processing cell of the triangular array should perform on average 24 floating point operations per data snapshot. Let d be the desired data rate, i.e. the snapshots per second to process, the systolic machine should perform $12 d M^2 N^2$ flops. As an example, let d be 1 MHz and $NM=100$ the corresponding processing power needed is 100 Gflops approximately. By down sampling the radar data of a factor ten, the required processing power is 10 Gflops.

3. LATTICE AND VECTORIAL LATTICE ALGORITHMS

An advanced processing architecture referred to as MVDR lattice processor requires $O(N^2 M)$ arithmetic operations per sample time ; it is described in [3]. It takes advantage of the time-shift invariance associated with STAP. The data entering the triangular array changes very little from one PRI to the next which means

that a large part of the computation is being repeated on successive PRIs albeit in different parts of the array. This repetition is eliminated in the lattice algorithm where the big trapezoidal array is decomposed in a lattice of smaller (i.e.: of dimension N) trapezoidal arrays; the lattice has M stages (see figure 2). The lattice based MVDR operates in a similar manner to the big trapezoidal array; details are found in [3]. If M=N=10 and the update rate is one tenth of 1 MHz, the required computational power is 1 Gflop. The lattice algorithm has also been designed and tested with simulated data for wideband STAP [10]; this architecture is particularly useful: (i) to deal with wideband radar, (ii) to compensate for amplitude and phase mismatching between the receiving channels, and (iii) to combat the hot clutter. The processing architecture, named vectorial lattice, operates on an array of N antennas, M PRIs and P samples taken within the radar range cell. The lattice has again M stages, each having trapezoidal arrays of dimension NP. The computational complexity of the scheme is $O(MN^2P^2)$.

In the above mentioned processing architectures, namely: the MVDR, the lattice and the vectorial lattice, the common processing module is the triangular systolic array. In the Sections 5 and 6 to follow we report the results concerning the mapping of the triangular systolic array onto parallel processors.

4. INVERSE QRD BASED ALGORITHMS

A further improvement of the triangular systolic array for STAP processing is called IQRD (Inverse QR Decomposition) and promises an additional decrease of the required computational power.

The need to reduce the computational requirements of the triangular systolic array was discussed in Section 2. It was mentioned the possibility to down sample of a factor ten, say, the update of the triangular array. This tacitly requires the extraction of the adaptive weights of the STAP at the low update rate and the application of the weights to the radar echoes at the natural rate of the data. This approach has the following practical problem. The MVDR systolic array of Figure 1 could extract the adapted weights via back substitution; however, pipelining the two steps of triangular update and back-substitution seems impossible. There are two possibilities to overcome this problem. The first is to use a triangular array in addition to the main one; the second triangular array being reversed with respect to the array which updates the matrix \mathbf{R} . This approach requires more hardware to be integrated on the chip. The second approach exploits a recursive equation which updates $(\mathbf{R}^H)^{-1}$ instead of \mathbf{R} . The update of $(\mathbf{R}^H)^{-1}$ serves to the purpose of extracting the weights. This algorithm, referred to as IQRD, can be implemented with just one triangular systolic array, which has a specular orientation of the basic triangular array to update \mathbf{R} (see figure 3). A limitation of this approach is related to the difficult schedule of the various processing steps. A detailed comparative analysis of the IQRD and QRD based MVDR algorithms is presented in [12]. Also an implementation of the corresponding systolic architectures with the use of the CORDIC algorithm, as basic building block is discussed.

5. EXPERIMENTS WITH GENERAL PURPOSE PARALLEL PROCESSORS

This section summarizes the findings described in details in [6]; today this study seems out of date for the advancement in the signal processing hardware, nevertheless it is still very instructive. We study the use of parallel processors of MIMD (Multiple Instruction streams Multiple Data streams) and SIMD (Single Instruction stream Multiple Data streams) types available on the market (early 1990s). This approach is meant to be propaedeutic to the VLSI solution. In fact, it provides guidelines for the design of the processing architecture to be implemented on silicon. The problems of synchronization of the whole systolic array by a master clock and the data transfer between processors can also be investigated. Additionally, an estimate of the computational performance of several candidate processing architectures is also possible.

With reference to the MIMD machine, a re-configurable Transputer based architecture (the MEIKO Computing Surface, using up to 128 T800 INMOS Transputers) has been adopted and three solutions have been proposed. The first uses a ring of Transputers. Then an improvement of performance is reached by

diminishing the amount of communication required; such a result has been achieved by using a linear array of processors. The mapping of the algorithm on a triangular array of processors has also been studied. This solution allows the use of an arbitrary number B of processors provided that $B = p(p+1)/2$, p being an integer number. This mapping shows performance better than the linear mapping. The investigation on MIMD computers is concluded with a comparison of the results achieved by using the nCUBE2 with 64 processing elements.

With reference to SIMD machine, tests on the Connection Machine CM-200 and the MasPar MP-1 have been performed. CM-200 is equipped with 8192 single bit processors, whereas MP-1 has 4096 four bit processors. The QRD has been mapped onto a mesh architecture for both machines.

Without going into the details, which are described in [6], the main conclusions of the work are the following. The experimental work done suggests to map the dependence graph of the systolic array for the QRD algorithm on a MIMD machine configured as a triangular array. An achievable data throughput is in the order of 10 KHz for a STAP with $MN=16$ and 120 PEs using the MEIKO Computing Surface. A data throughput in the order of 100 KHz should be feasible either with advanced Transputers or with devices like the Texas TMS320C40. These conclusions, which date back eight years ago, should be reconsidered in the light of the more powerful COTS (Commercial Off The Shelf) machine available today. Table 1 summarizes pros and cons of the hardware implementation of STAP based on COTS.

6. EXPERIMENTS WITH VLSI BASED CORDIC BOARD

To explore the possibility of achieving better computational performance and using compacter systems - for installation in an operational radar - a QRD algorithm has been mapped on an application specific prototyping platform which contains four VLSI CORDIC ASICs and some FPGAs (Field Programmable Gate Arrays) [9]; this work was done in co-operation with the Technical University of Delft (The Netherlands).

The test-bed platform mainly consists of a large (modular) memory buffer that is connected to a Sun Workstation via a VME bus. The memory buffer stores data that flow through the application board, back into the buffer. The application board consists of four CORDIC processors which are mesh-connected. These four processors perform complex rotations on two-dimensional complex vectors. The CORDIC processor is a pipeline processor operating in block floating point. The physical connections between the CORDIC has been implemented via Xilinx chips. In the benchmark described in [9], the triangular systolic array was mapped on the 2x2 CORDIC application board of the tested platform. This four CORDIC mesh corresponds functionally to one of the processing nodes constituting the triangular systolic array. However, as the CORDIC processors are pipelined processors, many of these rotations can be performed at a very high throughput rate (the clock rate of the pipe), provided a schedule can be found such that the pipe can be kept filled. Such a schedule can indeed be found for the QRD algorithm.

The results of the benchmark may be briefly summarized as follows. With a 100% pipeline utilization of the CORDIC, the throughput can be computed simply as,

$$\text{Throughput} = \frac{\text{clockfreqCORDIC}}{\text{number of rotations}} \quad (7)$$

where "clockfreqCORDIC" is the clock frequency of the CORDIC processor (only 5 MHz in the experiments, just to show that no extremal values are needed), and "number of rotations" is the number of rotations (vectorizations included) for the case where we simulate a system of MN degrees of freedom.

For $MN=10$ the throughput is approximately 80 KHz, i.e. 80000 input vectors could be processed per second, which is better than the results reported in Section 5 where larger computers and higher clock frequencies were used. In a non-experimental implementation of the CORDIC system described in this Section, clock

frequencies up to 40 MHz are easily achievable; this would improve the throughput even further within a factor of 8.

Table 2 summarizes the pros and cons of the hardware implementation of STAP based on custom VLSI. Selection between COTS and VLSI is still an open question; the specialized technical literature reports descriptions of experimental systems using both the two technologies: a consensus has not been found yet on which technology to use, even though the trend seems today in favor of COTS.

7. PROCESSING OF RECORDED LIVE DATA

The data recorded by the Naval Research Laboratory (NRL-USA) airborne multi-channel radar system have been processed by a systolic trapezoidal array which implements the STAP [7]. The performance of the algorithm have been evaluated against ground clutter, littoral clutter and jammer. Vehicular traffic has also been detected. The systolic array processing has been emulated with a MATLAB software tool.

The airborne radar system used by NRL for its STAP flight test program is a modified AN/APG-125 surveillance radar; the operating frequency is 420-450 MHz. The array consists of 10 hooked dipole antennas spaced approximately a half wave length apart, mounted in a 90 degree corner reflector to provide elevation pattern shaping. The two outer dipoles are terminated yielding eight channels with roughly equivalent element patterns and 3 dB beam widths of 80 degrees for both azimuth and elevation. The array was energized with a high power corporate feed which applied a taper on transmit such that the maximum azimuth sidelobe level is 25 dB down with respect the main beam.

The receiving system consists of 8 identical channels with each channel having a UHF preamplifier, mixer, VHF amplifier band pass filter and a synchronous demodulator. The synchronous demodulator consists of two demodulators, one referenced to the coherent oscillator (COHO) and the other referenced to the COHO shifted by 90 degrees. This yields two bipolar video channels, one in phase (I), the other quadrature phase (Q). Each I & Q signal is converted to digital by a 10 bit, 5 MHz analogue to digital converter. The radar Pulse Repetition Frequency (PRF) is 300/750 pps.

The output of the receiving system is 16 digital channels for a total digital word width of 160 bits with a clock rate of 200 nsec. This yields a data bandwidth of 800 Mbps which is buffered in real-time and stored in magnetic tape.

7.1 SYSTOLIC ALGORITHM FOR LIVE DATA PROCESSING

As indicated in Figure 1, the radar has an array of $N=8$ antennas and receiving channels. Each of these receives M echoes from a transmitted train of M (up to 18 in the actual radar) coherent pulses with a PRI of $T=K\tau$ seconds where τ is the Nyquist sampling period (i.e. the range cell duration). The STAP is a two-dimensional filter in the “direction of arrival (DOA)-Doppler frequency (f_D)” plane. As a result STAP focuses a main beam towards the target and nulls out the regions of the “DOA- f_D ” plane containing the interference.

QRD constitutes the fundamental component of voltage-domain algorithm. It operates recursively by using each snapshot of data to update the on-line estimation of the disturbing environment without forming the interference covariance matrix and only requires $O(N^2M^2)$ arithmetic operations to be performed every sample time. The scheme of Figure 1 has been applied to the data recorded by the NRL radar.

7.2 DATA FILES USED IN THE DATA REDUCTION EXPERIMENTS

This section describes the data files, recorded by NRL radar, used for space-time processing experiments. The files refer to ground clutter, land-sea clutter interface, and jamming. The following information have been extracted by the data files, namely: (i) echo power in a radar receiving channel versus range, (ii) the

probability density function (pdf) of the amplitude and phase of the radar echoes, (iii) the eigenvalue spectrum, and (iv) the two-dimensional power spectral density of the clutter versus f_D and DOA. In this paper, just a subset of these information is enclosed.

7.2.1 Ground clutter

Two data files were examined, namely DL050 and DL087. For these files we have calculated the amplitude and phase histograms of the radar echoes. The histograms have been estimated using 896 echoes along range. The amplitude histograms show visually a good fit with the Rayleigh pfd. One more test to verify whether the histogram adequately matches the Rayleigh pdf is to calculate the mean to median ratio. The estimated value is 1.115, while the exact value results 1.442. The histogram of phase is approximately uniform. For file DL050 the spectrum of eigenvalues of the interference covariance matrix is reported in Figure 4. The number of antenna is 8, while the number of PRIs is the parameter of the curves ranging from 1 to 18. The covariance matrix has been estimated by averaging 896 independent samples along range. The maximum eigenvalue has been normalised to 0 dB. The minimum eigenvalue, corresponding to the curve labelled with "18" gives a good estimate of the noise floor in each receiving channel; before normalisation this value is about 10 dB. The clutter plus noise power value amounts to 45 dB in each receiving channel; this value has been determined by averaging along range the received signal on the 1st antenna. Thus the clutter-to-noise power ratio is 35 dB.

7.2.2 Land-sea clutter

Figure 5 portrays the power vs. range of the echoes collected by the 1st antenna for the data DR075. At the 480th range cell the transition from sea to land is clearly visible. The sea clutter power, estimated along the first 200 range cells, amount to 12.8 dB. The land clutter power estimated from 600th to 800th range cells measures 30.2 dB.

7.2.3 Jamming

The data file DW015 refers to jamming overland. The jammer appears at the end fire, i.e. DOA=90°. Figure 6 reports the eigenvalues (normalised to 0 dB) of the estimated covariance matrix (over 300 range cells) for N=8 antenna and M=1 PRI (curve a) and N=8 and M=2 (curve b). The presence of one principal eigenvalue in the curve (a) indicates the presence of one jamming source. We also estimates (over 300 range cells) from the data file that the jammer plus noise power is equal to 36.5 dB. The thermal noise, evaluated by the minimum eigenvalue of the interference covariance matrix is 30 dB. Thus the jammer-to-noise power ratio is 6.5 dB.

7.3 PERFORMANCE EVALUATION

The detection performance of the systolic array of Figure 1 depends upon the array parameters, the interference environment and the target signal features. The parameters defining the trapezoidal array are: (i) the dimension N,M of the data snapshot vector which equal the number of input lines to the triangular systolic canceller, (ii) the forgetting factor of the QRD canceller and (iii) the number L of linear columns for constraints. Synthetic targets as well as signals injected in the receiver are used to determine the integration of target echoes. Performance during steady state are measured in terms of: (a) Improvement Factor (IF), (b) visibility curve, i.e. IF vs. target f_D sweeping across the PRF and (c) the two-dimensional response of the adaptive system versus DOA and f_D .

7.3.1 Performance against ground clutter

Consider the file DL087. Assume to have a trapezoidal array with one antenna (N=1), eighteen pulses (M=18) and L=3 linear columns (processing cells DE of Figure 1). The constraints in the three columns are set to detect a target having the following Doppler frequencies: 0.5 PRF, 0.25 PRF and 0 PRF. A synthetic target

having a Doppler frequency value of 0.5 PRF was added at the 264th range cell. Figure 7a, b and c show the power in dB of the residue signals at the output of the three columns. Note that the target echo appears only in the Figure 7a as expected; the estimated IF is 35 dB.

7.3.2 Performance against sea-land clutter

The file DR075 contains a test target, injected in the receiver at the 3547th range cell. The Doppler frequency of the target is 0.5 PRF and the DOA is 0°. Figure 8 portrays the power in dB of the residue signal obtained by adaptively processing the echoes received by N=8 and M=18 PRIs. The trapezoidal systolic array has one vertical column ($L=1$) with the constraints $f_D=0.5$ PRF and DOA=0° which are fully matched to the target signal. The spike appears at the 3691st cell which differs from the original target range due to the space-time filter delay which is equal to the total number of degrees of freedom, i.e. 144.

The visibility curve for a fictitious target having DOA=0° and Doppler frequency sweeping across the radar PRF is reported in Figure 9; the visibility curve is approximately flat except around $f_D=0$ which is the mean Doppler frequency of clutter after compensation of the platform speed. From visibility curve the maximum IF value amounts to 44 dB, while the optimum IF would be 45.5 dB which is just few dBs higher than the values shown in visibility curve.

7.3.3 Performance against jammer

The improvement factor of an array of N=8 antennas, one PRI (M=1) and one column constraint is shown in Figure 10 as a function of the DOA of a simulated target scanning the angular interval [-90°, +90°]. The jammer is that described in section 7.2.3. It is noted that the maximum IF is about 13 dB, while the optimum IF value would be 17 dB. The 4 dB loss is due to the adaptation of the systolic arrays.

7.4 DETECTION OF VEHICULAR TRAFFIC

The detection of vehicular traffic has been attempted along US route 50 (see, for details, [7]). Four points on the route have been selected (bearing angle relative to the array normal, with positive values coming from the right hand side of the array):

1st point: range=39268 m, azimuth=-5.8°; 2nd point: range=39268 m, azimuth=-3.4°;
 3rd point: range=39429 m, azimuth=-0.6°; 4th point: range=39429 m, azimuth=1.0°;

The systolic array processes the snapshots along the range cells received by 8 antennas and 18 PRIs (i.e. it works with the maximum number of adaptive degrees of freedom). The adapted residue along the range cells has been further processed by a CFAR thresholding device based on cell average (CA) technique. The CFAR-CA has two guard range cells on each side of the range cell under test and twenty range cells on each side to estimate the detection threshold. The CFAR-CA has been set to guarantee a P_{FA} of 10^{-4} . Figure 11 depicts the adapted residue vs. range when the receiving antenna pattern is focused at -5.8°, which is the azimuth value corresponding to the 1st point on the US route 50. The analysed Doppler frequency is 0.225 PRF which corresponds to a radial speed of 23.2 m/s (i.e. 83.52 km/h) compatible with vehicular traffic. A detection appears at the 932th range cell that comfortably compares with the expected location of the target. Similar results have been obtained for the other three points on the US route 50 [7].

8. CONCLUDING REMARKS

The research work described in this paper and the enclosed references are also relevant for other radar applications, sometimes simpler than the STAP, namely (i) ground based or ship-borne radars for clutter cancellation and (ii) ground based or ship-borne radars equipped with a multi-channel phased array antenna for

jamming cancellation. The STAP reverts to the first application by setting $N=1$, while becomes the second application for $M=1$. Thus, the adaptive processing architectures described in this paper are applicable also to the (i) and (ii) systems. In general, the number of degrees of freedom involved is one order of magnitude less than the STAP case; this makes less critical the implementation of a VLSI based systolic array. A practical application of systolic processing for classical ground based or ship borne radar is described in [17] where it is shown how to combine in one systolic scheme the two functions of adaptive interference cancellation and side lobe blanking. The application of STAP to Synthetic Aperture Radar for detecting and imaging of slowly moving targets is discussed in [5] and [13]. In this respect the procedure to form the SAR image by one-bit processing plays a role; this procedure is also applied in the along track interferometry (ATI) – SAR to detect moving targets [18]. It can be shown that this approach offers a considerable computational advantage; FPGA technology has been successfully applied to implement the one-bit SAR processing. The enormous progress done in the technology for signal processing is under our eyes. Today the key words are: heterogeneous processing (i.e.: based on VLSI, ASIC, FPGA, RISC, MEMS, photonic etc.), virtual and rapid prototyping, modularity and flexibility of processing architectures, re-use and porting of the same, COTS approach to software and hardware, software language (e.g.: System C; Handel C for FPGA), complex design tools like Ptolemy. All these techniques and technologies are conceived to contrast the obsolescence which is one of the most important problems to face today.

9. REFERENCES

- [1] A.Farina, “Antenna Based Signal Processing Techniques for Radar Systems”, Artech House , 1992.
- [2] A. Farina, L. Timmoneri, “Space-time processing for AEW radar”, Proc. of Int. Radar Conference, Radar 92, Brighton (UK), 12-13 October 1992, pp. 312-315.
- [3] L. Timmoneri, I.K. Proudler, A. Farina, J.C. McWhirter, “QRD-based MVDR algorithm for multipulse antenna array signal processing”, IEE Proc. Radar, Sonar and Navigation, Vol. 141, No. 2, April 1994, pp. 93-102.
- [4] A. Farina, S. Barbarossa, M. Ceccarelli, A. Petrosino, L. Timmoneri, F. Vinelli, “Application of the extreme eigenvalue analysis to signal and image processing for radar”, Invited paper, Colloque International sur le Radar, Paris, 3-6 May 1994, pp. 207-213.
- [5] A. Farina, S. Barbarossa, “Space-time-frequency processing of synthetic aperture radar signals”, IEEE Trans. on Aerospace and Electronic Systems, vol.30, no. 2, 1994, pp.341-358.
- [6] A. D’Acierno, M. Ceccarelli, A. Farina, A. Petrosino, L. Timmoneri, “Mapping QR decomposition on parallel computers: a study case for radar applications”, IEICE Trans. on Communications, Vol. E77-B, No. 10, October 1994, pp. 1264-1271.
- [7] A. Farina, R. Graziano, F. Lee, L. Timmoneri, “Adaptive space-time processing with systolic algorithm: experimental results using recorded live data”, Proc. of the Intl. Conference on Radar, Radar 95, Washington DC, May 8-11, 1995, pp. 595-602.
- [8] A. Farina, L. Timmoneri, “Antenna based signal processing techniques and space-time processing”. Tutorial, Int. Conference, Radar 95, Washington D.C. (USA), May 8-11, 1995.
- [9] P. Kapteijn, E. Deprettere, L. Timmoneri, A. Farina, “Implementation of the recursive QR algorithm on a 2x2 CORDIC test-board: a case study for radar application”, Proc. of the 25th European Microwave Conference, Bologna (Italy), 1995, pp. 490-495.
- [10] A. Farina, A. Saverione, L. Timmoneri, “The MVDR vectorial lattice applied to space- time processing for AEW radar with large instantaneous bandwitdh”, IEE Proc. Radar, Sonar and Navigation, Vol. 143, No. 1, February 1996, pp. 41-46.
- [11] A. Farina, L. Timmoneri, “Parallel algorithms and processing architectures for space-time adaptive processing”, CIE - International Conference on Radar - ICR96, Beijing (P. R. of China), Invited Paper for the Workshop on STAP, 1996, pp. 771-774.
- [12] P. Bollini, L. Chisci, A. Farina, M. Giannelli, L. Timmoneri, G. Zappa, “QR versus IQR algorithms for adaptive signal processing: performance evaluation for radar applications”, Proc. of IEE on Radar, Sonar and Navigation, October 1996, Vol. 143, No. 5, pp.328-340.

- [13] P. Lombardo, A. Farina, "Dual antenna baseline optimization for SAR detection of moving targets", Proc. of ICSP96, Beijing, P.R. China, pp. 431-433.
- [14] A. Farina, P. Lombardo: "Space-time adaptive signal processing", Tutorial, Int. Conference on Radar, Radar 97, Edinburgh (UK), 13 October 1997.
- [15] A. Farina, L. Timmoneri, "Real time STAP techniques", Proc. of IEE Symposium on Space Time Adaptive Processing, London, 6th April 1998, pp. 3/1-3/7.
- [16] A. Farina, L. Timmoneri, "Real time STAP techniques", Electronic, Communication and Engineering Journal (IEE) Special Issue on STAP, Vol. 11, No.1, February 1999, pp. 13-22.
- [17] A. Farina, L. Timmoneri, "Systolic schemes for joint SLB, SLC and adaptive phased-array", Proc. of the IEEE Intl. Conference Radar 2000, Washington DC, 7-12 May 2000, pp. 602-607.
- [18] V. Pascazio, G. Schirinzi, A. Farina, "Moving Target Detection by Along Track Interferometry", IGARSS 2001, Sidney (Australia), July 2001.

10. ACKNOWLEDGEMENTS

The Author sincerely acknowledges with thanks the cooperation of His Colleague Dr. L. Timmoneri (AMS) that has greatly contributed to the work described in this paper. Other Colleagues, duly quoted in the References, have noticeably contributed to the research.

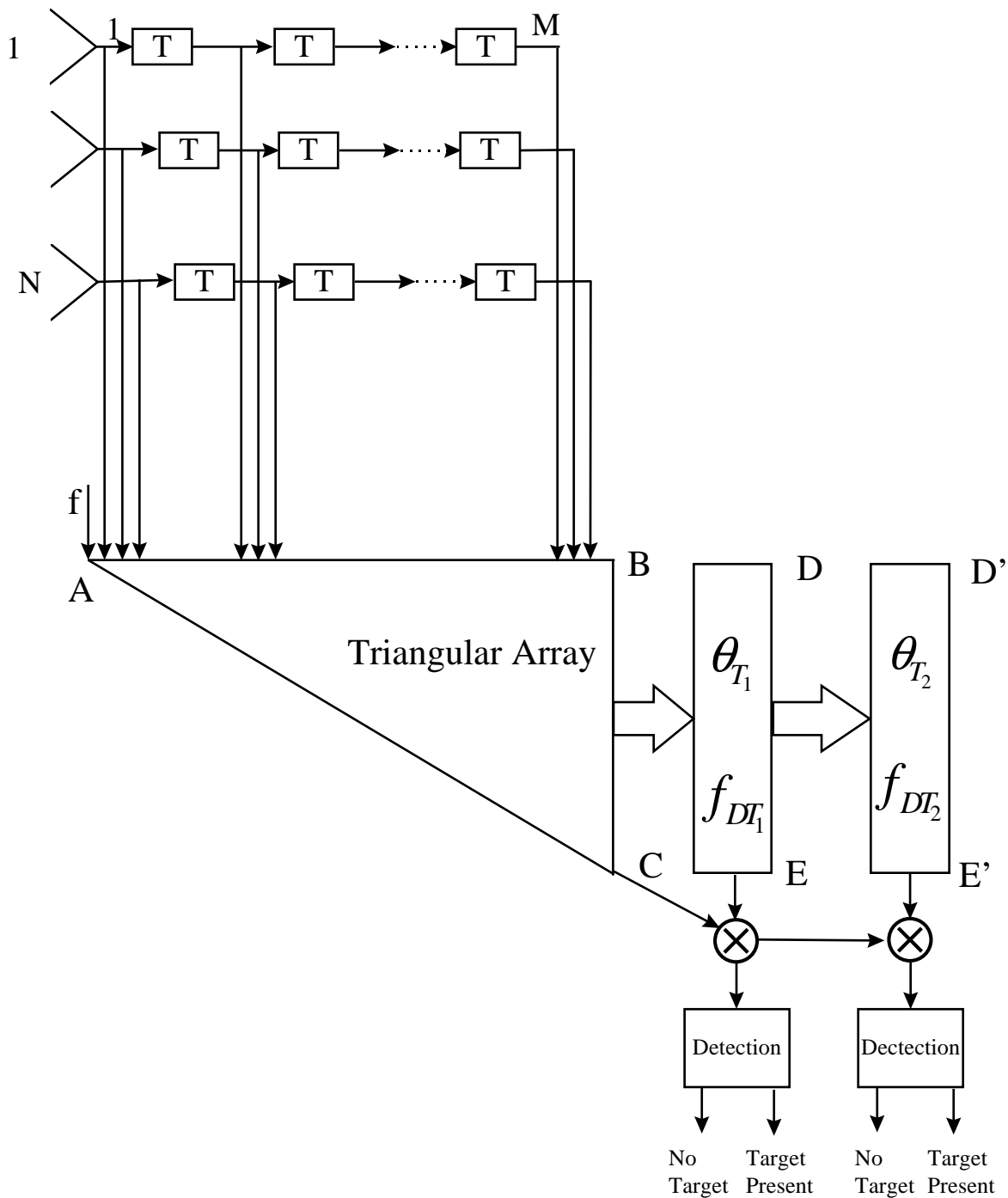


Figure 1: Baseline QRD based MVDR flow graph (after [3]).

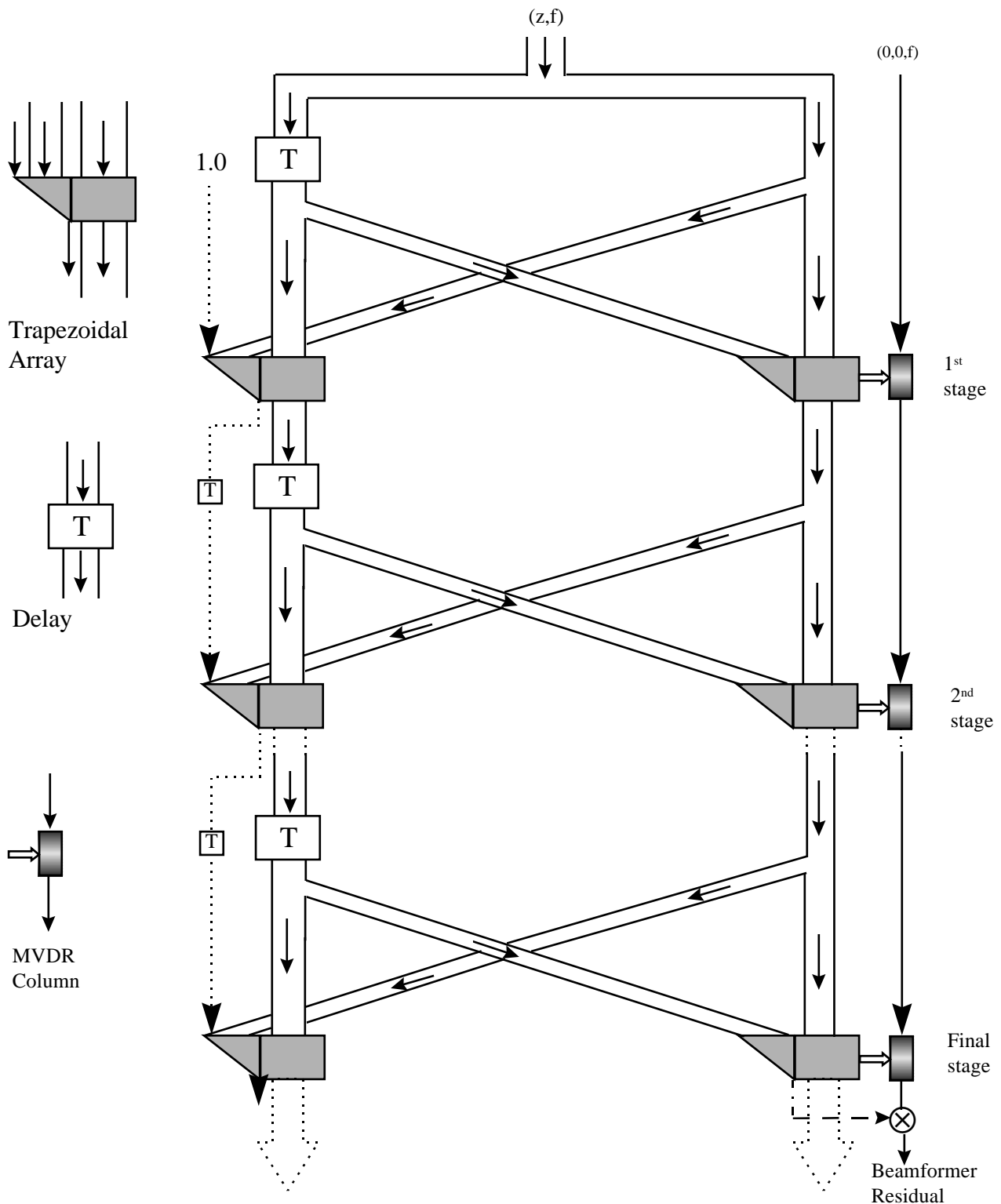


Figure 2: MVDR lattice processor (after [3]).

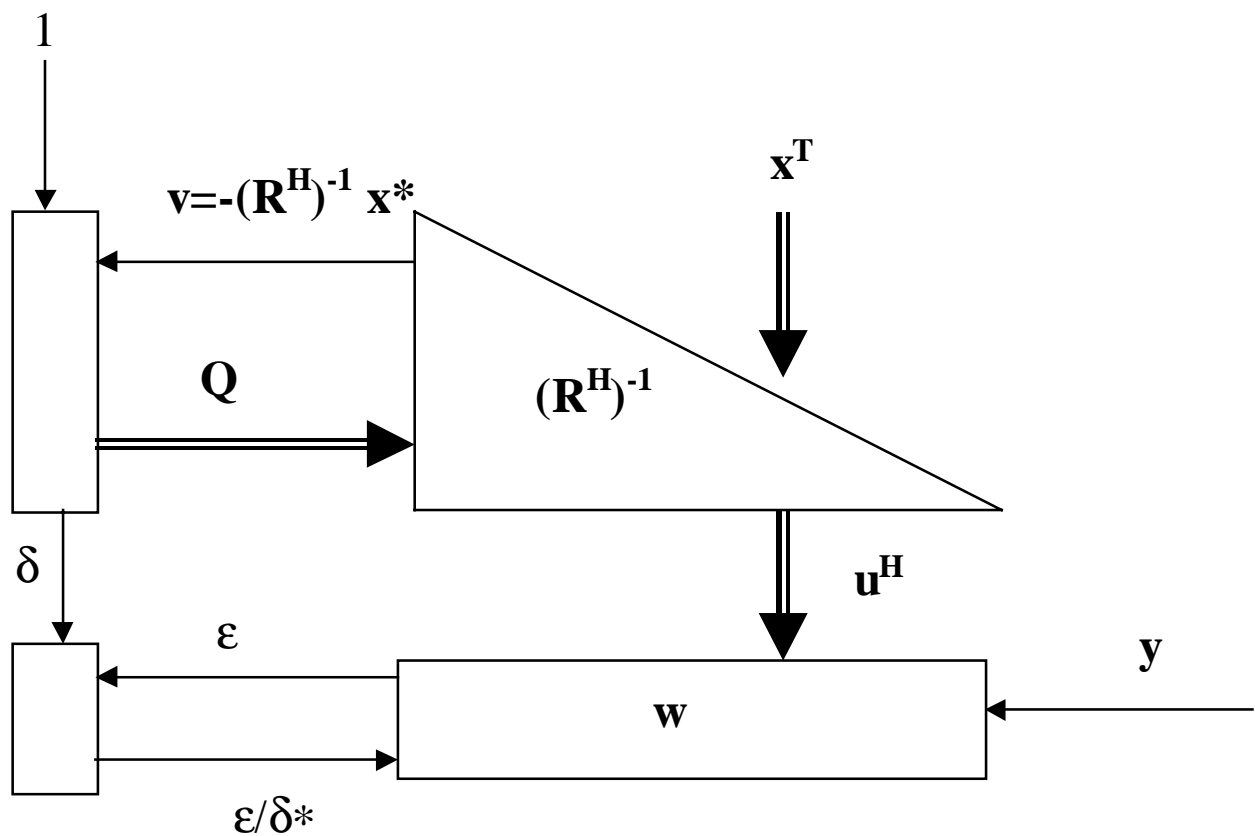


Figure 3: RLS-IQR array (after [12]).

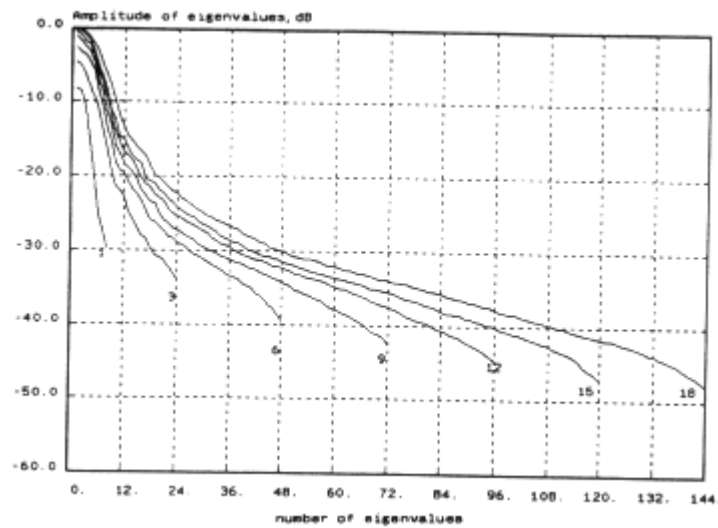


Figure 4: Eigenvalue spectrum for data file DL050 (ground clutter) (after [7]).

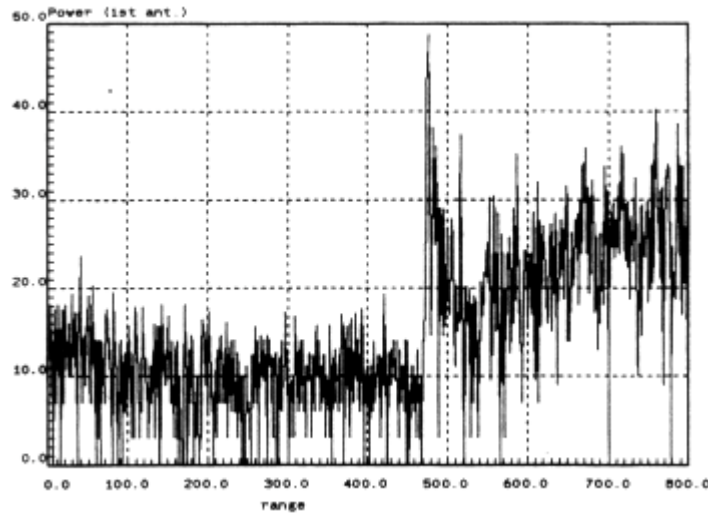


Figure 5: Power versus range of the radar echoes collected by the 1st antenna of the array (after [7]).

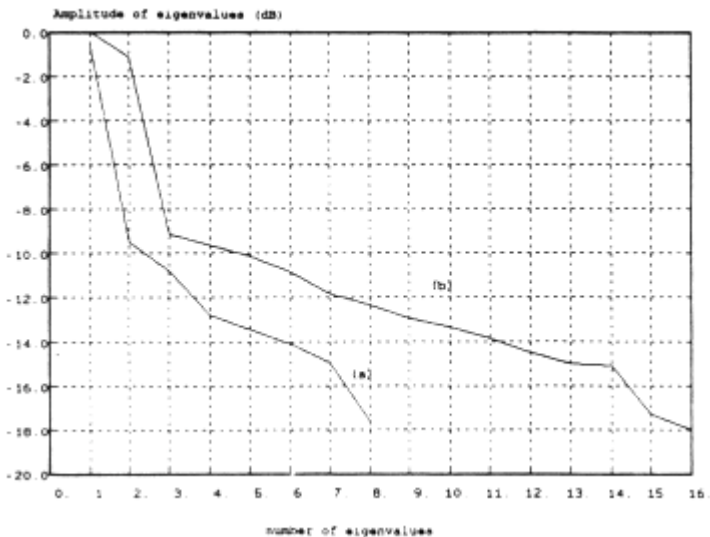


Figure 6: Spectrum of eigenvalues of jamming interference. Curve a: N=8 antennas and M=1 PRI; curve b: N=8, M=2 (after [7]).

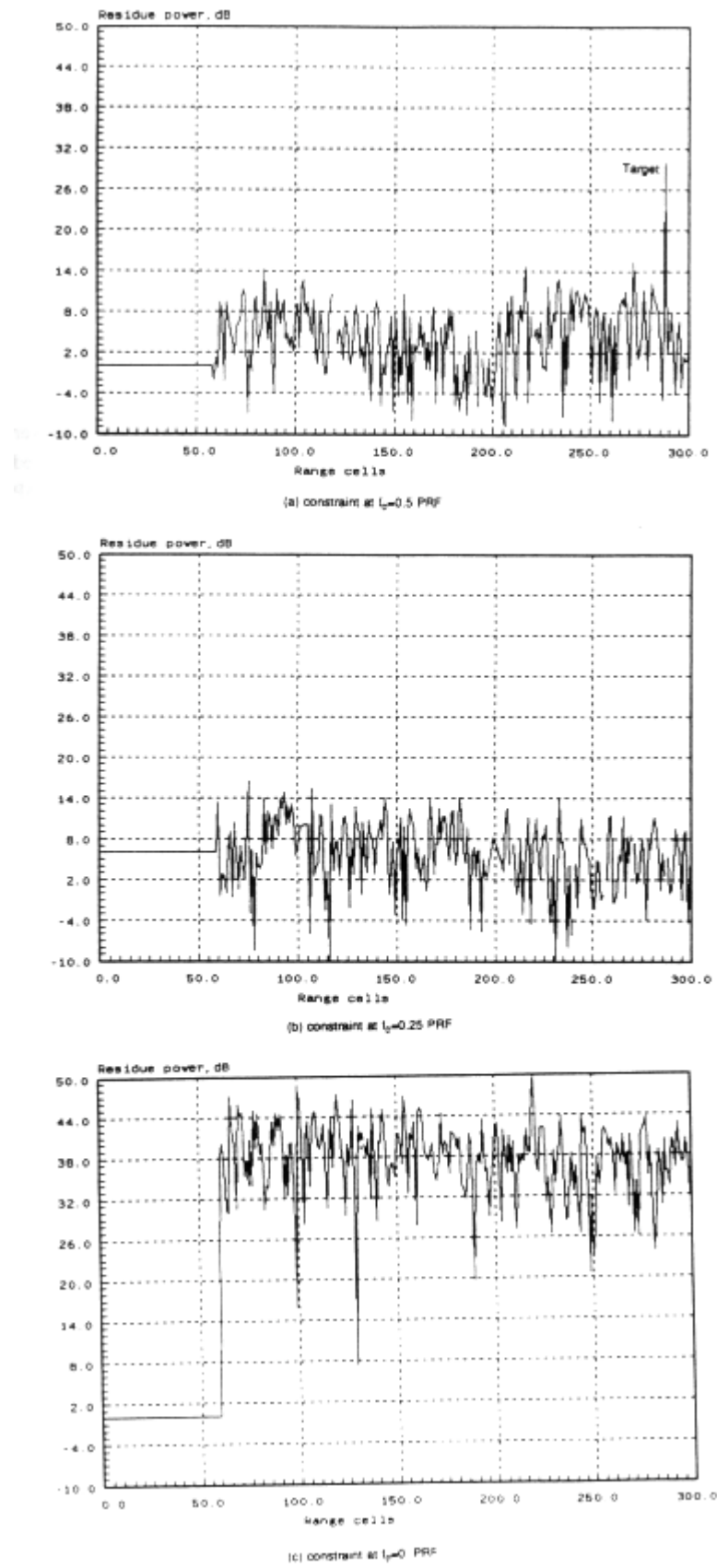


Figure 7: Processing of ground clutter live data (after [7]).

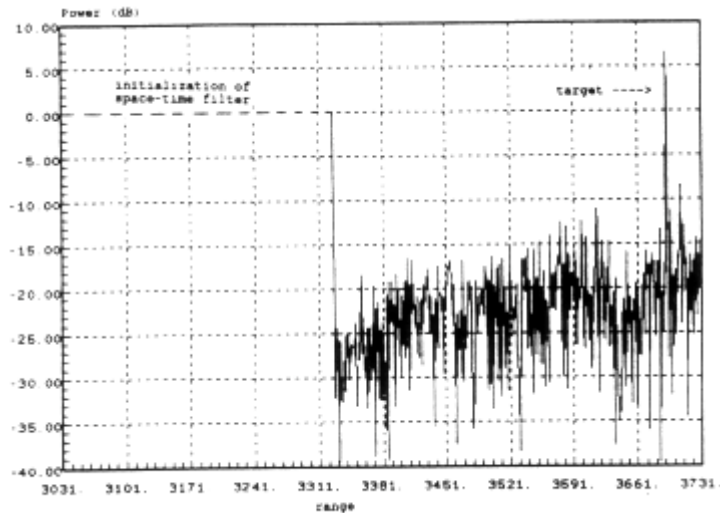


Figure 8: Power of residue signal for data file DR075 (after [7]).

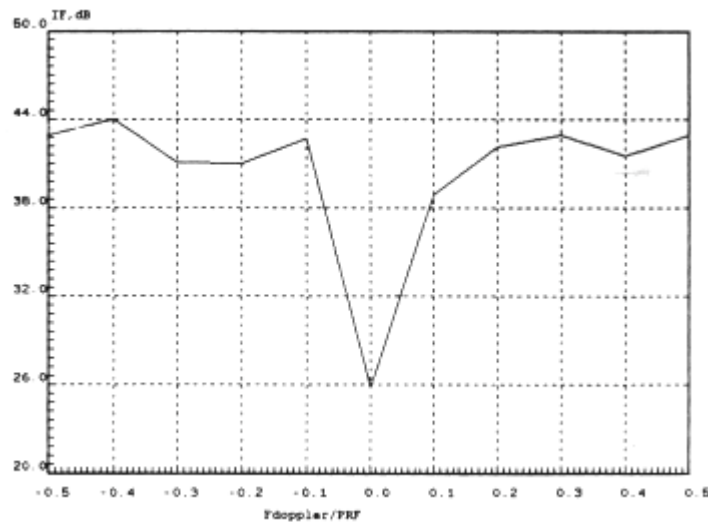


Figure 9: Visibility curve for data file DR075 (after [7]).

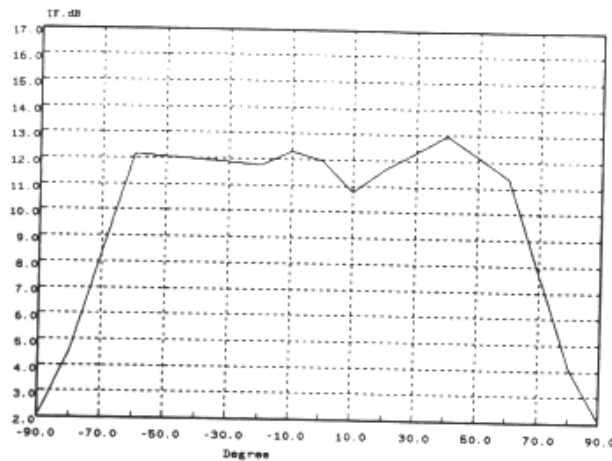


Figure 10: IF vs. DOA of a simulated target (after [7]).

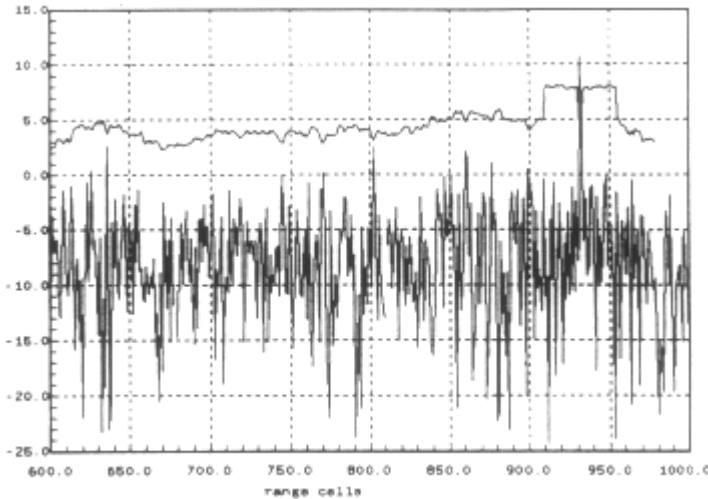


Figure 11: Adapted residue power and detection threshold curves vs. range cell (after [7]).

Pros	Cons
programmable & flexible	complex infrastructure including I/O control and protocols
robust to technology obsolescence	high speed data buses
re-use of previously developed software	high speed memory and memory control
essential in design trajectory of VLSI custom architecture (search for trade-off between flexibility and modularity, parallelisation options)	multi-DSP infrastructure requires extra-overhead which brings to a decline of ideal linear increment of computational power.

Table 1 : Pros and cons of COTS.

Pros	Cons
extremely high throughput (bulk processing)	low degree of flexibility
limited size and power consumption	expensive for limited number of pieces to produce

Table 2 : Pros and cons of VLSI.

This page has been deliberately left blank

Page intentionnellement blanche

Application of STAP in Advanced Sensor Systems

William L. Melvin

Georgia Tech Research Institute

7220 Richardson Road

Smyrna, GA 30080, USA

bill.melvin@gtri.gatech.edu

Summary

Space-time adaptive processing (STAP) is a multidimensional analog of the well-known, one-dimensional adaptive sidelobe canceler developed in the late 1950's. It enables adaptive cancellation of interference in a two-dimensional space. When the two-dimensional target power spectral density differs from that of the interference, STAP leads to enormous improvements in target detection potential. Owing to this potential, STAP has application to current and future airborne, spaceborne, bistatic and ground-based radar sensors; in this set of lecture notes, we consider the role STAP plays in each of these systems. We begin with the airborne case, describing the nature of ground clutter and its impact on target detection. This serves as segue to a discussion of STAP and its comparison with competing methods. Next, we consider spaceborne radar systems. Since STAP is a member of the class of super-resolution algorithms, it enables the design of spaceborne moving target indication radar with smaller aperture; this is an important consideration when launching the satellite radar system. Bistatic systems must contend with spectrally severe ground clutter returns, for which STAP offers a potential solution. Herein, we describe bistatic STAP, with particular emphasis on the nonstationary nature of the bistatic clutter environment. We conclude by considering STAP application to terrain scattered jamming; ground based radar serves as the focus of this final discussion.

1. Introduction

In [1], we discuss the basic theory of space-time adaptive processing (STAP) and related detection theory. This set of lecture notes considers practical aspects of STAP. Moving target indication (MTI) serves as our primary focus.

STAP is a higher dimensional version of the adaptive sidelobe canceler developed in the late 1950's and early 1960's [2]. Reed and Brennan discuss the theory of STAP for airborne radar in a seminal 1973 paper [3]. In years since the Brennan and Reed paper, STAP has been vigorously researched. The recent advancement of high speed, high performance digital signal processors now make fielding STAP-based radar systems a reality. We consider the use of STAP in diverse aerospace radar applications in this paper, examining airborne, spaceborne and bistatic systems. Additionally, we describe STAP for terrain scattered jamming (TSJ) mitigation.

Radar sensors can measure spatial direction of arrival in azimuth and elevation, or cone angle; slow-time phase progression; fast-time delay; and, polarization. Additionally, the processor can operate on data taken over multiple radar scans. Adaptive processing exploits this signal diversity to enhance detection capability. The Fourier transforms of slow-time and fast-time yield Doppler frequency and range information, respectively. By subarraying an electronically scanned antenna (ESA) into multiple receive channels, the radar can measure direction of arrival. A linear antenna measures cone angle [4], an ambiguous measurement resulting from the linear array's inability to separate time delay attributable to either azimuth or elevation angles.

Aerospace radar must cope with ground clutter while attempting to detect airbreathing or surface moving targets. The platform velocity induces a clutter Doppler shift varying over angle. Thus, ground clutter exhibits coupling in both angle and Doppler. The locus of points in the angle-Doppler power spectral density

(PSD) corresponding to ground clutter signals is known as the clutter ridge [4-5]. STAP provides a means of suppressing clutter by exploiting spatial and temporal signal diversity. In this case, slow-time measurements provide the necessary temporal degrees of freedom (DoF).

Since narrowband jamming is correlated in angle, spatial diversity (adaptive notching in azimuth or elevation sidelobes) adequately suppresses the jamming signal. Mainlobe jammer mitigation is much more challenging. Terrain scattered jamming (TSJ) – jamming energy scattered off the earth’s surface – enters the mainlobe of the antenna. For this reason, spatial diversity by itself does not provide adequate jammer suppression. Since the jammer does not exhibit correlation over slow-time, diversity in this domain is of no value. However, the jammer waveform exhibits correlation in the fast-time dimension. Hence, the digital signal processor can adaptively combine spatial and fast-time measurements to cancel TSJ while passing the target signal with maximal gain. This adaptive processing scheme is also referred to as STAP; fast-time signal diversity, versus slow-time, is implied.

In Section 2 we discuss fundamental aspects of ground clutter mitigation for the airborne radar platform. We define the airborne MTI and ground MTI missions and identify advantages STAP offers for these particular applications. Furthermore, we develop models for ground clutter and narrowband noise jamming. We delve into important aspects of the null-hypothesis covariance matrix and examine adaptive training issues. We include measured radar data examples.

Section 3 builds on results from Section 2, describing STAP for spaceborne radar systems. We investigate the key distinctions between airborne and spaceborne radar systems, examine STAP’s role in overcoming aperture limitations, and provide simulated data examples showing the behavior of ground clutter in a notional space-based radar (SBR). Section 4 develops a basic understanding of the issues in bistatic STAP. Clutter nonstationarity is the key consideration in the bistatic case. Using numerical simulation, we examine STAP performance applied to multichannel bistatic radar data. We conclude by examining TSJ suppression using STAP in Section 5. We develop basic jammer space and fast-time models and a space-(fast)time adaptive processing implementation.

In the following discussion, the term *interference* subsumes both clutter and noise jamming signals. Signal-to-interference-plus-noise-ratio (SINR) describes the output signal power relative to the interference. Signal-to-noise ratio (SNR) is characteristic of output signal power relative to uncorrelated system noise, and thus characterizes the noise-limited performance of the radar.

2. STAP in Airborne Radar

Moving target indication (MTI) radar must detect, track and identify targets of various classes. Adequate target detection is fundamental to all other processing steps. The target Doppler shift often helps distinguish a mover from stationary ground clutter. However, in many cases, Doppler processing alone does not adequately enhance SINR, and so missed detections result. By adapting over space and slow-time samples, STAP increases SINR, consequently improving detection performance.

Two classes of MTI radar exist. Airborne moving target indication (AMTI) involves the detection of airbreathing vehicles. Such targets generally have relatively high radial velocities and lower radar cross sections. The maneuverability of the target limits the coherent dwell, hence lessening the attainable integration gain and Doppler resolution. Sidelobe clutter is a major impediment in AMTI. On the other hand, ground moving target indication (GMTI) involves detecting slower moving surface targets. Ground targets generally are less mobile and exhibit higher radar cross section than their airborne counterparts. The potential for longer dwell time suggests enhanced output SNR. However, the low radial velocity of the target places it in direct competition with strong mainbeam clutter. Figure 1 is a notional view of clutter, jamming and a moving target signal. Projecting into the angle domain, we find that mainbeam clutter masks the target; conversely, projecting into the Doppler domain, the problematic nature of sidelobe clutter and noise jamming is evident. STAP attempts to optimize a two-dimensional space-time filter response at a given range cell to maximize SINR.

A collection of many scatterers along an iso-range comprises the ground clutter return. An approximation to the corresponding clutter space-time snapshot for the k^{th} range is

$$\mathbf{x}_{k/C} = \sum_{m=1}^{N_c} \sum_{n=1}^{N_a} \mathbf{a}_{m,n} \odot \mathbf{s}_{s-t}(\phi_{m,n}, \theta_{m,n}, f_{d/m,n}) \quad (1)$$

where N_c is the number of clutter patches, N_a is the number of range ambiguities, $\mathbf{a}_{m,n} \in \mathbb{C}^{NM \times 1}$ is the vector of voltages observed at each of M spatial channels over N pulses, and $\mathbf{s}_{s-t}(\phi_{m,n}, \theta_{m,n}, f_{d/m,n}) \in \mathbb{C}^{NM \times 1}$ is the space-time steering vector for the $m-n^{\text{th}}$ clutter patch. We denote azimuth as $\phi_{m,n}$, elevation as $\theta_{m,n}$ and Doppler frequency as $f_{d/m,n}$ for each clutter patch. Assuming statistical independence among clutter patches, the clutter covariance matrix is then given by

$$\begin{aligned} \mathbf{R}_{k/C} &= E[\mathbf{x}_{k/C} \mathbf{x}_{k/C}^H] = \sum_{m=1}^{N_c} \sum_{n=1}^{N_a} E\left[(\mathbf{a}_{m,n} \odot \mathbf{s}_{s-t}(\phi_{m,n}, \theta_{m,n}, f_{d/m,n})) (\mathbf{a}_{m,n} \odot \mathbf{s}_{s-t}(\phi_{m,n}, \theta_{m,n}, f_{d/m,n}))^H \right] \\ &= \sum_{m=1}^{N_c} \sum_{n=1}^{N_a} E[\mathbf{a}_{m,n} \mathbf{a}_{m,n}^H] \odot \mathbf{s}_{s-t}(\phi_{m,n}, \theta_{m,n}, f_{d/m,n}) \mathbf{s}_{s-t}^H(\phi_{m,n}, \theta_{m,n}, f_{d/m,n}). \end{aligned} \quad (2)$$

The symbol \odot denotes “element-wise” product. We also define $\mathbf{A}_c = E[\mathbf{a}_{m,n} \mathbf{a}_{m,n}^H]$ as the space-time correlation matrix. \mathbf{A}_c simultaneously describes the statistical nature of voltage fluctuations from pulse-to-pulse and any spatial decorrelation due to non-zero bandwidth. If the voltage due to each target scatterer is constant over the dwell, and the bandwidth is sufficiently narrow (a fraction of a percent of the radar center frequency), then (2) becomes

$$\mathbf{R}_{k/C} = E[\mathbf{x}_{k/C} \mathbf{x}_{k/C}^H] = \sum_{m=1}^{N_c} \sum_{n=1}^{N_a} \sigma_{C/m,n}^2 \mathbf{s}_{s-t}(\phi_{m,n}, \theta_{m,n}, f_{d/m,n}) \mathbf{s}_{s-t}^H(\phi_{m,n}, \theta_{m,n}, f_{d/m,n}), \quad (3)$$

where $\sigma_{C/m,n}^2$ is the single channel, single pulse clutter power for the $m-n^{\text{th}}$ patch.

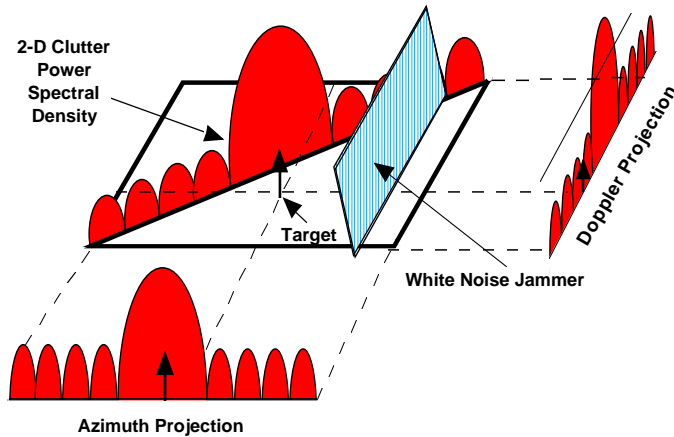


Figure 1. Notional view of the airborne radar detection problem. Clutter and jamming mask the target.

A model for the m^{th} narrowband jammer space-time snapshot is given by

$$\mathbf{x}_{k/J,m} = \sigma_{J/m} (\mathbf{u}_N \otimes \mathbf{s}_s(\phi_m, \theta_m)); \quad \mathbf{u}_N \sim CN(\mathbf{0}, \mathbf{I}_N) \quad (4)$$

where $\sigma_{J/m}$ is the single channel jammer power. The complete jammer snapshot is $\mathbf{x}_{k/J} = \sum_{m=1}^{N_j} \mathbf{x}_{k/J,m}$ for N_j noise jamming sources. Since each jammer is uncorrelated and the jamming voltage is Gaussian, the jammer covariance matrix for the k^{th} range is expressible as

$$\begin{aligned}\mathbf{R}_{k/J} &= \sum_{m=1}^{N_j} E\left[\mathbf{x}_{k/J,m} \mathbf{x}_{k/J,m}^H\right] = \sum_{m=1}^{N_j} \mathbf{R}_{k/J,m}; \\ \mathbf{R}_{k/J,m} &= E\left[\mathbf{x}_{k/J,m} \mathbf{x}_{k/J,m}^H\right] = \sigma_{J/m}^2 \left(\mathbf{I}_N \otimes \mathbf{s}_s(\phi_m, \theta_m) \mathbf{s}_s^H(\phi_m, \theta_m)\right),\end{aligned}\quad (5)$$

reflecting the fact that the jammer is spatially correlated (the $\mathbf{s}_s \mathbf{s}_s^H$ term in (5)), yet white in Doppler (the \mathbf{I}_N term in (5)).

The ultimate limitation on detection performance is additive thermal noise generated by the radar receiver. Though an approximation, it is common to assume the receiver noise is white in space and time. Under such circumstances, the receiver noise covariance matrix for the noise snapshot $\mathbf{x}_{k/n}$ takes the form

$$\mathbf{R}_{k/n} = \sigma_n^2 \mathbf{I}_{NM}, \quad (6)$$

where σ_n^2 is the single channel noise variance.

The space-time snapshot is the additive combination of clutter, jamming and receiver noise snapshots. Each component is statistically independent. Thus, the space-time snapshot and covariance matrix are

$$\begin{aligned}\mathbf{x}_k &= \mathbf{x}_{k/C} + \mathbf{x}_{k/J} + \mathbf{x}_{k/n}; \quad \mathbf{x}_k \sim \mathcal{CN}(\mathbf{0}, \mathbf{R}_k); \\ \mathbf{R}_k &= \mathbf{R}_{k/C} + \mathbf{R}_{k/J} + \mathbf{R}_{k/n}.\end{aligned}\quad (7)$$

The power spectral density (PSD) is the Fourier transform of the covariance matrix, $\mathbf{R}_k \xrightarrow{\mathcal{F}} \text{PSD}$, and is a typical approach for viewing those two-dimensional frequencies occupied by colored noise. Figure 2 is an example of a typical angle-Doppler PSD for a side-looking airborne radar system. Clutter and jamming are identified in the figure. Figure 3 shows a periodogram approximation to the PSD for actual measured airborne radar data taken from the Multichannel Airborne Radar Measurements (MCARM) program [6]; as one would expect, the clutter ridge is readily apparent in this figure.

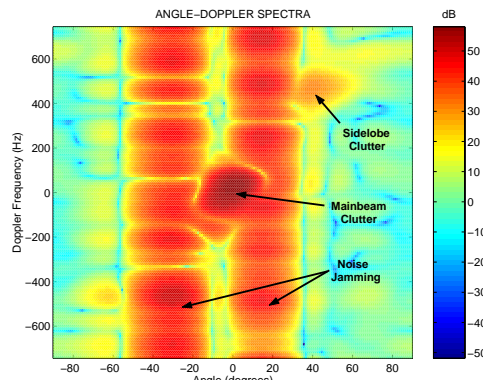


Figure 2. Angle-Doppler power spectral density, medium PRF, side-looking radar case.

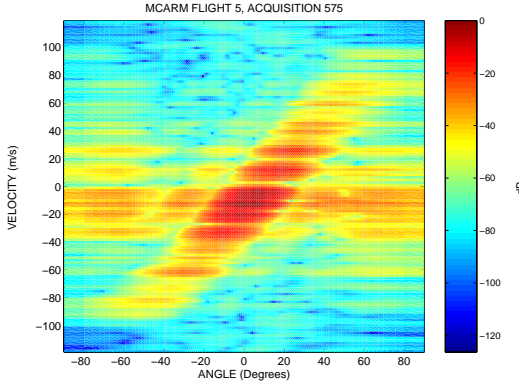


Figure 3. Clutter only power spectral density estimate for measured multi-channel airborne radar data collected as part of the Multi-Channel Airborne Radar Measurements (MCARM) effort.

An alternate spectral view is the minimum variance distortionless response (MVDR) spectra,

$$\text{MVDR}(\phi_m, \theta_m, f_{d/m}) = \frac{1}{\mathbf{s}_{s-t}^H(\phi_m, \theta_m, f_{d/m}) \mathbf{R}_k^{-1} \mathbf{s}_{s-t}(\phi_m, \theta_m, f_{d/m})}. \quad (8)$$

The MDVR spectra provides a super-resolution view of the interference. Figure 4 compares the MVDR spectra for the side-looking airborne radar example of Figure 2. In contrast, Figure 5 shows the MVDR spectra for the forward-looking radar case. The clutter ridge opens up into an ellipse for the forward-looking case; two stationary ground points on either side of the aircraft velocity vector possess the same Doppler but mirror symmetric direction of arrival.

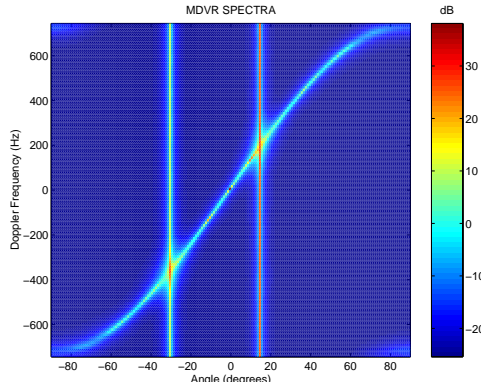


Figure 4. MVDR spectra, medium PRF, side-looking radar case.

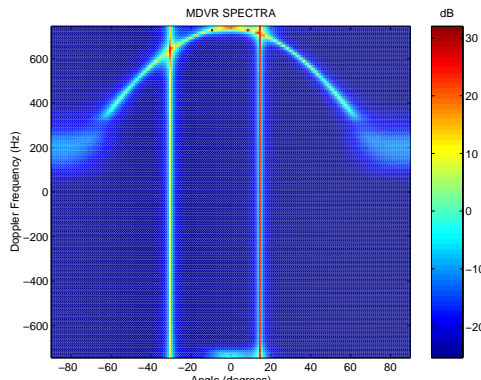


Figure 5. MVDR spectra, medium PRF, forward-looking radar case.

In contrast to the PSD or MVDR spectra, an alternate view of the characteristics arise from an eigen-decomposition. The stochastic space-time snapshot can be written via the Karhunen Loeve transform [7] as

$$\mathbf{x}_k = \sum_{m=1}^{NM} a_m \mathbf{q}_m; E[a_m a_m^*] = \lambda_m, \quad (9)$$

where \mathbf{q}_m is an eigenvector of the corresponding covariance matrix with corresponding eigenvalue λ_m . Specifically, from (9),

$$\mathbf{R}_k = \sum_{m=1}^{NM} \lambda_m \mathbf{q}_m \mathbf{q}_m^H. \quad (10)$$

The eigenvector represents a mode of the interference (direction of arrival and Doppler), while the eigenvalue represents the corresponding power. A plot of the rank-ordered eigenvalues is known as the eigenspectrum. The eigenspectrum provides insight into the interference-to-noise ratio and number of DoF the processor requires to cancel the interference. Figure 6 shows the eigenspectra for the side-looking and forward-looking cases yielding the MVDR spectra of Figures 4-5 with the jamming removed. We also include the low pulse repetition frequency (PRF) side-looking case. As a result of Doppler aliasing, the number of eigenvalues above the noise floor increases for the low PRF case; hence, more space-time DoFs are necessary to effectively cancel the interference.

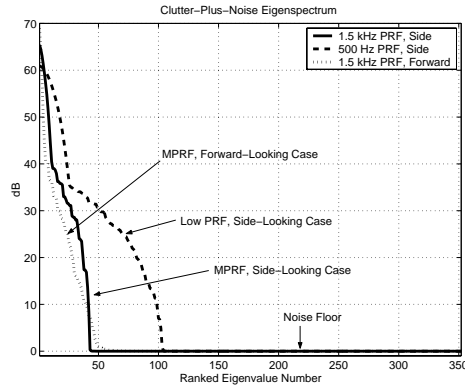


Figure 6. Eigenspectra for side-looking and forward-looking airborne platforms.

We described the SINR loss metric in [1]. Figure 7 shows the estimated SINR loss for the measured data example yielding the result in Figure 3. The legend on each plot indicates the range bin number used to estimate the unknown covariance matrix. The variability among the curves is a consequence of the heterogeneous nature of the clutter environment. For further discussion concerning the impact of heterogeneous clutter on STAP, see [1] and [8].

For comparison, Figure 8 shows a simulated SINR loss plot using the parameters taken from the measured data collection (such as transmit frequency, array size, number of subarrays, navigation data, etc.). We use the model given in (2) to simulate clutter. Observe that the clutter null between measured and simulated data matches perfectly. However, the spectral width of the measured data varies considerably from the simulated case. This occurs because the angle-Doppler relationship is deterministic, yet amplitude and spectral spread is a random process not precisely characterized in the simulation.

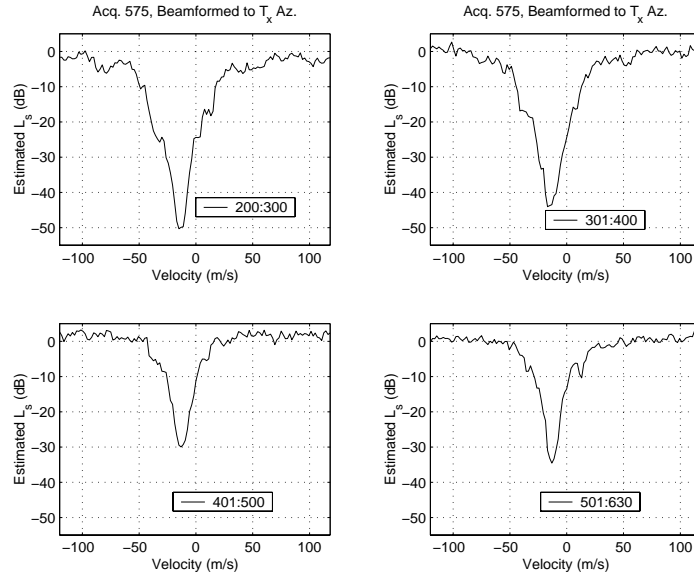


Figure 7. Estimated SINR loss for measured multi-channel airborne radar data.

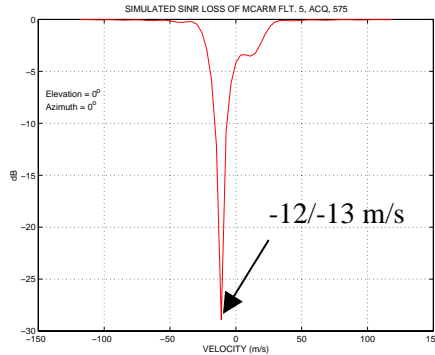


Figure 8. Simulated SINR loss using experimental parameters.

MTI radar operate with three basic PRF designations: low, medium and high. By definition, low PRF radar operate ambiguously in Doppler with no range ambiguity (range fold-over); medium PRF radar are slightly ambiguous in Doppler and range; and, high PRF radar is unambiguous in Doppler and highly ambiguous in range. Generally, high PRF modes are used for AMTI. The range fold-over is a disadvantage, since more clutter competes with the weak target. Also, special processing is necessary to unfold range. Low PRF radar is used in a variety of long range search modes; Doppler aliasing is its main disadvantage. Using STAP, the medium PRF mode is quite attractive. The adaptive processor can null competing sidelobe clutter. Staggering PRFs from dwell-to-dwell, the processor can disambiguate the target Doppler. Figure 9 compares the MVDR spectra for the low, medium and high PRF selections for our side-looking airborne radar example. The Doppler aliasing is notable in the low PRF case; the adaptive processor will use more DoF to cancel the interference in this case. Figure 6 further illustrates the expansion of the interference subspace in the low PRF case through a doubling of the number of significant eigenvalues. The requirement for more DoFs has important ramifications when implementing practical reduced-dimension and reduced-rank STAP [1].

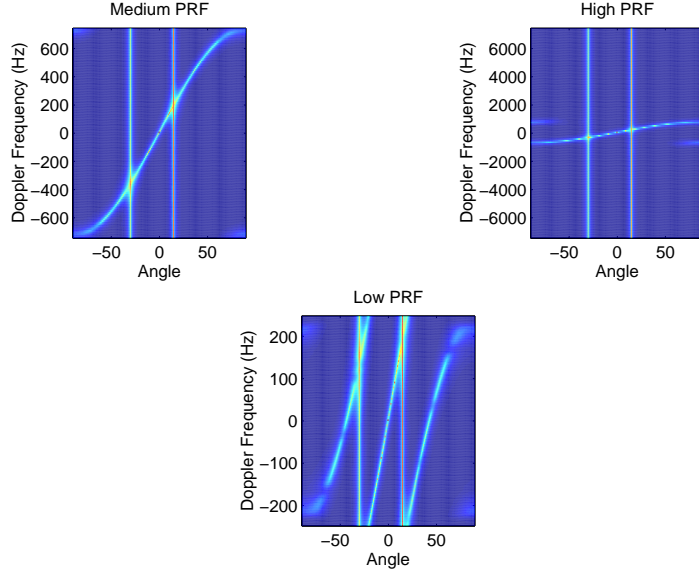


Figure 9. Comparison of MVDR spectra for varying PRF, side-looking airborne radar example.

We conclude this section with a brief discussion of airborne radar training issues. Recall, in [1] we discussed the famous Reed-Mallett-Brennan (RMB) rule [9]: in an iid environment, the STAP requires a secondary (training) data of size twice the total DoF to yield an average output SINR within 3 dB of optimal. Clutter heterogeneity complicates training the STAP processor [1,8]. However, even if the clutter environment were homogeneous, other training challenges exist. The classic configuration for airborne radar STAP analysis is the perfectly side-looking linear array; a perfectly side-looking linear array can experience no yaw or pitch. In this case, clutter Doppler and cone angle are proportional [4]. This implies range invariance among angle-Doppler contours. Hence, assuming a homogeneous clutter environment, the adaptive filter continually converges to the optimal response as the secondary data set size increases. In contrast, in the forward-looking case – the extreme of the side-looking case – angle Doppler contours vary for near in range. As a general rule-of-thumb, if the slant range divided by the platform altitude is less than five, nonstationarity among angle-Doppler contours will exist. Figures 10-11 compare the angle-Doppler contours for side-looking and forward-looking scenarios. All of the contours for varying range align in the side-looking case, but variation for near-in slant range is evident in the forward-looking configuration. Since the STAP must filter in angle and Doppler by using training data chosen over range, any range variation in clutter behavior leads to covariance estimation error and consequent filter mismatch. Hence, SINR and probability of detection decrease accordingly, while the false alarm rate may increase. The variation of angle-Doppler behavior is an especially important consideration in spaceborne and bistatic systems.

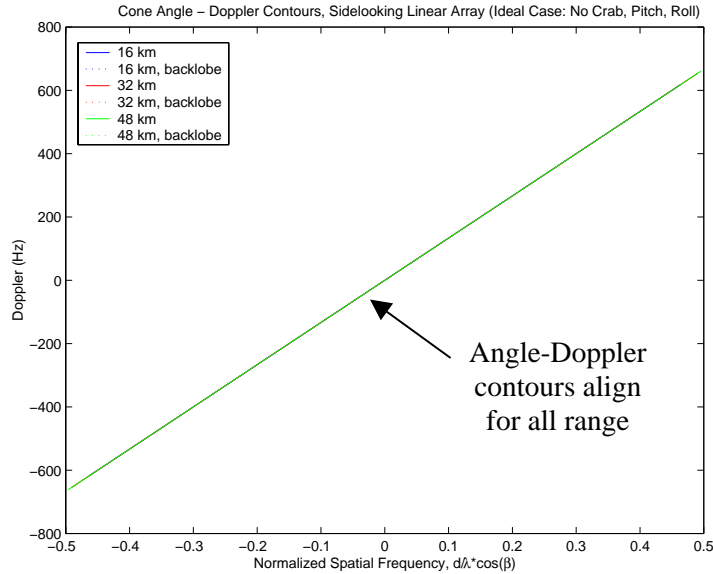


Figure 10. Angle-Doppler contours over range, side-looking airborne radar case.

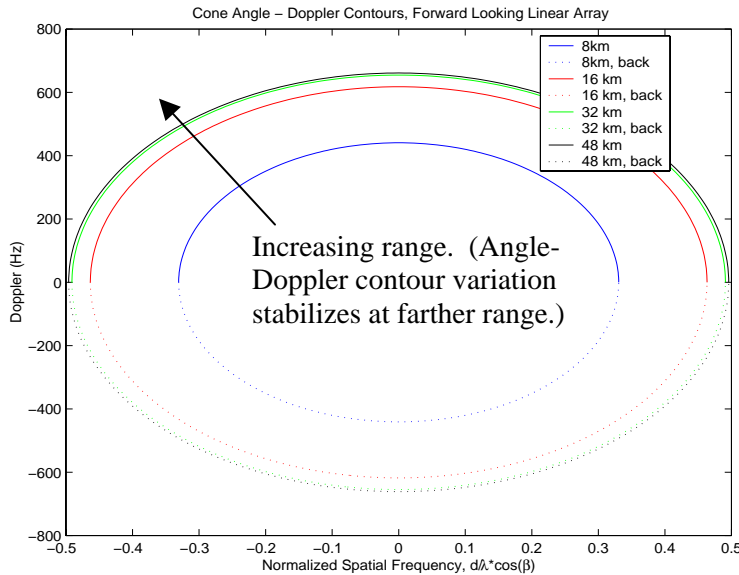


Figure 11. Angle-Doppler contours over range, forward-looking airborne radar case.

3. STAP in Spaceborne Radar

Space-based radar (SBR) provides the potential for continuous surveillance coverage. Since the SBR is down-looking, clutter and jammer mitigation techniques are integral parts of the MTI mode design. In this section we highlight STAP application in GMTI space-based radar. The importance of adequate antenna aperture is a key theme.

Major distinctions between spaceborne and airborne platforms include the very high satellite platform velocity, much steeper operational grazing angles, profound influence of the antenna pattern, the potential for dramatic variation in clutter statistics, size of the antenna footprint on the ground, and the deterministic nature of the satellite orbit. Additionally, the launch vehicle limits the size, power and weight of the SBR system. In low earth orbit, the satellite travels at approximately 7 km/s; this contrasts with the 120-200 m/s velocity of an airborne surveillance radar. At higher grazing angles, the clutter is more specular, thereby increasing the amount of clutter power competing with the target signal. The field of regard for SBR is very large. Hence,

the system can survey large areas, but clutter cultural features can change dramatically. Also, in GMTI SBR, the PRF is set to avoid range ambiguities in the radar footprint. The limited PRF leads to substantial Doppler aliasing. Also, the large footprint increases the number of undesirable emitters in the radar purview. Perhaps, most importantly, the azimuth dimension of the aperture strongly influences mainbeam clutter spread. STAP plays an important role in overcoming some of the diffraction-limited characteristics of deployable space-based arrays whose size is limited by launch vehicle constraints.

We now take a closer look at clutter behavior in SBR. Table 1 provides general simulation parameters, these values are taken from [10]. The effective platform speed incorporates both satellite orbital velocity and the velocity due to the earth's rotation. Effectively using the clutter model of (2), with additional modeling to incorporate orbital mechanics, we arrive at the clutter-plus-noise MVDR spectra of Figure 12. Sixty-four pulses comprise the coherent dwell and the array is linear with twelve spatial channels. Array dimensions are 16 meters in azimuth by 2.5 meters in elevation. The PRF is on the order of 2.2 kHz. The startling observation concerning Figure 12 is the high degree of aliasing, mainly in Doppler, but also in angle. (Angle ambiguity occurs because the separation between the twelve spatial channels far exceeds one-half of a wavelength; the pattern shown in Figure 12 repeats itself in angle.) Figure 12 makes it clear that SBR GMTI is an endo-clutter detection problem: the target signal directly competes with the aliased mainbeam clutter.

Table 1. General Space-Based Radar Analysis Parameters Taken From [10]

Parameter	Value
Array Aperture	40 m ²
Center Frequency	10 GHz
Bandwidth	180 MHz
Clutter Model	-10 dB constant gamma
Platform Altitude	770 km
Grazing Angle	45 degrees
Effective Platform Speed	7.16 km/s

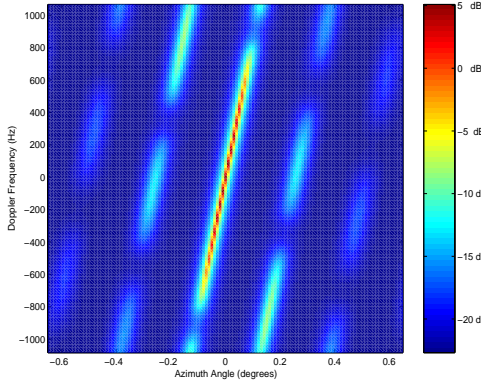


Figure 12. MVDR spectra for SBR example defined in Table 1.

Figure 13 shows the SINR loss curve using the optimal space-time processor (STAP with a clairvoyant covariance matrix) for our example in Table 1. The results provide a good match to those in [10]. Observe the poor performance of the 8 meter azimuth by 5 meter elevation array (40 m² total). The shorter azimuth dimension leads to increased beamwidth. The mainbeam clutter spread across this increased beamwidth is very large and due to signal aliasing affects all Doppler frequencies. The 16 meter azimuth by 2.5 meter elevation antenna maintains the required 40 meter-square aperture stow size, yet provides significantly better performance. Since the azimuth beamwidth is much narrower for the 16 meter dimension, mainbeam clutter spread is minimized. The reduced mainbeam clutter spread translates to much better SINR loss performance. Hence, STAP for SBR is a full system design task, coupling algorithm selection with the appropriate selection of radar system parameters.

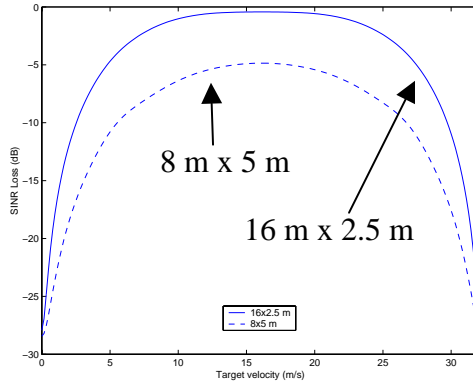


Figure 13. SBR SINR loss for varying antenna size and optimal space-time processing.

A notional signal processing architecture for GMTI is shown in Figure 14 [10]. A multi-channel array is broken into subarrays; the subarrays are then used for adaptive jammer and clutter cancellation. Sub-band filtering is used to compensate for signal bandwidth. Without sub-banding, dispersion across the array degrades cancellation performance. Jammer cancellation occurs in a separate step from clutter mitigation to reduce computational burden and reduce training data requirements. The jammer cancellation step requires a special training interval and operates in beamspace. Jammer canceled beams are then pulse compressed and fed into a beamspace STAP used to mitigate clutter. After clutter cancellation, the processor re-stitches the waveform in the sub-band combiner. Scalar data then proceeds to a detector, such as a cell averaging constant false alarm rate (CA-CFAR) circuit. The post-processor accomplishes target tracking. Adaptive array processing plays a key role in this architecture: a one-dimensional adaptive canceler suppresses the jammer, while the two-dimensional STAP minimizes the impact of clutter on detection performance. Other aspects of the design accommodate unique aspects of adaptive array processing (e.g., sub-banding enables more efficient use of adaptive DoFs). We also point out that by efficiently improving SINR, STAP enables high search rates required for wide area search.

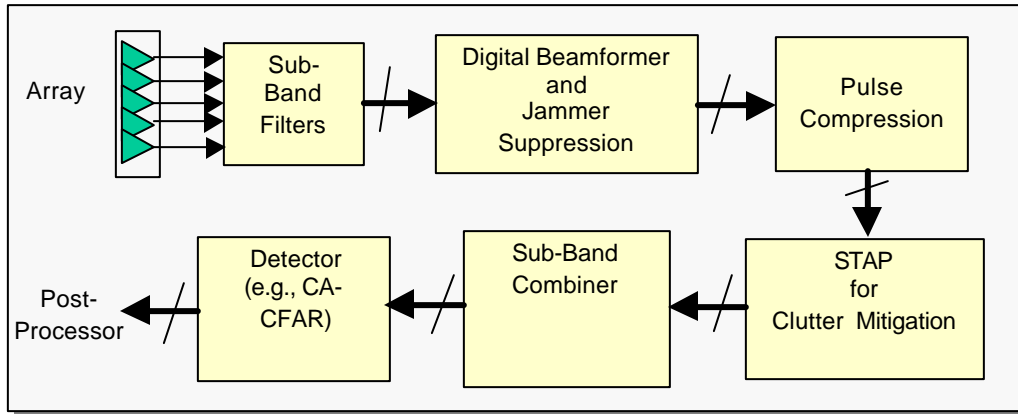


Figure 14. Notional GMTI signal processing chain for space-based radar.

4. Bistatic STAP

Bistatic radar systems use a transmitter and receiver separated by a considerable distance; the distance from transmitter to receiver is usually on the order of the separation from the transmitter to the target. Effective bistatic operation must provide suitable means for mitigating bistatic clutter. Figure 15 provides an overview of the origins of bistatic clutter. Four possible paths, identified in the figure, give rise to the clutter signal. Additionally, the two-way gain to points on the iso-range (an ellipse in bistatic radar) tends to be fairly high,

resulting in strong, spectrally diverse clutter. In light of Figure 15, adaptive clutter nulling appears to be an essential system component. Thus, extending STAP techniques developed for monostatic systems is a logical step in combating bistatic clutter. Bistatic STAP techniques are considered in [11-14].

In this section we highlight some key aspects of bistatic STAP. Specifically, bistatic clutter is nonstationary. Nonstationarity leads to covariance estimation errors and hence degrades adaptive filter performance. After considering the deleterious effect of nonstationarity, we investigate several ameliorating techniques, including localized STAP processing and time-varying weight methods.

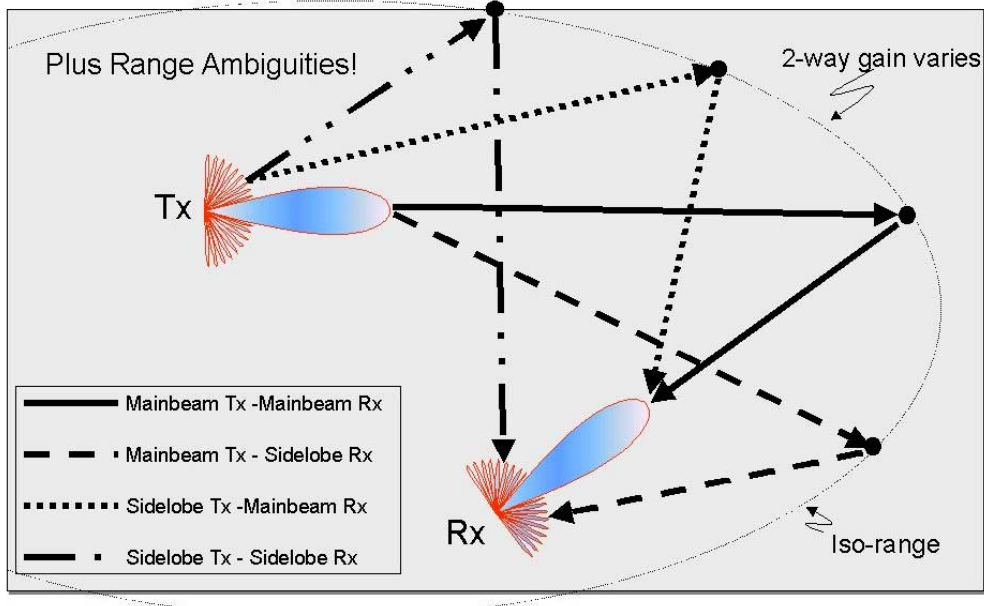


Figure 15. Overview of bistatic system and origin of diverse clutter.

Recall, when implementing the adaptive filter it is common to use the sample covariance estimate

$$\hat{\mathbf{R}}_k = \frac{1}{L} \sum_{\substack{m=1 \\ m \neq k}}^L \mathbf{x}_m \mathbf{x}_m^H \quad (11)$$

which is maximum likelihood when the data are jointly Gaussian and iid [9]. When the training data are iid, approximately $2NM$ vector samples are necessary in (11) to attain an average SINR loss of 3 dB between adaptive and optimal filters.

As a consequence of the iid assumption, $E[\hat{\mathbf{R}}_k] = \mathbf{R}_k$. Thus, in the iid case the adaptive filter asymptotically approaches the performance of the optimal filter. Typical bistatic radar environments deviate from iid conditions; under such circumstances, $\mathbf{R}_k \neq \mathbf{R}_m$ over many range realizations, m , and so the estimate of (11) does not asymptotically approach \mathbf{R}_k , but rather tends to an "average" response related to the variable properties of the training data. Bistatic geometry leads to range-varying clutter behavior (i.e., $\mathbf{R}_k \neq \mathbf{R}_m$).

Bistatic geometry is the source of clutter nonstationarity. Associate a right-handed coordinate system with both the transmitter and receiver. In each case, the x-axis points North, the y-axis points West and the z-axis points upwards. In general, a unit vector pointing from a given platform to a stationary point on the ground is

$$\mathbf{k}(\phi, \theta) = \cos \theta \sin \phi \hat{\mathbf{x}} + \cos \theta \cos \phi \hat{\mathbf{y}} + \sin \theta \hat{\mathbf{z}}, \quad (12)$$

where ϕ is azimuth measured positive in the clockwise direction from the y-axis and θ is elevation measured negative in the downward direction from the horizon. With these definitions, the bistatic Doppler of a given clutter patch is

$$f_{bistatic} = \frac{1}{\lambda} [\mathbf{k}_{Tx}(\phi_{Tx}, \theta_{Tx}) \cdot \mathbf{v}_{Tx} + \mathbf{k}_{Rx}(\phi_{Rx}, \theta_{Rx}) \cdot \mathbf{v}_{Rx}]. \quad (13)$$

The subscripts Tx and Rx denote transmitter and receiver quantities, respectively. Also, \mathbf{v}_{Tx} and \mathbf{v}_{Rx} are transmit and receive platform velocity vectors, respectively. Both transmitter and receiver contribute to the Doppler of the clutter patch. The spatial phase among receiver channels due to bistatic scattering from a stationary point varies with array mounting and scatterer location. Bistatic clutter angle-Doppler properties vary in a complex manner with the particular geometry. Numerical simulation is the best recourse for computing the varying angle-Doppler behavior with bistatic range sum. An example of angle-Doppler characteristics in the bistatic case is given in Figure 16; the variation of the clutter loci over range leads to filter mismatch and the potential for poor instantaneous performance.

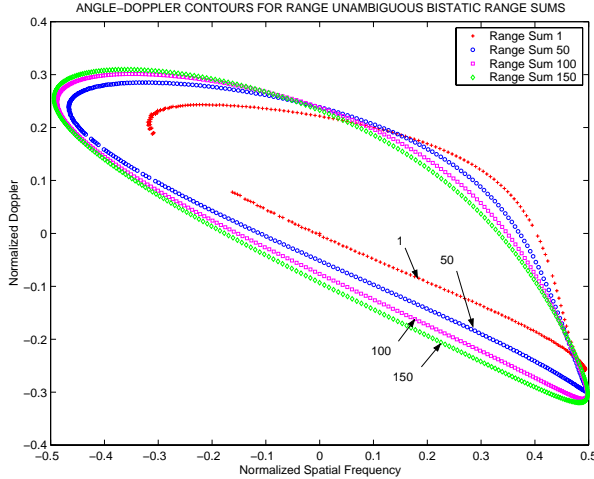


Figure 16. Angle-Doppler contours for varying bistatic range sum.

To further evaluate the impact of bistatic geometry on STAP, we consider an example bistatic configuration designed to extend the noise-limited performance of the transmit platform. The receiver is at an altitude of 4 km. With respect to the receiver, the transmitter is at 93 degrees elevation from nadir and 92 degrees azimuth from true-North. The transmit antenna boresight points 270 degrees in azimuth from true-North, while the receive antenna normal points to 268 degrees. The bistatic baseline is 100 km and the transmitter and receiver are in level flight, with the transmit velocity vector remaining at 100 m/s in the x-direction and the receiver velocity vector being 12 m/s in the x-direction and 97 m/s in the y-direction.

Figures 17 and 18 show the clairvoyant SINR loss ($L_{s,1}$, see [1]) and SINR loss due to adaptivity ($L_{s,2}$, see [1]). Nonstationarity is evident in Figure 17 since the contour curves through the range-Doppler map. The consequences of varying bistatic clutter behavior are seen in Figure 18: SINR losses are fairly substantial. In this latter case, the whole set of space-time snapshots are used for training and so we expect Figure 18 to represent a worst case scenario.

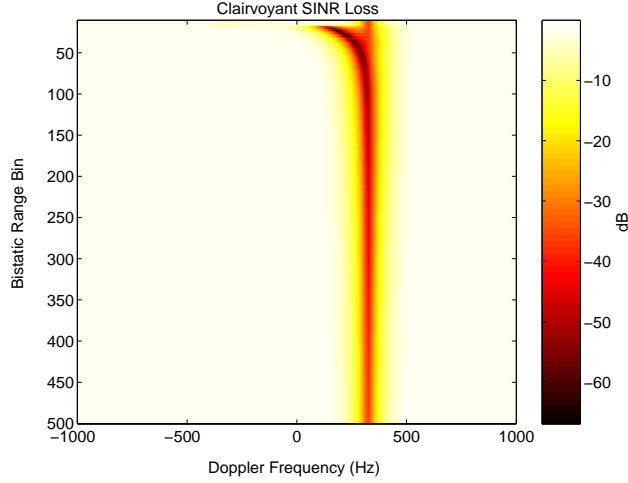


Figure 17. Clairvoyant SINR loss for example bistatic configuration.

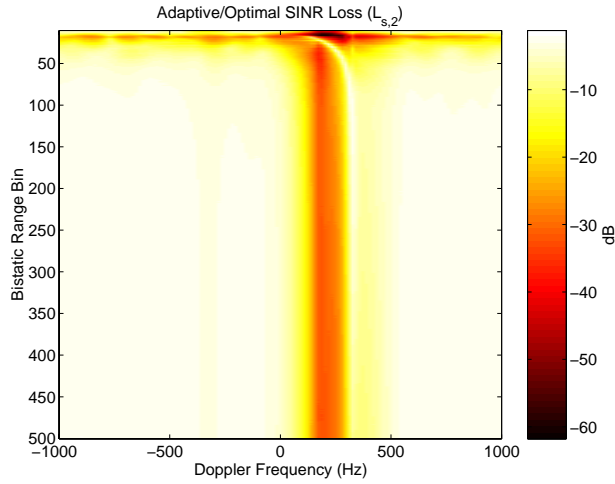


Figure 18. SINR loss between adaptive and optimal filters for example bistatic configuration.

Three approaches to enhance STAP performance, present in the available literature, include: localized STAP [12-14], time-varying weights [11,12,14], and angle-Doppler contour warping [11]. In the first approach, an appropriate reduced-dimension or reduced-rank STAP technique is used to minimize the training data set; minimal variation of bistatic angle-Doppler contours over the reduced training regions serves as the underlying assumption of this approach. A time-varying weight technique was first described in [15] for jammer cancellation in moving arrays and later extended to the bistatic STAP problem. The basic idea involves expanding the adaptive weight vector via a Taylor series over range r , discretizing and truncating the series to first order, and then forming the time-varying filter, viz.

$$\begin{aligned} \mathbf{w}(r) &= \mathbf{w}\Big|_{r=0} + r \dot{\mathbf{w}}\Big|_{r=0} + \frac{r^2}{2} \ddot{\mathbf{w}}\Bigg|_{r=0} + \dots; \\ \mathbf{w}_k &= \mathbf{w}_0 + k\Delta\mathbf{w}; \quad y_k = \underbrace{\begin{bmatrix} \mathbf{w}_0^H & \Delta\mathbf{w}^H \end{bmatrix}}_Z \begin{bmatrix} \mathbf{x}_k \\ k\mathbf{x}_k \end{bmatrix}; \\ \mathbf{z} &= \frac{\mathbf{R}_{\text{ext}}^{-1} \mathbf{s}_{\text{st,ext}}}{\mathbf{s}_{\text{st,ext}}^H \mathbf{R}_{\text{ext}}^{-1} \mathbf{s}_{\text{st,ext}}}, \end{aligned} \quad (14)$$

where \mathbf{R}_{ext} is the covariance matrix of the extended data vector $[\mathbf{x}_k^T \ k\mathbf{x}_k^T]^T$ and $\mathbf{s}_{s-t,\text{ext}}$ is the extended weight vector. From (14) we note the following: the dimensionality is doubled to accommodate a time-varying response, but required training data also doubles and computation load can increase substantially if the processor applies frequent updates (which the time-varying behavior may obviate). In the Doppler warping technique [11], the processor uses *a priori* knowledge to align angle-Doppler contours over range at specific points. We briefly consider the former two approaches.

Figure 19 shows the SINR loss for various reduced-dimension (RD) STAP methods applied to our bistatic example for bistatic ranges 25 and 150, along with the upper bound given by the clairvoyant joint domain optimum (JDO) implementation. $\text{JDL}_{3\times 3}$ and $\text{JDL}_{5\times 5}$ represent the Joint Domain Localized (JDL) method given in [16]; the subscript refers to the number of spatial beams and Doppler filters used to define the localized processing region. JDL adaptively combines select beams and Doppler filters, thereby managing both spatial and temporal DoFs. The minimum training size for $\text{JDL}_{3\times 3}$ is 18 range bins, while 50 range bins define the minimum size for $\text{JDL}_{5\times 5}$. EFA_{3temp} signifies the Extended Factored Algorithm [17] with three temporal degrees of freedom. EFA uses all spatial DoFs and a subset (three in this case) of the temporal DoFs; the minimum training size is 66 bistatic range bins. Adaptive Displaced Phase Center Antenna (ADPCA) processing uses a covariance matrix to whiten the clutter and a steering vector resembling a pulse-to-pulse canceler to further suppress interference [18]. ADPCA_{2temp} uses all spatial channels and two temporal DoFs in its implementation; 44 range bins is the minimum sample size for covariance estimation.

Figure 19 indicates that all RD-STAP methods significantly improve performance over the joint space-time approach. $\text{JDL}_{5\times 5}$ exhibits the best capability for both ranges of interest, while ADPCA_{2temp} performs the worst (pre-steering the ADPCA temporal steering vector to the center of the clutter spectra is a challenge in both instances). The performance of EFA_{3temp} and $\text{JDL}_{3\times 3}$ varies: $\text{JDL}_{3\times 3}$ outperforms EFA_{3temp} for the near range, while the opposite is true for range bin 150. This figure suggests the complexity in allocating spatial and temporal DoFs versus minimizing the required sample support. $\text{JDL}_{5\times 5}$ appears to represent the best trade in this regard.

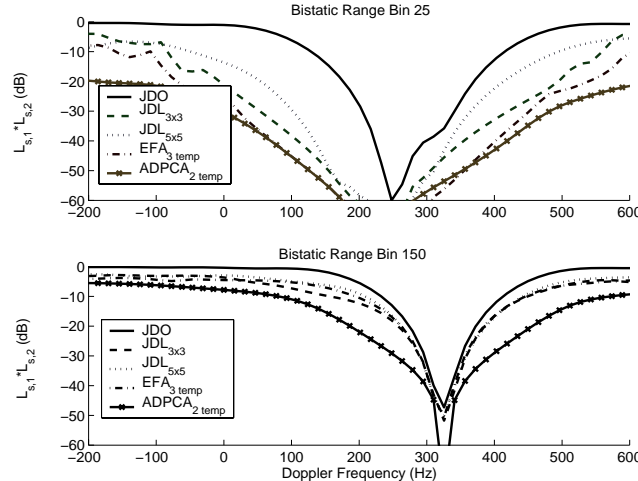


Figure 19. Comparison of reduced-dimension STAP performance applied to example bistatic configuration.

Incorporating the time-varying weight approach of [15] with JDL affords the potential to exploit localized processing while tracking clutter nonstationarity. As previously mentioned, the time-varying weight method effectively doubles the processor's DoFs, and so the minimum training set size also doubles. Figure 20 shows the successful application of the time-varying method of Hayward to JDL for bistatic STAP. The minimum detectable velocity (MDV) of the radar is significantly enhanced when using the time-varying weight procedure. Overall performance gains range from 5 dB to 10 dB, depending on Doppler frequency and JDL implementation (3x3 or 5x5).

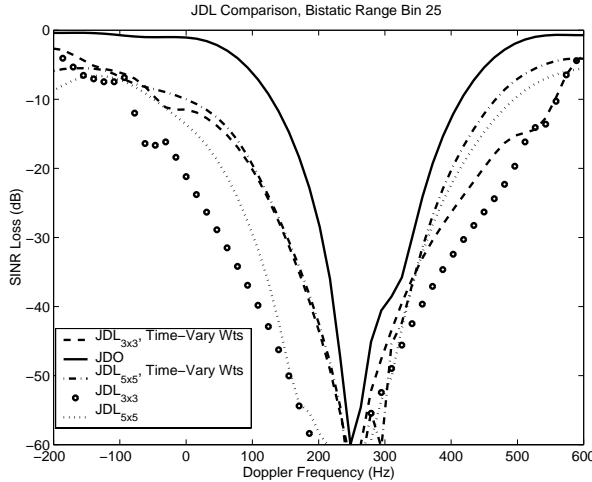


Figure 20. Application of time-varying weight procedure to example bistatic configuration.

5. Terrain Scattered Jamming Suppression

Our prior examples involve using spatial and slow-time degrees of freedom to mitigate ground clutter and narrowband jamming. In this previous discussion, we assume the jamming is a direct path signal. Terrain scattered jamming (TSJ) occurs when the radar aperture captures jamming energy reflecting off the earth's surface. Note, terrain scattered jamming may or may not be intentional. Commonly, a direct path jamming signal is present and the TSJ enters the antenna mainbeam. Spatial and slow-time degrees of freedom are not applicable in this instance. Rather, the processor must make use of spatial and fast-time taps to suppress the TSJ signal. An excellent overview of TSJ is available in [19]. Synonyms for terrain scattered jamming include jammer multipath and hot clutter. The approach to TSJ suppression has analogous application in communication systems.

We briefly highlight some aspects of TSJ mitigation for a ground-based radar example. The geometry of interest is shown in Figure 21. The direct path jamming prevents the radar from determining the range to the target (jammer). Burn-through is a costly option, affecting the radar time-line. In this case, unintentional jamming reflects off the earth's surface. The specular point occurs where the angle of incidence, a_i , roughly equals the angle of reflection a_r . A region of diffuse scattering is known as the glistening surface; its extent relates to the roughness of the terrain in a root mean square (RMS) sense. Since the jammer enters the antenna mainbeam, applying a spatial null cancels not only the jammer, but the target signal as well.

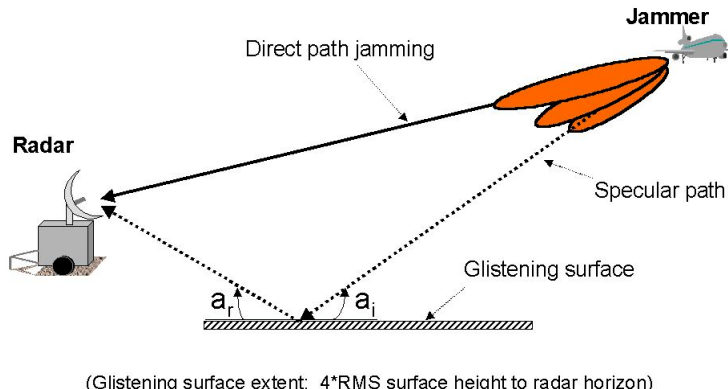


Figure 21. TSJ geometry for ground-based radar example.

The jammer space and fast-time snapshot is given by

$$\bar{\mathbf{x}}_k(l) = \sum_{m=0}^q \alpha_m \mathbf{s}_s(\phi_m, \theta_m) e^{-j2\pi f_{d/m}(lT_p + k\tau)} w(lT_p + k\tau - D_m) \quad (15)$$

where α_m is the amplitude factor of the m^{th} signal term and is proportional to the reflection coefficient and square root of the jammer power, $\mathbf{s}_s(\theta_m, \phi_m) \in C^{M \times 1}$ represents the direct or TSJ (multipath) spatial steering vector measured over the M spatial channels, θ_m is elevation angle, ϕ_m is azimuth angle, $f_{d/m}$ is the Doppler offset due to the jammer motion, $w(t)$ is the complex jammer waveform, and D_m is the path length delay for the m^{th} signal with respect to the direct path. Also, T_p is the pulse repetition interval and τ is the fast-time sampling rate (generally, τ is the reciprocal of the receiver bandwidth). Fast and slow-time indices are given by k and l , respectively. It is important to note from (15) that each TSJ component is a scaled, time-delayed version of the direct path jamming.

The application of STAP to TSJ mitigation is best understood by considering the generalized sidelobe canceler (GSC) STAP architecture [7]. The GSC is shown in Figure 22. The space and fast-time steering vector is $s_{s-ft}(\phi, \theta, k)$, \mathbf{B} is a blocking matrix preventing the desired signal from entering the lower leg of the filter, d_o is the quiescent response, $\mathbf{w}_{\text{GSC}/k}$ is the weight vector chosen to minimize the mean square error ε_o between d_o and its estimate $\hat{d}_o = \mathbf{w}_{\text{GSC}/k}^H \bar{\mathbf{x}}_{k/0}$. The weight vector follows from the Wiener-Hopf equations [7], taking the form

$$\mathbf{w}_{\text{GSC}/k} = \mathbf{R}_{\bar{\mathbf{x}}_{k/0}}^{-1} \mathbf{r}_{d_o, \bar{\mathbf{x}}_{k/0}}; \quad \mathbf{R}_{\bar{\mathbf{x}}_{k/0}} = E[\bar{\mathbf{x}}_{k/0} \bar{\mathbf{x}}_{k/0}^H]; \quad \mathbf{r}_{d_o, \bar{\mathbf{x}}_{k/0}} = E[d_o^* \bar{\mathbf{x}}_{k/0}] \quad (16)$$

Thus, in the top leg, the GSC forms a quiescent beam in the target (jammer) direction, blocks the desired signal in the bottom leg, and then attempts to estimate the TSJ in the top leg using correlated information in the bottom leg to minimize the mean square error output. Effectively, the GSC scales and time-delays the TSJ in the bottom leg to cancel the TSJ competing with the desired signal in the top leg. The target signal will appear as residue in ε_o . If the residue is substantial, it will cross the detection threshold and the processor will declare target presence. Interestingly, the TSJ provides a source for overcoming the direct path, mainbeam jamming!

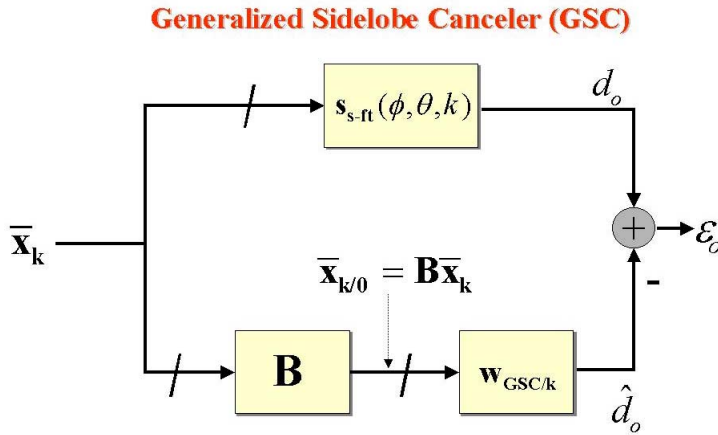


Figure 22. Generalized sidelobe canceler architecture for space and fast-time adaptive cancellation.

We may specify $w(t)$ stochastically by choosing an appropriate power spectral density or autocorrelation model. Such models for the jammer autocorrelation function, $\Phi(\tau)$, typically include

$$\Phi(\tau) = \begin{cases} \sin c(\pi \cdot BW \cdot \tau) \\ \exp(-BW^2 \cdot \tau^2); \quad BW = \min(BW_{Rx}, BW_{Jammer}), \\ \delta(\tau) \end{cases} \quad (17)$$

where BW_{Rx} and BW_{Jammer} signify receiver (Rx) and jammer bandwidth. The delta function model is unrealistic. Figure 23 depicts the autocorrelation function for the former cases. The choice of model will impact the effectiveness of the STAP [20].

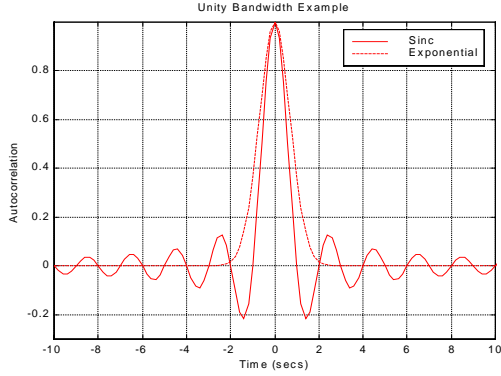


Figure 23. Potential autocorrelation functions for the jammer waveform.

Figures 24 and 25 correspond to the scenario of a mainbeam escort jammer masking the detection of the desired target. Figure 24 indicates that effective STAP performance relies on adequate terrain bounce energy; a strong signal is needed for the adaptation. Figure 25 compares the filter output for a non-adaptive beamformer and the STAP architecture of Figure 23. The target signal is marked in the figure and is clearly visible for the STAP case, whilst buried in the noise for the non-adaptive beamforming method.

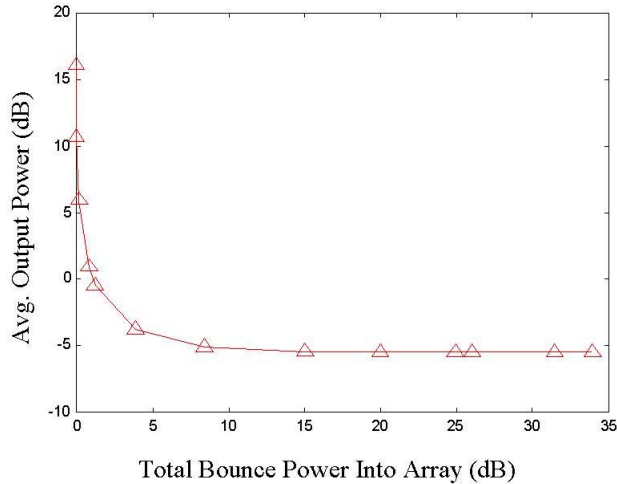


Figure 24. Effective processing relies on adequate multipath signal.

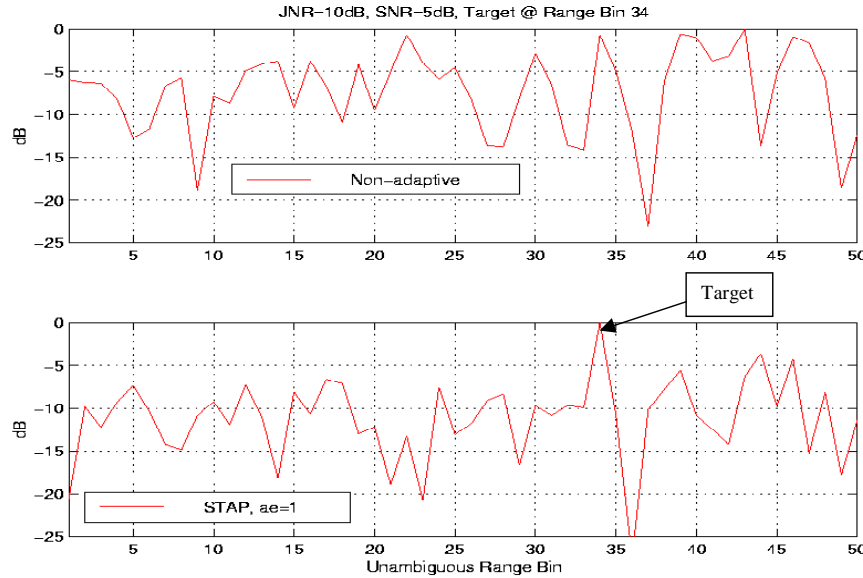


Figure 25. Comparison of non-adaptive beamformer and STAP.

6. Summary

In this set of lecture notes we apply the basic STAP theory developed in [1] to several practical applications. We begin by considering STAP in airborne radar systems. Topics covered include development of basic space-time models for ground clutter and noise jamming, clutter and jamming power spectral densities and minimum variance spectra, the impact of pulse repetition frequency on clutter characteristics, comparison of simulated and actual measured data, and some training-related issues. Next, we build on the airborne STAP discussion by describing STAP's role in ground moving target indication from spaceborne platforms. The key theme in our discussion is the importance of aperture on overall detection performance and application of STAP to overcome diffraction-limited performance bounds. We then describe airborne bistatic STAP. Bistatic clutter environments are nonstationary. Nonstationarity affects STAP implementation by corrupting the covariance estimation procedure. We consider localized STAP and a time-varying weight procedure to enhance bistatic STAP performance. Finally, we overview adaptive space and fast-time processing for terrain scattered and mainbeam jammer suppression. In this case, the terrain scattered jamming appears as scaled, time-delayed replicas of the mainbeam jamming signal. Using the generalized sidelobe canceler architecture, we investigate the manner in which STAP suppresses both mainbeam and terrain scattered jamming signals to enable target detection.

References

- [1] W.L. Melvin, "Space-time detection theory," *Proceedings of the Research and Technology Agency, North Atlantic Treaty Organization (RTA-NATO) Lecture Series 228 – Military Applications of Space-Time Adaptive Processing*, September 2002.
- [2] I.S. Reed, "A brief history of adaptive arrays," Sudbury/Wayland Lecture Series (Raytheon Div. Education) Notes, 23 October 1985.
- [3] L.E. Brennan and I.S. Reed, "Theory of adaptive radar," *IEEE Trans. AES*, Vol. 9, No. 2, March 1973, pp. 237-252.
- [4] R. Klemm, Space-Time Adaptive Processing: Principles and Applications, IEE Radar, Sonar, Navigation and Avionics 9, IEE Press, 1998.
- [5] J. Ward, *Space-Time Adaptive Processing for Airborne Radar*, Lincoln Laboratory Tech. Rept., ESC-TR-94-109, December 1994.

- [6] D.K. Fenner and W.F. Hoover, "Test results of a space-time adaptive processing system for airborne early warning radar," *Proc. 1996 IEEE Natl. Radar Conf.*, Ann Arbor, MI, 13-16 May 1996, pp. 88-93.
- [7] S. Haykin, *Adaptive Filter Theory, Third Ed.*, Prentice-Hall, Upper Saddle River, NJ, 1996.
- [8] W.L. Melvin, "Space-time adaptive radar performance in heterogeneous clutter," *IEEE Trans. AES*, Vol. 36, No. 2, April 2000, pp. 621-633.
- [9] I.S. Reed, J.D. Mallett, and L.E. Brennan, "Rapid convergence rate in adaptive arrays," *IEEE Trans. AES*, Vol. 10, No. 6, November 1974, pp. 853-863.
- [10] D. Rabideau and S. Kogon, "A signal processing architecture for space-based GMTI radar," *Proc. 1999 IEEE Radar Conference*, Waltham, MA, pp. 96-101.
- [11] S.M. Kogon and M.A. Zatman, "Bistatic STAP for airborne radar systems," *Proc. IEEE SAM 2000*, Lexington, MA, March 2000.
- [12] W.L. Melvin, M.J. Callahan and M.C. Wicks, "Adaptive clutter cancellation in bistatic radar," *Proc. 34th Asilomar Conf.*, Pacific Grove, CA, 29-31 Oct 00, pp. 1125-1130.
- [13] B. Himed, J.H. Michels and Y. Zhang, "Bistatic STAP performance analysis in radar applications," *Proc. 2001 IEEE Radar Conf.*, Atlanta, GA, May 2001, pp. 198-203.
- [14] W.L. Melvin, M.J. Callahan and M.C. Wicks, "Bistatic STAP: application to airborne radar," to appear in *Proc. 2002 IEEE Radar Conference*, Long Beach, CA, 22-25 April 2002.
- [15] S.D. Hayward, "Adaptive beamforming for rapidly moving arrays," *Proc. CIE Int'l Conf of Radar* (IEEE Press), Beijing, China, October 1996, pp. 480-483.
- [16] H. Wang and L. Cai, "On adaptive spatial-temporal processing for airborne surveillance radar systems," *IEEE Trans. AES*, Vol. 30, No. 3, July 1994, pp. 660-670.
- [17] R.C. DiPietro, "Extended factored space-time processing for airborne radar," *Proc. 26th Asilomar Conf.*, Pacific Grove, CA, Oct. 1992, pp. 425-430.
- [18] R. Blum, W. Melvin and M. Wicks, "An analysis of adaptive DPCA," *Proceedings of the 1996 IEEE National Radar Conference*, Ann Arbor, Michigan, May 13-16, 1996, pps. 303-308.
- [19] P. Techau, J. Guerci, T. Slocumb, L. Griffiths, "Performance bounds for hot and cold clutter mitigation," *IEEE Trans. AES*, Vol. 35, No. 4, October 1999, pp. 1253-1265.
- [20] P.M. Techau, "Effects of receiver filtering on hot clutter mitigation," *Proc. 1999 IEEE Radar Conf.*, Waltham, MA, 20-22 April 1999, pps. 84-89.

Stochastic-Constraints Method in Nonstationary Hot-Clutter Cancellation — Part II: Unsupervised Training Applications

Prof. Yuri I. Abramovich^{1,2}

¹ Surveillance Systems Division, Defence Science and Technology Organisation (DSTO)
PO Box 1500, Edinburgh S.A. 5111, Australia

² Cooperative Research Centre for Sensor Signal and Information Processing (CSSIP)
SPRI Building, Technology Park Adelaide, Mawson Lakes S.A. 5095, Australia

yuri@cssip.edu.au

Abstract

We consider the use of “stochastically constrained” spatial and spatio-temporal adaptive processing in multimode nonstationary interference (“hot clutter”) mitigation for scenarios that do not allow access to a group of range cells that are free from the backscattered sea/terrain signal (“cold clutter”). Since supervised training methods for interference covariance matrix estimation using the cold-clutter-free ranges are inappropriate in this case, we introduce and analyze adaptive routines which can operate on range cells containing a mixture of hot and cold clutter and possible targets (unsupervised training samples). Theoretical and simulation results are complemented by surface-wave over-the-horizon data processing, recently collected during experimental trials in northern Australia.

1. Introduction

In this lecture, we continue our study into the adaptive spatial and spatio-temporal mitigation of nonstationary interference in the field of high frequency (HF) over-the-horizon radar (OTHR). The preceding lecture discussed the fundamental ideas behind the new “stochastic-constraints” approach, which has been proposed to achieve effective hot-clutter suppression whilst maintaining distortionless output cold-clutter post-processing stationarity. The introduced operational implementation is based on the availability of range cells specifically free of cold clutter, a situation that is quite typical of pulse-waveform (PW) OTHR.

Meanwhile, even within the PW OTHR architecture, attempts to increase the radar duty cycle (*i.e.* the transmitted energy) usually lead to multifrequency operation with a transmission pause for each given frequency, limited to the operational range depth. For surface-wave (SW) OTHR, such a multifrequency mode of operation leaves little room for (sea-) clutter-free ranges being available. For frequency-modulated continuous waveform (FMCW) OTHR, the accessibility of such range cells, containing interference/jamming and noise signals only, is also problematic. Traditionally, FMCW systems operate with a linear frequency-modulated (LFM) waveform and have receiving systems which employ a mixing of the received waveform with a time-delayed version of the transmitted waveform. This process is known as “deramping” and is followed by spectral analysis (weighted Fourier transform) within the comparatively narrow bandwidth of a low-pass filter at the output of the mixer. This bandwidth is usually adjusted to the operational range depth, so that the frequencies corresponding to the “skip zone” ranges are usually filtered out at this stage. Thus only “operational” range cells which contain interference, cold clutter and possible targets (unsupervised training samples) are available for any type of processing.

Note that the “simple” solution of increasing the low-pass filter bandwidth has its limit because of the significant increase in range sidelobes, due to the frequency mismatch [1]. Unfortunately, these range sidelobes also smear the multimodal interference structure somewhat.

Obviously the type of operational routines discussed in [2] based on access to cold-clutter-free ranges are not applicable to these types of OTHR. It is important to emphasize that most existing adaptive algorithms are unable to address the problem of effective interference and cold-clutter mitigation simultaneously. Indeed, the number of “sweeps” (or repetition periods, N) within the coherent processing interval (CPI, “dwell”), combined

with the number of spatial receiving channels M , is typically too large to consider even slow-time-only STAP as a solution to this problem, since the problem has MN degrees of freedom, and we have $M \simeq 32$ to 64 and $N \simeq 128$ to 256 for typical radar facilities. Not only is this solution impractical for computational reasons, but the number of available range cells T within the bandwidth of the above-mentioned low-pass filter is usually too small ($T \simeq 50$ to 70) compared with the product MN to provide reliable convergence for the STAP filter to the efficiency given by the true (deterministic) covariance matrix as $T \rightarrow \infty$.

Moreover, this problem is aggravated if severe multimode ionospheric propagation [3, 4, 5, 6] gives rise to the so-called “hot-clutter” phenomenon, whereby a signal produced by a single interference source is seen as a multiplicity of interference signals at the receiving array. According to [4]:

Ionospherically propagated signals may consist of several modes, nonstationary in bearing and highly correlated with each other. Furthermore, due to the signal being refracted from an inhomogeneous region, each mode can be considered to consist of a specular ray surrounded by a cone of diffracted rays. The resulting wavefront for each mode may therefore be far from planar.

When the temporal support of such multimode is significant, fast-time STAP with Q consecutive range bins (“taps”, Nyquist intervals) involved in adaptive processing is one way to enhance hot-clutter rejectability. In some situations this is the only way to reject multimode interference, especially if one of these modes affects the main beam of the receiving array [2]. Obviously if MN -variate slow-time STAP is considered to be impractical, this is much more the case for the “fully adaptive” MNQ -variate STAP described in [7, 8].

Thus from a practical viewpoint, we should consider a scheme whereby each “finger beam” is associated with an M -variate spatial-only adaptive process (SAP), or at most with an MQ -variate fast-time STAP for interference-only (hot-clutter) mitigation. The output signals of each beam should then be processed by some standard slow-time inter-sweep coherent processing technique. Most existing HF OTHR facilities adopt a weighted Fourier transform for the detection of moving targets in the Doppler frequency domain. Clearly these standard cold-clutter post-processing techniques can only be effective if the properties of the (scalar) cold clutter signal at the output of the adaptive beamformer are not contaminated by beamformer fluctuations caused by adaptation. This consideration is of great importance, since spatial and spatio-temporal properties of the ionospherically propagated jamming signal (hot clutter) are highly nonstationary over the CPI. One possible analytic model that involves variations of the ionospheric propagation medium during the CPI is introduced in [6], and further mentioned in [2].

While the interference mitigation efficiency of an adaptive filter that is constant over a CPI may be quite poor in such cases, we may achieve a substantial improvement only if the corresponding SAP or STAP system can track perturbations of the hot-clutter covariance matrix along the CPI. When perturbations of the antenna array pattern due to the tracking are unconstrained, we observe a significant degradation in the properties of the cold-clutter Doppler spectrum (peak-to-sidelobe ratio, “subclutter visibility”) [2]. It has been demonstrated [9, 10, 11, 12, 2] that additional data-dependent (“stochastic”) constraints could be imposed on adaptive interference rejection filters to maintain distortionless output cold-clutter processing stationarity.

Here we introduce and analyze operational stochastically constrained (SC) SAP/STAP routines that implement the same fundamental principle, but for unsupervised training. The basic idea of the first introduced approach is straight-forward: we reject the cold clutter using a moving-target indicator (MTI), calculate the STAP weights from this data that will reject hot clutter but maintain cold-clutter stationarity, then apply these weights to the original data, enabling the cancellation of cold clutter using standard Doppler processing.

When the MTI filter can be designed in a nonadaptive fashion, the implementation of this basic idea is quite simple, and appears to be already discussed in classified papers [13, 14, 15]. Therefore we concentrate on the efficiency analysis of this approach for typical HF OTHR scenarios. In the more general case when the cold-clutter spectral properties are unknown *a priori*, implementation of the basic idea is less trivial, and the hot-clutter-only rejection filter should be properly retrieved from the associated 3-D STAP.

2. Operational Routine for Unsupervised Training

Our goal is now to construct a complementary operational routine which implements an approximated version of the generic solution for the unsupervised training scenario. We may formulate a similar approach, providing we can somehow obtain proper rejection of the hot-clutter component. Clearly we must be prepared to sacrifice some performance compared with supervised training, due to the absence of samples containing only hot clutter and noise.

2..1 Known (Local) Cold-Clutter Model

In [2], we demonstrated using real OTHR sea-clutter data that, despite the quite complicated nature of the sea-clutter Doppler spectrum over the entire dwell, stabilization by stochastic constraints can be quite effective, even if we adopt a simplified local low-order AR model (*i.e.* accurate only for a limited number of consecutive sweeps). In fact, it has long been known that a simplified one-stage MTI filter, for example, can effectively reject cold clutter even if this clutter is much more complicated than an ordinary Markov chain, when such a filter is truly optimal.

According to the general philosophy discussed in Section I, our goal is to apply the “shortest” possible MTI filter to reject the backscattered cold-clutter first, in order to extract the hot-clutter samples that can be later used for hot-clutter covariance matrix sample averaging. Here it is crucial to involve the minimum possible number of repetition periods, due to the nonstationarity of the hot clutter, which increases the signal subspace dimension of the averaged covariance matrix $\tilde{R}_{\kappa+1}^{av}$. On the other hand, if the cold-clutter residues are significant, the hot-clutter covariance matrix estimate will be significantly compromised.

Since the AR model for SC purposes also needs to be of minimum possible order (κ), it could be used directly to design the MTI filter providing that the parameters b_j ($j = 1, \dots, \kappa$) and σ_{ξ}^2 are known *a priori* or estimated. Thus we assume that a $(\kappa+1)$ -variate slow-time preprocessing filter

$$\tilde{\mathbf{z}}_{kt}^{\kappa} = \tilde{\mathbf{z}}_{kt} + \sum_{j=1}^{\kappa} b_j \tilde{\mathbf{z}}_{k-j,t} \quad \text{for } k = \kappa+1, \dots, N \quad (1)$$

would lead to effective cold-clutter mitigation within the output snapshot $\tilde{\mathbf{z}}_{kt}^{\kappa}$, *i.e.*

$$\mathcal{E}\{\tilde{\mathbf{z}}_{kt}^{\kappa} \tilde{\mathbf{z}}_{kt}^{\kappa H}\} = \sigma_{\xi}^2 \tilde{R}_0^{\mathbf{y}} + \sum_{j=0}^{\kappa} |b_j|^2 \tilde{R}_{k-j}^{\mathbf{x}\eta} + \sigma_{\eta}^2 I_{MQ} \quad (2)$$

with $b_0 = 1$, and

$$\left\| \sigma_{\xi}^2 \tilde{R}_0^{\mathbf{y}} \right\| \ll \left\| \sum_{j=0}^{\kappa} |b_j|^2 \tilde{R}_{k-j}^{\mathbf{x}\eta} \right\|. \quad (3)$$

This gives rise to the following straight-forward operational routine.

Algorithm 1

Step 1 Given the observed M -variate snapshots \mathbf{z}_{kt} ($k = 1, \dots, N$; $t = 1, \dots, T$), form the “stacked” MQ -variate samples $\tilde{\mathbf{z}}_{kt}$ ($k = 1, \dots, N$; $t = 1, \dots, T-Q+1$).

Step 2 Preprocess the samples $\tilde{\mathbf{z}}_{kt}$ by the $(\kappa+1)$ -variate slow-time preprocessing filter with impulse response $[1, b_1, \dots, b_{\kappa}]$ to get the cold-clutter-free training samples $\tilde{\mathbf{z}}_{kt}^{\kappa}$ using (1).

Step 3 Compute the sample estimate of the hot-clutter-plus-noise averaged covariance matrix

$$\hat{\tilde{R}}_k^{av} = \frac{1}{T-Q+1} \sum_{t=1}^{T-Q+1} \tilde{z}_{kt}^\kappa \tilde{z}_{kt}^{\kappa H} \quad \text{for } k = \kappa+1, \dots, N. \quad (4)$$

Step 4 Construct the initial ($k = \kappa+1$) STAP filter

$$\tilde{w}_{\kappa+1,t}^{av} = \left(\hat{\tilde{R}}_{\kappa+1}^{av} \right)^{-1} \tilde{A}_q(\theta_0) \left[\tilde{A}_q^H(\theta_0) \left(\hat{\tilde{R}}_{\kappa+1}^{av} \right)^{-1} \tilde{A}_q(\theta_0) \right]^{-1} \mathbf{e}_q \quad (5)$$

Note that this filter is stochastically unconstrained and so is range-invariant ($\tilde{w}_{\kappa+1,t}^{av} = \tilde{w}_{\kappa+1}^{av}$).

Step 5 For the next adaptive filter $\tilde{w}_{\kappa+2,t}^{av}$ (now range-dependent and stochastically constrained), apply “sliding window” averaging to the preprocessed input data $\tilde{z}_{\kappa+2,t}^\kappa$:

$$\hat{\tilde{R}}_{\kappa+2}^{av} = \frac{1}{T-Q+1} \sum_{t=1}^{T-Q+1} \tilde{z}_{\kappa+2,t}^\kappa \tilde{z}_{\kappa+2,t}^{\kappa H} \quad (6)$$

in order to ensure hot-clutter rejection over the repetition periods $k = 2, \dots, \kappa+2$.

Compute all subsequent STAP filters ($k = \kappa+2, \dots, N$) by

$$\tilde{w}_{kt}^{av} = \left(\hat{\tilde{R}}_k^{av} \right)^{-1} \tilde{A}_{kt}^z \left[\tilde{A}_{kt}^{zH} \left(\hat{\tilde{R}}_k^{av} \right)^{-1} \tilde{A}_{kt}^z \right]^{-1} \mathbf{e}_{q+\kappa} \quad (7)$$

where

$$\hat{\tilde{R}}_k^{av} = \frac{1}{T-Q+1} \sum_{t=1}^{T-Q+1} \tilde{z}_{kt}^\kappa \tilde{z}_{kt}^{\kappa H} \quad (8)$$

and the system of stochastic constraints is

$$\tilde{A}_{kt}^z = \left[\tilde{A}_q(\theta_0) \mid \left(\tilde{I}_{MQ} - \frac{\tilde{s}(\theta_0) \tilde{w}_{k-1,t}^{avH}}{\tilde{w}_{k-1,t}^{avH} \tilde{s}(\theta_0)} \right) \tilde{Z}_{kt} \right] \quad (9)$$

where

$$\tilde{Z}_{kt} = \left[\tilde{z}_{k-1,t} \mid \tilde{z}_{k-2,t} \mid \dots \mid \tilde{z}_{\kappa,t} \right]. \quad (10)$$

Note that the particular parameters used in [9, 2] to simulate HF scattering from the sea

$$\kappa = 2, \quad b_0 = 1, \quad b_1 = -1.9359, \quad b_2 = 0.998, \quad \sigma_\xi = 0.009675 \quad (11)$$

means that all three covariance matrices \tilde{R}_j^{av} ($j = 1, 2, 3$) are almost equally weighted by $|b_j|^2$, while the cold-clutter component in $\tilde{z}_{k+1,t}^\kappa$ is rejected to the level of the weak temporally white noise.

In Step 5, note that the κ repetition periods $k = 2, \dots, \kappa+1$ are common in the construction of $\hat{\tilde{R}}_{\kappa+1}^{av}$ and $\hat{\tilde{R}}_{\kappa+2}^{av}$. The system of κ stochastic constraints corresponding to

$$\tilde{w}_{kt}^H \tilde{z}_{k-j,t} = \tilde{w}_{k-1,t}^H \tilde{z}_{k-j,t} \quad \text{for } j = 1, \dots, \kappa. \quad (12)$$

may then be written as

$$\tilde{w}_{\kappa+1,t}^{av} \tilde{z}_{kt} = \tilde{w}_{\kappa+2,t}^{av} \tilde{z}_{kt} \quad \text{for } k = 2, \dots, \kappa+1. \quad (13)$$

It is worth emphasizing that the hot-clutter covariance matrix estimates are computed using the preprocessed samples $\tilde{\mathbf{z}}_{kt}^\kappa$, while the stochastic constraints use the original snapshots $\tilde{\mathbf{z}}_{kt}$. Thus the right-hand sides of these constraints consist of the cold-clutter samples mainly due to the properties of the estimate (6), while condition (3) ensures that the filter $\tilde{\mathbf{w}}_{k+2,t}^{av}$ properly processes the cold-clutter samples, since the hot clutter is to be rejected.

Our final comment is a reminder that the matrix in the square brackets in (5) has dimension $q \times q$, while that of (7) is $(q+\kappa) \times (q+\kappa)$, since all STAP filters but the first have κ additional data-dependent linear constraints.

A comparison of this algorithm with its counterpart for supervised training (the subject of the previous lecture), reveals that the only significant difference between these two techniques is how we obtain the cold-clutter-free training samples to estimate the hot-clutter-plus-noise covariance matrix. For unsupervised training, we heavily rely on the ability of the κ -order slow-time filter rejecting the cold-clutter signal practically to the level of white noise. In this regard, we stress that such rejectability validates the use of a low-order AR cold-clutter model. On the other hand, suitability of a low-order AR model to real cold clutter over a very limited number of repetition periods (*ie.* locally) does not mean that the same model is appropriate for describing cold clutter over the entire CPI (*ie.* globally). Therefore the proposed preprocessing cannot be used as a moving target indicator (MTI) filter as such since, for low-speed targets, this processing is far from being globally optimal and leads to an unacceptably broad range of “blind” Doppler frequencies. It is thus essential that the proposed preprocessing is applied only to extract hot clutter which is uniformly distributed over the entire Doppler frequency band, while, for proper target detection, we retain the output scalar cold-clutter signal as close as possible to its original form.

It was demonstrated in [2], by processing of real skywave and surface-wave OTHR data, that the low-order AR model supports the stochastic-constraints approach by preserving the *global* structure of the output scalar cold-clutter signal, which is more complicated than suggested by the model. In Section V, we shall demonstrate that the low-order AR model also provides effective real cold-clutter rejection by the associated preprocessing filter. Nevertheless, none of the preprocessing schemes can entirely reject real cold clutter and so some cold-clutter residues are always present within the training sample $\tilde{\mathbf{z}}_{kt}^\kappa$. This means that additional losses are expected compared with supervised training, especially if these residues are above the white noise level.

Another source of loss stems from a reduction in the training sample size: for supervised training we separately estimate each $\hat{\tilde{R}}_k^{x\eta}$ using the set of hot-clutter training samples within each repetition period k , while, for unsupervised training, we use only one set of $(T-Q+1)$ ranges to estimate a single matrix which approximates the sum of all $(\kappa+1)$ matrices $\tilde{R}_k^{x\eta}$.

2.2 Known Order of the (Local) Cold-Clutter Model

In some applications it is reasonable to admit that a preprocessing MTI-type filter can be defined based on some fairly standard *a priori* assumptions. In the field of SW OTHR, for example, such a local model might be inferred from an analytical description of the sea-echo Doppler spectra [16]. In general, though, our prior information is much more limited. To accommodate this, we specify only the AR model order κ prior to data processing, while the actual parameters values b_j are unknown. Therefore, both the cold-clutter temporal properties, as well as the hot-clutter spatial (for SAP) or fast-time spatio-temporal (for STAP) properties, are to be estimated simultaneously using the unsupervised data $\tilde{\mathbf{z}}_{kt}$. It should be clear that this can be achieved only by incorporating slow-time to deal with the cold clutter.

The main idea behind the algorithm that we propose is again straight-forward. For the properly chosen AR model of order κ , the appropriate $MQ(\kappa+1)$ -variate 3-D STAP filter $\tilde{\mathbf{w}}_{kt}$ should then effectively reject both hot and cold clutter. On the other hand, since the hot-clutter signal is uncorrelated over adjacent sweeps, effective mitigation will occur *only* if each of the $(\kappa+1)$ fast-time MQ -variate 2-D STAP subfilters effectively rejects hot clutter. Thus, using the first MQ components of the 3-D STAP filter, we may reject the hot-clutter component, while the cold-clutter contribution should remain unperturbed. Clearly we are decomposing the overall 3-D STAP filter, extracting the component responsible for hot-clutter mitigation only.

Let us introduce the $MQ(\kappa+1)$ -variate “doubly stacked” vector

$$\tilde{\mathbf{z}}_{kt} = \begin{bmatrix} \tilde{\mathbf{z}}_{k-\kappa,t} \\ \vdots \\ \tilde{\mathbf{z}}_{k-1,t} \\ \tilde{\mathbf{z}}_{kt} \end{bmatrix} \quad (14)$$

In the absence of a target signal, we may write

$$\mathcal{E}\left\{\tilde{\mathbf{R}}_k^z\right\} \equiv \mathcal{E}\left\{\tilde{\mathbf{z}}_{kt} \tilde{\mathbf{z}}_{kt}^H\right\} = \mathcal{E}\left\{\tilde{\mathbf{x}}_{kt} \tilde{\mathbf{x}}_{kt}^H\right\} + \mathcal{E}\left\{\tilde{\mathbf{y}}_{kt} \tilde{\mathbf{y}}_{kt}^H\right\} + \sigma_{\eta}^2 I_{MQ(\kappa+1)} \quad (15)$$

since the hot- and cold-clutter signals are mutually independent. Correspondingly,

$$\mathcal{E}\left\{\tilde{\mathbf{R}}_k^{\mathbf{x}\eta}\right\} = \mathcal{E}\left\{\tilde{\mathbf{x}}_{kt} \tilde{\mathbf{x}}_{kt}^H\right\} + \sigma_{\eta}^2 I_{MQ(\kappa+1)} = \begin{bmatrix} \tilde{\mathbf{R}}_{k-\kappa}^{\mathbf{x}\eta} & & & 0 \\ & \tilde{\mathbf{R}}_{k-\kappa+1}^{\mathbf{x}\eta} & & \\ & & \ddots & \\ 0 & & & \tilde{\mathbf{R}}_k^{\mathbf{x}\eta} \end{bmatrix} \quad (16)$$

since the hot clutter is uncorrelated over adjacent repetition periods. For a cold-clutter component described by the scalar multivariate model

$$\mathbf{y}_{kt} + \sum_{j=1}^{\kappa} b_j \mathbf{y}_{k-j,t} = \boldsymbol{\xi}_{kt} \quad (17)$$

we have

$$\mathcal{E}\left\{\tilde{\mathbf{R}}_k^{\mathbf{y}}\right\} = \mathcal{E}\left\{\tilde{\mathbf{y}}_{kt} \tilde{\mathbf{y}}_{kt}^H\right\} = \mathcal{R}_{\kappa+1} \otimes \tilde{\mathbf{R}}_0^{\mathbf{y}} \quad (18)$$

where

$$\mathcal{R}_{\kappa+1} = \text{Toep}[r_0, \dots, r_{\kappa}] \quad (19)$$

r_j ($j = 0, \dots, \kappa$) are the inter-period (scalar) correlation lags, and $\tilde{\mathbf{R}}_0^{\mathbf{y}}$ is defined by the correlation property

$$\mathcal{E}\left\{\mathbf{y}_{kt} \mathbf{y}_{k't'}^H\right\} = \delta(t-t') R_{k-k'}^{\mathbf{y}} \quad (20)$$

and by (2).

In order to justify some of our assertions, let us temporarily simplify our problem. Suppose we ignore the nonstationarity of the hot clutter over the interval of $(\kappa+1)$ adjacent repetition periods, and let us assume that the cold-clutter spatial covariance matrix is diagonal, *i.e.* $\tilde{\mathbf{R}}_0^{\mathbf{y}} = I_{MQ}$. (The angular distribution of cold clutter is always assumed to be sufficiently wide to exclude any possibility that pure SAP can solve the problem; further discussion appears in [2].) Thus the covariance matrix $R_0^{\mathbf{y}}$ is always well-conditioned, and so this second assumption does not change the essence of the problem.

Under these two simplifying assumptions, we may present the overall $MQ(\kappa+1)$ -variate covariance matrix $\tilde{\mathbf{R}}_k^z$ in the form

$$\mathcal{E}\left\{\tilde{\mathbf{z}}_{kt} \tilde{\mathbf{z}}_{kt}^H\right\} \equiv \tilde{\mathbf{R}}_k^z = I_{\kappa+1} \otimes \tilde{\mathbf{R}}_k^{\mathbf{x}\eta} + \mathcal{R}_{\kappa+1} \otimes I_{MQ}. \quad (21)$$

It is known [17] that if λ_s^A and \mathbf{u}_s^A ($s = 1, \dots, m$) are respectively the eigenvalues and eigenvectors of some m -variate matrix A , while λ_t^B and \mathbf{u}_t^B ($t = 1, \dots, n$) correspond to some n -variate matrix B , then the eigenvectors \mathbf{u}_j^C ($j = 1, \dots, mn$) of the matrix

$$C = I_m \otimes B + A \otimes I_n \quad (22)$$

are given by

$$\mathbf{u}_j^C = \mathbf{u}_s^A \otimes \mathbf{u}_t^B \quad \text{for } s = 1, \dots, m; t = 1, \dots, n \quad (23)$$

and correspond to the eigenvalues of C equal to $(\lambda_s^A + \lambda_t^B)$.

By this property, the $MQ(\kappa+1)$ -variate vector $\tilde{\tilde{w}}'_k$ which minimizes the overall hot- and cold-clutter power

$$\tilde{\tilde{w}}_k'^H \tilde{\tilde{R}}_k \tilde{\tilde{w}}_k' \quad \text{subject to} \quad \tilde{\tilde{w}}_k'^H \tilde{\tilde{w}}_k' = 1 \quad (24)$$

is given by

$$\tilde{\tilde{w}}_k' = \mathbf{u}_1(\mathcal{R}_{\kappa+1}) \otimes \mathbf{u}_1(\tilde{\tilde{R}}_k^{x\eta}) \quad (25)$$

where $\mathbf{u}_1(\cdot)$ denotes the eigenvector corresponding to the minimum eigenvalue of the indicated matrix. We also have that the total output power is $\sigma_{\text{out}}^2 \simeq \sigma_\eta^2 + \sigma_\xi^2$.

These considerations illustrate two important issues. Firstly, when the specified order κ is sufficient for effective cold-clutter mitigation by the corresponding κ -variate MTI-type filter, “augmented” $MQ(\kappa+1)$ -variate STAP can simultaneously reject hot and cold clutter. The hot-clutter rejection can be achieved up to the spatial (or more generally, fast-time spatio-temporal) optimum processing limit, while the cold-clutter rejection can be achieved up to the temporal optimum processing limit, *ie.* the simultaneous rejection is uncompromising on its effect on the other component. Secondly, each of the $(\kappa+1)$ blocks of this filter effectively mitigates the hot-clutter component, since $\tilde{\tilde{R}}_k^{x\eta}$ has a block-diagonal structure. Indeed, each of the MQ -variate components of the vector $\tilde{\tilde{w}}'_k$ in (25) is proportional to the minimum eigenvector of $\tilde{\tilde{R}}_k^{x\eta}$.

Now suppose that the total sample size $(T-Q+1)$ used for (loaded) sample averaging in the calculation of $\hat{\tilde{R}}_k^{x\eta}$ [2] is sufficiently large to essentially approach the efficiency of the true (deterministic) value for the STAP filter

$$\tilde{\tilde{w}}_k = \left(\hat{\tilde{R}}_k^{x\eta} \right)^{-1} \tilde{\tilde{s}}(\theta_0) \quad (26)$$

where $\tilde{\tilde{s}}(\theta_0) = [\tilde{s}^T(\theta_0) | \mathbf{O} | \dots | \mathbf{O}]^T$, then we expect the first MQ -variate section of this “augmented” solution to provide effective fast-time STAP rejection of the hot clutter for the k^{th} repetition period. It was demonstrated in [2] that the minimal sample volume sufficient for 3dB average losses compared with the ideal solution (25) *double the signal subspace dimension (ie. rank) of the noise-free covariance matrix*. Since the covariance matrix rank is comparatively small, we may introduce the following operational routine.

Algorithm 2

Step 1 Given the observed M -variate snapshots \mathbf{z}_{kt} ($k = 1, \dots, N$; $t = 1, \dots, T$), form the “stacked” MQ -variate samples $\tilde{\mathbf{z}}_{kt}$ ($k = 1, \dots, N$; $t = 1, \dots, T-Q+1$), and the “doubly stacked” $MQ(\kappa+1)$ -variate samples $\tilde{\tilde{\mathbf{z}}}_{kt}$ ($k = \kappa+1, \dots, N$; $t = 1, \dots, T-Q+1$) using (14).

Step 2 Compute the (loaded) sample covariance matrix estimates

$$\hat{\tilde{R}}_k^{x\eta} = \frac{1}{T-Q+1} \sum_{t=1}^{T-Q+1} \tilde{\tilde{\mathbf{z}}}_{kt}^\kappa \tilde{\tilde{\mathbf{z}}}_{kt}^{\kappa H} + \alpha I_{MQ(\kappa+1)} \quad (27)$$

for $k = \kappa+1, \dots, 2\kappa+1$ and some small constant α , then compute the averaged matrix

$$\tilde{\tilde{R}}_{\kappa+1}^{av} = \frac{1}{\kappa+1} \sum_{j=0}^{\kappa} \hat{\tilde{R}}_{\kappa+j}. \quad (28)$$

Step 3 Let $\tilde{\tilde{A}}_q(\theta_0) = \left[\tilde{\tilde{A}}_q^T(\theta_0) \mid \mathbf{O} \mid \dots \mid \mathbf{O} \right]^T$ then define the initial ($k = \kappa+1$) stochastically unconstrained and range-independent $MQ(\kappa+1)$ -variate filter

$$\tilde{\tilde{\mathbf{w}}}^{av}_{\kappa+1,t} = \left(\tilde{\tilde{R}}_{\kappa+1}^{av} \right)^{-1} \tilde{\tilde{A}}_q(\theta_0) \left[\tilde{\tilde{A}}_q^H(\theta_0) \left(\tilde{\tilde{R}}_{\kappa+1}^{av} \right)^{-1} \tilde{\tilde{A}}_q(\theta_0) \right]^{-1} \mathbf{e}_q . \quad (29)$$

The first MQ elements of this vector form the first fast-time STAP filter $\ddot{\tilde{\mathbf{w}}}^{av}_{\kappa+1,t}$, ie.

$$\ddot{\tilde{\mathbf{w}}}^{av}_{\kappa+1,t} = E_{MQ}^T \tilde{\tilde{\mathbf{w}}}^{av}_{\kappa+1,t} \quad (30)$$

where $E_{MQ} = [I_{MQ} \mid \mathbf{O} \mid \dots \mid \mathbf{O}]^T$.

Step 4 For the next fast-time STAP filter $\ddot{\tilde{\mathbf{w}}}^{av}_{\kappa+2,t}$ (now range-dependent and stochastically constrained), compute the $MQ(\kappa+1)$ -variate filter $\tilde{\tilde{\mathbf{w}}}^{av}_{\kappa+2,t}$ by applying “sliding window” averaging:

$$\tilde{\tilde{R}}_{\kappa+2}^{av} = \frac{1}{\kappa+1} \sum_{j=0}^{\kappa} \tilde{\tilde{R}}_{\kappa+1+j}^{av} . \quad (31)$$

in order to ensure hot-clutter rejection over the repetition periods $k = 2, \dots, \kappa+2$.

Compute all subsequent operational fast-time STAP filters $\ddot{\tilde{\mathbf{w}}}^{av}_{kt}$ ($k = \kappa+2, \dots, N$) by

$$\ddot{\tilde{\mathbf{w}}}^{av}_{kt} = E_{MQ}^T \tilde{\tilde{\mathbf{w}}}^{av}_{kt} \quad (32)$$

$$\tilde{\tilde{\mathbf{w}}}^{av}_{kt} = \left(\tilde{\tilde{R}}_k^{av} \right)^{-1} \tilde{\tilde{A}}_{kt}^z \left[\tilde{\tilde{A}}_{kt}^{zH} \left(\tilde{\tilde{R}}_k^{av} \right)^{-1} \tilde{\tilde{A}}_{kt}^z \right]^{-1} \mathbf{e}_{q+\kappa} \quad (33)$$

where

$$\tilde{\tilde{R}}_k^{av} = \frac{1}{\kappa+1} \sum_{j=0}^{\kappa} \tilde{\tilde{R}}_{k+j}^{av}, \quad \tilde{\tilde{A}}_{kt}^z = \left[\tilde{\tilde{A}}_{kt}^{zT} \mid \mathbf{O} \mid \dots \mid \mathbf{O} \right]^T \quad (34)$$

and the system of stochastic constraints is

$$\tilde{\tilde{A}}_{kt}^z = \left[\tilde{\tilde{A}}_q(\theta_0) \mid \left(\tilde{I}_{MQ} - \frac{\tilde{s}(\theta_0) \ddot{\tilde{\mathbf{w}}}^{avH}_{k-1,t}}{\ddot{\tilde{\mathbf{w}}}^{avH}_{k-1,t} \tilde{s}(\theta_0)} \right) \tilde{\tilde{Z}}_{kt} \right] \quad (35)$$

where $\tilde{\tilde{Z}}_{kt}$ is defined by (10).

In Step 3, while the entire $MQ(\kappa+1)$ -variate filter $\tilde{\tilde{\mathbf{w}}}^{av}_{\kappa+1,t}$ would provide effective cancellation for both hot and cold clutter, we expect that constructing a fast-time STAP vector $\ddot{\tilde{\mathbf{w}}}^{av}_{\kappa+1,t}$ from its first MQ elements will deliver equally effective cancellation of the hot clutter only, over the first $(\kappa+1)$ repetition periods. This will be true provided that the number of degrees of freedom in the vector exceeds the rank of the averaged hot-clutter covariance matrix $\tilde{\tilde{R}}_{\kappa+1}^{av}$, ie.

$$MQ \gg (\kappa+1) \left[P(L+Q-1) \right] \quad (36)$$

or more precisely, taking into account the number of deterministic and stochastic constraints:

$$MQ > (\kappa+1) \left[P(L+Q-1) \right] + (q+\kappa) . \quad (37)$$

In Step 4, for our standard example of $\kappa = 2$, once again the initial filter $\tilde{\tilde{\mathbf{w}}}^{av}_{3,t}$ rejects hot clutter over

the repetition periods $k = 1, 2, 3$, while the second filter $\tilde{\mathbf{w}}_{4t}^{av}$ rejects over $k = 2, 3, 4$, thus ensuring that κ covariances $\tilde{\mathbf{R}}_k$ are common for each successive average $\tilde{\mathbf{R}}_k$. The system of κ stochastic constraints which ensures the stationarity of the cold-clutter component is

$$\tilde{\mathbf{w}}_{4t}^{avH} E_{MQ} \tilde{\mathbf{z}}_{kt} \equiv \tilde{\mathbf{w}}_{4t}^{avH} \tilde{\mathbf{z}}_{kt} = \tilde{\mathbf{w}}_{3t}^{avH} E_{MQ} \tilde{\mathbf{z}}_{kt} \equiv \tilde{\mathbf{w}}_{3t}^{avH} \tilde{\mathbf{z}}_{kt} \quad \text{for } k = 2, \dots, \kappa+1 \quad (38)$$

and in general

$$\tilde{\mathbf{w}}_{kt}^{avH} \tilde{\mathbf{z}}_{k-j,t} = \tilde{\mathbf{w}}_{kt}^{avH} \tilde{\mathbf{z}}_{k-j,t} \quad \text{for } j = 1, \dots, \kappa. \quad (39)$$

Thus both sides of these constraints will consist mainly of cold clutter, since the hot-clutter component is rejected.

As usual, the stochastic-constraints approach forms the kernel of this algorithm. The main difference with all previous routines is the method of separating hot and cold clutter: here we embed the fast-time STAP solution into the more general “augmented” 3-D STAP one to extract the desired solution as the component of the $MQ(\kappa+1)$ -variate filter.

It should be clear that the augmented STAP is only suitable for extracting the fast-time STAP solution, and cannot be used by itself as a final operational routine for target detection. As before, this is because the very small number of slow-time lags (κ) involved in cold-clutter mitigation leads to a wide range of “blind” Doppler frequencies, where any targets would be rejected along with the cold clutter.

3. Operational SC STAP Algorithm: Simulation and Real Data Processing

Naturally both of the proposed operational algorithms need to be verified. The most important question for Algorithm 1 is the relevance of the low-order AR cold-clutter model, and this shall now be addressed by real data processing, since there is no point filtering simulated cold clutter of a known AR model. The other important question on the convergence rate of the process to the true value as $T \rightarrow \infty$ for Algorithm 1 has been partly addressed in our previous papers on supervised training [9, 18, 2] with the established sample size $T \simeq 2(\kappa+1)[P(L+Q-1)]$ necessary to guarantee average losses of 3dB compared with the optimal solution.

Thus in order to justify the first operational routine we have to demonstrate that via a low-order AR model we can construct a preprocessing MTI-type filter that can efficiently reject cold clutter. Firstly, we make use of the same real SW OTHR data as in [2], where the CPI is 100 seconds. The solid line in Fig. 1(a) shows the standard Doppler spectrum for one particular range cell; note that the subclutter visibility (the main-peak-to-sidelobe ratio) is approximately 50dB in this case. Forward and backward averaging has been used to define the 3×3 ($\kappa = 2$) inter-sweep temporal covariance matrix $\hat{\mathcal{R}}_3$. The preprocessing filter has been defined as

$$\mathbf{w}_3 = \left(\hat{\mathcal{R}}_3 \right)^{-1} \mathbf{e}_3 \left[\mathbf{e}_3^H \left(\hat{\mathcal{R}}_3 \right)^{-2} \mathbf{e}_3 \right]^{-\frac{1}{2}} \quad (40)$$

in order to keep unchanged the white-noise output power (since $\|\mathbf{w}_3\| = 1$). The dotted line in Fig. 1(a) illustrates the Doppler spectrum of the residues after preprocessing. We see that the “noise floor” obtained by this pre-filtering is essentially the same as in the initial spectrum. Moreover, the eigenvalues of the sample matrix $\hat{\mathcal{R}}_3$

$$\hat{\lambda}_1 = 3.42, \quad \hat{\lambda}_2 = 0.0833, \quad \hat{\lambda}_3 = 0.0020 \quad (41)$$

suggest that the cold clutter could be rejected by about 27dB compared to the input level. This agrees with the subclutter visibility, taking into account the compression gain of $N = 1000$ repetition periods ($\simeq 30$ dB).

Note that Fig. 1(a) also confirms our expectation of the very wide “blind” Doppler bandwidth which makes this type of processing inappropriate for target detection.

Fig. 1(b) illustrates similar processing results of data obtained from DSTO’s HF SWR facility located at Port Wakefield, South Australia. This radar employs a 16-element linear receiving array and operates over the frequency band 5 – 17MHz. The LFMCW waveform sweep rate and bandwidth are selectable over a wide

range; typically the waveform repetition frequency is around 4Hz and the bandwidth 50kHz. Since the repetition period is almost three times longer than in the previous data, the energetic components of the sea-clutter Doppler spectrum (solid line) obviously occupy a significantly wider range of relative Doppler frequencies. Consequently, the third-order preprocessing filter ($\kappa = 2$) shown by the dotted line is not extremely effective, rejecting the most prominent Bragg lines barely to the noise floor level. The “peak-to-noise” ratio at the output of this preprocessing filter (followed by a standard weighted FFT) is about 30dB, while the initial subclutter visibility is about 65dB. Nevertheless, if we increase the order of the AR model to $\kappa = 3$, then the corresponding fourth-order preprocessing filter (dashed line) rejects all input energetic cold-clutter components far below the input white noise level.

Thus for typical SW OTHR data, small-order AR models are proven to provide quite effective cold-clutter suppression, in turn enabling effective hot-clutter-only sample extraction.

Verification of the second operational routine is not so simple, but the following two important questions may be addressed by simulation studies. Firstly, we need to demonstrate that for some standard hot- and cold-clutter models, hot-clutter alone can be rejected by an MQ -variate component of the “augmented” $MQ(\kappa + 1)$ -variate optimal solution. This optimal solution is constructed from the exact covariance matrix, and is interpreted as the limit solution, when the number of training samples tends to infinity. Secondly, we need to demonstrate that the convergence rate with respect to T is sufficiently high, since the number of range bins available in most HF OTHR applications is usually limited.

The following simulations are based on the simple scenario of pure SAP with an $M = 16$ element antenna array and a single fluctuating jamming source. The generalized Watterson model described in [6, 2] has been used to simulate the spatial and temporal (Doppler) fluctuations of the jammer. The spatial and temporal correlation coefficients have been chosen to reflect typical spatial fluctuations which make traditional mitigation techniques ineffective; in the notation of [2], these parameters are $\zeta^{1\ell} = 0.90$ and $\rho^{1\ell} = 0.89$ respectively, with 50dB HCNR and $\theta^{1\ell} = 59.1$ degrees. The second-order AR model with $N = 256$ sweeps per dwell and the parameters of (11) have again been used to simulate HF scattering from the sea surface. Fig. 2(a) shows the Doppler spectrum for the cold clutter, uncorrupted by any jamming signal, at the output of the conventional beamformer (curve labeled “CBF Y”). We see that the subclutter visibility benchmark is approximately 80dB, which is an upper bound for most practical situations. Also illustrated is the Doppler spectrum of the cold-clutter signal at the output of the standard (unconstrained) optimal SAP/STAP filter:

$$\tilde{\mathbf{w}}_{STAP} = \left(\tilde{\mathbf{R}}^{\mathbf{x}\boldsymbol{\eta}} \right)^{-1} \tilde{\mathbf{s}}(\theta_0) \quad (42)$$

(note that here $\tilde{\mathbf{R}}^{\mathbf{x}\boldsymbol{\eta}} = \mathbf{R}^{\mathbf{x}\boldsymbol{\eta}}$ and $\tilde{\mathbf{s}}(\theta_0) = \mathbf{s}(\theta_0)$, since $Q = 1$) (the look direction is $\theta_0 = 0$). Clearly the spatial nonstationarity of the jammer leads to a significant degradation in subclutter visibility (~ -30 dB), due to the fluctuations of the spatial (antenna array) weight vector. For this simulation, the instantaneous (per sweep) hot-clutter-to-cold-clutter ratio (HCCR) per antenna array element was chosen to be 0dB, so that the subclutter visibility for the conventional beamformer (“CBF Z”) is also about 50dB. Therefore in this particular case, as far as the final subclutter visibility is concerned, conventional hot-clutter mitigation is as ineffective as no hot-clutter mitigation at all.

Fig. 2(b) shows the results of our analysis into the limit efficiency of the algorithm described by Eqns. (32)–(35), calculated by replacing the sample matrix $\tilde{\mathbf{R}}_k^{\mathbf{z}}$ by the true covariance matrix $\tilde{\mathbf{R}}_k^{\mathbf{z}}$, *i.e.* the sample volume is infinitely large. The curve labeled “long Z” presents the power of the total output signal for the “augmented” $MQ(\kappa + 1)$ -variate STAP filter $\tilde{\mathbf{w}}_{kt}^{av}$; “long Y” shows the power of the cold-clutter component at the output of this filter; “long X” corresponds to the hot clutter power for the same filter, while “short X” illustrates the hot clutter output power from the truncated 16-element SAP filter $\tilde{\mathbf{w}}_{kt}^{av}$, simply formed from the first 16 elements of the 48-variate vector $\tilde{\mathbf{w}}_{kt}^{av}$.

We see that in the given scenario, the hot-clutter component is rejected far below the level of the cold-clutter residues at the output of the augmented STAP filter $\tilde{\mathbf{w}}_{kt}^{av}$. Not surprisingly, the short filter $\tilde{\mathbf{w}}_{kt}^{av}$ rejects the hot clutter slightly better than the augmented filter due to the independence of the hot clutter over adjacent

repetition periods. Thus the potential effectiveness of the proposed routine is extremely high, since the scalar output of the operational filter $\ddot{\mathbf{w}}_{kt}^{av}$ consists almost entirely of cold clutter only.

The most important remaining question deals with finite sample size. In this regard, Fig. 2(c) differs from the previous figure only by the use of the finite sample size $T = 41$. For this reason, the “gap” between the hot- and cold-clutter residues is smaller than in the previous case using deterministic covariance matrix calculations. Nevertheless, this gap is still large enough to guarantee that the hot-clutter component at the output of the filter $\ddot{\mathbf{w}}_{kt}^{av}$ will be negligible.

Correspondingly, the Doppler spectrum of the total signal at the output of the operational filter $\ddot{\mathbf{w}}_{kt}^{av}$ (curve labeled “Op SC STAP” in Fig. 2(d)) is practically indistinguishable from the cold-clutter-only component Doppler spectrum at the output of the conventional beamformer (“CBF Y”), and from the spectrum of the signal at the output of the SC STAP filter computed with the true covariance matrix (“Det SC STAP”).

Thus the ability of the operational routine to suppress fluctuating jamming signals and to retain the initial subclutter visibility (very high in this example) is verified in this case.

In order to explore the limitations of the proposed technique within the framework of the adopted model, we conducted similar simulations for input HCCCRs equal to 10dB, 20dB and 30dB (Figs. 3, 4 and 5 respectively). We see that only in the (worst) last case does the hot-clutter output power approach the power of the cold-clutter residues at the output of the augmented adaptive filter $\tilde{\mathbf{w}}_{kt}^{av}$. Meanwhile, subclutter visibility at the output of the operational filter $\ddot{\mathbf{w}}_{kt}^{av}$ is degraded up to the level of about 70dB, compared with the initial value of about 80dB.

It is worth mentioning that even for this worst case (HCCCR=30dB), the potential efficiency of hot-clutter mitigation is still extremely high. This means that with an appropriate sample volume, one can approach the initial subclutter visibility level.

Finally, we present some results of recent field trials to illustrate the efficiency of the supervised and unsupervised SC methods. The experimental facility involved has recently been developed near Darwin by the Australian Defence Science and Technology Organisation (DSTO), in collaboration with Telstra Applied Technologies (TAT) and the Cooperative Research Centre for Sensor Signal and Information Processing (CSSIP); the system was designed to function primarily as a SW OTHR, though it can operate in a variety of other data acquisition modes. The facility consists of two transmit sites, at Stingray Head (65km south-west of Darwin) and Lee Point (10km north-east of Darwin), together with a receive site at Gunn Point (30km north-east of Darwin) [19]. The receiving system is based on a 32-element uniform linear array, some 500m long, connected to a high dynamic range 32-channel HF receiver. The antenna element noise figures for the operational frequency range of 5–10MHz do not exceed 5dB, with a figure of near 1.5dB at the middle of the band. Such an antenna design permits a maximum possible external-to-internal noise ratio, and thus enables efficient external noise mitigation.

Our results illustrate an example of low-power transmitter operation, where the last 30 or so range cells of the 80 available ranges have the sea-clutter signal deeply submerged into the environmental noise. Therefore we were able to use these last 30 ranges for supervised training, and compare the efficiency of supervised and unsupervised training SC techniques against the conventional beamformer (CBF) and standard SAP beamformer averaged over the entire dwell. For unsupervised training, we use the last 75 ranges, since the first five ranges are affected by the extremely strong direct-wave propagation.

Algorithm 1 has been employed with the 30 range cells involved in cold-clutter AR parameter estimation for the MTI-filter design, averaging across all antenna array elements. Figs. 6—8 present the detailed range profiles for the target range cell 19 and 37, and the target-free range 12. The total noise power across the frequency bins 32 to 224 has been calculated to compare the signal-to-noise ratio improvement (SNRI) with respect to the CBF, bearing in mind that in the look direction (ideal planar waveform), all beamformers are normalised to the same gain. Interestingly, this analysis demonstrates that unsupervised training (10–15dB SNRI) is slightly better than supervised training (8–13dB SNRI) in this case. This could be explained by an improved interference averaging with most of the available ranges involved (75 out of 80). Practically, though, this improvement is not indicated by the actual SNRIs for the reference targets. This discrepancy between the expected and actual SNRIs is once again explained by the fact that the MTI residues that contain the target components have been used for interference covariance matrix estimation. Since perfect antenna calibration is

not attainable in practice, some degradation in SNRI is inevitable. This is a well-known phenomenon, and a straight-forward modification that excludes target-suspicious range cells from averaging provides one antidote.

Nevertheless, both SC SAP options demonstrate the considerable improvement achievable in practice compared with CBF and averaged SAP in this environmental noise situation.

4. Summary and Conclusions

We have extended the domain of practical application of the stochastic-constraints (SC) method to unsupervised training scenarios, typical of existing FMCW OTHR systems.

Two operational routines have been proposed here. The first technique includes “slow-time” preprocessing of the input data by the MTI-type filter that can suppress the cold-clutter component far below the jamming signal level. We have demonstrated by real SW OTHR data processing that effective cold-clutter rejection can be achieved by involving a very modest number of repetition periods in preprocessing. In fact, the order of the preprocessing filter is equal to the order of the AR cold-clutter model, which in turn is equal to the number of stochastic constraints that secure the stationarity of the output cold-clutter signal. It is highly significant that low-order AR models have now been proven to be adequate only for the local description of the cold clutter, *ie.* over a very small number of consecutive repetition periods. Correspondingly, the preprocessing approach that we have introduced can only be used for the extraction of the hot-clutter signal, and is completely inappropriate for target detection due to the unacceptably broad “blind” Doppler frequency bandwidth.

Within this first approach, the AR model, and consequently the preprocessing filter, are assumed to be known *a priori* (or estimated). The second, more general approach, relies only upon the chosen order of pre-processing filter sufficient for cold-clutter rejection, while the second-order moments for both hot and cold clutter are unknown. In this second method, the desired fast-time SAP/STAP hot-clutter rejection filter is defined as part of the “augmented” STAP filter which involves $(\kappa+1)$ consecutive repetition periods for additional cold-clutter mitigation. More precisely, the MQ -variate fast-time operational STAP filter (or M -variate SAP filter) $\tilde{\mathbf{w}}_{kt}^{av}$ is defined as the vector consisting of the first MQ (or M) elements of the augmented $MQ(\kappa+1)$ -variate STAP filter (or the $M(\kappa+1)$ -variate STAP filter) $\tilde{\mathbf{w}}_{kt}^{av}$.

While this augmented filter $\tilde{\mathbf{w}}_{kt}^{av}$ simultaneously provides both hot- and cold-clutter rejection, the short version $\tilde{\mathbf{w}}_{kt}^{av}$ was demonstrated to reject effectively only the hot-clutter component, far below the cold-clutter signal level. The proposed stochastic-constraints method ensures the stationarity of the scalar cold-clutter signal at the output of the operational filter $\tilde{\mathbf{w}}_{kt}^{av}$.

Simulation results presented demonstrate that, for a typical scenario, the SC technique provides effective jammer mitigation, retaining the initial high level of subclutter visibility. These simulations involved a quite modest number of range resolution cells, typical of existing FMCW OTHR installations. The boundaries of usefulness of the SC method are explored in terms of subclutter visibility as a function of input hot- to cold-clutter ratio. Most of the efficiency analysis results presented here are obtained by direct simulations, while a proper analytic study of the convergence properties of the SC approach remains to be done. Nevertheless, we have demonstrated by real SW OTHR data processing that unsupervised training scenarios typical of FMCW OTHR can be successfully treated in an operational mode using stochastic-constraints principles.

Naturally the techniques introduced here could be useful for applications other than HF OTHR. The similarities between HF OTHR and airborne radar have already been discussed in [2].

References

- [1] D.E. Barrick, “FMCW radar signals and digital processing,” NOAA Tech Report ERL 283-WPL26, 1973.
- [2] Y.I. Abramovich, N.K. Spencer, S.J. Anderson, and A.Y. Gorokhov, “Stochastic-constraints method in nonstationary hot-clutter cancellation — Part I: Fundamentals and supervised training applications,” *IEEE Trans. Aero. Elect. Sys.*, vol. 34 (4), pp. 1271–1292, 1998.

- [3] E.M. Warrington and C.A. Jackson, “Some observations of the directions of arrival of an ionospherically reflected HF radio signal on a very high latitude path,” in *Proc. Conf. HF Radio Systems and Techniques*, IEE Conf. Publ. No. 411, 1997, pp. 65–69.
- [4] M. Zatman and H. Strangeways, “The effect of the covariance matrix of ionospherically propagated signals on the choice of direction finding algorithm,” in *Proc. Conf. HF Radio Systems and Techniques*, IEE Conf. Publ. No. 392, 1994, pp. 267–272.
- [5] C.M. Keller, “HF noise environment models,” *Radio Science*, vol. 26 (4), pp. 981–995, 1991.
- [6] Y.I. Abramovich, C. Demeure, and A.Y. Gorokhov, “Experimental verification of a generalized multivariate propagation model for ionospheric HF signals,” in *Proc. EUSIPCO-96*, Trieste, 1996, vol. 3, pp. 1853–1856.
- [7] R. Fante and J.A. Torres, “Cancellation of diffuse jammer multipath by an airborne adaptive radar,” *IEEE Trans. Aero. Elect. Sys.*, vol. 31 (2), pp. 805–820, 1995.
- [8] S. Kogan *et al.*, “Joint TSI mitigation and clutter nulling architectures,” in *Proc. 5th DARPA Adv. Sig. Proc. Hot Clutter Tech. Interchange Meeting*, Rome Laboratory, 1997.
- [9] Y.I. Abramovich, V.N. Mikhaylyukov, and I.P. Malyavin, “Stabilisation of the autoregressive characteristics of spatial clutters in the case of nonstationary spatial filtering,” *Soviet Journal of Communication Technology and Electronics*, vol. 37 (2), pp. 10–19, 1992, English translation of *Radioteknika i Elektronika*.
- [10] Y.I. Abramovich, F.F. Yevstratov, and V.N. Mikhaylyukov, “Experimental investigation of efficiency of adaptive spatial unpremeditated noise compensation in HF radars for remote sea surface diagnostics,” *Soviet Journal of Communication Technology and Electronics*, vol. 38 (10), pp. 112–118, 1993, English translation of *Radioteknika i Elektronika*.
- [11] Y.I. Abramovich, A.Y. Gorokhov, V.N. Mikhaylyukov, and I.P. Malyavin, “Exterior noise adaptive rejection for OTH radar implementations,” in *Proc. ICASSP-94*, Adelaide, 1994, vol. 6, pp. 105–107.
- [12] Y.I. Abramovich and A.Y. Gorokhov, “Adaptive OTHR signal extraction under nonstationary ionospheric propagation conditions,” in *Proc. RADAR-94*, Paris, 1994, pp. 420–425.
- [13] L.E. Brennan, “Cancellation of terrain scattered jamming in airborne radars,” in *Proc. ASAP-96*, MIT Lincoln Laboratory, 1996.
- [14] T.H. Slocumb, J.R. Guerci, and P.M. Techau, “Hot and cold clutter mitigation using deterministic and adaptive filters,” in *Proc. 5th DARPA Adv. Sig. Proc. Hot Clutter Tech. Interchange Meeting*, Rome Laboratory, 1997.
- [15] D.J. Rabideau, “Advanced stap for TSI modulated clutter,” in *Proc. ASAP-98*, MIT Lincoln Laboratory, 1998.
- [16] D.E. Barrick, “*Remote sensing of sea state by radar*,” in *Remote Sensing of the Troposphere*, V.E. Derr, Ed. Government Printing Office, Washington DC, 1972, Chapter 12.
- [17] R.A. Horn and C.R. Johnson, *Matrix Analysis*, Cambridge University Press, England, 1990.
- [18] Y.I. Abramovich, A.Y. Gorokhov, and N.K. Spencer, “Convergence analysis of stochastically-constrained sample matrix inversion algorithms,” in *Proc. ISCAS-96*, Atlanta, USA, 1996, vol. 2, pp. 449–452.
- [19] “Innovative radar for export,” *Australian Defence Science*, vol. 6 (3), pp. 12, 1998.

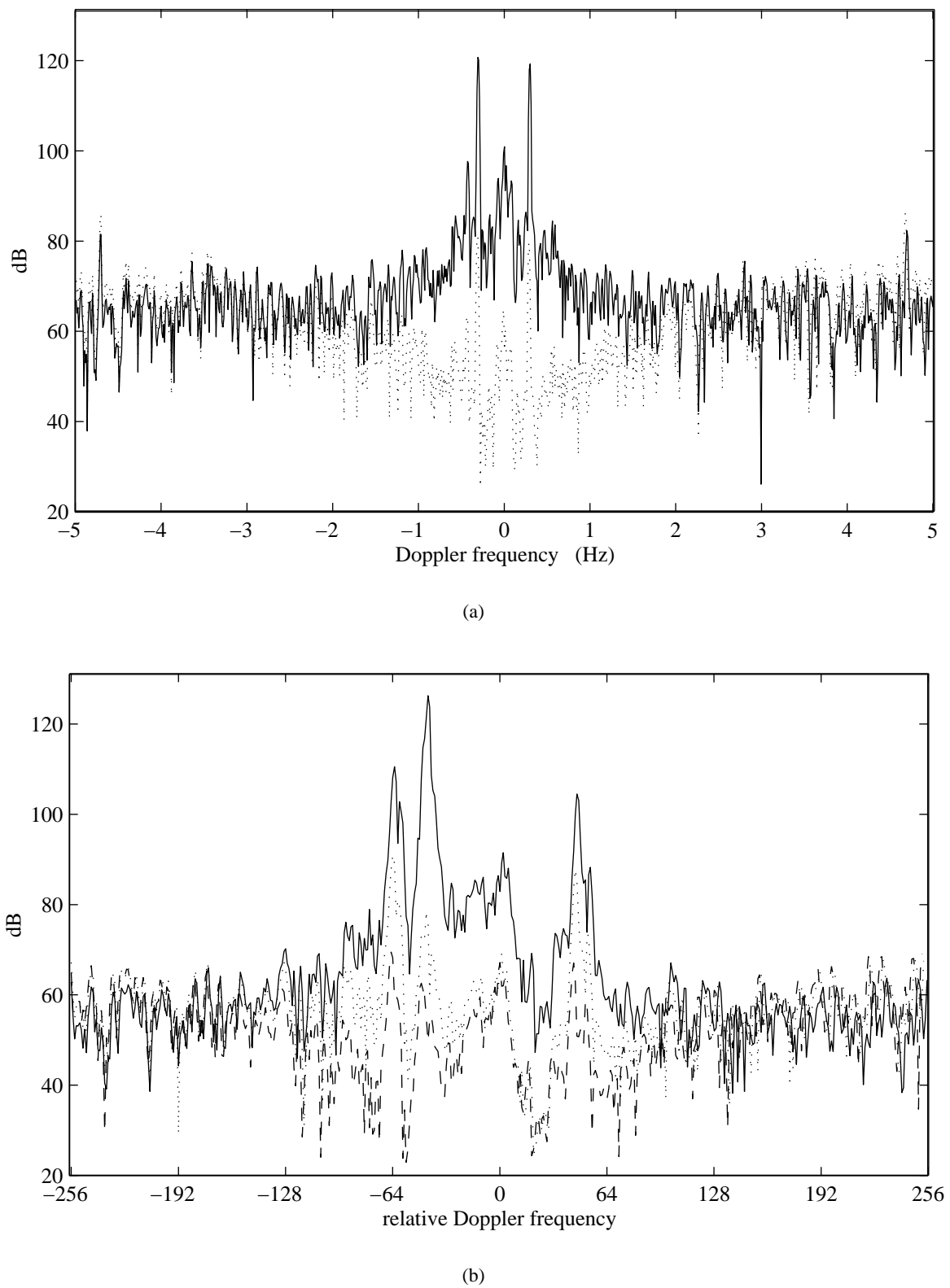
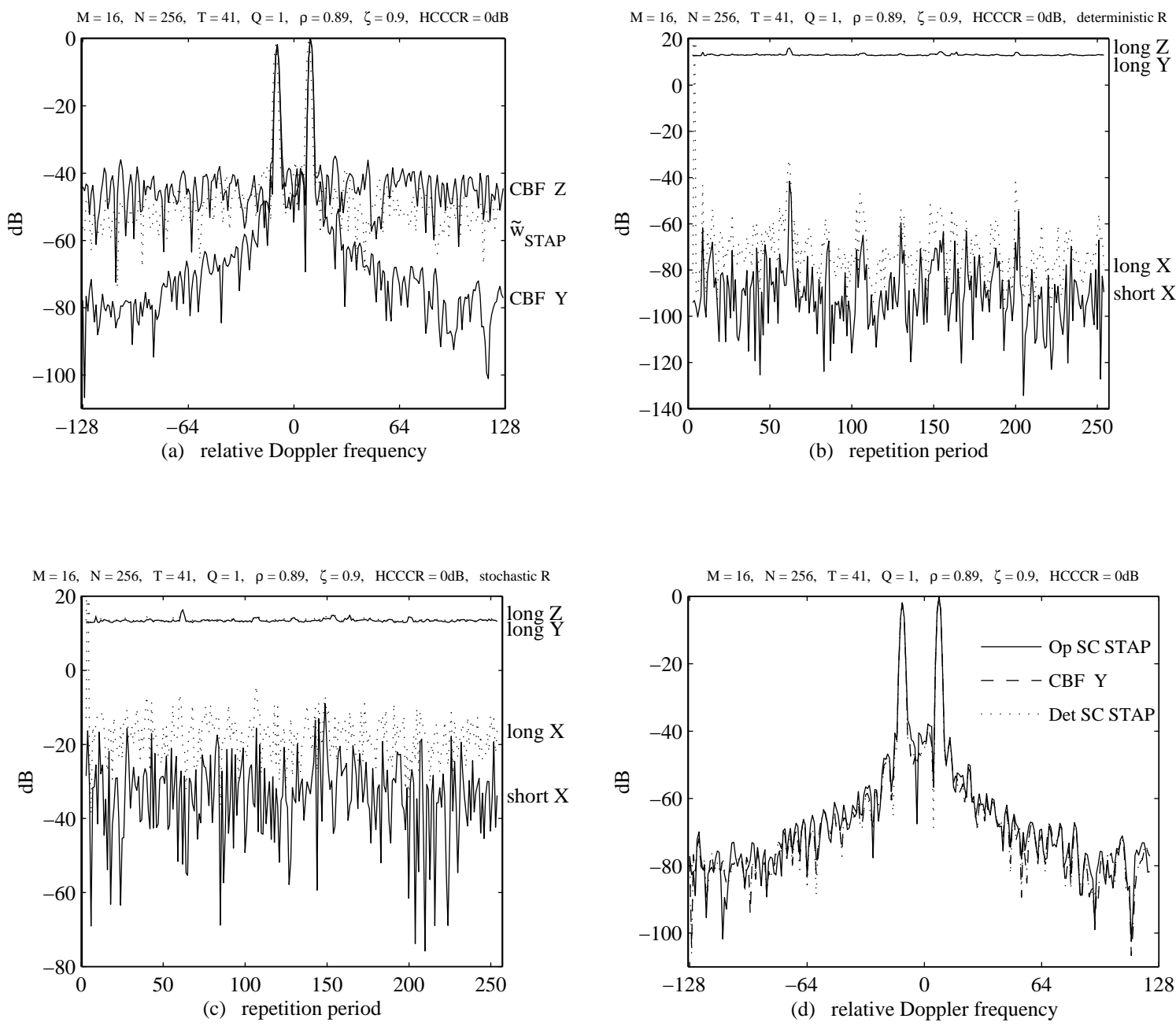


Figure 1: Noise-floor comparison in two sets of real surface-wave OTHR data.

Figure 2: Simulation results for a hot-clutter-to-cold-clutter ratio (HCCCR) of 0dB: (a) standard processing Doppler spectra, (b) and (c) scalar filter output, (d) Doppler spectra for proposed techniques.



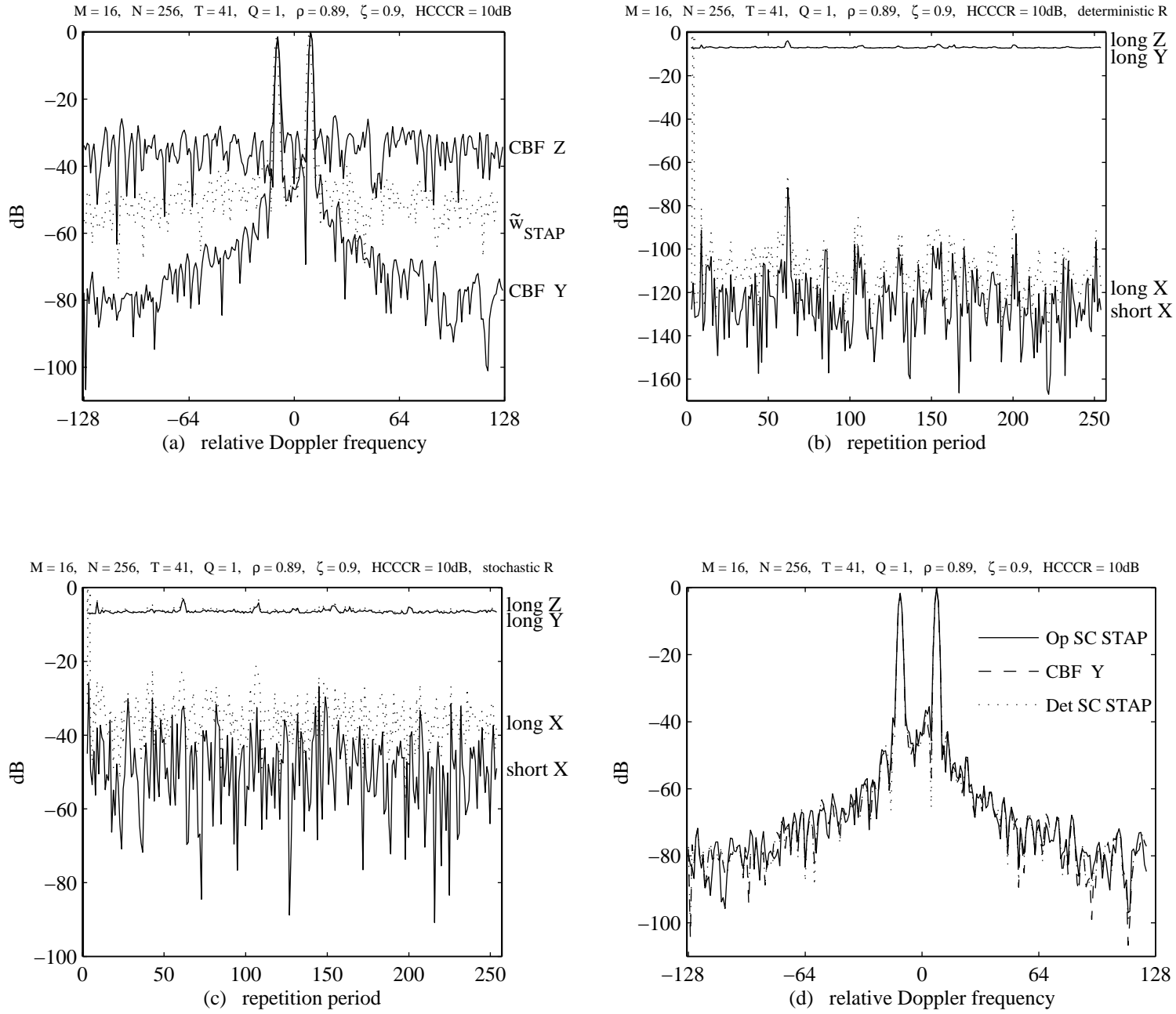
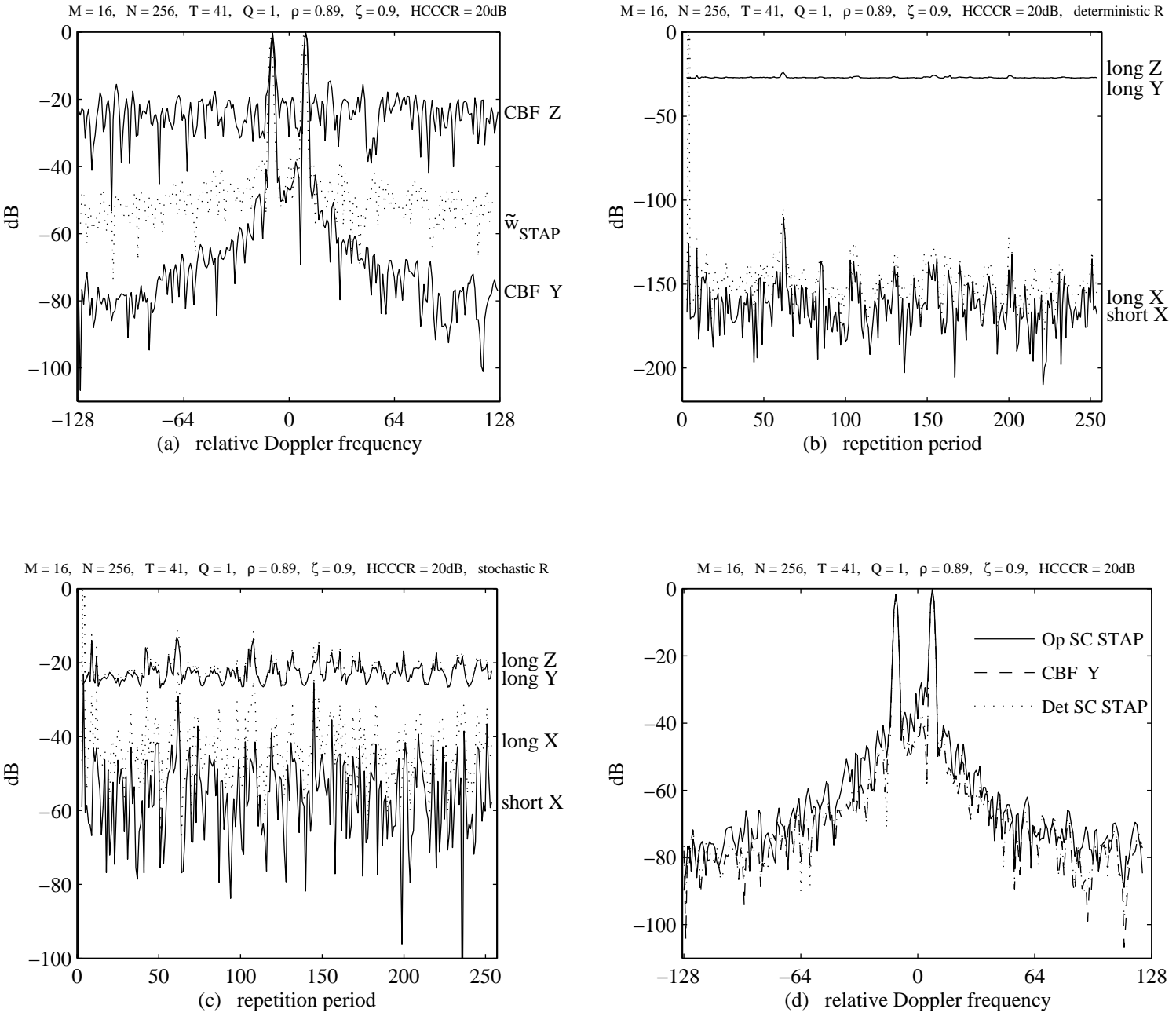


Figure 3: Same simulation as in Fig. 2 but for a hot-clutter-to-cold-clutter ratio (HCCCR) of 10dB.

Figure 4: Same simulation as in Fig. 2 but for a hot-clutter-to-cold-clutter ratio (HCCCR) of 20dB.



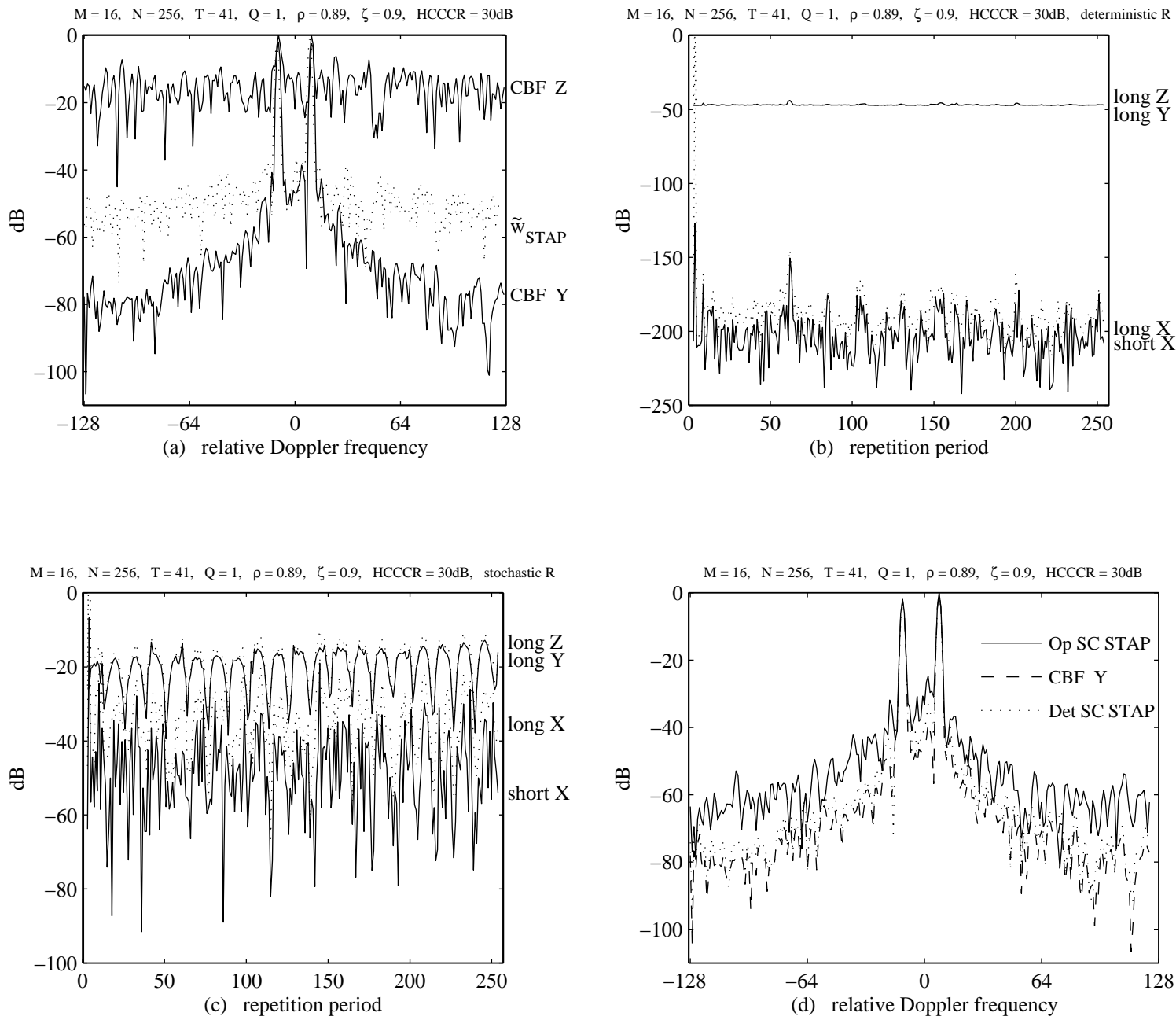


Figure 5: Same simulation as in Fig. 2 but for a hot-clutter-to-cold-clutter ratio (HCCCR) of 30dB.

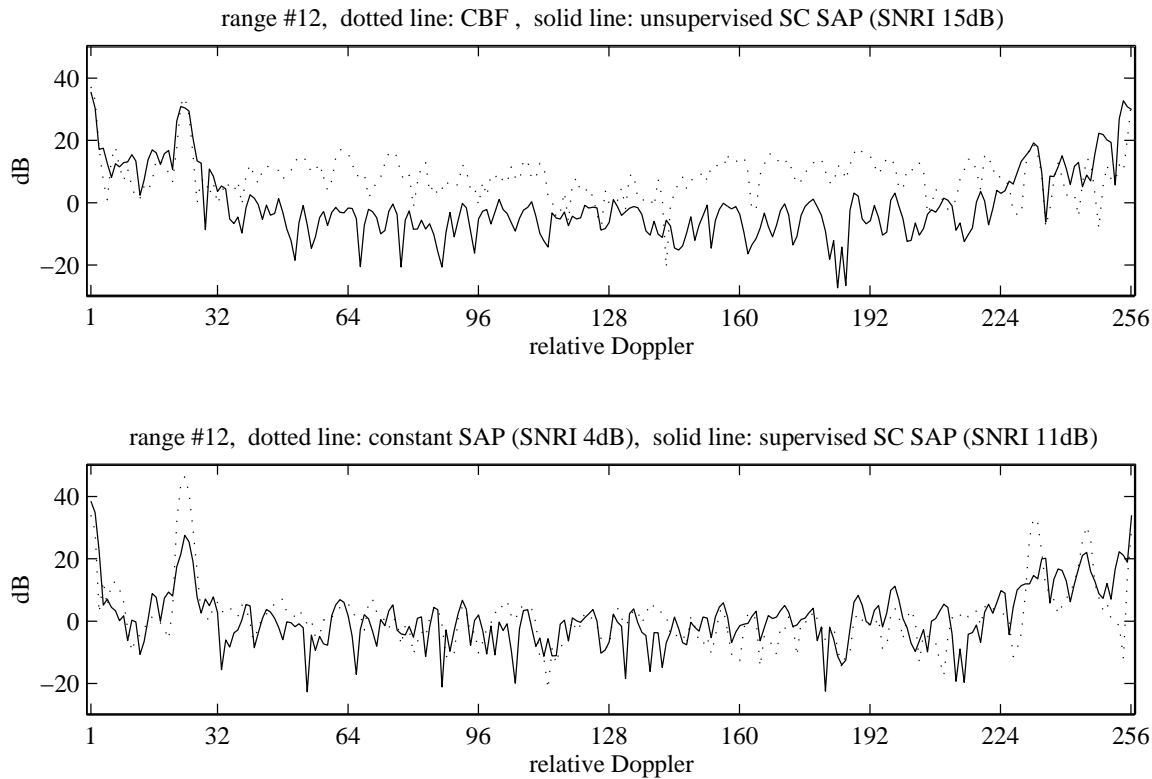


Figure 6: Comparison of “range cuts” for range cell 12.

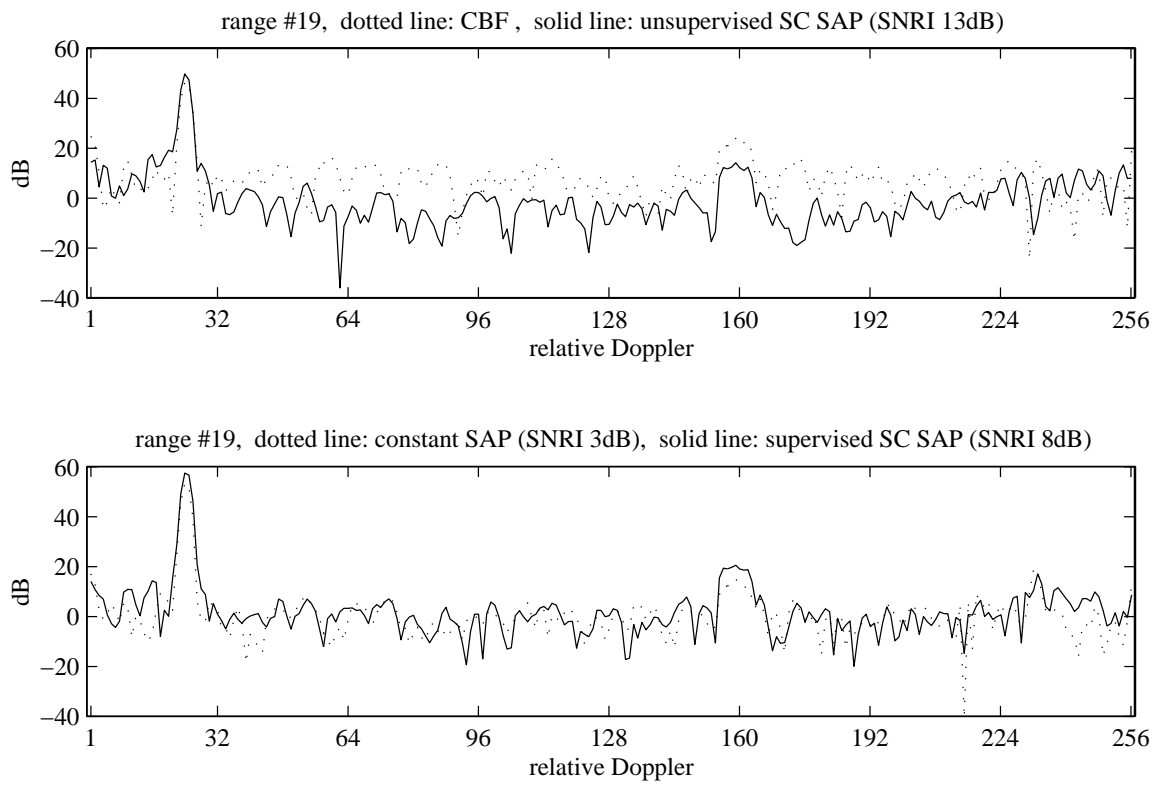


Figure 7: Comparison of “range cuts” for range cell 19.

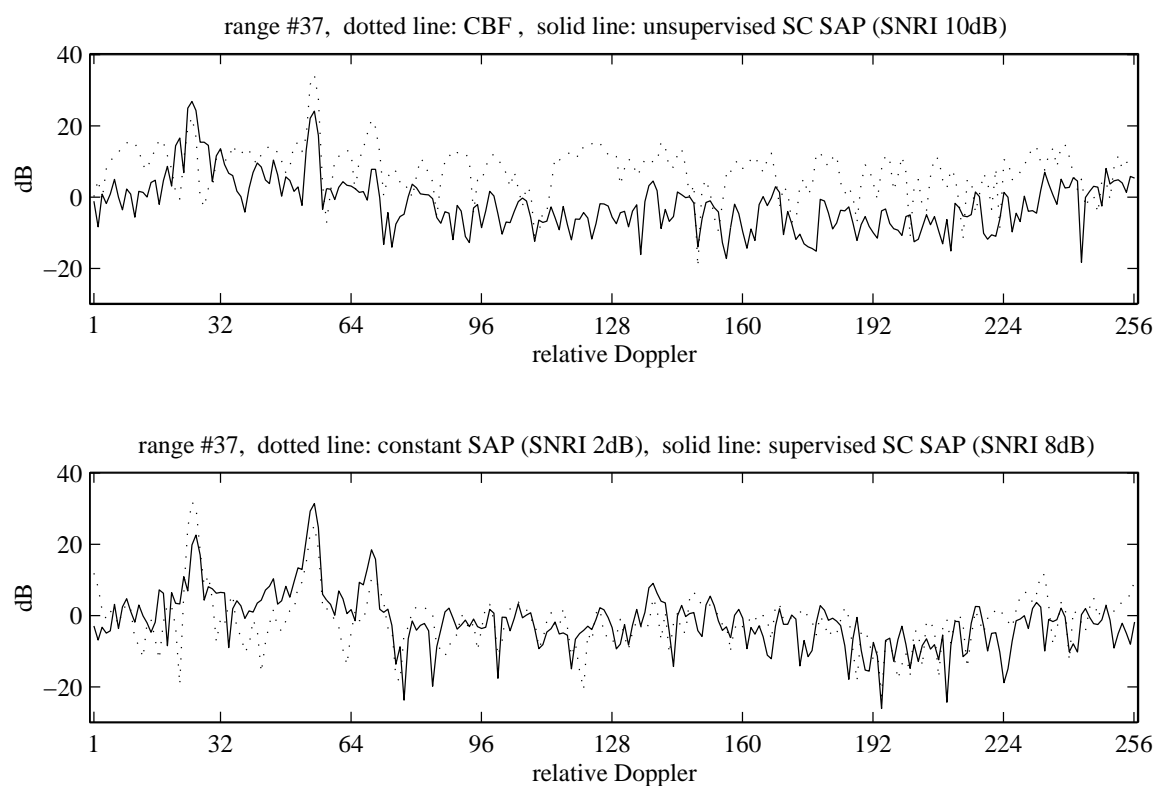


Figure 8: Comparison of “range cuts” for range cell 37.

REPORT DOCUMENTATION PAGE			
1. Recipient's Reference	2. Originator's References	3. Further Reference	4. Security Classification of Document
	RTO-EN-027 AC/323(SET-057)TP/41	ISBN 92-837-1064-9	UNCLASSIFIED/ UNLIMITED
5. Originator	Research and Technology Organisation North Atlantic Treaty Organisation BP 25, F-92201 Neuilly-sur-Seine Cedex, France		
6. Title	Military Application of Space-Time Adaptive Processing		
7. Presented at/sponsored by	the Sensors and Electronics Technology Panel (SET) and the Consultant and Exchange Programme of RTO presented on 16-17 September 2002 in Istanbul, Turkey, on 19-20 September 2002 in Wachtberg, Germany and on 23-24 September 2002 in Moscow, Russia.		
8. Author(s)/Editor(s)	Multiple		9. Date April 2003
10. Author's/Editor's Address	Multiple		11. Pages 184
12. Distribution Statement	There are no restrictions on the distribution of this document. Information about the availability of this and other RTO unclassified publications is given on the back cover.		
13. Keywords/Descriptors	Adaptive processing algorithms Adaptive systems Algorithms Bistatic radar Clutter cancellation Ground clutter Moving target indicators Over the horizon detection Radar detection Real time operations Signal processing Spaceborne detectors Spaceborne radar STAP (Space Time Adaptive Processing) Surface targets Synthetic aperture radar Target acquisition		
14. Abstract	Space-time adaptive processing (STAP) is a signal processing technique for detection of moving targets buried in ground clutter by means of a moving (air- or spaceborne) radar. No future military air- or spaceborne radar will be designed without this feature. This Lecture Series gives a comprehensive overview of the broad field of STAP, starting with fundamentals, clutter characteristics, application to synthetic aperture radar (SAR), and issues in over-the-horizon radar (OTH). Beside the principles and underlying fundamentals special aspect are covered, such as economic STAP architectures, limiting effects, algorithms for real-time processing, and special applications such as bistatic radar configurations and terrain scattered jamming.		

This page has been deliberately left blank

Page intentionnellement blanche



RESEARCH AND TECHNOLOGY ORGANISATION

BP 25 • 7 RUE ANCELLE
F-92201 NEUILLY-SUR-SEINE CEDEX • FRANCE
Télécopie 0(1)55.61.22.99 • E-mail mailbox@rta.nato.int

DIFFUSION DES PUBLICATIONS
RTO NON CLASSIFIEES

L'Organisation pour la recherche et la technologie de l'OTAN (RTO), détient un stock limité de certaines de ses publications récentes, ainsi que de celles de l'ancien AGARD (Groupe consultatif pour la recherche et les réalisations aérospatiales de l'OTAN). Celles-ci pourront éventuellement être obtenues sous forme de copie papier. Pour de plus amples renseignements concernant l'achat de ces ouvrages, adressez-vous par lettre ou par télécopie à l'adresse indiquée ci-dessus. Veuillez ne pas téléphoner.

Des exemplaires supplémentaires peuvent parfois être obtenus auprès des centres nationaux de distribution indiqués ci-dessous. Si vous souhaitez recevoir toutes les publications de la RTO, ou simplement celles qui concernent certains Panels, vous pouvez demander d'être inclus sur la liste d'envoi de l'un de ces centres.

Les publications de la RTO et de l'AGARD sont en vente auprès des agences de vente indiquées ci-dessous, sous forme de photocopie ou de microfiche. Certains originaux peuvent également être obtenus auprès de CASI.

CENTRES DE DIFFUSION NATIONAUX**ALLEMAGNE**

Streitkräfteamt / Abteilung III
Fachinformationszentrum der
Bundeswehr, (FIZBw)
Friedrich-Ebert-Allee 34
D-53113 Bonn

BELGIQUE

Etat-Major de la Défense
Département d'Etat-Major Stratégie
ACOS-STRAT-STE – Coord. RTO
Quartier Reine Elisabeth
Rue d'Evêre, B-1140 Bruxelles

CANADA

DSIGRD2
Bibliothécaire des ressources du savoir
R et D pour la défense Canada
Ministère de la Défense nationale
305, rue Rideau, 9^e étage
Ottawa, Ontario K1A 0K2

DANEMARK

Danish Defence Research Establishment
Ryvangs Allé 1, P.O. Box 2715
DK-2100 Copenhagen Ø

ESPAGNE

INTA (RTO/AGARD Publications)
Carretera de Torrejón a Ajalvir, Pk.4
28850 Torrejón de Ardoz - Madrid

ETATS-UNIS

NASA Center for AeroSpace
Information (CASI)
Parkway Center
7121 Standard Drive
Hanover, MD 21076-1320

FRANCE

O.N.E.R.A. (ISP)
29, Avenue de la Division Leclerc
BP 72, 92322 Châtillon Cedex

GRECE (Correspondant)

Defence Industry & Research
General Directorate
Research Directorate
Fakinos Base Camp
S.T.G. 1020
Holargos, Athens

HONGRIE

Department for Scientific
Analysis
Institute of Military Technology
Ministry of Defence
H-1525 Budapest P O Box 26

ISLANDE

Director of Aviation
c/o Flugrad
Reykjavik

ITALIE

Centro di Documentazione
Tecnico-Scientifica della Difesa
Via XX Settembre 123a
00187 Roma

LUXEMBOURG

Voir Belgique

NORVEGE

Norwegian Defence Research
Establishment
Attn: Biblioteket
P.O. Box 25, NO-2007 Kjeller

PAYS-BAS

Royal Netherlands Military
Academy Library
P.O. Box 90.002
4800 PA Breda

POLOGNE

Armament Policy Department
218 Niepodleglosci Av.
00-911 Warsaw

PORTUGAL

Estado Maior da Força Aérea
SDFA - Centro de Documentação
Alfragide
P-2720 Amadora

REPUBLIQUE TCHEQUE

DIC Czech Republic-NATO RTO
VTÚL a PVO Praha
Mladoboleslavská ul.
Praha 9, 197 06, Česká republika

ROYAUME-UNI

Dstl Knowledge Services
Kentigern House, Room 2246
65 Brown Street
Glasgow G2 8EX

TURQUIE

Millî Savunma Başkanlığı (MSB)
ARGE Dairesi Başkanlığı (MSB)
06650 Bakanlıklar - Ankara

AGENCES DE VENTE**The British Library Document**

Supply Centre
Boston Spa, Wetherby
West Yorkshire LS23 7BQ
Royaume-Uni

**Canada Institute for Scientific and
Technical Information (CISTI)**

National Research Council
Acquisitions
Montreal Road, Building M-55
Ottawa K1A 0S2, Canada

**NASA Center for AeroSpace
Information (CASI)**
Parkway Center
7121 Standard Drive
Hanover, MD 21076-1320
Etats-Unis

Les demandes de documents RTO ou AGARD doivent comporter la dénomination "RTO" ou "AGARD" selon le cas, suivie du numéro de série (par exemple AGARD-AG-315). Des informations analogues, telles que le titre et la date de publication sont souhaitables. Des références bibliographiques complètes ainsi que des résumés des publications RTO et AGARD figurent dans les journaux suivants:

Scientific and Technical Aerospace Reports (STAR)
STAR peut être consulté en ligne au localisateur de ressources uniformes (URL) suivant:
<http://www.sti.nasa.gov/Pubs/star/Star.html>
STAR est édité par CASI dans le cadre du programme NASA d'information scientifique et technique (STI)
STI Program Office, MS 157A
NASA Langley Research Center
Hampton, Virginia 23681-0001
Etats-Unis

Government Reports Announcements & Index (GRA&I)
publié par le National Technical Information Service
Springfield
Virginia 2216
Etats-Unis
(accessible également en mode interactif dans la base de données bibliographiques en ligne du NTIS, et sur CD-ROM)



Imprimé par Groupe d'imprimerie St-Joseph inc.
(Membre de la Corporation St-Joseph)
1165, rue Kenaston, Ottawa (Ontario), Canada K1G 6S1



RESEARCH AND TECHNOLOGY ORGANISATION

BP 25 • 7 RUE ANCELLE
F-92201 NEUILLY-SUR-SEINE CEDEX • FRANCE
Telefax 0(1)55.61.22.99 • E-mail mailbox@rta.nato.int

DISTRIBUTION OF UNCLASSIFIED
RTO PUBLICATIONS

NATO's Research and Technology Organisation (RTO) holds limited quantities of some of its recent publications and those of the former AGARD (Advisory Group for Aerospace Research & Development of NATO), and these may be available for purchase in hard copy form. For more information, write or send a telefax to the address given above. **Please do not telephone.**

Further copies are sometimes available from the National Distribution Centres listed below. If you wish to receive all RTO publications, or just those relating to one or more specific RTO Panels, they may be willing to include you (or your organisation) in their distribution.

RTO and AGARD publications may be purchased from the Sales Agencies listed below, in photocopy or microfiche form. Original copies of some publications may be available from CASI.

NATIONAL DISTRIBUTION CENTRES

BELGIUM

Etat-Major de la Défense
Département d'Etat-Major Stratégie
ACOS-STRAT-STE – Coord. RTO
Quartier Reine Elisabeth
Rue d'Evêre, B-1140 Bruxelles

CANADA

DRDKIM2
Knowledge Resources Librarian
Defence R&D Canada
Department of National Defence
305 Rideau Street, 9th Floor
Ottawa, Ontario K1A 0K2

CZECH REPUBLIC

DIC Czech Republic-NATO RTO
VTÚL a PVO Praha
Mladoboleslavská ul.
Praha 9, 197 06, Česká republika

DENMARK

Danish Defence Research
Establishment
Ryvangs Allé 1, P.O. Box 2715
DK-2100 Copenhagen Ø

FRANCE

O.N.E.R.A. (ISP)
29 Avenue de la Division Leclerc
BP 72, 92322 Châtillon Cedex

GERMANY

Streitkräfteamt / Abteilung III
Fachinformationszentrum der
Bundeswehr, (FIZBw)
Friedrich-Ebert-Allee 34
D-53113 Bonn

**NASA Center for AeroSpace
Information (CASI)**
Parkway Center
7121 Standard Drive
Hanover, MD 21076-1320
United States

Requests for RTO or AGARD documents should include the word 'RTO' or 'AGARD', as appropriate, followed by the serial number (for example AGARD-AG-315). Collateral information such as title and publication date is desirable. Full bibliographical references and abstracts of RTO and AGARD publications are given in the following journals:

Scientific and Technical Aerospace Reports (STAR)

STAR is available on-line at the following uniform resource locator:

<http://www.sti.nasa.gov/Pubs/star/Star.html>

STAR is published by CASI for the NASA Scientific and Technical Information (STI) Program
STI Program Office, MS 157A
NASA Langley Research Center
Hampton, Virginia 23681-0001
United States

GREECE (Point of Contact)

Defence Industry & Research
General Directorate
Research Directorate
Fakinos Base Camp
S.T.G. 1020
Holargos, Athens

HUNGARY

Department for Scientific
Analysis
Institute of Military Technology
Ministry of Defence
H-1525 Budapest P O Box 26

ICELAND

Director of Aviation
c/o Flugrad
Reykjavik

ITALY

Centro di Documentazione
Tecnico-Scientifica della Difesa
Via XX Settembre 123a
00187 Roma

LUXEMBOURG

See Belgium

NETHERLANDS

Royal Netherlands Military
Academy Library
P.O. Box 90.002
4800 PA Breda

NORWAY

Norwegian Defence Research
Establishment
Attn: Biblioteket
P.O. Box 25, NO-2007 Kjeller

SALES AGENCIES

The British Library Document

Supply Centre
Boston Spa, Wetherby
West Yorkshire LS23 7BQ
United Kingdom

POLAND

Armament Policy Department
218 Niepodleglosci Av.
00-911 Warsaw

PORTUGAL

Estado Maior da Força Aérea
SDFA - Centro de Documentação
Alfragide
P-2720 Amadora

SPAIN

INTA (RTO/AGARD Publications)
Carretera de Torrejón a Ajalvir, Pk.4
28850 Torrejón de Ardoz - Madrid

TURKEY

Millî Savunma Başkanlığı (MSB)
ARGE Dairesi Başkanlığı (MSB)
06650 Bakanlıklar - Ankara

UNITED KINGDOM

Dstl Knowledge Services
Kentigern House, Room 2246
65 Brown Street
Glasgow G2 8EX

UNITED STATES

NASA Center for AeroSpace
Information (CASI)
Parkway Center
7121 Standard Drive
Hanover, MD 21076-1320

**Canada Institute for Scientific and
Technical Information (CISTI)**

National Research Council
Acquisitions
Montreal Road, Building M-55
Ottawa K1A 0S2, Canada

Government Reports Announcements & Index (GRA&I)

published by the National Technical Information Service
Springfield
Virginia 22161
United States
(also available online in the NTIS Bibliographic Database or on CD-ROM)



Printed by St. Joseph Print Group Inc.

(A St. Joseph Corporation Company)

1165 Kenaston Street, Ottawa, Ontario, Canada K1G 6S1